Geomechanical and petrological characterisation of exposed slip zones, Alpine Fault, New Zealand

---

Bernhard Schuck

kumulative Univ.-Diss.
zur Erlangung des akademischen Grades
“doctor rerum naturalium”
(Dr. rer. nat.)
in der Wissenschaftsdisziplin Geologie

eingereicht an der
Mathematisch-Naturwissenschaftlichen Fakultät
Institut für Geowissenschaften
der Universität Potsdam

Ort und Tag der Disputation: Potsdam, den 17. Januar 2020

Hauptbetreuer: Prof. Dr. Georg Dresen
Zweitbetreuerin: Prof. Dr. Virginia Toy
Externer Gutachter: Prof. Dr. Giorgio Pennacchioni

Published online at the
Institutional Repository of the University of Potsdam:
https://doi.org/10.25932/publishup-44612
https://nbn-resolving.org/urn:nbn:de:kobv:517-opus4-446129

Contents

Affidavit

I hereby declare that this thesis represents my own work and that I have used no sources and aids other than those indicated. All passages quoted from publications or paraphrased from these sources are properly cited and attributed. I further declare that I have not submitted this thesis at any other institution in order to obtain an academic degree.

Potsdam, 3rd March 2020

_____

Bernhard Schuck

Abstract

The Alpine Fault is a large, plate-bounding, strike-slip fault extending along the north-western edge of the Southern Alps, South Island, New Zealand. It regularly accommodates large ($M_W > 8$) earthquakes and has a high statistical probability of failure in the near future, i.e., is late in its seismic cycle. This pending earthquake and associated co-seismic landslides are expected to cause severe infrastructural damage that would affect thousands of people, so it presents a substantial geohazard. The interdisciplinary study presented here aims to characterise the fault zone's 4D (space and time) architecture, because this provides information about its rheological properties that will enable better assessment of the hazard the fault poses.

The studies undertaken include field investigations of principal slip zone fault gouges exposed along strike of the fault, and subsequent laboratory analyses of these outcrop and additional borehole samples. These observations have provided new information on (I) characteristic microstructures down to the nanoscale that indicate which deformation mechanisms operated within the rocks, (II) mineralogical information that constrains the fault's geomechanical behaviour and (III) geochemical compositional information that allows the influence of fluid-related alteration processes on material properties to be unraveled.

Results show that along-strike variations of fault rock properties such as microstructures and mineralogical composition are minor and / or do not substantially influence fault zone architecture. They furthermore provide evidence that the architecture of the fault zone, particularly its fault core, is more complex than previously considered, and also more complex than expected for this sort of mature fault cutting quartzofeldspathic rocks. In particular our results strongly suggest that the fault has more than one principal slip zone, and that these form an anastomosing network extending into the basement below the cover of Quaternary sediments.

The observations detailed in this thesis highlight that two major processes, (I) cataclasis and (II) authigenic mineral formation, are the major controls on the rheology of the Alpine Fault. The velocity-weakening behaviour of its fault gouge is favoured by abundant nanoparticles promoting powder lubrication and grain rolling rather than frictional sliding. Wall-rock fragmentation is accompanied by co-seismic, fluid-assisted dilatancy that is recorded by calcite cementation. This mineralisation, along with authigenic formation of phyllosilicates, quickly alters the petrophysical fault zone properties after each rupture, restoring fault competency. Dense networks of anastomosing and mutually cross-cutting calcite veins and intensively reworked gouge matrix demonstrate that strain repeatedly localised within the narrow fault gouge. Abundantly undeformed euhedral chlorite crystallites and calcite veins cross-cutting both fault gouge and gravels that overlie basement on the fault's footwall provide evidence

that the processes of authigenic phyllosilicate growth, fluid-assisted dilatancy and associated fault healing are processes active particularly close to the Earth's surface in this fault zone.

Exposed Alpine Fault rocks are subject to intense weathering as direct consequence of abundant orogenic rainfall associated with the fault's location at the base of the Southern Alps. Furthermore, fault rock rheology is substantially affected by shallow-depth conditions such as the juxtaposition of competent hanging wall fault rocks on poorly consolidated footwall sediments. This means microstructural, mineralogical and geochemical properties of the exposed fault rocks may differ substantially from those at deeper levels, and thus are not characteristic of the majority of the fault rocks' history. Examples are (I) frictionally weak smectites found within the fault gouges being artefacts formed at temperature conditions, and imparting petrophysical properties that are not typical for most of fault rocks of the Alpine Fault, (II) grain-scale dissolution resulting from subaerial weathering rather than deformation by pressure-solution processes and (III) fault gouge geometries being more complex than expected for deeper counterparts.

The methodological approaches deployed in analyses of this, and other fault zones, and the major results of this study are finally discussed in order to contextualize slip zone investigations of fault zones and landslides. Like faults, landslides are major geohazards, which highlights the importance of characterising their geomechanical properties. Similarities between faults, especially those exposed to subaerial processes, and landslides, include mineralogical composition and geomechanical behaviour. Together, this ensures failure occurs predominantly by cataclastic processes, although aseismic creep promoted by weak phyllosilicates is not uncommon. Consequently, the multidisciplinary approach commonly used to investigate fault zones may contribute to increase the understanding of landslide faulting processes and the assessment of their hazard potential.

Zusammenfassung

Die Alpine Fault ist eine große Plattengrenze mit lateralem Versatz, die sich entlang des nordwestlichen Fußes der Südalpen, Südinsel Neuseeland, erstreckt. Regelmäßig ereignen sich große ($M_W > 8$) Erdbeben und gegenwärtig befindet sich die Störung am Ende ihres Erdbebenzyklus, so dass ein baldiges Beben sehr wahrscheinlich ist. Die Alpine Fault stellt eine bedeutende Naturgefahr dar und so wird davon ausgegangen, dass tausende Menschen von dem anstehenden Erdbeben, ko-seismischen Hangrutschungen und den damit einhergehenden großen Schäden an der Infrastruktur betroffen sein werden. Daher zielt die hier vorgestellte interdisziplinäre Studie darauf ab, den Aufbau der Störungszone in 4D (räumlich und zeitlich) zu charakterisieren, weil dies Aufschluss über ihre rheologischen Eigenschaften liefert und damit einen Beitrag zur Einschätzung der von der Störung ausgehenden Gefahr leisten wird.

Die durchgeführten Arbeiten umfassen Felduntersuchungen der entlang der Störung aufgeschlossenen Hauptscherzone und sich daran anschließende Laboruntersuchungen dieser Aufschluss- und zusätzlicher Bohrlochproben. Diese geben Aufschluss über (I) charakteristische Mikrostrukturen bis in den Nanometerbereich, was erlaubt Deformationsmechanismen abzuleiten, (II) die Mineralogie und ihren Einfluss auf das geomechanische Verhalten und (III) die geochemische Zusammensetzung, die es ermöglicht, den Einfluss fluid-bezogener Alterationsprozesse auf Materialeigenschaften besser zu verstehen.

Die Ergebnisse zeigen, dass Variationen der Eigenschaften der Störungsgesteine, wie Mikrostrukturen und mineralogische Zusammensetzung, entlang der Störung nur untergeordnet auftreten und den Aufbau der Störungszone nicht oder nur unwesentlich beeinflussen. Darüber hinaus zeigen sie, dass der Aufbau der Störungszone, vor allem ihres Kerns, komplexer ist als bisher angenommen. Dies ist unerwartet für eine Störung in quartz- und feldspatreichem Gestein dieses Alters. Diese Sicht wird von Ergebnissen gestützt, die nahelegen, dass die Störung mehr als eine Hauptscherzone hat und dass diese ein anastomisierendes Netzwerk bilden, das sich bis in das Festgestein unterhalb der Deckschicht aus quartären Sedimenten erstreckt.

Die Beobachtungen dieser Arbeit zeigen, dass zwei Prozesse, (I) Kataklase und (II) authigenes Mineralwachstum, den größten Einfluss auf die Rheologie der Alpine Fault haben. Das “velocity-weakening”-Verhalten der Hauptscherzonen und ihres Gesteinsmehls wird durch die große Anzahl von Nanopartikeln begünstigt, die das Rollen der Partikel zu Ungunsten von Gleitreibungsrutschen fördern. Die Zerstückelung des Umgebungsgesteins geht mit koseismischer, fluid-unterstützter Dilatanz einher, die die anschließende Zementierung durch Kalzit begünstigt. Diese, in Kombination mit authigenen Schichtsilikaten, stellt die petrophysikalischen Eigenschaften der Störungszone nach jedem Erdbeben schnell wieder her. Dichte Netzwerke anastomisierender und sich gegenseitig durchschlagender Kalzitadern und

umfassend aufgearbeitetes Gesteinsmehl belegen, dass Verformung wiederholt in den dünnen Hauptscherbahnen lokalisiert wurde. Kalzitadern durschlagen sowohl das Gesteinsmehl der Hauptscherbahnen als auch das Geröll, das die oberflächennahe Sedimentabdeckung des Festgesteins im Liegenden darstellt. Dies und allgegenwärtige, undeformierte, euhedrale Chlorit-Kristalle belegen, dass authigenes Schichtsilikatwachstum, fluid-unterstütze Dilatanz und das damit einhergehende Heilen der Störung Prozesse sind, die auch nahe der Erdoberfläche wirken.

Freigelegte Gesteine der Alpine Fault sind intensiver Verwitterung als direkter Folge des reichlich vorhandenen Steigungsregens, der sich aus der Lage der Störung am Fuß der Südalpen ergibt, ausgesetzt. Darüber hinaus wird die Rheologie der Störungsgesteine erheblich durch oberflächennahen Randbedingungen wie die Gegenüberstellung kompetenter Störungsgesteine des Hangenden mit wenig-konsolidierten Sedimenten des Liegenden beeinflusst. Dies hat zur Folge, dass sich mikrostrukturelle, mineralogische und geochemische Eigenschaften der freigelegten Störungsgesteine erheblich von denen in größeren Tiefen unterscheiden können und folglich nicht charakteristisch für den Großteil der Deformationsgeschichte sind. Beispiele hierfür sind (I) Smektitphasen in den Hauptscherzonen, die einen niedrigen Reibungskoeffizienten aufweisen, allerdings Artefakte von für die Mehrheit der Gesteine dieser Störung atypischer Temperaturen und petrophysikalischer Eigenschaften sind, (II) angelöste Minerale als Ergebnis oberflächennaher Verwitterung und nicht von Drucklösung und (III) ein interner Aufbau des Gesteinsmehls der Hauptscherbahnen, der komplexerer ist, als dies für das Äquivalent in größerer Tiefe zu erwarten wäre.

Schließlich werden die Ergebnisse dieser Arbeit gemeinsam mit den Hauptbefunden und methodischen Ansätzen anderer Studien zu Störungszonen diskutiert und in Kontext zu Analysen von Scherzonen in Störungen und Hangrutschungen gestellt. Hangrutschungen sind, wie Störungen, bedeutende Naturgefahren, was die Notwendigkeit, ihre geomechanischen Eigenschaften zu charakterisieren, herausstreicht. Störungen, vor allem jene, die Oberflächenprozessen ausgesetzt sind, und Hangrutschungen teilen viele Gemeinsamkeiten wie mineralogische Zusammensetzung und geomechanisches Verhalten, was vor allem zu Versagen mittels kataklastischer Mechanismen führt; allerdings ist aseismisches Kriechen, befördert durch Schichtsilikate mit niedrigem Reibungskoeffizienten, nicht ungewöhnlich. Folglich könnte der multidisziplinäre Ansatz, der in der Regel zur Untersuchung von Störungszonen herangezogen wird, dazu beitragen das Verständnis von Hangrutschungen zu verbessern und ihr Gefährdungspotential abzuschätzen.

Statement of contribution

The main part of this thesis comprises three papers, each of them presented as an individual chapter (Chapters 2 to 4). Two of the chapters were published in 2018 (Chapter 3) and 2020 (Chapter 2), respectively, while the third one (Chapter 4) has been submitted and accepted for peer review. References for all chapters are presented in one final bibliography. The PhD candidate is the lead author of all papers and his contributions are outlined in the following.

Chapter 2: Schuck, B., Schleicher, A.M., Janssen, C., Toy, V.G. and Dresen, G. (2020): Fault zone architecture of a large plate-bounding strike-slip fault: a case study from the Alpine Fault, New Zealand. *Solid Earth* 11, 95 - 124, doi:10.5194/se-11-95-2020. The PhD candidate was in charge of sample collection and preparation, data acquisition and evaluation. Other contributions are noted in the acknowledgements. The manuscript was drafted by the PhD candidate and substantially improved by co-author contributions.

Chapter 3: Schuck, B., Janssen, C., Schleicher, A.M., Toy, V.G. and Dresen, G. (2018): Microstructures imply cataclasis and authigenic mineral formation control geomechanical properties of New Zealand's Alpine Fault. *Journal of Structural Geology* 110, 172 - 186, doi:10.1016/jsg.2018.03.001. The PhD candidate was responsible for field work (initially accompanied by V.G. Toy), sample preparation, data acquisition and evaluation. Assistance during these stages is explicitly acknowledged in the last section of the chapter. Again, the manuscript was drafted by the PhD candidate and substantially improved by co-author contributions.

Chapter 4: Schuck, B. and Janssen, C. (submitted to *Geochemistry, Geophysics, Geosystems*): Fault and landslide slip zone comparisons yield new insight about the processes that operate within them, and their hazard potential. Both authors contributed equally to this manuscript. C. Janssen was responsible for data acquisition presented in Section 4.4.1.3 and the first draft. Subsequently, the PhD candidate revised and enlarged the scope of the manuscript and produced its final version. Supervisors provided comments that helped to improve the manuscript – these are acknowledged in the last section of this chapter.

Acknowledgements

First of all, I would like to thank Georg Dresen for giving me the opportunity to pursue this project. His constructive criticism helped to improve this work.

Virginia Toy, wherever on the globe she has been, was always willing to provide advice, feedback and support, when needed. I am grateful for her excellent supervision enabling the success of this project.

Christoph Janssen was a great mentor to me. In times of frustration, he always had advice and supported me to pursue my own ideas.

I am grateful that Anja Schleicher did not hesitate a moment to train me in XRD analyses and that she was always keen to discuss draft manuscripts.

It was a pleasure to have such nice colleagues. Maria, Johannes, Livia and Stephan, I always enjoyed spending time with you. Furthermore, I am happy that Livia was always willing to listen to my thoughts and never hesitated to tell me what she thought about them and that Johannes was always willing to solve my computer issues. I am not only happy that I had such great colleagues in Potsdam, but also that my "part-time" colleagues in Aachen always had time to discuss things over a coffee or two.

Maike, thank you for your support and having been there for so many years!

1 Introduction

Faults are major discontinuities in the crust that have accumulated significantly higher displacements than the surrounding host rock (Twiss and Moores, 2007; Ben-Zion, 2008; Bürgmann and Dresen, 2008; Fossen and Cavalcante, 2017) and that strongly impact the crust's rheology (Townend and Zoback, 2000; Bürgmann and Dresen, 2008). Earth's largest faults are those that form the major part of tectonic plate boundaries (Wells and Coppersmith, 1994). Many such structures cut through the entire crust and into the mantle lithosphere (Ergintav et al., 2007; Freed et al., 2006; Fuis et al., 2012; Norris and Toy, 2014). Consequently, substantial portions of these structures deform aseismically by plastic processes (Kohlstedt et al., 1995; Bürgmann and Dresen, 2008; Rybacki et al., 2008; Fossen and Cavalcante, 2017). While rheology and strain localisation mechanisms at these deep crustal and upper mantle levels provide important controls on plate tectonics (e.g., Bercovici, 2003), the brittle geomechanical behaviour of these structures, which depends on boundary conditions at shallow to mid-crustal levels, has more impact on the hazard these structures present (e.g., Scholz, 2002; Ben-Zion, 2008; Martínez-Garzón et al., 2015).

It is only possible to infer the geomechanical properties of these faults at seismogenic depths through teleseismic observations (e.g., Raub et al., 2017) or by extrapolating laboratory analyses to crustal conditions (Kohlstedt et al., 1995; Bürgmann and Dresen, 2008; Rybacki et al., 2008). Alternatively, deformation processes can be deduced from analyses of exhumed fault rocks (de Bresser, 1996; Passchier and Trouw, 2005; Rybacki et al., 2011). Scientific drilling also allows recovery of fault rocks less affected by superficial processes, but this is an expansive method of exploration that yields quite small samples, and we can question how representative these are (e.g., Zoback et al., 2007; Toy et al., 2015). Indeed, most natural fault rock analyses reported to date have relied on exhumed samples, even though the records of initial processes that operated within these are commonly obscured by weathering (Faulkner et al., 2008; Mitchel and Faulkner, 2009). There are two possible scenarios leading to exhumed fault rocks: (I) if deformation ceases at depth, the rocks will be 'passively' exhumed and overprints due to shallow-level processes should be minor; (II) if the rocks continuously deform as they are exhumed, mineralogical and microstructural records of processes that operated at depth will be overprinted, and it will be challenging to unravel the deformation (Cooper and Norris, 1994; Kirkpatrick and Rowe, 2013; Toy et al., 2015).

The Alpine Fault is a mantle-penetrating, plate-bounding strike-slip fault that extends along the north-western edge of the New Zealand's Southern Alps (Norris and Toy, 2014). It fails quasi-periodically in large ($M_W > 8$) earthquakes associated with up to 9 m lateral and up to 1 m normal displacement (Sutherland et al., 2007; Nicol et al., 2016). Over 300 years have passed since it last failed in 1717 AD and it has a recurrence interval of 263 ± 68

years, so presents a major geohazard (Howarth et al., 2018). An Alpine Fault earthquake and co-seismic landslides will have substantial adverse effects on the infrastructure of the narrow strip of cultivated land extending between the Southern Alps and the west coast of South Island, and will affect more than 10,000 people (Robinson, 2018).

Future characterisation of this fault's brittle structure will tell us a lot more about the seismic hazard it offers. Furthermore, this fault is comparable to other plate- bounding transform faults worldwide such as the San Andreas Fault, the North Anatolian Fault Zone or the Dead Sea Transform (Norris and Toy, 2014). The local structure (decimeter – hundreds of meter) of the fault is quite complex (e.g., Barth et al., 2012). However, few along-strike variations in lithology, shallow depth of mechanical transitions in combination with rapid exhumation of fault rocks along a moderately inclined fault plane provide a continuous record from mid-crustal to subaerial deformation conditions (Sibson et al., 1979; Stern et al., 2001; Little et al., 2005; Edbrooke et al., 2015; Toy et al., 2015). This makes the fault a prime target to study plate boundary processes (Townend et al., 2009; Toy et al., 2017).

This thesis aims to characterise the dominating deformation processes in the Alpine Fault's brittle regime by investigating its narrow (< 0.5 m thick) fault gouge constituting the fault's principal slip zone (e.g., Sutherland et al., 2012; Toy et al., 2015; Williams et al., 2016). To this end, an interdisciplinary approach explores microstructural (optical, scanning and transmission electron microscopy), mineralogical (X-ray diffraction) and geochemical (X-ray fluorescence and inductively coupled plasma – optical emission spectrometry) properties down to the nanoscale. Most of the analysed samples were exposed fault rocks and we devote particular attention to understanding the shallow-depth processes, and to considerations of how these relate to seismogenic processes. For an extensive review addressing the deep structure of this continental transform the reader is referred to Norris and Toy (2014).

Through analyses of principal slip zone fault gouges and immediately over- and underlying units, Chapter 2 describes an investigation on the geometry of the Alpine Fault principal slip zone, including along-strike variations of structural, mineralogical and geochemical properties and how they relate to fault zone architecture. Chapter 3 presents a high-resolution study of a transect from hanging wall cataclasites across the PSZ fault gouge into footwall gravels focused on identifying dominating deformation mechanisms and the factors controlling them.

Analyses of fault rocks and controlling factors presented in Chapters 2 and 3 profit from a broad methodological approach developed by various preceding studies. Chapter 4 broadens the scope of the thesis: it reviews these techniques to characterise slip zones of faults and compares them with strategies deployed to investigate landslide slip zones. Landslides are of global relevance as they pose a significant geohazard to increasingly dense populated areas. The plethora of studies characterising fault zones, especially those investigating exposed slip surfaces being affected by similar boundary conditions like most landslide slip zones, may contribute to better understand these structures. This comparison also allows better diagnosis of how subaerial processes of alteration and deformation under low confining pressure have modified the Alpine Fault's record of deeper fault-related processes.

Chapter 5 provides the broader context for the work presented in the preceding chapters and examines how results obtained from investigating a crustal-scale fault based on exposed

samples might be biased by structural, mineralogical and geochemical artefacts. Furthermore, this chapter compares the major results of this study with other large-scale fault zones. Finally, Chapter 6 suggests directions for future research.

2 Fault zone architecture of a large plate-bounding strike-slip fault: a case study from the Alpine Fault, New Zealand

2.1 Abstract

New Zealand's Alpine Fault is a large, plate-bounding strike-slip fault, which ruptures in large ($M_W > 8$) earthquakes. We conducted field and laboratory analyses of fault rocks to assess its fault zone architecture. Results reveal that the Alpine Fault Zone has a complex geometry, comprising an anastomosing network of multiple slip planes that have accommodated different amounts of displacement. This contrasts with the previous perception of the Alpine Fault Zone, which assumes a single principal slip zone accommodated all displacement. This interpretation is supported by results of drilling projects and geophysical investigations. Furthermore, observations presented here show that the young, largely unconsolidated sediments that constitute the footwall at shallow depths have a significant influence on fault gouge rheological properties and structure.

2.2 Introduction

A fault, a planar discontinuity in rock where one side has moved relative to the other parallel to the discontinuity plane, constitutes a rheological and mechanical manifestation of localised deformation (Twiss and Moores, 2007; Ben-Zion, 2008; Fossen, 2016; Fossen and Cavalcante, 2017). Large fault zones are typically composed of networks of smaller, individual, but related and interacting faults of self-similar geometry (Ben-Zion and Sammis, 2003; Twiss and Moores, 2007; Peacock et al., 2016). The structure, composition, hydrological properties and seismo-mechanical behaviour of faults are typically intimately related. These interactions also govern strain distribution and depend on various factors, such as lithology (Faulkner et al., 2003; Schleicher et al., 2010; Holdsworth et al., 2011; Rybacki et al., 2011), fluid pressure (Hickman et al., 1995; Janssen et al., 1998; Fagereng et al., 2010), stress field and stress magnitudes (Sibson, 1985; Faulkner et al., 2006; Lindsey et al., 2014).

Faults control the strength of the Earth's lithosphere (Townend and Zoback, 2000; Bürgmann and Dresen, 2008) and govern substantially fluid flow (Caine et al., 1996; Wibberley et al., 2008). Hydrocarbon production from fault-compartmentalised reservoirs (Van Eijs et al., 2006), exploitation of fault-hosted mineral deposits (Cox et al., 1986) and long-term integrity of potential nuclear waste repositories (Laurich et al., 2018) are practical examples demonstrating how important it is to understand fault zone properties and their spatial and temporal evolution.

Furthermore, large, plate-bounding strike-slip faults such as the Alpine Fault (New Zealand), the North Anatolian Fault Zone (Turkey) and the San Andreas Fault (USA) rupture in large ($M_W > 7$) earthquakes (Toppozada et al., 2002; Sutherland et al., 2007; Bohnhoff et al., 2016). Many of these faults are located in densely populated areas; so they pose a significant geohazard (Eguchi et al., 1998; Sahin and Tari, 2000; Martínez-Garzón et al., 2015). Thus, from a georesource, seismic hazard and risk perspective, it is important to characterise the seismo-mechanical properties of faults (Aksu et al., 2000; Zoback et al., 2007; Hollingsworth et al., 2017).

Caine et al. (1996) presented a conceptual model of the structure of fault zones that has three primary components (Fig. 2.1a). The protolith (I) hosts a damage zone (II) that is characterised by a fracture density significantly higher than the background values of the surrounding host rock (Chester et al., 1993; Biegel and Sammis, 2004; Faulkner et al., 2010). The damage zone contains the fault core (III) where most of the displacement has been accommodated (Caine et al., 1996). This conceptual framework has been found to be applicable to faults across the full range of natural and experimental spatial scales (Anders and Wiltschko, 1994). Biegel and Sammis (2004) suggested that a fault core should be defined as the zone within a fault where strain leads to granulation of rocks, distinct from a damage zone within which fracture density is high but fracturing has "not [been] sufficient to produce distinct particles". A fault core can be structurally and lithologically heterogeneous, and most

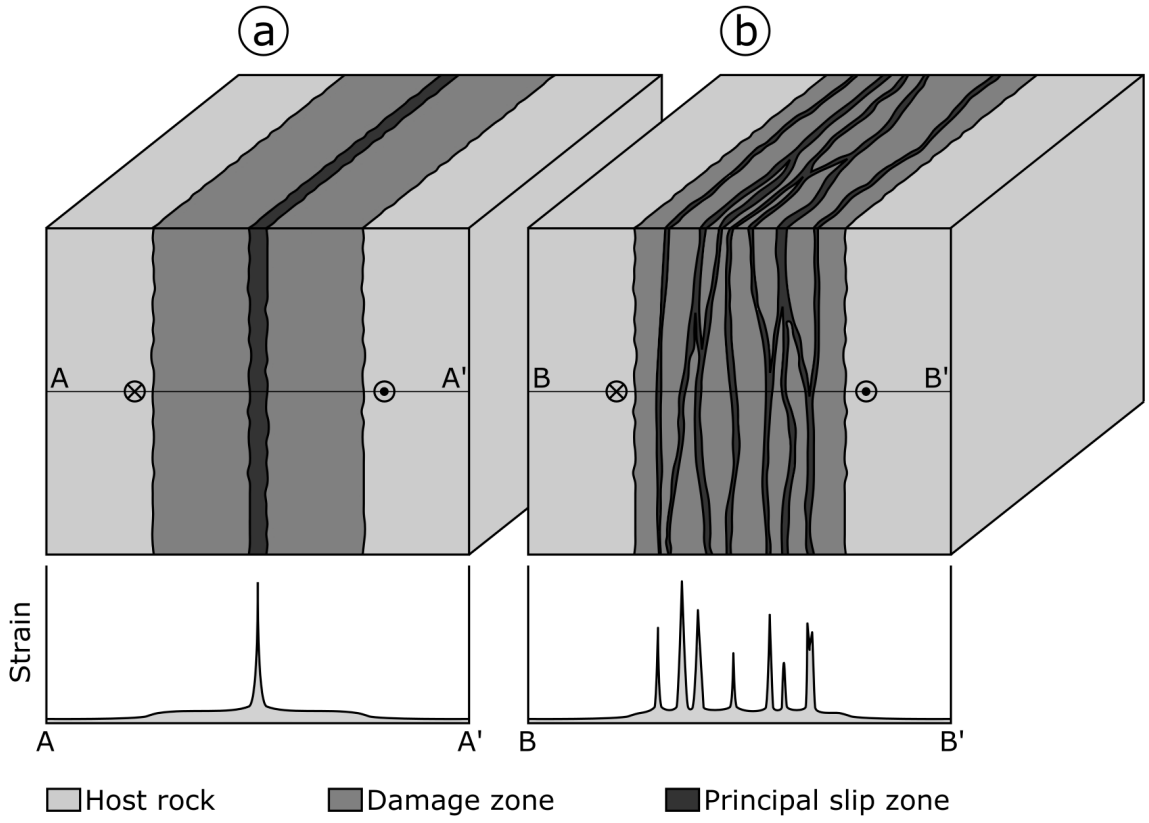

Figure 2.1: Conceptual end-member models of fault zone architecture. **(a)** According to the model of Caine et al. (1996) a fault is a relatively simple structure, where most of the strain is accommodated at a single, quite narrow fault core hosting a principal slip zone. **(b)** Faults described by the model of Faulkner et al. (2003) are more complex and consist of a damage zone hosting multiple, anastomosing principal slip zones forming a complex network.

of the displacement it accommodates may be localised along one or more principal slip zones (PSZs) defined by ultracataclasites or fault gouges (Sibson, 2003; Janssen et al., 2014; Toy et al., 2015). Although most commonly less than 10 cm thick, PSZs may be up to 1 m thick (Sibson, 2003) and thicknesses tend to increase with increasing displacement (Evans, 1990; Faulkner et al., 2010; Ben-Zion and Sammis, 2003, and references therein). In general, fault zone thicknesses may range from millimeters (e.g., Antonellini and Aydin, 1994) to a few hundred of meters (e.g., Bruhn et al., 1994).

The Punchbowl Fault, an inactive, exhumed part of the San Andreas Fault system, typifies this conceptual model of fault zone architecture. It has a single PSZ embedded in a fault core and the surrounding damage zone. A single, continuous gouge layer with 30 cm thickness on average hosts the ~1 mm thick PSZ. The core of the Punchbowl Fault is surrounded by an approximately 15 m thick damage zone (Chester and Logan, 1986; Chester et al., 2005).

However, other faults show a more complex structure with changing properties along strike or down dip (e.g., Wibberley et al., 2008; Faulkner et al., 2010). For example, detailed studies of the Carboneras Fault, Spain, yielded a conceptual model that is suitable for broader, typically phyllosilicate-rich fault zones, which tend to contain multiple high-strain zones (Fig. 2.1b; Faulkner et al., 2003). The Carboneras Fault is a predominantly strike-slip structure, that comprises an ~1 km thick tabular zone of continuous and anastomosing strands of phyllosilicate-rich fault gouge containing lenses of fractured protolith surrounded by an approximately 100 m wide damage zone. Scaly clays, which typically contain anastomosing shear planes, are examples of this distributed fault zone model on the hand specimen scale (Vannucchi et al., 2003; Laurich et al., 2017).

The fault zone architecture of New Zealand's Alpine Fault, a large, transpressional plate-bounding fault and a significant geohazard, has attracted increasing attention in the last 10 years. Considered to be appropriately described by the conceptual model of Caine et al. (1996), a single PSZ is commonly supposed to accommodate displacement along the Alpine Fault (e.g., Barth et al., 2012; Sutherland et al., 2012; Barth et al., 2013; Norris and Toy, 2014; Toy et al., 2015; Williams et al., 2016; Townend et al., 2017; Lukács et al., 2018; Schuck et al., 2018; Williams et al., 2018). Here, by combining results of these previous studies on the Alpine Fault's structure with new field observations, microstructural, mineralogical and geochemical analyses, we show that the Alpine Fault has a complex fault geometry manifested by PSZ thicknesses differing substantially between investigated outcrops. This complexity is not controlled by lithology, which is unexpected given that the Alpine Fault is hosted in a quartzofeldspathic protolith, which commonly fosters localization compared to phyllosilicate host rocks (Faulkner et al., 2003). This implies that the Alpine Fault does not fit our paradigmatic models of fault zone architecture.

2.3 Geological setting

2.3.1 The Alpine Fault and associated hazard

The Alpine Fault localises most of the deformation associated with the relative displacement between the Australian Plate and the Pacific Plate. The fault is dominantly dextral

transpressive and runs through the South Island of New Zealand. The straight, 800 km long surface trace extends from Milford Sound in the SW to Hokitika in the NE, where it transfers displacement onto the four main fault strands of the Marlborough Fault System (the Wairau, Awatere, Clarence and Hope Faults; Fig. 2.2a). The Alpine Fault maintains a constant NE - SW strike for its entire length, but the fault dip changes from 80° - 90° SE SW of the Dun Mountain Ophiolite Belt (DMOB) to 30° - 50° SE in the central segment (Barth et al., 2013). The shallowest 1 - 2 km of the fault NE of Haast display "serial partitioning", i.e., northerly striking oblique thrust sections alternate with easterly striking dextral strike slip sections of 1 - 10 km length (Norris and Cooper, 1995; Barth et al., 2012).

A 470 km right-lateral offset of the DMOB defines the minimum cumulative displacement along the fault (Sutherland et al., 2007). Displacement-normal shortening is on the order of 90 ± 20 km (Little et al., 2005). Strike-slip displacement rates are between 21 mm yr^{-1} and 29 ± 6 mm yr^{-1} (Norris and Cooper, 2000) corresponding to 60 - 80 % of the total relative velocity between the bounding plates (DeMets et al., 2010). Seismic investigations indicate a maximum exhumation of ~ 35 km from a deep crustal, subhorizontal, NE-dipping detachment (Stern et al., 2001; Little et al., 2005). Long-term exhumation rates of 6 - 9 mm yr^{-1} are inferred from ^{40}Ar / ^{39}Ar ages encountered between Franz Josef Glacier and Fox Glacier (Little et al., 2005). A combination of these high exhumation rates and meteoric fluid circulation driven by steep topographic gradients results in a very high geothermal gradient of up to 125 °C km^{-1} encountered in valleys (Menzies et al., 2016; Sutherland et al., 2017).

Currently, the Alpine Fault does not exhibit creep and is thought to be seismically locked to a depth of 12 - 18 km (Beavan et al., 2007). It is known to rupture in large earthquakes ($M_W > 8$), while generating up to 8 - 9 m of lateral and up to 1 m of normal displacement (Sutherland et al., 2007; Nicol et al., 2016). Offset and deformed Quaternary features demonstrate that Alpine Fault earthquakes rupture the ground surface (e.g., Cooper and Norris, 1990; Berryman et al., 2012; Schuck et al., 2018). While events like the most recent one in 1717 AD might rupture the entire fault, differing recurrence intervals of 263 ± 68 years for the central segment and 291 ± 23 years for the southern segment demonstrate that individual sections of the fault might fail independently (Fig. 2.2a; Sutherland et al., 2007; Howarth et al., 2018, and references therein). Considering the potential to produce large magnitude earthquakes and the time passed since the last event, the Alpine Fault is late in its seismic cycle and thus constitutes one of the South Island's major geohazards.

2.3.2 Lithology

The Australian Plate footwall assemblage encompasses Paleozoic to Cretaceous plutonic rocks intruded into metasediments (Fig. 2.2b). As these units are mostly overlain by Quaternary fluvioglacial sediments, footwall rocks are poorly exposed (e.g., Toy et al., 2015). In the Pacific Plate hanging wall, a narrow, 12 - 25 km wide elongated belt of metamorphosed sediments, the Alpine Schist, is exposed from the SW of Jackson Bay to the fault's NE termination (e.g., Sibson et al., 1979; Grapes and Watanabe, 1992; Scott et al., 2015). The Alpine Schist originates mostly from the Torlesse Terrane. This terrane is a polygenetic metamorphic suite

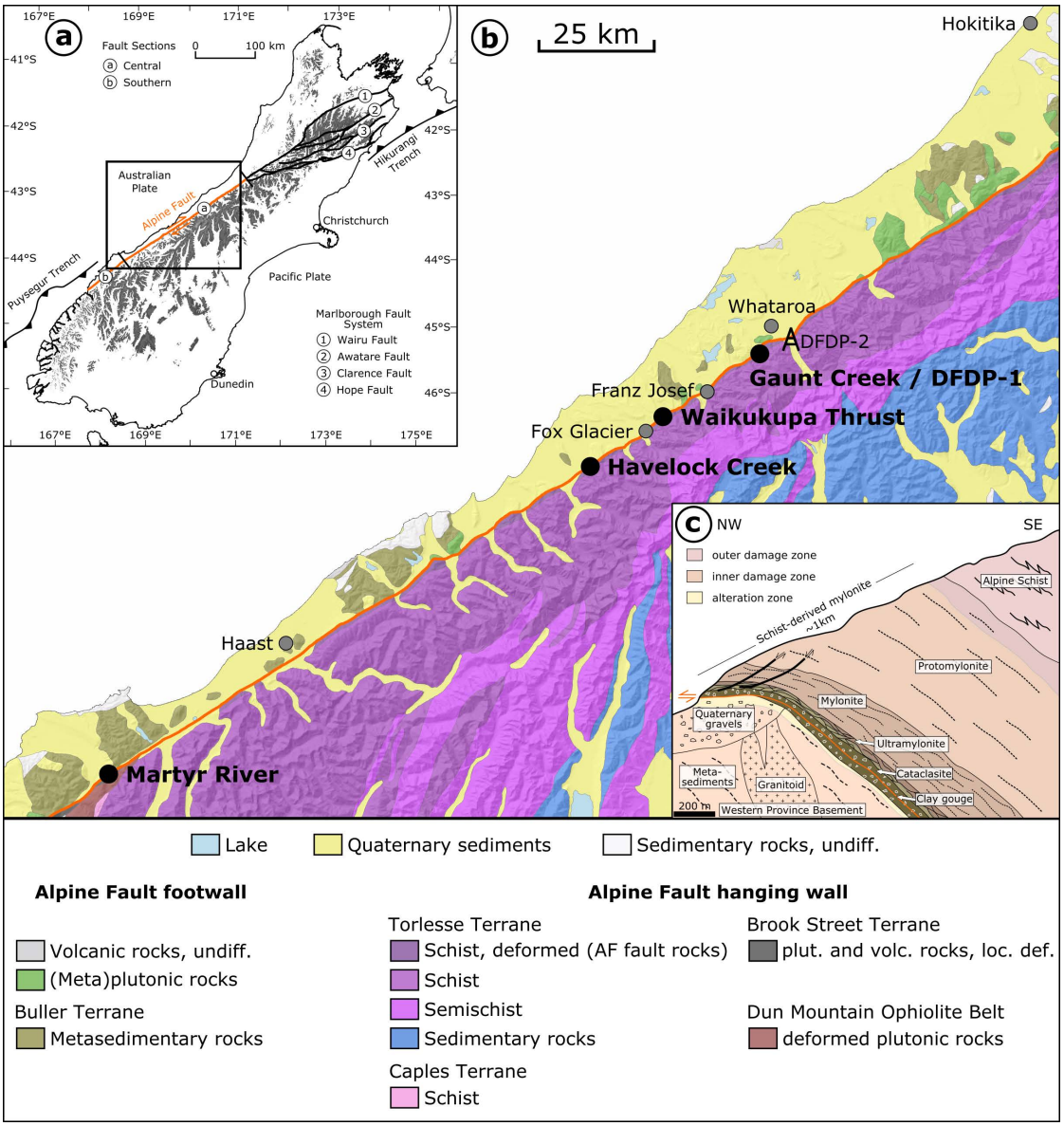

Figure 2.2: **(a)** Plate tectonic setting of New Zealand's South Island with the Alpine Fault's onshore segment being highlighted in orange. Position of (b) is indicated by black box. **(b)** Simplified geological map of the study area. Alpine Fault trace shown in orange. Locations of investigated outcrops: Martyr River, 43°7'47" S 168°33'40" E; Havelock Creek, 43°32'15" S 169°52'15" E; Waikukupa Thrust, 43°26'22" S 170°40'8" E; Gaunt Creek, 43°18'58" S 170°19'20" E. Map is based on the geological map of New Zealand's South Island (Edbrooke et al., 2015) and the digital elevation model of Columbus et al. (2011). **(c)** Typical shallow-depth sequence of Alpine Fault rocks. The figure was modified from Norris and Cooper (2007). Extents of alteration zone were derived from Sutherland et al. (2012) and extents of inner and outer damage zone from Townend et al. (2017)

.

with the Alpine Schist being its high grade, and most recently formed (Late Cretaceous) part (Roser and Cooper, 1990; Scott et al., 2015).

The amphibolite–greenschist facies rocks of the Alpine Schist have dominantly metapelitic to metapsammitic compositions, with rare metabasite and metachert. Metamorphic grade decreases from K-feldspar and oligoclase amphibolite facies through garnet, biotite and chlorite greenschist facies to pumpellyite–actinolite and prehnite–pumpellyite facies with increasing SE distance from the fault plane (e.g., Grapes and Watanabe, 1992; Scott et al., 2015). However, a combination of significant right-lateral displacement and high exhumation rates resulted

in 200 - 300 m wide inverted metamorphic sequences cropping out structurally above brittle fault rocks in the central segment (Cooper and Norris, 2011). Irrespective of local variations, typical mineral phases encountered in Alpine Schist-derived fault rocks are quartz, feldspar, garnet, muscovite, biotite, other minor phases and, in the case of metabasites, hornblende and epidote (Norris and Cooper, 2007). At the Waikukupa Thrust there are remnants of highly disrupted, intensely strained and sheared granite pegmatites indicating simple shear strains of more than 150 and coeval pure shear stretches of ~3.5 (Norris and Cooper, 2003; Toy et al., 2013).

Whereas the Alpine Schist constitutes the protolith of fault rocks in the central portion of the Alpine Fault, a comparatively small (~550 m thick) sliver of the Brook Street Terrane (BST) is the protolith of samples from the southern segment (Fig. 2.2b). The sliver is surrounded by the DMOB and bound to the NE by the Alpine Fault. The BST is the remnant of a Permian island-arc system, mainly composed of basaltic to andesitic volcaniclastic and sedimentary rocks of prehnite to pumpellyite and locally greenschist metamorphic grade (Spandler et al., 2005).

2.3.3 Fault rocks of the Alpine Fault

Exhumation from deep-crustal levels resulted in the formation of an approximately 1 km wide characteristic sequence of hanging wall fault rocks (Fig. 2.2c; e.g., Reed, 1964; Sibson et al., 1979; Cooper and Norris, 2011; Toy et al., 2015). Progressive northwestward-increasing strain of the Alpine Schist yielded protomylonites to ultramylonites that are overprinted by a cataclastic fault zone displaying increasing damage towards the PSZ (Williams et al., 2016). Cataclastic shears in the ultramylonites are filled with phyllosilicates and exhibit strike-slip, normal and reverse kinematics. Cataclasites are composed of comminuted mylonite fragments within a matrix of pulverised host rock, authigenic chlorite, muscovite and illite (Sibson et al., 1979; Norris and Cooper, 2007; Boulton et al., 2012). Intense chloritisation imparted a typical pale green colour to these 10 - 30 m wide cataclasites (Warr and Cox, 2001), which are cemented by authigenic phases, dominantly phyllosilicates and carbonates (Sutherland et al., 2012; Toy et al., 2015; Williams et al., 2016). The fault's PSZ cross-cuts all other structures, which indicates that it is the last active part of the fault system and accommodates the coseismic displacements that manifest as offset Quaternary features (e.g., Cooper and Norris, 1990; Berryman et al., 2012; Schuck et al., 2018). It is an incohesive and fine-grained gouge up to ~50 cm in thickness (Norris and Cooper, 2007; Boulton et al., 2012). Authigenic phyllosilicates cement the PSZ converting it into an impermeable hydraulic barrier preventing cross-fault fluid flow (Sutherland et al., 2012; Menzies et al., 2016). There is no location providing a continuous section from hard rock hanging wall to hard rock footwall (Townend et al., 2009).

2.3.4 The Deep Fault Drilling Project

Studying the physical character of tectonic deformation at depth within a continental fault late in its interseismic period provided the motivation for the Deep Fault Drilling Project

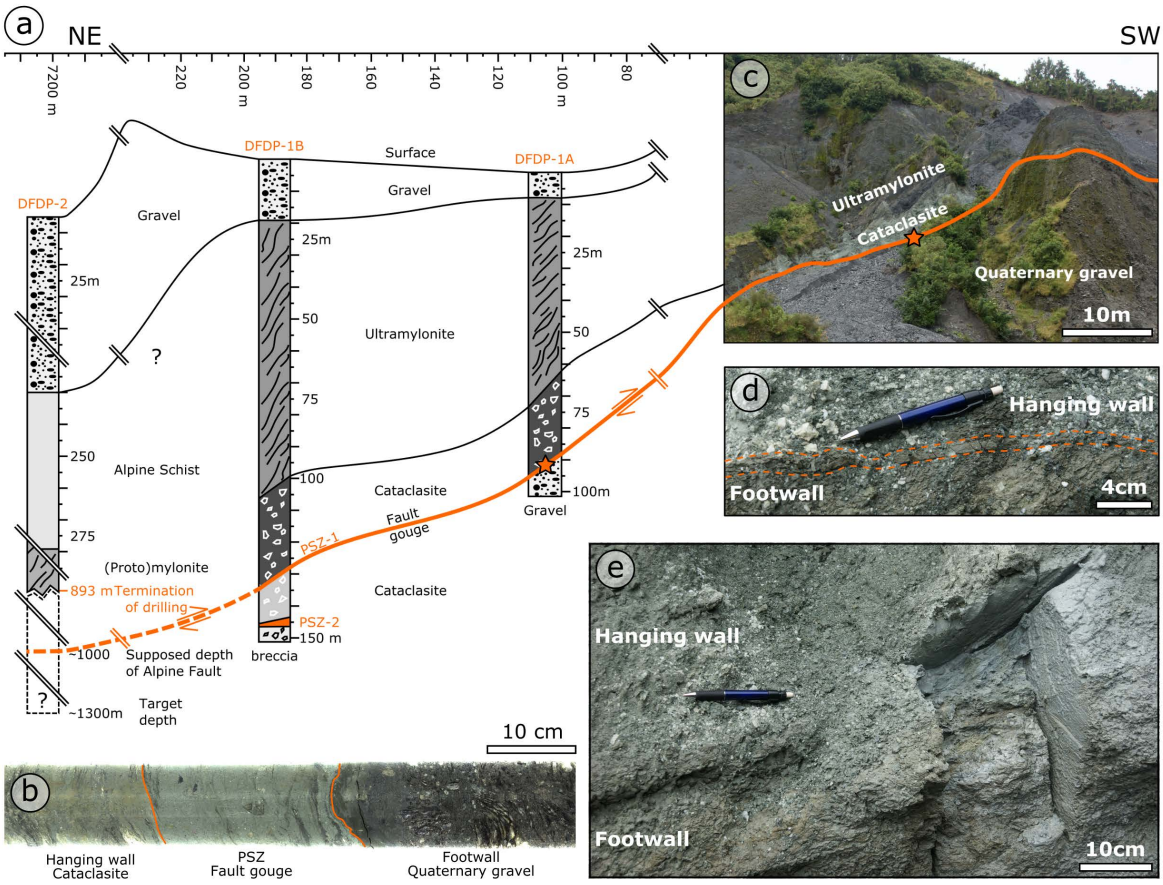

Figure 2.3: (a) Schematic overview of Deep Fault Drilling Project (DFDP) boreholes drilled in phase 1 at Gaunt Creek and phase 2 within the Whataroa River valley. Star at DFDP-1A indicates location of (b). **(b)** Segment of 180° scan of PSZ encountered at DFDP-1A drill core (run 66, section 1). **(c)** Individual fault rock units of the Alpine Fault Zone are well-recognisable at the outcrop Gaunt Creek, in close proximity to the DFDP boreholes. Star indicates location of (d) and (e). **(d)** An approximately 1 cm thick, brown layer indicated by stippled orange lines, was interpreted to represent the PSZ at Gaunt Creek. **(e)** Sample location (specimen shown in Figure 2.5b) some 10s of centimeter SW of location shown in (d). Figure modified according to Sutherland et al. (2012) and Boulton et al. (2014).

(DFDP; Fig. 2.3a; Townend et al., 2009). Phase 1 drilled two ~100 m (DFDP-1A) and ~150 m (DFDP-1B) deep pilot holes in January 2011 (Sutherland et al., 2012; Toy et al., 2015). These DFDP-1 boreholes provide a continuous section of fault rocks from hanging wall ultramylonites to footwall gravels enabling lithological (Toy et al., 2015), mineralogical (Schleicher et al., 2015), geomechanical (Boulton et al., 2014; Carpenter et al., 2014) and geophysical analyses (Sutherland et al., 2012; Townend et al., 2013). In total, three ~20 cm thick PSZs were encountered. In DFDP-1A, the PSZ is located between 90.67 and 90.87 m depth (Figs. 2.3a & b), and in DFDP-1B two PSZs were encountered at 128.30 - 128.50 m and 143.96 - 144.16 m depth, respectively (Fig. 2.3a; Toy et al., 2015).

Another two boreholes were drilled in DFDP phase 2 (DFDP-2A: 212.6 m MD - measured depth, DFDP-2B: 893.1 m MD) about 7.5 km ENE of the location of DFDP-1 (Fig. 2.2b; Toy et al., 2017). Phase 2 yielded cuttings for petrographic investigations (Toy et al., 2017) and provided various insights into fault zone architecture by wireline logs (e.g., Janku-Capova et al., 2018; Massiot et al., 2018) but was not able to penetrate and sample the fault core due to scientific and technical difficulties (Toy et al., 2017). DFDP boreholes from both phases

provide the opportunities for long-term monitoring of the Alpine Fault (e.g., Sutherland et al., 2015).

2.3.5 Study locations

For this study, all known outcrops with accessible PSZ between Martyr River in the SW and Kokatahi River, SSE of Hokitika in the NE were investigated in the austral summer 2015/16 (Fig. 2.2b). Furthermore, cataclasite and the fault gouge samples were available from the DFDP-1A core. Four of the five investigated locations, Havelock Creek, Waikukupa Thrust, Gaunt Creek and the core of DFDP-1A, are in the central segment of the Alpine Fault with the Alpine Schist as hanging wall host rock. Rocks of the BST constitute the host of fault rocks encountered at Martyr River, the fifth and southwestern-most location. All outcrops are located along river banks providing good outcrop conditions.

Waikukupa Thrust is the only studied site that is considered to be inactive. Incision of the Waikukupa River resulted in a geomechanically unfavourable geometry leading to the abandonment of this thrust segment and re-localisation of deformation approximately 700 m to the NE at Hare Mare Creek (Norris and Cooper, 1997).

2.4 Methods

2.4.1 Sampling

Fault rocks at Martyr River and Havelock Creek were sampled using hammer and chisel. At Waikukupa Thrust and Gaunt Creek samples were recovered using a hand-held chainsaw equipped with a silicon carbide chain. After recovery, all outcrop samples were immediately wrapped in aluminum and plastic foil to slow down drying. This procedure allowed for continuous transects across the PSZ, which juxtapose hanging wall cataclasites and footwall gravels, to be sampled from Martyr River and Waikukupa Thrust. However, the samples broke apart along the PSZ during shipping. An intact contact of PSZ on footwall material was only preserved from Gaunt Creek.

In summary, hanging wall fault rocks are available from Martyr River, Waikukupa Thrust and DFDP-1A. PSZ samples originate from all five locations and footwall rocks were taken at Martyr River, Waikukupa Thrust and Gaunt Creek.

2.4.2 Microstructural analysis

Samples from Martyr River, Waikukupa Thrust and Gaunt Creek were cut dry with a low-speed saw perpendicular and parallel to the fault trace. From all locations, subsamples were selected for microstructural analyses and subsequently embedded in resin prior to the preparation of 29 dry-polished thin sections using otherwise standard techniques.

Microstructural investigations were conducted using optical microscopy, scanning electron microscopy (SEM), transmission electron microscopy (TEM) and cathodoluminescence analyses (CL). Thin sections were studied with a Leica DM RX optical microscope and a FEI Quanta 3D SEM with focused ion beam (FIB; dual-beam machine). The SEM, equipped with a

field emission gun, operated at 20 kV in backscatter electron mode (BSE) and allowed semi-quantitative geochemical analyses with its EDAX energy dispersive X-ray analyser (EDX). For TEM analyses, a platinum strip was deposited on the sites selected with the FIB of the SEM to enable subsequent preparation of 14 thin foils ($10 \times 8 \times 0.15\,\mu m$) with a FEI FIB 200 following the procedure outlined by Wirth (2004) and Wirth (2009). A FEI Tecnai G2 F20 X-Twin TEM with Gatan Tridiem energy filter, Fischione high-angle annular dark field detector (HAADF) and EDX operated at 200 kV and allowed nanoscale investigation. CL analyses on calcite veins and cement were performed on thin sections using an Olympus polarising microscope. The Lumic HC1-LM hot cathode CL microscope operated at 14 kV, 0.0001 mbar and ~0.6 mA electron beam and 2.5 A filament current, respectively.

Microstructural analyses are mostly based on qualitative observations, but some quantitative information was obtained by image analysis using the open source software FIJI / ImageJ (Schindelin et al., 2012; Schneider et al., 2012).

2.4.3 Mineralogical and geochemical investigations

18 bulk rock powder samples for mineralogical and geochemical analyses were prepared with a jaw crusher and subsequently sieved to grain sizes $< 62\,\mu m$. A McCrone micronization mill provided the $< 10\,\mu m$ grain size fraction for the quantitative mineralogical analysis.

2.4.3.1 X-ray diffraction analysis

The mineralogical compositions of the samples were determined by X-ray diffraction (XRD) analysis on random powder samples loaded from the back side of the sample holders (⌀ 16 mm). XRD analyses were performed with a PANalytical Empyrean X-ray diffractometer operating with Bragg–Brentano geometry at 40 mA and 40 kV with CuKα radiation and a PIXel3D detector at a step size of 0.013 °2Θ from 4.6 to 85 °2Θ and 60 s per step.

Mineralogy was determined qualitatively with the EVA software (version 11.0.0.3) by Bruker. Rietveld refinement for quantitative mineralogy was performed using the program BGMN and the graphical user interface Profex (version 3.10.2; Döbelin and Kleeberg, 2015) calibrated for the used diffractometer. The error of quantitative analyses is expected to be in the range of 3 wt%. Goodness of fit was assessed by visually inspecting the differences between measured and modeled diffractograms and by aiming to obtain R_{wp} values lower than 3, a value arbitrarily chosen (Toby, 2006).

Bulk powder subsamples (45 mg), dispersed in 1.5 ml of de-ionized water and disaggregated in an ultrasonic bath, were placed on round (⌀ 3.1 cm) glass slides and air-dried for subsequent smectite and chlorite analyses. Identification of smectite was performed after ethylene glycolation at 45 °C for at least 12 h (2.4 - 25 °2Θ), and heating to 500 °C for 1 hour allowed us to differentiate between chlorite and kaolinite (2.4 - 25 °2Θ; Moore and Reynolds, 1997).

Illite polytype analyses to differentiate between authigenic and detrital (i.e., comminuted muscovite) species were conducted on selected samples with high illite and / or muscovite concentrations (Moore and Reynolds, 1997; Haines and van der Pluijm, 2008). Diffractograms for polytype analyses were acquired between 16 and 44 °2Θ at a step size of 0.013 °2Θ with

200 s per step. All diffractograms and R_{wp} values are provided in the electronic supplementary material.

2.4.3.2 X-ray fluorescence spectrometry

X-ray fluorescence spectrometry (XRF) with a PANalytical AXIOS Advanced spectrometer enabled study of geochemical variations of major elements. For this purpose, after drying of ~1.1 g of bulk rock powder overnight at 105 °C, 1 g of sample material, 6 g of $LiBO_2$ and 0.5 - 0.7 g of ammonium nitrate, acting as oxidising agent, were fusion digested at increasing temperatures from 400 °C to 1150 °C with a dilution of 1:6. The loss on ignition (LOI) providing volatile contents was determined on 20 - 30 mg of powder samples with a Euro EA Elemental Analyser.

To evaluate fluid-related element mobilisation, XRF data were analysed based on the equation of Gresens (1967) for composition – volume relationships resulting from metasomatic alterations, employing the isocon method (Grant, 1986; Grant, 2005). In this, the chemical composition of each investigated fault rock sample (i.e., altered rock) is plotted against the chemical composition of the host rock (i.e., unaltered rock). An isocon, a straight line through the origin, separates species enriched relative to the host rock plotting above from those depleted plotting below. It follows the equation

$$C^A = m \times C^H \tag{2.1}$$

with C^A and C^H being element concentrations of the altered and the host rock, respectively, and m referring to the isocon's slope. Enrichment or depletion (ΔC_i) of an element i relative to its host rock equivalent is calculated as follows:

$$\frac{\Delta C_i}{C_i^H} = m^{-1} \times \frac{C_i^A}{C_i^H} - 1 \tag{2.2}$$

The inverse of the isocon's slope (m^{-1}) indicates overall mass gain ($m^{-1} > 1$) or loss ($m^{-1} < 1$), respectively. Mass gains (%) are calculated as $(m^{-1} - 1) \times 100\,\%$. A negative mass gain corresponds to a mass loss (%).

To derive isocon slopes, Grant (2005) suggested five approaches: (I) clustering of C_i^A / C_i^H, (II) a best fit of data forming a linear array through the origin on an isocon diagram as graphical equivalent to (I), (III) assuming that certain elements are immobile, or assuming (IV) mass or (V) volume to be constant during alteration. However, it has previously been shown that Al and Ti – elements commonly assumed to be not affected by fluid-related alteration (e.g., Grant, 2005; Dolejš and Manning, 2010) – are mobilized by fluid-related alteration at the Alpine Fault. Furthermore, authigenic mineral formation is thought to affect both fault rock mass and rock volume (Schuck et al., 2018). As identification of clusters (I) or linear arrays (II) selects only a subset of all data points, and these selections may be biased, we used a linear best fit through all data points to determine isocon slopes.

Identification of the host rock is just as important as correctly determining the slopes of the isocons (Grant, 1986). We defined a reference protolith composition for fault rocks from

Havelock Creek, Waikukupa Thrust, Gaunt Creek and DFDP-1A (Tab. S2.1) based on the average of geochemical compositions of Alpine Schist data reported by Grapes et al. (1982), Roser and Cooper (1990) and Toy et al. (2017). These analyses are derived from the entire central segment of the Alpine Fault and individual datra points display little variation.

At Martyr River, the geochemical compositions by Spandler et al. (2005, see their Table 1) have been averaged, and used as host rock composition (Tab. S2.1). Their analyses from Bluff Complex and Takitimu Mountains were excluded, because the origin and some geochemical features, respectively, are different from the bulk BST (Spandler et al., 2005). We also note the isocon method has limitations for understanding fluid-assisted alteration related to fault activity at Martyr River. This is because the width of the Alpine Fault deformation zone at this location is larger than the thickness of the BST (Fig. 2.2b), so faulting-related fluid-rock interaction likely occurred with the DMOB and the geochemical composition of the reference protolith was already affected by fluid-related alteration. Furthermore, the BST is compositionally very heterogeneous due to magmatic differentiation so it is difficult to choose a single representative host rock geochemical composition. Fortunately, these variations only substantially affect the absolute quantification. The method nevertheless allows for relative geochemical changes within the fault zone at this location to be accounted for. The limitations regarding absolute quantification of concentration changes as result of hydrothermal alteration also apply to the Alpine Schist.

2.5 Results

2.5.1 Field observations

Individual units of the Alpine Fault rock sequence - (ultra)mylonites, cataclasites and footwall gravels - can be identified clearly at all sites investigated. However, weathering and landslides complicate the unambiguous identification of the PSZ at Gaunt Creek and Havelock Creek. This is exemplified by an approximately 1 cm thick, fine-grained, brown, fractured and discontinuous layer interpreted to represent the PSZ at Gaunt Creek (Figs. 2.3c - e) that was identified through sampling to be a footwall feature approximately 8 cm below the PSZ (see Section 2.5.2.3). Furthermore, measurements of fault orientation are only robust in the well-exposed outcrops at Waikukupa Thrust (50°/44° SE) and Martyr River (59°/51° SE) and those from Gaunt Creek (61°/32° SE) and Havelock Creek (102°/55° SE) should be treated with caution.

Thicknesses of fault gouges constituting the PSZ vary among individual locations, including the DFDP-1A core (Figs. 2.3 - 2.5), and decrease in the following order: Havelock Creek (~ 50 cm; Figs. 2.4a & 2.5a), Gaunt Creek (~ 30 - 40 cm; Figs. 2.3c - e & 2.5b), DFDP-1A (20 cm; Fig. 2.3b), Waikukupa Thrust (~ 4 cm; Figs. 2.4b & 2.5c) and Martyr River (~ 1 - 2 cm; Figs. 2.4c, d & 2.5d). Except for Martyr River, these locations have the same protolith (Fig. 2.2b; see Section 2.5.3). Furthermore, there is no systematic variation of PSZ thickness in distance along strike in these outcrops.

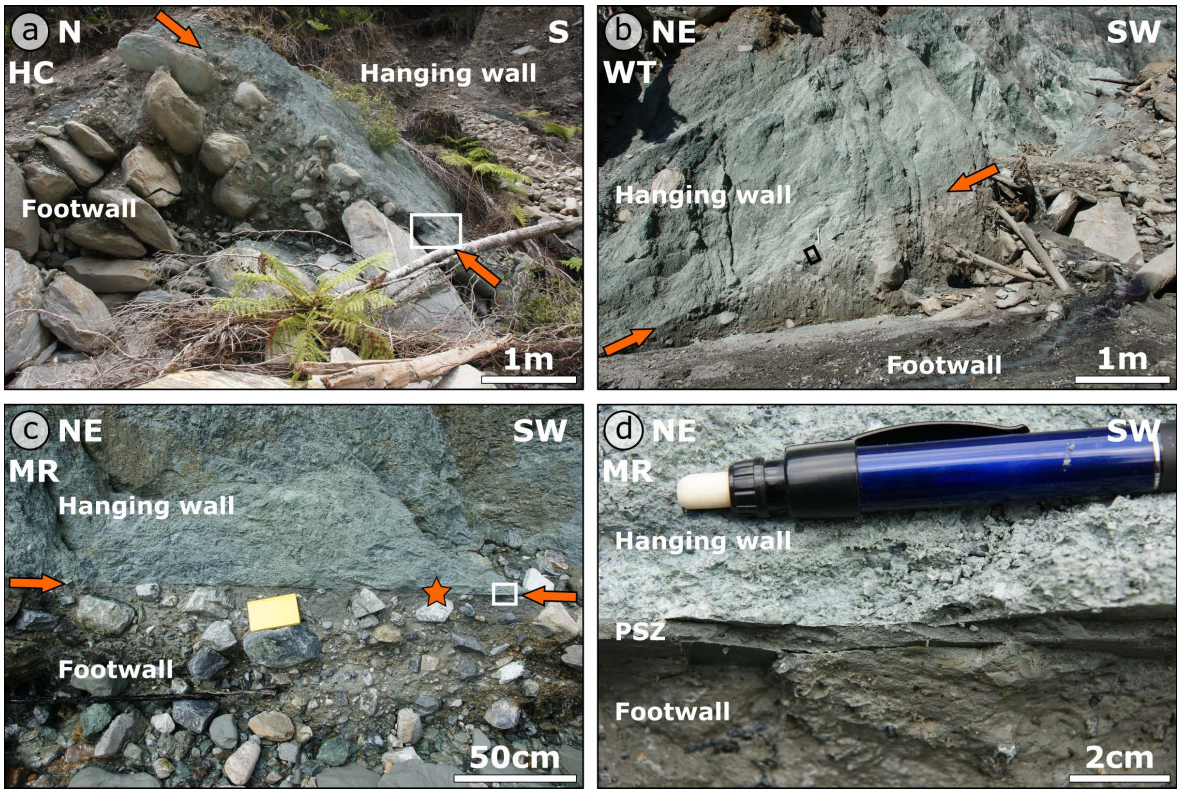

Figure 2.4: Outcrops of Alpine Fault Zone rocks. **(a)** Whereas pale green hanging wall cataclasites and larger Quaternary footwall gravels are clearly identified at Havelock Creek, the contacts and hence thickness of the PSZ (indicated by arrows) to overlying and underlying units, respectively, are only poorly constrained. The white box indicates position of Figure 2.5a. **(b)** The PSZ at Waikukupa Thrust as indicated by arrows is well-defined and straight. The black box gives location of sample presented in Figure 2.5c. **(c)** At Martyr River, hanging wall and footwall rocks are sharply separated by a well-defined PSZ (indicated by arrows). The white box indicates position of (d). The star gives the sample location for the specimen shown in Figure2.5d. **(d)** The PSZ at Martyr River is between 1 and 2 cm thick. HC: Havelock Creek; WT: Waikukupa Thrust; MR: Martyr River.

2.5.2 Microstructures

The fault rocks of Alpine Fault hanging wall, PSZ and footwall contain clasts embedded in a fine-grained matrix. We define matrix as fine particles – detrital and authigenic – belonging to the clay-size fraction, i.e., $< 2\,\mu m$ (Fig. 2.6a). In fact, the typical matrix grain size is $\ll 1\,\mu m$. The matrix is composed of abundant phyllosilicates of detrital (see Section 2.5.3) and authigenic (e.g., Fig. 2.6a) origin and detrital particles, mostly quartz and feldspar. The latter are subangular to rounded in shape with elongate to moderate sphericity and commonly with edges that have been affected by dissolution and mineral alteration processes (Fig. 2.6a).

Clasts embedded in the fault rock matrix are predominantly comminuted quartz, feldspar and mica grains, as well as fragments of Alpine Schist and mylonite. In addition, there are two more groups of clasts. The first one comprises compact, almost pore-free, fine particles with distinct boundaries but of similar composition compared to the surrounding matrix (Fig. 2.6b). This group of clasts is termed *matrix clasts* in the following. The second group comprises small areas, which are microstructurally similar to matrix clasts. These features are characterised by brighter grey values in BSE mode, and typically high porosities so they are easy to differentiate from the surrounding material (Fig. 2.6c). EDX analyses demonstrate that they are compositionally identical to the surrounding matrix. Because comparison of

optical and scanning electron microscopy images reveals that these structures look like matrix clasts under plain polarised light (Figs. 2.6d & e), we refer to them as *bright matrix clasts* in the following.

The distinct lithological and (micro-to-macro) structural characteristics of all units are described in detail in the following sections and summarised in Tables 2.1 (hanging wall), 2.2 (PSZ) and 2.3 (footwall).

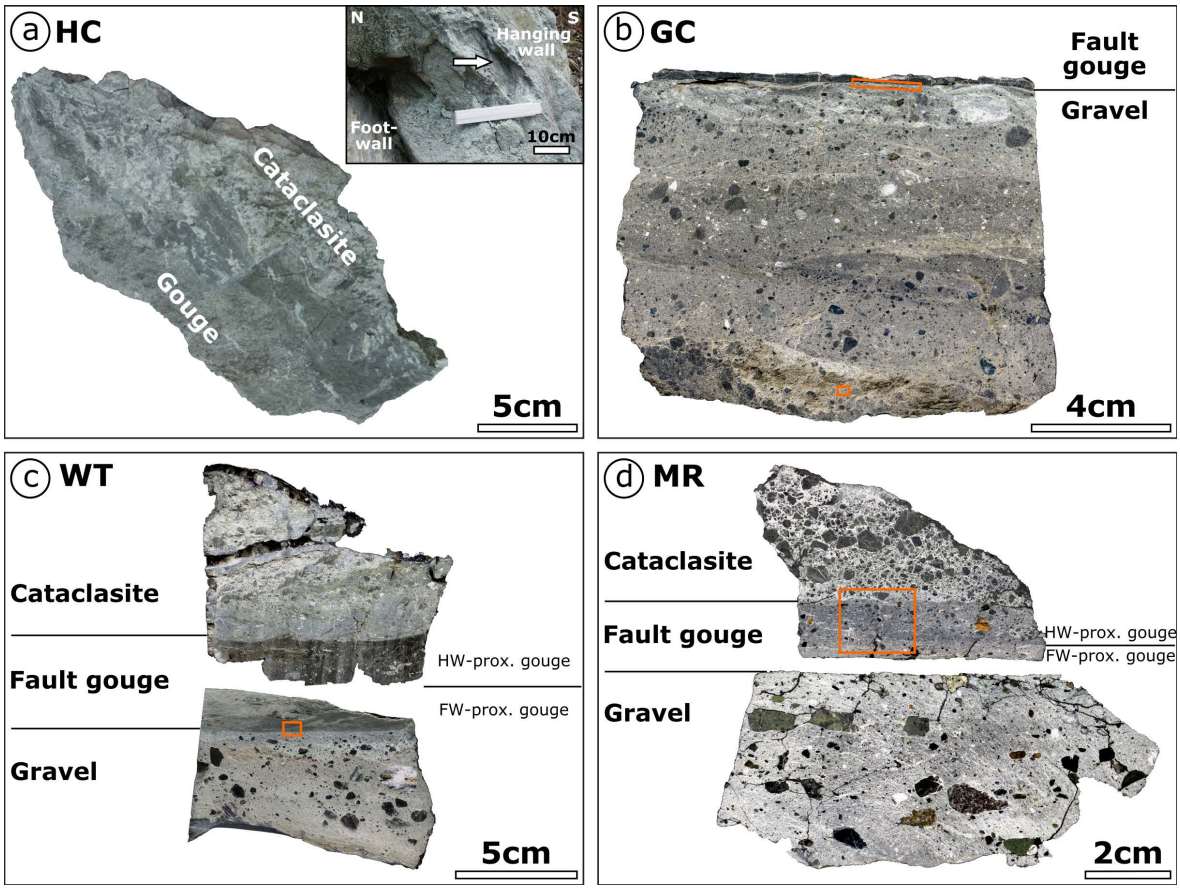

Figure 2.5: Investigated outcrop samples. **(a)** The contact between hanging wall cataclasites and thick fault gouge at Havelock Creek is poorly developed and appears to be transitional over ~8 cm. The inset provides a close-up of the sample location (indicated by the arrow). **(b)** Identifying the fault gouge in the field at the location Gaunt Creek turned out to be difficult. Consequently, only the lowermost part of the PSZ has been sampled. Contact between the PSZ and footwall is sharp. The orange box at the contact indicates location of Figures 3.7k - m; the orange box at the bottom indicates location of Figure 2.6d. **(c)** The thin fault gouge at Waikukupa Thrust consists of a hanging wall-proximal and footwall-proximal layer. The orange box gives location of Figure 3.7j. **(d)** The contacts of the thin PSZ with hanging wall and footwall rocks, respectively, are sharp at Martyr River. Fault gouge consists of a hanging wall-proximal and a footwall-proximal layer. The orange box gives location of Figures 3.7a & b. HC: Havelock Creek; GC: Gaunt Creek; WT: Waikukupa Thrust; MR: Martyr River.

2.5.2.1 Hanging wall cataclasites

Clasts embedded in the fine-grained cataclasite matrix at DFDP-1A and Waikukupa Thrust are mostly quartz and feldspars, with commonly fractured, dissolved and altered edges (Fig. 2.6a). Furthermore, matrix clasts are encountered close to the contact with the PSZ (< 1.35 m at DFDP-1A and < 10 cm at Waikukupa Thrust, respectively). In contrast, quartz and feldspars only constitute ~5 % of clasts at Martyr River. There, most clasts are polymineralic aggregates consisting of quartz, feldspar, chlorite and rarely biotite and fragments of calcite

veins (Figs. 2.6f & g). There are subordinately fragments of Alpine Schist (all locations) and mylonites (Waikukupa Thrust). At DFDP-1A and Waikukupa Thrust these fragments display ~150 µm wide, gouge-filled microfaults (Tab. 2.1). At Waikukupa Thrust, there are also clay-clast aggregates (CCAs; Boutareaud et al., 2008). At both thin section and outcrop scale, the amount and size of clasts generally decrease towards the PSZ and both vary systematically with PSZ thickness (Tab. 2.1; see also Boulton et al., 2012; Toy et al., 2015): locations with a thinner PSZ contain more clasts in the hanging wall, which tend to be larger, compared to locations with a thicker PSZ.

Open cracks, typically several millimeters long and up to hundreds of micrometer wide, increase in abundance towards the PSZ at DFDP-1A and Waikukupa Thrust. Furthermore, microfaults (~5 - 130 µm thick) cross-cut cataclasites at these locations. They contain comminuted particles and authigenic phyllosilicates and range in maturity: mature microfaults display a well-developed fine-grained fault gouge with particles up to tens of micrometers in size but mostly smaller than 2 µm (Fig. 2.6h). In contrast, juvenile microfaults contain poorly sorted particles up to a few hundred micrometers in size with the majority larger than 10 µm. In addition, some microfaults have cores made of coarser-grained matrix and clasts (Fig. 2.6h) or calcite veins (Fig. 2.6i) surrounded by fine-grained gouge.

Locally, there are patches almost completely devoid of clastic particles but with abundant authigenic flake- to needle-shaped chlorite crystals cementing pores and fractures at Waikukupa Thrust and DFDP-1A (Figs. 2.6j & k). The amount of these chlorite-dominated areas and authigenic phyllosilicates in general increases with decreasing distance to the PSZ and progressively cements the fault rocks. Furthermore, the matrix is cemented by calcite (Tab. 2.1). Whereas finely dispersed calcite is abundant at Martyr River, calcite at Waikukupa Thrust is usually present only in direct vicinity (< 3 cm) to the PSZ. There, mutually cross-cutting calcite veins (~15 µm thick) display small (< 20 µm) dextral offsets (see Figure 3f in Schuck et al., 2018). Furthermore, there are < 100 µm large calcite-cemented breccias composed of angular fragments of clastic particles and matrix clasts (see Figure 3c in Schuck et al., 2018). At DFDP-1A, calcite is encountered in lenses and veins, which frequently cross-cut clasts but rarely the matrix and generally increase in abundance towards the PSZ.

Locally, cataclasites are foliated. At DFDP-1A, clasts together with microfaults define a weak foliation (Fig. 2.6l) varying non-systematically across the investigated interval, locally displaying SC geometry. At Waikukupa Thrust and close to the PSZ, cataclastic lenses exhibit a very weak foliation parallel to the shear plane.

2.5.2.2 Principal slip zone fault gouges

The type of contact between hanging wall cataclasites and the fault gouge appears to correlate with PSZ thickness: where the PSZ is thicker, contacts are transitionally manifested by decreasing grain sizes (Tab. 2.2), as exemplified at Havelock Creek with its transitional, poorly developed contact over 8 cm (Fig. 2.5a). In contrast, Waikukupa Thrust has a sharp contact on the outcrop and hand specimen scale (Figs. 2.4b & 2.5c), but displays a transition over 4 mm from a porous, clast-rich cataclasite matrix to a very dense PSZ-matrix as revealed by microscopic inspection (see Figure 3a in Schuck et al., 2018). Identification of the sharp

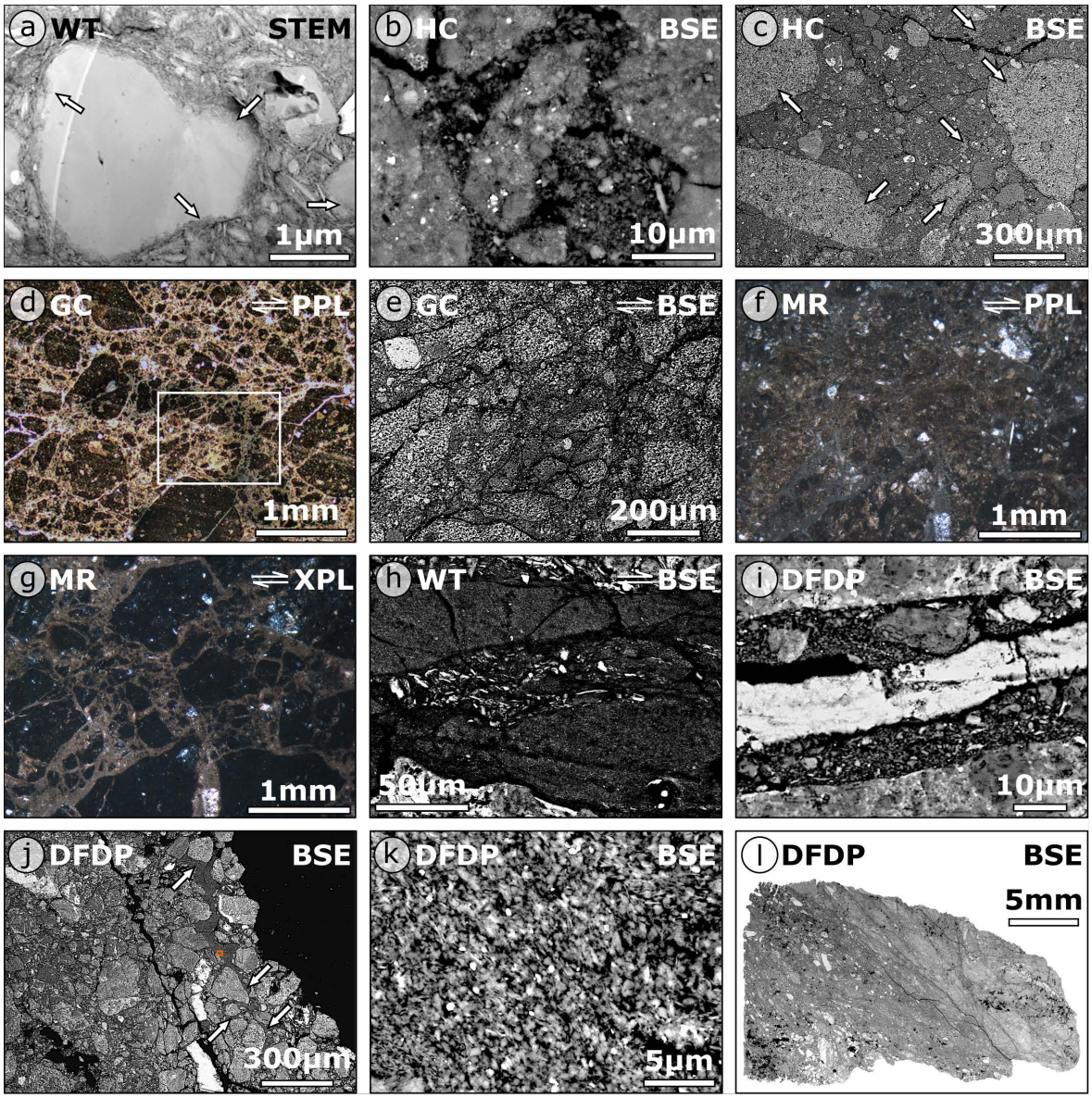

Figure 2.6: **(a)** Particles forming the fault rock matrix are defined as smaller than 2 µm. Abundant authigenic phyllosilicates cement the matrix. Arrows indicate albite dissolution and alteration to phyllosilicates. **(b)** Matrix clasts, low-porosity, compact and clast-like areas of similar composition as the matrix, are embedded within the fault rock matrix at all outcrops. **(c)** Bright matrix clasts (arrows) surrounded by fine-grained matrix and some clasts. **(d)** Lens of *matrix clasts* within footwall gravels at Gaunt Creek (see Figure2.5b). The white box indicates location of (e). **(e)** SEM analysis shows that clasts within a lens ~8 - 8.5 cm below the PSZ at Gaunt Creek are *bright matrix clasts*. **(f & g)** Corresponding PPL (f) and XPL (g) photomicrographs of hanging wall clasts at Martyr River. Identification of constituting mineral phases - mostly quartz, feldspar, chlorite - is only possible by EDX analysis. **(h)** Mature microfault filled by fine-grained authigenic phyllosilicates with typical grain sizes < 2 µm and a core of coarser-grained material. **(i)** Microfault displaying a calcite vein within its core surrounded by a fine-grained matrix and some larger clasts. **(j)** Locally, pores and cracks are cemented by fine-grained, authigenic phyllosilicates (arrows). The orange box indicates location of (k). **(k)** Matrix-cementing authigenic phyllosilicates are mostly flake- to needle-shaped chlorite crystallites. **(l)** Foliated cataclasite (top left to bottom right) sampled 25 cm above the PSZ. WT: Waikukupa Thrust; HC: Havelock Creek; GC: Gaunt Creek; MR: Martyr River; DFDP: Deep Fault Drilling Project core 1A; STEM: scanning transmission electron microscopy; BSE: backscatter electron microscopy; PPL: plane polarised light; XPL: cross-polarised light.

but undulating contact at Martyr River is simple on the outcrop and hand specimen scale (Figs. 2.4c, d & 2.5d), but difficult on the microscale (Figs. 3.7a & b).

Matrix clasts are the prevailing type of clast at Waikukupa Thrust and Havelock Creek (Figs. 3.7c & d), but constitute less than 5 % of clasts at Martyr River. Furthermore, the phyllosilicate-cemented fault gouge at Martyr River hosts individual mineral phases, which

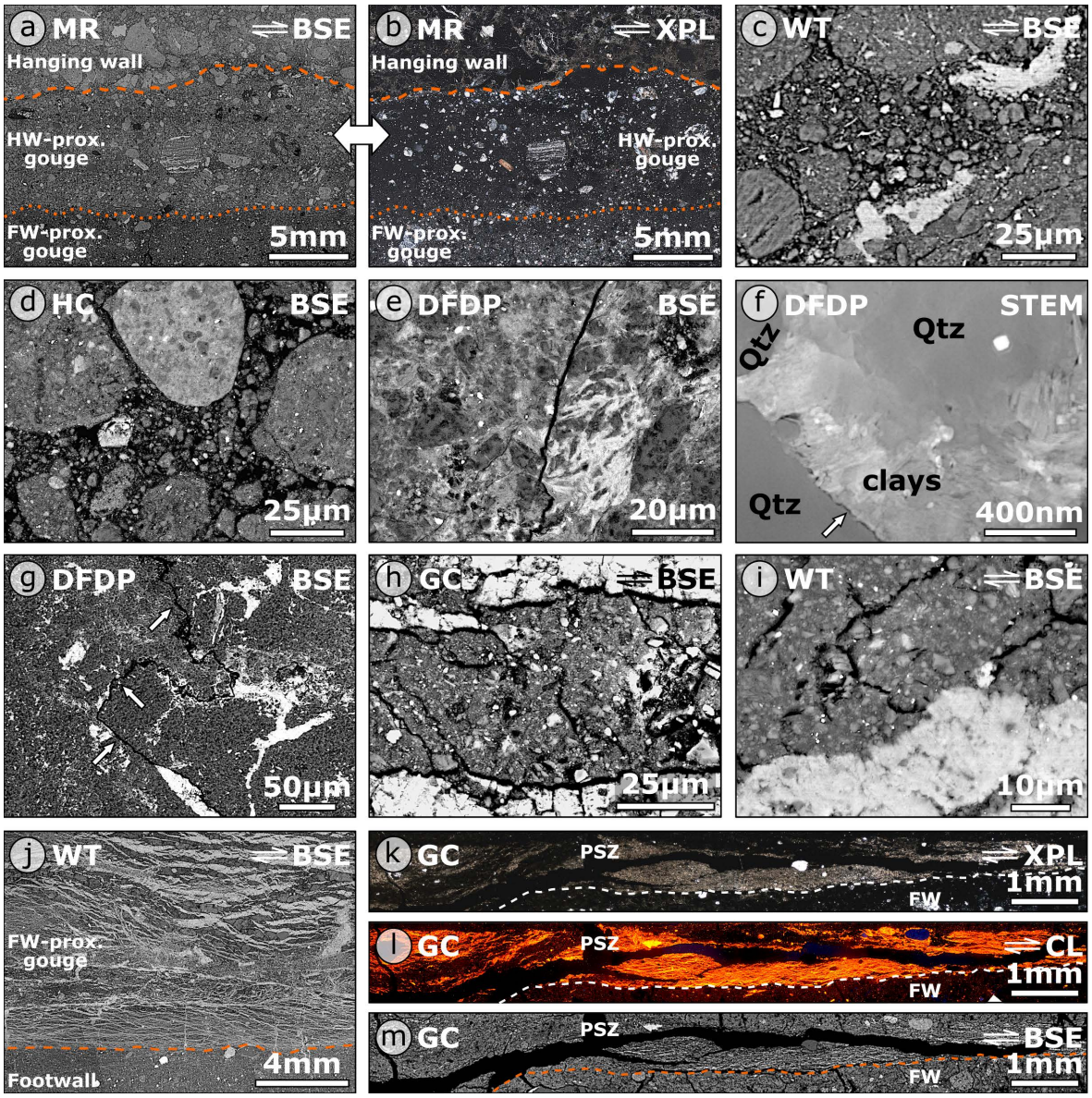

Figure 2.7: **(a)** BSE and **(b)** XPL photomicrographs of the fault core at Martyr River. Identification of the contact between the hanging wall and PSZ (stippled line) and that between the hanging wall- and footwall-proximal gouge (dotted line), respectively, is difficult. **(c & d)** The hanging wall-proximal gouge at Waikukupa Thrust (c) with its large amount of matrix clasts is microstructurally similar to the PSZ at Havelock Creek (d). **(e)** Photomicrograph of typical microstructures of cemented PSZ at DFDP-1A core. **(f)** Cemented PSZ matrix of the DFDP-1A core. Pores between comminuted and dissolved (arrow) quartz grains are cemented by authigenic phyllosilicates, mostly chlorite. **(g)** Slickolite (white arrows) indicative of pressure solution. **(h & i)** Fault gouge at Gaunt Creek (h) is microstructurally similar to footwall-proximal gouge at Waikukupa Thrust (i). **(j)** Network of anastomosing calcite veins within footwall-proximal gouge layer at Waikukupa Thrust. The contact between fault gouge and footwall (orange line) is sharp. **(k - m)** The basal part of the PSZ at Gaunt Creek hosts a network of calcite veins terminating at the sharp contact (white / orange stippled line) with the footwall (FW). MR: Martyr River; WT: Waikukupa Thrust; HC: Havelock Creek; DFDP: Deep Fault Drilling Project core 1A; GC: Gaunt Creek; BSE: backscatter electron microscopy; XPL: cross-polarised light; STEM: scanning transmission electron microscopy; CL: cathodoluminescence.

is distinctly different from its hanging wall, where large, fine-grained chloritised particles dominate (Fig. 3.7b). Bright matrix clasts are present at all locations, but are abundant only at Havelock Creek and Gaunt Creek, where they, in addition to clast-like shapes, occupy areas of several hundred of micrometers. In general, the amount and size of clasts weakly correlate with PSZ thickness (Tab. 2.2). Where the PSZ is thinner, clasts tend to be more abundant and sizes tend to be larger. Clast sizes increase in the following order: Gaunt Creek

(~75 µm), Havelock Creek (~75 µm), Waikukupa Thrust (~100 µm) and Martyr River (tens of micrometers to ~200 µm).

It is not possible to determine the amount and size of clasts within the DFDP-1A core, because more than 90 % of this unit is cemented by authigenic phyllosilicates, mostly chlorite (Figs. 3.7e & f). Authigenic phyllosilicates tend to nucleate along crack and grain boundaries of fractured grains. Additionally, newly formed phyllosilicates replace dissolved larger particles and mimic their original shape. Non-cemented areas are restricted to fractures. Many of these fractures contain up to 350 µm wide calcite cores, locally surrounded by gouge, microstructurally similar to microfaults observed within the DFDP-1A cataclasites (see Fig. 2.6i). These non-cemented, fracture-related locations host patches of fine-grained, randomly oriented and needle-shaped, authigenic chlorite crystallites. The presence of these patches within the PSZ is restricted to DFDP-1A.

We only saw evidence of pressure solution at one location, DFDP-1A, where there are indications of deformation by pressure-solution as evidenced by a slickolite (Fig. 3.7g), a stylolite with teeth oblique to the stylolite surface (see Passchier and Trouw, 2005). However, enrichment of insoluble material or secondary phases along teeth-crowns is not observed.

PSZs at Waikukupa Thrust and Martyr River are layered and display a hanging wall-proximal and a footwall-proximal layer, respectively (Figs. 2.5c & d). At Martyr River, the contact is best recognised on the hand specimen scale (Figs. 2.4d, 2.5d, 3.7a & b), where the fault gouge is blueish-grey proximal to the hanging wall and greenish-grey proximal to the footwall. Minor differences between both gouge layers are manifested by slightly more and larger clasts in the ~0.8 - 1 cm thick hanging wall-proximal layer than the ~0.3 - 0.5 cm thick footwall-proximal layer (20 - 25 % vs. 25 - 30 %; Tab. 2.2).

At Waikukupa Thrust, a sharp but undulating contact separates a brown-dark grey hanging wall-proximal layer with 5 - 10 % clasts from a medium-light grey footwall-proximal layer, which is clast-poor (< 1 % clasts; usually < 5 µm large).

The dense, clast-poor (< 1 % clasts) fault gouge at Gaunt Creek is microstructurally identical to the footwall-proximal layer at Waikukupa Thrust (Figs. 3.7h & i). Furthermore, both gouges exhibit calcite vein networks close to the contact with the footwall (Figs. 3.7j - m). At Waikukupa Thrust, veins display mutual cross-cutting relationships with dextral offsets. For a detailed description of these calcite veins, the reader is referred to the preceding work of Schuck et al. (2018). At Gaunt Creek, the 350 - 800 µm wide vein network (Figs. 3.7k - m) has been subsequently affected by intensive fracturing and calcite dissolution, which hampers the identification of cross-cutting relationships. Furthermore, the contact between calcite veins and the surrounding gouge is poorly developed. Veins are typically 5 - 10 µm wide and tend to be thicker, less dissolved and deformed close to the footwall. CL colours are yellow–orange but slightly brighter and more yellow towards the footwall (Fig. 3.7l).

Apart from these vein networks, calcite veins cross-cut matrix clasts at Martyr River and the hanging wall-proximal gouge layer of Waikukupa Thrust, but are very rare at Havelock Creek. Additional hanging wall-proximal microstructures are clasts forming a weak foliation parallel to displacement at Martyr River and CCAs at Waikukupa Thrust. Furthermore, hanging wall-proximal microstructures at Waikukupa Thrust are similar to those of Havelock Creek

(Figs. 3.7c & d), except that clasts are not homogeneously distributed but cluster randomly at Havelock Creek. Apart from the hanging wall-proximal fault gouge layer of Waikukupa Thrust, where typical clast size decreases while the size of matrix clasts increases towards the footwall, trends regarding microstructures are not observed. Most remarkably, discrete slip planes are not observed within the fault gouges.

2.5.2.3 Footwall gravels

Where sufficiently exposed, the contact between clast-poor PSZ and clast-bearing footwall is sharp (Figs. 2.4b - d, 2.5b & c, 3.7j – m). Footwall gravels are compositionally similar to overlying hanging wall cataclasites and fault gouges (Tab. 2.3). Furthermore, the same correlations regarding amount and size of clasts observed in hanging wall cataclasites and fault gouges are seen within footwall gravels (Tab. 2.3): locations with thin PSZ tend to contain more and larger clasts than locations with thicker PSZ. In addition, grain size increases with increasing distance from the PSZ. Whereas there are some bright matrix clasts at Martyr River and Gaunt Creek, matrix clasts are only encountered at Gaunt Creek. At Martyr River, footwall clasts are slightly imbricated and form a weak foliation parallel to displacement.

Calcite is absent at Martyr River and restricted to a ~3 mm thick layer immediately adjacent to the PSZ at Waikukupa Thrust. There, calcite constitutes finely dispersed cement, veinlets and $< 5\,\mu$m thick rims at grain edges parallel to displacement. In contrast, at Gaunt Creek, calcite is predominantly found in veins and lenses cross-cutting the matrix and detrital clasts.

The ~1 cm thick, fine-grained, brown layer erroneously interpreted as PSZ at Gaunt Creek (Figs. 2.3d & e), is mainly composed of fractured, subangular to subrounded matrix clasts (Fig. 2.6d). The amount of quartzofeldspathic clasts within this lens is $< 5\,\%$. Fractures between the individual clasts are filled with a fine-grained matrix. SEM analysis reveals that these clasts are actually bright matrix clasts (Fig. 2.6e).

2.5.3 Mineralogy

There are only minor variations in the qualitative fault rock composition (Tab. 2.4). Quartz, feldspar, calcite and phyllosilicates (chlorite, kaolinite, muscovite, illite, and biotite) and traces of apatite, pyrite and rutile are always present. Additionally, Waikukupa Thrust and Havelock Creek contain amphiboles, mainly hornblende, and there is epidote at Waikukupa Thrust and Martyr River. Serpentine minerals are only encountered within the fault gouge at Martyr River.

Analysed fault rocks do not contain smectite, and kaolinite is present only in traces. Furthermore, polytype analysis demonstrates that illite identified by Rietveld refinement predominantly constitutes detrital but comminuted muscovite (see electronic supplement).

2.5.3.1 Hanging wall cataclasites

Quartz and feldspars are the dominant mineral phases in hanging wall cataclasites. They do not exhibit any clear trend towards the PSZ (Tab. 2.4). Phyllosilicates appear to decrease in content towards the PSZ. This probably is an artifact of Rietveld refinement based on

Table 2.1: Summary of observed hanging wall (cataclasites) microstructures. PSZ: principal slip zone.

	poor	**localisation**	**high**
	DFDP-1A	**Waikukupa Thrust**	**Martyr River**
fractures	X	X	X
- amount increases towards PSZ	X	X	/
microfaults	~5 to ~130 µm wide	~5 to ~130 µm wide	/
detrital clasts			
- main phases	quartz and feldspar	quartz and feldspar	polymineralic aggregates (mainly quartz, feldspar and chlorite)
- minor phases	/	micas (elongated, kinked and fractured), hornblende and chlorite aggregates (up to 0.6×1 mm large)	quartz and feldspar (< 5 %)
- roundness	angular - rounded	angular - rounded	angular - rounded
- sphericity	low - moderate	low - moderate	low - moderate
- amount			
- PSZ-proximal	~50 % (at ~3 m above PSZ)	~60 to ~70 % (at ~70 cm above PSZ)	not sampled
- at contact to PSZ	~10 %	~20 to ~25 %	~40 to ~50 %
- size			
- PSZ-proximal	~100s of µm (at ~3 m above PSZ)	~100s of µm (at ~70 cm above PSZ)	not sampled
- at contact to PSZ	~100 µm	~100 µm	~100 - 200 µm
- maximum	~550×600 µm	~550×600 µm	~200 µm
fragments			
- schist	1.6×3.4 mm large	2.8×5.4 mm large	1.1 mm large
- fractured and gouge-filled	X	X	/
- mylonite	/	9 - 12 mm large	/
- fractured and gouge-filled	/	X	/
matrix clasts	X	X	/
- first observation	~1.35 m above PSZ	~10 cm above PSZ	/
- max. size	650×750 µm	1.3×3.4 mm	
patches of authigenic chlorite crystallites	X	X	/
- amount increases towards PSZ	X	X	/
bright matrix clasts	X	X	X

Table 2.1: continued

	poor	**localisation**	**high**
	DFDP-1A	**Waikukupa Thrust**	**Martyr River**
calcite			
- occurrence	all samples	mostly in direct vicinity to PSZ	all samples
- kind: cement	within some fractures; local	within some fractures; generally insignificant; slightly more pronounced within ~3 cm of PSZ	within some fractures; finely-dispersed and abundant
- kind: lenses	up to 1.2×4 mm	/	/
- kind: veins	frequent with increasing abundance towards the PSZ; mostly restricted to clasts; up to 5 - 300 µm thick; typically between 50 and 70 µm thick	~ < 15 µm thick; mutually cross-cutting with small (< 20 µm), dextral offsets	/
foliation	locally and weak; formed by clasts and microfaults; locally with SC-geometry	clast lenses parallel to PSZ	/
other	/	breccias (< 100µm large) within some centimeters above the PSZ; clay-clast-aggregates	/

Table 2.2: Summary of observed principal slip zone (fault gouge) microstructures. PSZ: principal slip zone; HW: hanging wall; FW: footwall.

	poor		**localisation**		**high**
	Havelock Creek	**Gaunt Creek**	**DFDP-1A**	**Waikukupa Thrust**	**Martyr River**
contact HW - PSZ	transitional over 8 cm	not sampled	not sampled	sharp at macro- and mesoscale; transitional over 4 mm at microscale	sharp at macro- and mesoscale; difficult to identify at microscale
major differences compared to hanging wall	not sampled	not sampled	~90 % of PSZ is cemented	FW-prox. gouge: dense anastomosing network of mutually cross-cutting calcite veins	(I) clasts are small individual mineral phases and not chloritsed aggregates; (II) no calcite cement, but less porous due to authigenic phyllosilicates
kind of PSZ	single structure	single structure	single structure	layered; HW-prox. gouge 2 cm thick; FW-prox. gouge 2 cm thick	layered; HW-prox. gouge 0.8 - 1 cm thick; FW-prox. gouge 0.3 - 0.5 cm thick
- contact between PSZ layers	/	/	/	sharp & undulating & poorly developed at microscale	
- major differences between PSZ layers	/	/	/	FW-prox. gouge hosts dense, anastomosing network of mutually cross-cutting calcite veins	20 - 25 % clasts in HW-prox. gouge vs. 25 - 30 % clasts in FW-prox. gouge

Table 2.2: continued

	poor		**localisation**		**high**
	Havelock Creek	**Gaunt Creek**	**DFDP-1A**	**Waikukupa Thrust**	**Martyr River**
similarities between investigated PSZs	HW-prox. gouge at Waikukupa Thrust	FW-prox. gouge at Waikukupa Thrust	/	Havelock Creek (HW-prox. gouge); Gaunt Creek (FW-prox. gouge)	/
detrital clasts					
- main phases	quartz & feldspar	quartz & feldspar	quartz & feldspar	quartz & feldspar	quartz & feldspar
- minor phases	hornblende & mica fragments ($50 \times 350\,\mu m$ large)	/	/	/	hornblende; mica fragments ($< 20\,\mu m$ large) & needle-shaped serpentines ($< 20\,\mu m$ large)
- roundness	(sub)angular - rounded	(sub)angular - rounded	(sub)angular - rounded	(sub)angular - rounded	(sub)angular - rounded
- sphericity	elongate - moderate	elongate - moderate	elongate - moderate	elongate - moderate	elongate - moderate
- amount	10 %	< 1 %	/	HW-prox. gouge: 5 - 10 %; FW-prox. gouge: < 1 %	20 - 30 %
- size	$\sim 75\,\mu m$	$\sim 15\,\mu m$	/	$\sim 100\,\mu m$; decreases towards FW	HW-prox. gouge tens µm to $\sim 200\,\mu m$; FW-prox. gouge $< 100\,\mu m$
- maximum	$160 \times 250\,\mu m$	$90 \times 130\,\mu m$	/	$110 \times 180\,\mu m$	1 mm
- fragments					
- kind	schist	/	/	/	schist, mylonite, cataclasite
- roundness	subangular - -rounded	/	/	/	subangular - -rounded
- sphericity	low - moderate	/	/	/	low - moderate
- size	15 - 50 µm	/	/	/	100s of micrometer (schist)
- maximum	$400 \times 450\,\mu m$	/	/	/	$> 2.2 \times 3.7$ mm (schist); 3×7.5 mm (mylonite); 5×6 mm (cataclasite)
- other	/	/	/	clast size decreases towards FW	/
matrix clasts	prevailing type of clast	/	/	prevail in HW-prox. gouge	< 5 % of clasts
- maximum size	$650 \times 830\,\mu m$	/	/	$3\,\mu m$ to > 6 mm	$\sim 20\,\mu m$ to 3×3.5 mm
patches of authigenic chlorite crystallites	/	/	associated with non-cemented fractures	/	/
bright matrix clasts					
- abundance	high	high	low (local)	/	low (local)
calcite veins	very rare	network	rare	rare (HW-prox. gouge); network (FW-prox. gouge)	rare
- thickness					
- vein network	/	350 - 800 µm	/	~ 2 cm (FW-prox. gouge)	/

Table 2.2: continued

	poor		**localisation**		**high**
	Havelock Creek	**Gaunt Creek**	**DFDP-1A**	**Waikukupa Thrust**	**Martyr River**
- individual veins	/	5 - 10 µm, up to 30 µm, increases slightly towards FW	up to 350 µm	HW-prox. gouge ~ 10 µm; FW-prox. gouge typically ~ 60 µm, between 1.5 - 200 µm decreases to FW	15 - 900 µm
- spacing	/	20 - 30 µm; between 10 - 80 µm	/	200 µm (close to HW-prox. gouge), 10 µm (close o FW)	/
- orientations	/	/	/	FW-prox. gouge; (I) subparallel to displacement; (II) oblique to displacement; (III) normal to displacement	/
- CL colour	/	mostly uniform yellow – orange; slightly brighter and more yellow to FW	/	uniform yellow – orange	/
- other	/	/	/	small (< 5 µm), blocky & euhedral crystals	/
foliation	/	/	/	/	in HW-prox. gouge, weak, parallel to PSZ, formed by clasts
other	/	/	slickolite	HW-prox. gouge: clay-clast aggregates & breccias (0.6×1.2 mm)	/

Table 2.3: Summary of observed footwall (Quaternary gravel) microstructures. PSZ: principal slip zone; FW: footwall.

	poor	**localisation**	**high**
	Gaunt Creek	**Waikukupa Thrust**	**Martyr River**
contact PSZ - FW	sharp	sharp	not sampled
detrital clasts			
- main phases	quartz and feldspar	quartz and feldspar	quartz and feldspar
- minor phases	mica	mica	mica, serpentine
- roundness	subangular - subrounded	subangular - subrounded	subangular - subrounded
- sphericity	low - moderate	low - moderate	low - high
- amount	25 - 30 %	40 - 50 %	50 - 60 %
- size	~140 to 185 µm	~60 to 130 µm	~100 to 200 µm
- trend	/	increases with increasing distance to PSZ	increases with increasing distance to PSZ
- fragments	schist and cataclasite	schist, mylonite and cataclasite	schist and cataclasite
- maximum size			
- schist	~4.1 × 5.3 mm	~1 × 1.5 cm	0.7 × 1.4 cm
- mylonite	/	~0.7 cm	/
- cataclasite	~3.4 × 5.6 mm	0.5 - 0.7 cm	0.5 × 1.1 ,cm
matrix clasts	~300 µm (up to 4.3 × 7.4 mm)	/	/
patches of authigenic chlorite crystallites	X	/	/
bright matrix clasts			
- abundance	high	/	low
calcite		in general, mostly restricted to ~3 mm within contact to PSZ	
- kind: cement	/	finely dispersed	/
- kind: veins	up to ~350 µm thick; cross-cut detrital clasts	veinlets & a few displacement-normal veins extending from FW-prox. gouge into footwall	/
- kind: other	lenses (up to 1 × 1.4 mm large) within detrital clasts	calcite rims (< 5 µm) at clasts parallel to displacement	/
foliation	/	/	weak; parallel to PSZ; formed by slightly imbricated clasts
other	0.75 - 1.6 cm thick lens of matrix clasts (size: ~100 to 300 µm; up to 1.4 × 2.1 mm); fractures between individual clasts are gouge-filled; < 5 % detrital clasts	/	/

the $< 10\,\mu m$ instead of the clay-size fraction. In the DFDP-1A drill core material, the concentrations of detrital muscovite/illite decrease towards the PSZ compared to authigenic chlorite/kaolinite, which show an opposite trend. Furthermore, calcite also increases towards the PSZ at DFDP-1A.

2.5.3.2 Principal slip zone fault gouges

Quartz and feldspar contents vary by more than 50 % among individual locations (21 wt% at Waikukupa Thrust vs. 52 wt% at Havelock Creek; Fig. 2.8; Tab. 2.4). In general, these clastic phases tend to be less abundant in thinner than in thicker PSZs (Fig. 2.8). Phyllosilicate concentrations exhibit the opposite pattern: thinner PSZs tend to be more phyllosilicate-rich than thicker PSZs. Furthermore, chlorite/kaolinite and muscovite/illite show inverse correlations but do not vary systematically with respect to PSZ thickness. Calcite concentrations of Waikukupa Thrust (29 %) and Gaunt Creek (6 %) reflect mineralisation manifested in vein networks. As calcite veins are rare at Havelock Creek, the relatively high (11 %) concentrations potentially reflect calcite cementation. In contrast, calcite concentrations within PSZs of DFDP-1A and Martyr River are lower compared to the hanging wall.

2.5.3.3 Footwall gravels

At Gaunt Creek, quartz and feldspar concentrations increase with increasing distance from the PSZ, while those of phyllosilicates decrease, and calcite concentrations remain constant (Tab. 2.4). Conversely, at Waikukupa Thrust, footwall concentrations of clastic phases and calcite are comparable to those of the hanging wall close to the contact with the PSZ, and phyllosilicates are slightly more abundant in the footwall compared to the hanging wall adjacent to the PSZ. Compared to the PSZ, clastic phases are significantly more abundant and amounts of phyllosilicate are lower.

2.5.4 Geochemistry

Element concentrations commonly scatter and, if at all, increase or decrease only slightly towards the PSZs (Tab. 2.5). The isocon analysis reveals a slight but recognizable correlation between the amount of fluid-related alteration and PSZ thickness: using the slope of the isocon as a proxy to assess the overall degree of fluid-related alteration, with a larger deviation from one indicating a higher amount of alteration, the hanging walls and footwalls of locations characterised by a thinner PSZ are generally less affected by metasomatism (Fig. 2.9; Tabs. 2.6 and S2.1). The PSZs display the same trend, but less pronounced. This is especially valid for the PSZ at Waikukupa Thrust, which is affected by a fluid-related mass change of up to 68 % (Tab. 2.6). However, microstructural observations (see Section 2.5.2.2 and Schuck et al., 2018) suggest this is most likely related to the extraordinarily large amount of calcite veins.

Enrichment of individual elements confirms this correlation: enrichment of Al_2O_3, CaO, LOI, MnO, P_2O_5 and TiO_2 in hanging wall and footwall rocks is more pronounced at locations with thicker PSZ compared to those with thinner PSZ (Tabs. 2.6 and S2.2). Element enrichment of PSZ fault gouges exhibits a similar but less pronounced trend. Comparable to the general

Table 2.4: Mineralogical composition [wt%] of investigated samples as determined by XRD analysis and subsequent Rietveld refinement. Mineral abbreviations are: Qtz: quartz; Plg: plagioclase; KFsp: potassium feldspar; Cc: calcite; Ank: ankerite; Chl: chlorite; Kln: kaolinite; Ms: muscovite; Ill: illite; Bt: biotite; Amp: amphibole; Ep: epidote; Srp: serpentine group minerals; Ap: apatite; Py: pyrite.

sample	location	lithology	dist. to PSZ[a]	Qtz	Plg[b]	KFsp	Cc	Ank	Chl	Kln	Ms	Ill	Bt	Amp[c]	Ep	Srp[d]	Ap	Py
129	Havelock Creek	gouge	0 cm	23	25	4	11		19	2	4	5	3	3				< 1
130_1	Gaunt Creek	gouge	0 cm	22	14	7	6		6		46							
130_2		gravel	- 2.5 cm	23	21	7	6		12		3	25	2					
130_3		gravel	- 4.75 cm	25	20	15	6		8	1	14	6	5					
120	DFDP-1A	cataclasite	292 cm	32	9	4	3		10	1	20	14	7				< 1	
119		cataclasite	270 cm	26	26	7	5		9	2	23		2				< 1	
118		cataclasite	135 cm	29	7	4	2		14	22	18	3	< 1				1	
117		cataclasite	87 cm	37	11	7	8		11	1	23	2	1					
116		cataclasite	25 cm	22	6	18	18		22	4	3	4	2				< 1	
115		gouge	0 cm	27	8	5	2		5	30	10	11	2				< 1	
132	Waikukupa Thrust	cataclasite	70 cm	23	41		3	1	16	< 1	2		4	9				< 1
124		cataclasite	25 cm	29	36	1	2		9	1	1	1	2	12	6			< 1
125_1		cataclasite	8 cm	32	36	1	2		11	1	1		3	8	6			< 1
131_2		gouge	2 cm	22	17	4	16		10	1	28	< 1	1	1			1	< 1
131_1		gouge	0 cm	11	8	2	29	1	5	1	< 1	41	1				1	< 1
133		gravel	- 10 cm	31	33	1	1		7		4	10	7	4	2			
127_3	Martyr River	cataclasite	2 cm	20	23	5	10		15	17	3	1	1		7			
127_4		gouge	0 cm	13	9	4	3		9	38	4	8	2			5	< 1	

[a] Datum to calculate distance to PSZ refers to center of PSZ at Martyr River, Havelock Creek and the DFDP-1A borehole and to the contact between PSZ and footwall at Waikukupa Thrust and Gaunt Creek.
[b] Albite is the main plagioclase phase.
[c] Amphibole minerals encountered are typically hornblende.
[d] Main serpentine group minerals are to equal amounts lizardite and amesite.

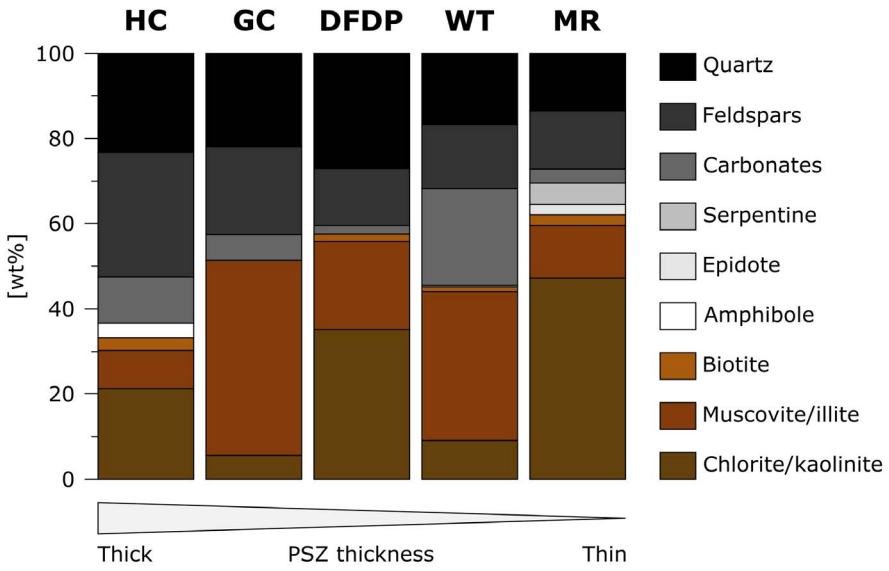

Figure 2.8: Simplified mineralogical composition of investigated PSZs based on the results presented in Table 2.4. HC: Havelock Creek; GC: Gaunt Creek; DFDP: Deep Fault Drilling Project core 1A.; WT: Waikukupa Thrust; MR: Martyr River.

pattern of isocon slopes described above, the PSZ at Waikukupa Thrust represents an outlier, because the large volume of calcite veins results in extraordinarily enriched CaO.

Looking at cross-fault transects, PSZs are more affected by metasomatism than hanging walls and footwalls. Furthermore, footwalls are generally less affected by metasomatism than hanging walls. However, DFDP-1A constitutes an exception, because the PSZ is less affected by metasomatism than the hanging wall cataclasites: the degree of fluid-related alteration increases towards the PSZ and displays the highest hanging wall amounts immediately adjacent to it (Tab. 2.6). This contrasts with Waikukupa Thrust, where samples display a continuing trend to higher amounts of fluid-related alteration from the hanging wall to the base of the PSZ close to the footwall.

2.6 Discussion

2.6.1 Fluid-related alteration and fluid transport within Alpine Fault rocks

Isocon analyses clearly demonstrate that all investigated fault rocks have been substantially altered by fluids (Fig. 2.9; Tab. 2.6), which is also shown by the presence of authigenic phyllosilicates (Figs. 2.6a & k) and calcite vein networks (Figs. 3.7j – m). In general, metasomatic alteration of the fault rocks resulted in element enrichment and mass gain, which is in agreement with previous work (Schuck et al., 2018). Analyses of Martyr River fault rocks seem to show an opposite pattern but this may be an artifact related to inappropriate choice of the protolith's geochemical composition (see Section2.4.3.1).

It is recognised that the Alpine Fault's PSZ constitutes an impermeable barrier restricting fluid circulation to its hanging wall (Sutherland et al., 2012; Menzies et al., 2016). Consequently, fluid-related element mobilisation can be expected in the hanging wall. This is confirmed by isocon analyses: DFDP-1A samples show increasing amounts of fluid-related alteration

Table 2.5: Geochemical composition [wt%] of investigated samples as determined by XRF.

sample	location	lithology	dist. to PSZ[a]	MnO	P_2O_5	TiO_2	Na_2O	K_2O	CaO	MgO	Fe_2O_3[b]	Al_2O_3	SiO_2	LOI	total
129	Havelock Creek	gouge	0 cm	0.13	0.20	0.81	1.77	1.39	7.85	4.20	6.49	13.60	51.7	11.49	99.62
130_1	Gaunt Creek	gouge	0 cm	0.13	0.19	0.76	1.94	3.27	6.78	3.64	6.66	13.43	51.40	11.38	99.58
130_2		gravel	- 2.5 cm	0.10	0.21	0.84	2.08	3.01	4.84	3.81	6.38	14.11	54.56	9.67	99.61
130_3		gravel	- 4.75 cm	0.11	0.21	0.74	2.11	2.86	5.60	3.53	5.72	13.73	56.13	8.90	99.63
120	DFDP-1A	cataclasite	292 cm	0.06	0.17	0.70	1.15	4.20	1.94	3.01	5.66	16.12	60.54	6.08	99.63
119		cataclasite	270 cm	0.07	0.15	0.63	2.32	2.42	3.79	2.23	3.95	12.72	53.31	18.2	99.79
118		cataclasite	135 cm	0.04	0.17	0.58	1.19	4.17	1.76	2.52	4.20	14.31	65.95	4.88	99.76
117		cataclasite	87 cm	0.08	0.16	0.54	0.84	3.16	3.97	3.13	4.23	11.75	53.10	18.77	99.73
116		cataclasite	25 cm	0.17	0.18	0.71	0.38	3.56	10.99	4.48	5.70	11.64	44.66	17.15	99.62
115		cataclasite	0 cm	0.06	0.18	0.56	1.29	3.80	2.03	2.12	4.00	13.25	62.62	9.71	99.62
132	Waikukupa Thrust	cataclasite	70 cm	0.13	0.11	0.89	4.20	0.52	3.74	4.93	7.73	14.37	59.25	3.77	99.64
124		cataclasite	25 cm	0.12	0.09	0.52	3.25	0.30	4.41	3.16	5.58	12.81	55.58	13.81	99.64
125_1		cataclasite	8 cm	0.11	0.10	0.61	3.11	0.44	4.34	3.44	5.57	12.73	58.13	11.00	99.57
131_2		gouge	2 cm	0.15	0.16	0.72	1.38	2.11	10.09	2.98	6.15	12.75	50.31	14.73	101.53
131_1		gouge	0 cm	0.27	0.13	0.57	0.85	1.78	24.96	2.42	5.18	10.07	38.62	12.73	97.58
133		gravel	- 10 cm	0.11	0.15	0.81	3.03	1.82	2.47	2.74	6.12	14.75	64.98	2.74	99.73
127_3	Martyr River	cataclasite	2 cm	0.11	0.18	0.69	2.27	1.80	8.74	4.50	6.11	13.45	52.67	8.96	99.47
127_4		gouge	0 cm	0.10	0.14	0.56	2.09	1.55	3.50	10.59	5.99	11.07	56.61	7.34	99.54

[a] Datum to calculate distance to PSZ refers to center of PSZ at Martyr River, Havelock Creek and the DFDP-1A borehole and to the contact between PSZ and footwall at Waikukupa Thrust and Gaunt Creek.
[b] Fe_2O_3 is total Fe content.

towards the PSZ with peak values immediately above it. However, at all other locations the fault gouges are more affected by fluid-related alteration than either hanging wall or footwall rocks (Fig. 2.9). This suggests, in combination with networks of anastomosing calcite veins (Figs. 3.7j – m; Schuck et al., 2018), that there is repeated transient fluid flow within the PSZ, most likely along-fault, because the veins are parallel to the shear plane.

Overall, results of isocon analyses confirm outcomes of previous studies, which demonstrated that fluid-related alteration significantly changed the petrophysical, mineralogical, geochemical and geomechanical properties of the Alpine Fault Zone (e.g., Boulton et al., 2012; Townend et al., 2013; Carpenter et al., 2014). This supports the proposal of Sutherland et al. (2012) that an "alteration zone" within ~50 m of the PSZ should be included as a fundamental and additional part of the Alpine Fault Zone architectural model (Fig. 2.2c).

Except for the slickolite observed in the DFDP-1A fault core (Fig. 3.7g), unambiguous microstructural evidence for pressure solution such as dissolution seams or indented and embayed clasts was not found. Annual rainfall along the NW edge of the Southern Alps is very high (e.g., Norris and Cooper, 1997, and references therein), and we suggest the observed dissolution of grain edges is related to weathering rather than deformation processes.

In summary, both the microstructures and the predominant enrichment of elements show that fluids are not responsible for stress-driven dissolution processes or for substantial mass transfer out of the fault zone. However, given that the amount of phyllosilicates and the degree of fluid-related alteration are negatively correlated (Figs. 2.8 & 2.9), the results of this study do not identify alteration mechanisms that completely explain the observed element mobilisation within the fault rocks, except at Waikukupa Thrust and Gaunt Creek, where Ca enrichment is associated with the formation of calcite networks (Figs. 3.7j – m).

2.6.2 Influence of shallow-depth conditions on fault gouge structure

In the following, we consider to what extent the fault gouges formed at shallow depths, thus do not provide information about deeper fault zone architecture.

Fault gouges at Waikukupa Thrust and Martyr River are layered. Continuous transects across the fault core would sample contacts of fault gouge with both hanging wall and footwall rocks. Furthermore, they would allow for microstructures to be described across the entire PSZ. However, these continuous transects are only available from Waikukupa Thrust and Martyr River. Consequently, the absence of layered fault gouges at other locations seems to be more appropriately explained by a sampling bias than by fault gouge layers being site-specific features.

Cowan et al. (2003) analysed low-angle detachment faults in Death Valley. There, layered fault gouges, consisting of a hanging wall- and a footwall-proximal layer, separate footwall cataclasites from weakly consolidated hanging wall sediments. Cowan et al. (2003) compare the footwall-proximal gouge layer to the hanging wall-proximal layer (i.e., the layer juxtaposed to the weakly consolidated sediments), finding the former to be fine-grained, clast-poor and supposed to have accommodated most of the strain. They interpret the formation of these layered fault gouges to reflect changing p–T conditions during exhumation, which in combination with fluid-related alteration, formed authigenic phyllosilicates within the PSZs

before fault rocks were brought in contact with weakly consolidated hanging wall sediments. This juxtaposition resulted in mechanical layering, enabling the hanging wall-proximal layer to accommodate most of the strain.

By considering the different fault kinematics of the Alpine Fault compared to these faults in Death Valley (thrust vs. low-angle detachment fault), the Alpine Fault with its layered gouges described in this and previous work (e.g., Boulton et al., 2012; Schuck et al., 2018) is structurally identical to the faults analysed in Death Valley (Fig. 2.10; for details see Biegel and Sammis, 2004). Furthermore, studied fault gouges bound footwall gravels, which are poorly consolidated and thus assumed to be mechanically weak. In addition, fault gouge layers juxtaposed on these weakly consolidated rocks (footwall-proximal layer at the Alpine Fault; hanging wall-proximal layer in Death Valley) are microstructurally comparable, as they contain fewer and preferentially smaller clasts than the other layers of the fault gouges (see also Tab. 2.2). Furthermore, microstructures of the calcite network in the footwall-proximal layer at Waikukupa Thrust suggest localised and cyclic faulting (Schuck et al., 2018) supporting the interpretation that this gouge unit accommodated most of the strain. Consequently, layered fault gouges and associated microstructures demonstrate that strain localisation and associated structural complexities within the Alpine Fault core are, at least partially, affected by shallow, hence late, processes, considering that exhumation of investigated rocks to subaerial level is accommodated entirely by the Alpine Fault's PSZ (e.g., Little et al., 2005; Toy et al., 2015).

This interpretation has major consequences for structural investigations of the Alpine Fault's PSZ, because it implies that formation of microstructures observed in outcrops was influenced by boundary conditions not representative of those along most of the fault rocks' exhumation path. This highlights the importance of continuing to attempt to obtain samples for microstructural investigations of Alpine Fault rocks from locations and/or depths where hanging wall and PSZ fault rocks are not juxtaposed on weakly consolidated footwall sediments. Acknowledging that there is no outcrop where the hard rock hanging wall is in contact with hard rock footwall (Townend et al., 2009), drilling projects aiming to penetrate the Alpine Fault at depths where Quaternary gravels do not constitute the footwall appear to be the only promising approach to achieve this end. This would also overcome the problem of data sparsity due to the limited amount of outcrops, improving the robustness of the results.

2.6.3 Architecture of Alpine Fault Zone

2.6.3.1 Alpine Fault damage zone

Norris and Cooper (2007) suggested an average brittle damage zone width of ~100 m, which is based on a compilation of outcrop studies in the fault's central segment. More recent investigations indicate wider damage zones: Alpine Fault outcrops in the segment south of Haast have damage zone widths between 90 and 240 m (Barth et al., 2013). Analyses of downhole geophysical data and recovered cores from the DFDP-2 borehole indicate that the Alpine Fault's hydrologically active damage zone contains an "inner zone" affected by earthquake rupture processes that is 0.5 km wide at up to 8 km depth and about 1 km wide at the surface (Fig. 2.2c). This inner damage zone is surrounded by an "outer zone" up to a few

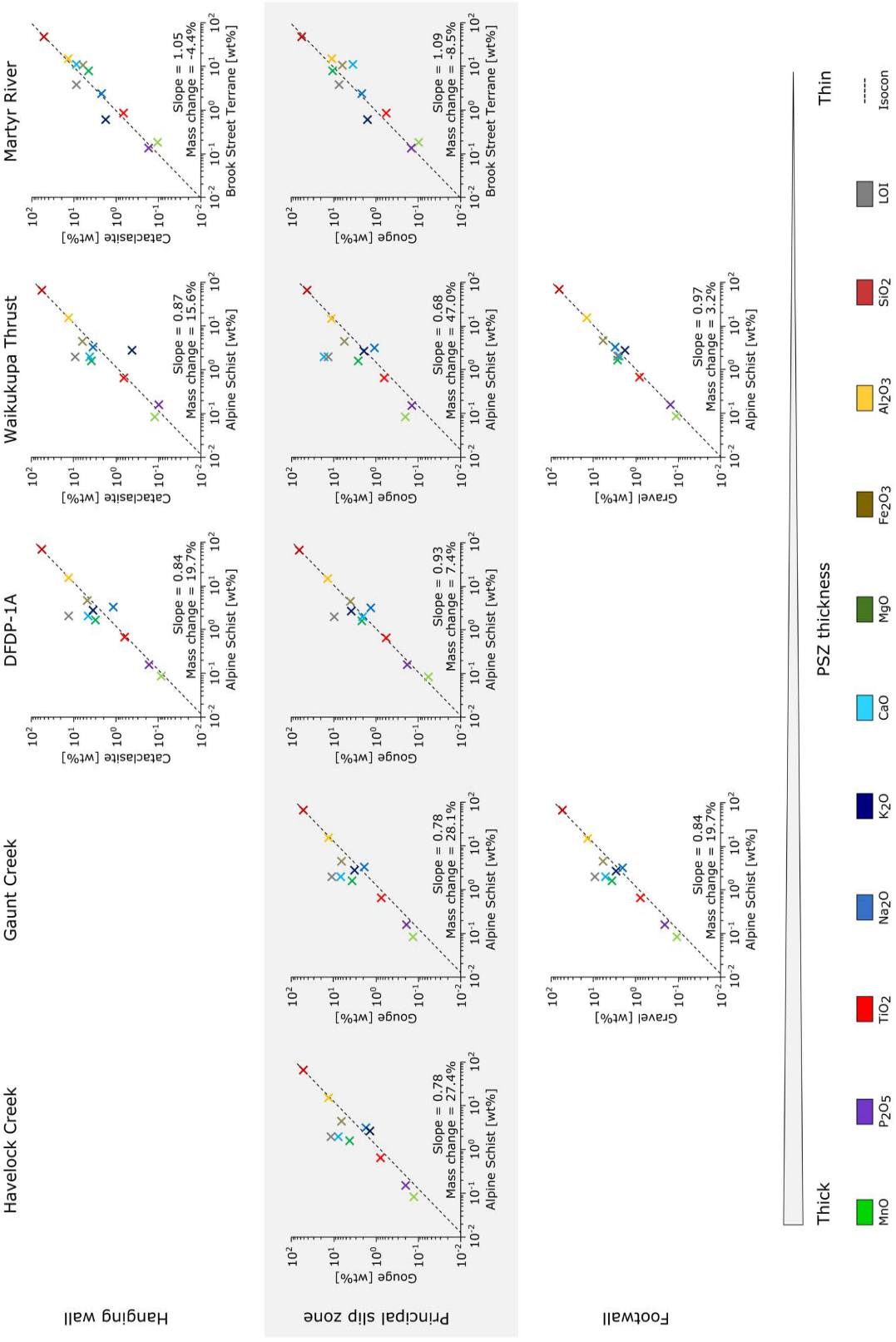

Figure 2.9: Isocon analysis of locations investigated. In the case of multiple measurements per structural unit (hanging wall, PSZ, footwall), data were averaged to derive single values. Values are given in Table S2.1.

Table 2.6: Slope m of the isocon and derived mass change (%), enrichment (positive values) and depletion (negative values) of elements for samples investigated relative to the host rocks. Geochemical composition of fault rocks is taken from Table 2.5 and composition of host rocks from Table S2.1. All concentrations are in wt%.

sample	location	unit	dist. to PSZ[a]	m	mass	MnO	P_2O_5	TiO_2	Na_2O	K_2O	CaO	MgO	Fe_2O_3[b]	Al_2O_3	SiO_2	LOI
129	Havelock Creek	gouge	0 cm	0.78	27.40	94.85	65.08	55.91	-31.00	-35.68	395.11	228.83	84.44	12.86	-1.98	629.70
130_1	Gaunt Creek	gouge	0 cm	0.78	28.07	98.89	52.93	47.97	-23.97	52.11	329.87	186.48	90.26	12.03	-2.03	626.44
130_2		gravel	- 2.5 cm	0.83	21.15	48.23	60.06	54.69	-22.89	32.45	190.29	183.66	72.42	11.34	-1.63	483.80
130_3		gravel	- 4.75 cm	0.85	18.29	55.86	54.02	32.90	-23.63	22.87	227.92	156.59	50.92	5.78	-1.19	424.59
120	DFDP-1A	cataclasite	292 cm	0.91	9.66	-18.72	17.71	16.38	-61.41	67.28	5.32	102.84	38.45	15.14	-1.20	232.57
119		cataclasite	270 cm	0.80	24.44	8.34	20.93	18.08	-11.66	9.38	133.48	70.53	9.64	3.10	-1.28	1028.87
118		cataclasite	135 cm	0.98	2.07	-48.36	7.62	-10.89	-62.83	54.59	-11.07	58.07	-4.37	-4.86	0.18	148.29
117		cataclasite	87 cm	0.80	25.34	17.97	23.40	2.57	-67.78	43.86	146.35	141.09	18.27	-4.07	-0.95	1072.90
116		cataclasite	25 cm	0.68	46.33	194.38	68.22	56.85	-82.99	89.20	696.11	302.84	86.05	10.94	-2.75	1150.83
115		gouge	0 cm	0.93	7.37	-26.74	22.07	-8.06	-57.62	48.18	7.90	39.87	-4.20	-7.34	0.05	419.42
132	Waikukupa Thrust	cataclasite	70 cm	0.89	12.28	77.01	-21.55	51.38	44.30	-78.79	107.89	240.17	93.61	5.09	-0.99	110.95
124		cataclasite	25 cm	0.84	19.72	70.42	-28.52	-5.12	19.06	-86,96	161.36	132.47	49.01	-0.11	-0.98	724.23
125_1		cataclasite	8 cm	0.87	15.00	47.46	-30.61	6.33	9.43	-81.62	147.07	143.09	42.88	-4.65	-0.52	530.30
131_2		gouge	2 cm	0.76	30.82	135.48	30.45	43.20	-44.76	0.26	553.46	139.57	79.46	8.64	-2.05	860.76
131_1		gouge	0 cm	0.60	67.79	427.04	38.54	45.71	-56.36	8.47	1973.23	149.52	93.87	10.05	-3.57	964.81
133		gravel	- 10 cm	0.97	3.22	37.22	0.31	26.31	-4.30	-31.77	26.22	73.80	40.91	-0.83	-0.18	41.14
127_3	Martyr River	cataclasite	2 cm	1.05	- 4.44	- 43.42	26.05	- 21.40	- 9.39	189.57	- 25.18	- 43.95	- 43.67	- 15.12	5.29	128.73
127_4		gouge	0 cm	1.09	- 8.54	- 49.46	- 1.42	- 39.56	- 20.16	138.65	- 71.32	26.24	47.15	33.13	8.31	79.31

[a] Datum to calculate distance to PSZ refers to center of PSZ at Martyr River, Havelock Creek and the DFDP-1A borehole and to the contact between PSZ and footwall at Waikukupa Thrust and Gaunt Creek.
[b] Fe_2O_3 is total Fe content.

kilometers wide, which might be a near-surface, topographically controlled feature (Townend et al., 2017; Massiot et al., 2018; Williams et al., 2018).

Outcrop and drill core investigations demonstrate quite constant fracture densities within at least 500 m of the PSZ in the hanging wall and 30 m in the footwall (Williams et al., 2016; Williams et al., 2018), which is different from decreasing fracture densities towards the fault cores observed elsewhere (e.g., Chester et al., 2005; Faulkner et al., 2006; Mitchel and Faulkner, 2009). In fact, DFDP investigations show that apparent fracture density decreases with depth, i.e., towards the PSZ (Townend et al., 2013; Williams et al., 2016). However, this is considered as an artifact resulting from rapid exhumation and associated unloading (Williams et al., 2016). Furthermore, despite its presence across the entire damage zone, gouge-filled fractures within < 160 m of the PSZ tend to be thinner (< 1 cm) and more abundant (Williams et al., 2018).

2.6.3.2 Alpine Fault core

Extent of fault core

As a result of the pervasive alteration zone surrounding the PSZ, the fault core of the Alpine Fault is rather diffuse (Sutherland et al., 2012; Townend et al., 2013; Williams et al., 2018). Commonly, the fault gouge forming the PSZ and part of the surrounding cataclasites are considered to constitute the fault core (e.g., Williams et al., 2017). However, there is some ambiguity when it comes to actually defining the width of the fault core: Toy et al. (2015) consider a 20 - 30 m wide zone around the PSZ as fault core, and Sutherland et al. (2012) and Townend et al. (2017) narrow it down to 2 m surrounding the PSZ with an additional degree of localisation manifested in the < 0.5 m wide PSZ (Sutherland et al., 2012; Williams et al., 2016). However, by defining the damage zone as having elevated fracture densities compared to the host rock (Chester et al., 1993; Faulkner et al., 2010), and noting that there is no observable variation in fracture density within 30 m of the PSZ (Williams et al., 2016), it seems reasonable to exclusively consider the fault gouge forming the PSZ as core of the Alpine Fault's central segment. This view is supported by fault gouge microstructures:

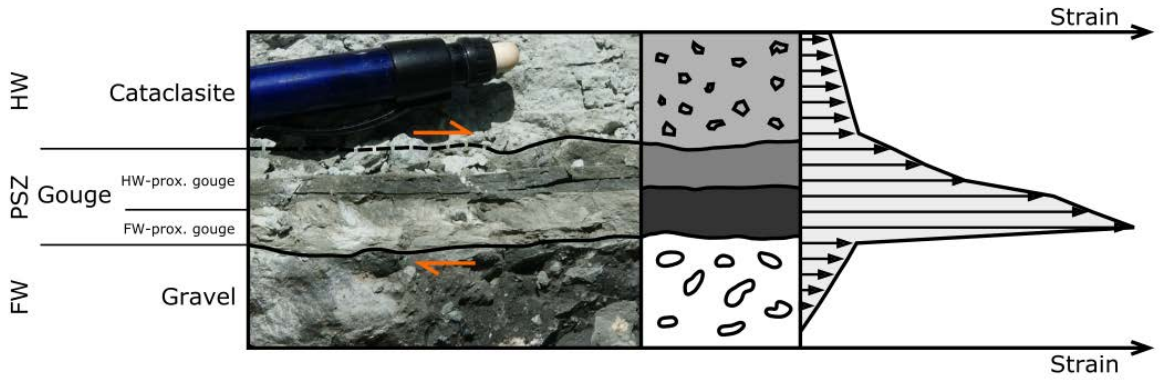

Figure 2.10: Conceptual model providing a potential explanation of how layered principal slip zones observed at Martyr River and Waikukupa Thrust could have been formed. Resulting from the juxtaposition of weakly consolidated sediments in the footwall and relatively competent fault rocks, strain localised non-homogenously in the PSZ. The photograph example is from Waikukupa Thrust. The stippled line indicates where the contact between cataclasite and gouge is obscured by debris. The figure was modified from Cowan et al. (2003).

microfaults (Figs. 2.6h & i), predominantly encountered in hanging wall cataclasites but also present in fault gouges (Tab. 2.3), show that strain is localised to discrete structures within the PSZ. Furthermore, the fault breccias encountered in these microfaults exhibit a broad range in degree of sorting (poorly to very well) and grain size (< 2 - 100s of micrometer), which demonstrates that they accommodated different amounts of strain. However, microfaults appear to be a local phenomenon and there are no continuous, discrete slip planes within the PSZ, despite the large finite displacement accommodated.

This interpretation is further backed by distinct geophysical (e.g., Townend et al., 2013), petrophysical (e.g., Carpenter et al., 2014), mineralogical (e.g., Schleicher et al., 2015), microstructural (e.g., Toy et al., 2015) and geochemical (Schuck et al., 2018) properties of the PSZ. To the SW of the study area, the fault core might be more complex, because of its different lithological composition and fault orientation (Barth et al., 2013).

Implications of fault core along-strike variations for fault zone architecture

Investigated fault rocks are mostly comparable in terms of microstructures and mineralogy (Tabs. 2.1 - 2.4). However, individual outcrops display distinct differences, which will be discussed in the context of the Alpine Fault Zone's architecture in the following.

The most remarkable difference among individual locations is the variation in PSZ thickness by a factor of 25 (2 cm at Martyr River vs. 50 cm at Havelock Creek; Figs. 2.3 – 2.5). Similar along-strike variations of PSZ thickness have been reported previously from other faults (e.g., Sagy and Brodsky, 2009; Kirkpatrick et al., 2018). It has been suggested that such variations may be a result of the active mechanisms of deformation (Hobbs et al., 1990; Schrank et al., 2008; Sagy and Brodsky, 2009), or initial presence of heterogeneities subsequently amplified during continuous deformation (Segall and Pollard, 1983; Schrank et al., 2008; Norris and Toy, 2014; Fossen and Cavalcante, 2017). Common examples are variations in mechanical strength reflecting differing viscosities as result of compositional heterogeneities (Chester et al., 1993; Faulkner et al., 2003; Schrank et al., 2008; Rybacki et al., 2014; Nardini et al., 2018), varying geometric properties (Cowan et al., 2003; Schrank et al., 2008) or a combination of these factors (Schrank et al., 2008; Boese et al., 2012; Czaplinska et al., 2015).

As will be elaborated in the following, these explanations do not appear to be responsible for the observed variations. PSZ thickness does not vary systematically along-strike in the sampled locations (Fig. 2.2b). Furthermore, all locations, except Martyr River, are in the central segment of the Alpine Fault where the Torlesse Terrane Alpine Schist is the protolith. This demonstrates that variations of protolith mineralogy have no significant influence on the observed differences in PSZ thickness. However, fault gouge thickness correlates with mineralogy: thicker gouges at Havelock Creek, Gaunt Creek and the DFDP-1A core are richer in clastic phases and poorer in phyllosilicates than the thin gouges of Martyr River and Waikukupa Thrust (Fig. 2.8). This is astonishing, because elsewhere phyllosilicate-rich fault gouges generally tend to be wider (Faulkner et al., 2003) owing to the frictionally weak nature of these phases (Moore et al., 1997; Moore and Lockner, 2007; Lockner et al., 2011; Carpenter et al., 2015). Conversely, other fault zones with quartzofeldspathic compositions like the Alpine Fault have been found to be fairly narrow (Chester et al., 1993; Faulkner et al.,

2003). Consequently, unlike these fault zones, the Alpine Fault displays a negative correlation between phyllosilicate content and fault core thickness. This suggests that strain localisation within the fault core might be governed by processes insensitive to rheological variations caused by differing fault rock composition, although observed slight microstructural differences such as grain size (see also Tabs. 2.1 - 2.3) could influence localisation. However, data are too scarce to derive robust conclusions. In addition, orientation of the fault (Figs. 2.2a & b), magnitude of stress and the stress field itself (Boese et al., 2012; Warren-Smith et al., 2017) are fairly constant along the central segment of the Alpine Fault, thus it is less likely that these parameters are responsible for the observed variations of fault gouge thickness. However, it is still possible that the extreme variations in topography typical of the Alpine Fault hanging wall generated quite different stress fields at our investigated sites (see Upton et al., 2017). Biegel and Sammis (2004) suggested that along-strike variations of gouge thickness record rupture arrest. However, our observations (and the nature of Alpine Fault outcrops in general) do not easily lend themselves to a systematic analysis of this kind in the Alpine Fault Zone.

Another approach to explain observed thickness variations is to examine the relation between fault core width and displacement. Wear models based on empirical observations describe a positive correlation between gouge thickness and displacement (e.g., Hull, 1988; Scholz, 1987). However, quantitative models of fault core evolution have so far failed to reproduce data sets compiled on natural faults (e.g., Blenkinsop, 1989; Evans, 1990; Sibson, 2003). Nevertheless, faults that accommodated larger displacements do appear to generally have thicker fault cores (Evans, 1990; Ben-Zion and Sammis, 2003; Sagy and Brodsky, 2009; Faulkner et al., 2010, and references therein). In other words: the more earthquakes a fault has seen, the thicker its PSZ may be (Ma et al., 2006; Li et al., 2013). Four of the five fault gouges investigated are located in the Alpine Fault's central segment, which is believed to rupture entirely during an earthquake (Sutherland et al., 2007; Howarth et al., 2018) and to have done so for at least the last ~8000 years (Berryman et al., 2012). If we employ the simple relationship that shear strain in a fault zone is equal to zone width multiplied by boundary displacement, and assume constant strain distribution within the PSZ gouges, the PSZ thickness variations we describe suggest the studied fault gouges accommodated different amounts of coseismic displacement.

Other examples where PSZ thickness varies by 1 order of magnitude within tens of meters along strike are not comparable to the Alpine Fault, because these faults accommodated substantially less displacement than the Alpine Fault: Shervais and Kirkpatrick (2016) and Kirkpatrick et al. (2018) investigate a fault which accommodated displacement of the order of 10 – 30 km. The fault core contains at least 13 individual slip layers, suggesting that slip accommodated by these individual slip layers is most likely substantially smaller than the overall fault displacement. Consequently, observed PSZ thickness variations potentially reflect fault roughness, which is supposed to smooth as displacement increases (Sagy and Brodsky, 2009; Brodsky et al., 2011). In contrast, the Alpine Fault not only accommodated at least 470 km of displacement (Sutherland et al., 2007), its fault gouge also does not display discrete slip planes (see Section 2.5.2.2). Furthermore, contacts between the fault gouge and the hanging wall and between the fault gouge and the footwall are – where sufficiently exposed – smooth (Figs. 2.4b – d & 2.5b – d).

Consequently, Alpine Fault PSZ thickness variations reflecting different amounts of displacement imply that the studied PSZs are not part of the same shear plane, and that the Alpine Fault Zone hosts multiple fault strands, which may not be active simultaneously (Figs. 2.1b & 2.11). Figure 2.11 demonstrates how difficult it will be to identify the fault strand active during the most recent event.

Further evidence for a more complex Alpine Fault Zone architecture

This assumption of a more complex Alpine Fault Zone geometry is further supported by microstructural, mineralogical and geophysical observations to be discussed in the following. Most obviously, DFDP results promote a more complex view of the fault zone architecture of the Alpine Fault: DFDP-1B is the only location in the fault's central segment where there are two PSZs, both bound by brittle fault rocks (Fig. 2.3a; Sutherland et al., 2012; Toy et al., 2015). This is substantially different from other locations at the Alpine Fault, where multiple fault strands have been identified in Quaternary sediments, which are poorly consolidated and several tens of meters to a few hundred meters thick, covering the hanging wall and the footwall (Kaiser et al., 2009; Carpentier et al., 2012). The presence of these two PSZs in

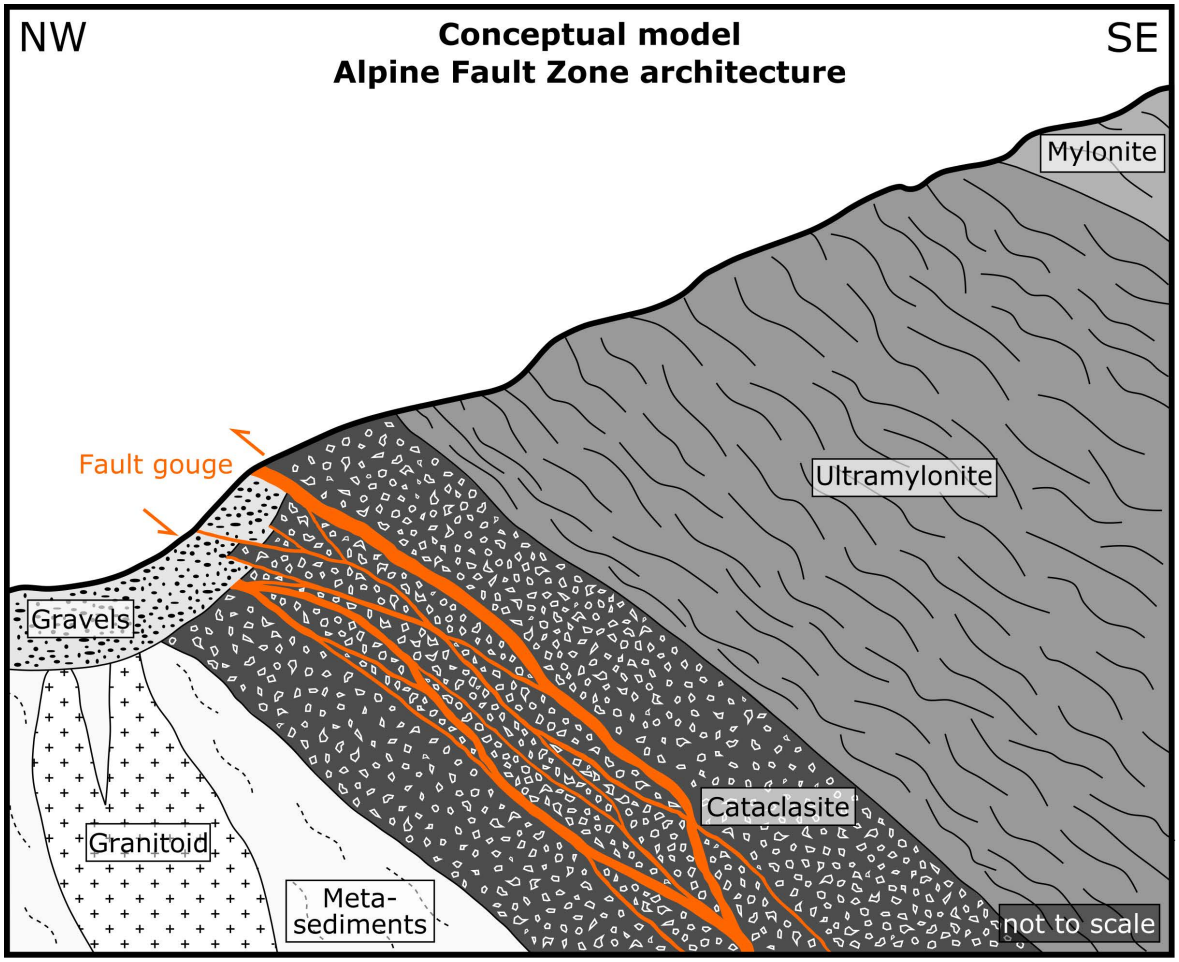

Figure 2.11: Proposed conceptual model of the Alpine Fault Zone architecture. Multiple fault strands, with gouge thicknesses varying between a few and several tens of centimeters, accommodate displacement. Different fault gouge thicknesses represent different amounts of displacement accommodated by individual fault strands. This demonstrates the difficulty to identify the fault strand active during the last event.

DFDP-1B could reflect that displacement was accommodated by more than one PSZ, which is dissimilar to the paradigm of uplift along a single fault plane (e.g., Little et al., 2005; Toy et al., 2015), and/or that one PSZ was abandoned and displacement transferred to another PSZ. Fault gouge dating could help answer this question, but is beyond the scope of this paper.

Furthermore, although the shallower DFDP-1B PSZ and the PSZ of DFDP-1A have so far been assumed to belong to the same fault plane (Fig. 2.3a), they exhibit different mineralogical and hence geomechanical properties (Boulton et al., 2014; Schleicher et al., 2015). This is unexpected given the close proximity of the boreholes and thus sample spacing of less than 100 m (Sutherland et al., 2012), because the distinct mineral compositions of these two PSZs represent high (DFDP-1A) and low (DFDP-1B) temperature alteration, respectively. Considering the proximity of the two drill sites, the distinct mineralogies reflecting different temperatures – and hence depths – of formation appear to go beyond what one would expect as common along-strike variation observed in the field. Similarly, although mineralogically comparable (Fig. 2.8), fault gouge microstructures of DFDP-1A and Gaunt Creek, also within only ~100 m distance (Fig. 2.3a), differ remarkably, as exemplified by the almost completely cemented DFDP-1A PSZ compared to the PSZ at Gaunt Creek (Tab. 2.2; Figs. 3.7e, f, k – m).

In light of this interpretation, the ~1 cm thick, matrix clast-bearing layer sampled ~8 cm below the PSZ at Gaunt Creek (Figs. 2.3d, e, 2.5b & 2.6d), which is microstructurally similar to the investigated fault gouges at Havelock Creek and Waikukupa Thrust (hanging wall-proximal layer), could be considered to constitute another PSZ of the Alpine Fault, currently starting to accommodate larger amounts of slip, or an inactive one as observed in the fault's southern segment (Barth et al., 2013).

Geometric and spatial relationships, mineralogical composition and geomechanical properties of the various (potential) PSZs at Gaunt Creek / DFDP-1 (Fig. 2.3a) support our hypothesis that displacement along the Alpine Fault is accommodated by more than one PSZ.

The Alpine Fault's more complex geometry: a shallow-depth phenomenon?

The multidisciplinary approach presented here reveals that the Alpine Fault Zone has a complex geometry (see Figs.2.1b & 2.11), which is different from other quartzofeldspathic faults but typical for carbonate or phyllosilicate-hosted ones (Faulkner et al., 2003). However, it cannot be excluded that the observations we present in favor of a more complex fault zone geometry simply reflect shallow-depth phenomena like layered fault gouges do. Active seismic source investigations at the DFDP-2 site and around Haast also support a more complex fault zone model. These studies imaged a series of subparallel reflectors, interpreted as multiple fault strands (Lay et al., 2016; Lukács et al., 2018), which are comparable to those hosted by the Quaternary sediments covering the hanging wall and the footwall (Kaiser et al., 2009; Carpentier et al., 2012). There are also indications that these fault strands at the DFDP-2 site and around Haast extend into the basement. So far, it is debated if these separate fault strands are isolated or anastomosing and if they are / were active contemporaneously or consecutively (Lukács et al., 2018). Note that this structural complexity differs from the situation encountered at Waikukupa Thrust, as the second fault strand encountered at Hare

Mare Creek, 700 m to the NE of this location, resulted from incision of the Waikukupa River and subsequent stress reorientation (Norris and Cooper, 1997).

2.7 Conclusions

Layered fault gouges reflect a structural complexity of the Alpine Fault's PSZ, which originates from shallow-depth processes. At depths where Quaternary gravels comprise the footwall, rheological contrasts resulting from the juxtaposition of these poorly consolidated and mechanically weak footwall sediments with more competent hanging wall cataclasites control the distribution of strain within the fault gouge and result in the layered structure at shallow depths. Consequently, rheological interpretations based on these rocks are biased as their microstructures mostly record modifications in just the latest part of the exhumation trajectory. These results also show that careful analyses are necessary in order to study actively exhuming fault zones and that samples should be taken at greater depths to fully investigate these kinds of faults.

Variations of PSZ fault gouge thickness among individual study sites suggest that fault rocks at these locations accommodated different amounts of displacement. Assuming that the Alpine Fault's central segment, where most of the sites are located, is activated entirely during an earthquake, these thickness variations suggest that investigated PSZs are not located on the same fault plane. This implies that multiple fault strands accommodate Alpine Fault displacement. These findings, which are based on field and microstructural analyses, are further supported by the results of the Deep Fault Drilling Project and geophysical investigations.

Consequently, these results show that the Alpine Fault Zone architecture is more appropriately described by the broad and complex conceptual model of Faulkner et al. (2003) rather than the simple single PSZ model of Caine et al. (1996).

2.8 Acknowledgements

We thank Stefan Gehrmann for the preparation of thin sections as well as Hartmut Liep and Marina Ospald for preparing powder samples. We would also like to thank Lina Harfenmeister and Andrea Gotsche for help with XRF and Marie Bonitz for assistance with XRD analyses. Anja Schreiber and Richard Wirth are acknowledged for TEM-foil preparation and TEM analysis, respectively. Uwe Wollenberg (EMR Group, Geological Institute, RWTH Aachen University) enabled access to and provided help with CL analyses. We are grateful to Christoph Schrank and an anonymous reviewer who stimulated fruitful discussions that helped to substantially improve the manuscript. This research has been funded by the German Research Foundation (DFG) (grant no. JA 573/8-2). Furthermore, the project was supported by the Royal Society of New Zealand Rutherford Discovery Fellowship (RDF) (grant no. 16-UOO-1602).

3 Microstructures imply cataclasis and authigenic mineral formation control geomechanical properties of New Zealand's Alpine Fault

3.1 Abstract

The Alpine Fault is capable of generating large ($M_W > 8$) earthquakes and is the main geohazard on South Island, NZ, and late in its 250 - 291-year seismic cycle. To minimise its hazard potential, it is indispensable to identify and understand the processes influencing the geomechanical behaviour and strength-evolution of the fault. High-resolution microstructural, mineralogical and geochemical analyses of the Alpine Fault's core demonstrate wall rock fragmentation, assisted by mineral dissolution, and cementation resulting in the formation of a fine-grained principal slip zone (PSZ). A complex network of anastomosing and mutually cross-cutting calcite veins implies that faulting occurred during episodes of dilation, slip and sealing. Fluid-assisted dilatancy leads to a significant volume increase accommodated by vein formation in the fault core. Undeformed euhedral chlorite crystals and calcite veins that have cut footwall gravels demonstrate that these processes occurred very close to the Earth's surface. Microstructural evidence indicates that cataclastic processes dominate the deformation and we suggest that powder lubrication and grain rolling, particularly influenced by abundant nanoparticles, play a key role in the fault core's velocity-weakening behaviour rather than frictional sliding. This is further supported by the absence of smectite, which is reasonable given recently measured geothermal gradients of more than $120\,^{\circ}\mathrm{C\,km^{-1}}$ and the impermeable nature of the PSZ, which both limit the growth of this phase and restrict its stability to shallow depths. Our observations demonstrate that high-temperature fluids can influence authigenic mineral formation and thus control the fault's geomechanical behaviour and the cyclic evolution of its strength.

3.2 Introduction

Large plate-bounding faults, such as the Alpine Fault (NZ), the Japan Trench (JPN), the San Andreas Fault (USA) and the North Anatolian Fault Zone (TR), often lie in close proximity to densely populated areas and thus constitute major geohazards with the potential to cause many fatalities (Sutherland et al., 2006; Martínez-Garzón et al., 2015; Bohnhoff et al., 2017).

A key-prerequisite for the capability of a fault to generate large earthquakes and tsunamis is its ability to accumulate large amounts of elastic energy (Fialko, 2006; Townend et al., 2013).

The mechanical response of faults to tectonic loading, especially if it will release stress continuously by creep or catastrophically by large events, depends mainly on spatial and temporal variations in frictional strength (Sibson, 1977; Sibson, 1992a; Byerlee, 1978; Warren-Smith et al., 2017), which are affected by changes in mineralogical composition, porosity and microstructural fabric of wall rock and fault gouge (Lockner et al., 2011; Janssen et al., 2016; Boulton et al., 2017b; Kaduri et al., 2017). Initially, fault nucleation and strain localisation may result from strength heterogeneities and viscosity contrasts in the host rock (Pennacchioni and Mancktelow, 2007; Jessell et al., 2009).

A number of field and laboratory observations and numerical studies suggest that progressive shear involves a complex interplay of structural and poroelastic stress changes as well as mineral reactions resulting in fault weakening (e.g., Ben-Zion and Sammis, 2003; Bradbury et al., 2015; Gardner et al., 2017; Smeraglia et al., 2017). This may change the mechanical response of faults, such as fostering aseismic creep at the expense of seismic faulting and consequently reduce their hazard potential (Fialko, 2006; Ikari et al., 2009; Schleicher et al., 2012; Boulton et al., 2017b).

In particular, changes of fluid pressure have been found to significantly affect the mechanical behaviour and seismic response of faults up to the crustal-scale (Sibson, 1992a; Hickman et al., 1995; Faulkner and Rutter, 2001). In exposed fault zones, the presence of quartz and calcite veins is commonly interpreted as manifestation of changing fluid pressures (Sibson et al., 1988; Cox, 1995). These microstructures allow estimates of the variations in shear stress, fluid pressure and near-field stress perturbations during faulting (Cox, 1995; Rybacki et al., 2011; Bons et al., 2012).

In addition, fluids act as agents in chemical reactions leading to alteration, dissolution and authigenic clay formation. Such mineral reactions may contribute to fault weakening (Hickman et al., 1995; Moore and Lockner, 2007; Schleicher et al., 2010; Morrow et al., 2017) or to fault healing and strengthening, significantly changing porosity and permeability (Chester and Logan, 1986; Zoback et al., 2007; Schleicher et al., 2009; Sutherland et al., 2012). However, as the mineral phases responsible for fault weakening or strengthening are only stable within certain pressure and temperature fields, their presence and influence on the rheological behaviour of the fault vary during uplift or burial (e.g., Toy et al., 2010; Sutherland et al., 2017).

Microstructural, mineralogical and geochemical variations within the fault rocks provide evidence for the physical, chemical and mechanical conditions during deformation and are essential to understand fault nucleation and propagation and associated earthquake hazards (Janssen et al., 2016; Bohnhoff et al., 2017; Boulton et al., 2017b). While seismic and seismological analyses provide information on fault geometries at depth (Little et al., 2005), the presence of fluids (Stern et al., 2001) and stress accumulation (Bohnhoff et al., 2017), outcrops provide excellent opportunities to directly study fault rocks originating from seismogenic depths and to deduce deformation mechanisms by characteristic microstructures (Chester and Logan, 1986). However, during exhumation, structures formed at depth are overprinted by a

variety of mechanisms all active under specific pressure and temperature conditions (Toy et al., 2015). While this disturbs the original rock signatures, detailed observations may enable the identification of petrogenetic sequences providing valuable information on deformation conditions during uplift (Boulton et al., 2017a).

The Alpine Fault in New Zealand rapidly exhumes rocks from mid-crustal levels (Little et al., 2005). The initial lithological setting is relatively simple along large portions of the fault's central segment (Roser and Cooper, 1990), which makes it an excellent study area to investigate microstructures resulting from deformation at depth in the ductile regime followed by brittle deformation during exhumation (Toy et al., 2015). Consequently, a plethora of field studies, laboratory work, seismological surveys and drilling campaigns have investigated the petrological, mechanical, petrophysical and chemical properties of the Alpine Fault. The hanging wall in the central segment, where rocks from seismogenic depths are exhumed most rapidly (Little et al., 2005), was the focus of many of these studies (e.g., McClintock and Cooper, 2003; Toy et al., 2010; Boese et al., 2012; Ikari et al., 2015). While many of them targeted individual structural units, only a few have examined the changes of these properties associated with the transition from one type of fault rock to another one (e.g., Boulton et al., 2012; Williams et al., 2016).

Regarding the fault's core and its principal slip zone (PSZ), these analyses are technically challenging, because of the very small grain sizes and the great abundance of phyllosilicates (Warr and Cox, 2001; Schleicher et al., 2015). Nonetheless, as the Alpine Fault is the main geohazard on New Zealand's South Island (Boulton et al., 2017b), identifying the dominant deformation mechanisms is key to understanding its seismic behaviour. In this study, we focus on high-resolution microstructural, geochemical and mineralogical analyses of material sampled from the Alpine Fault's core and adjacent hanging and footwall rocks at the Waikukupa Thrust (Fig. 3.1) to determine the deformation mechanisms that operated within it, particularly focusing on the role of fluids on mineralisation, alteration, rupture nucleation and propagation, and slip along the fault.

3.3 Geological Setting

The transpressive Alpine Fault has a surface trace of about 800 km and is the main structure forming the Australian and the Pacific Plate boundary within New Zealand's South Island. The cumulative right-lateral offset amounts to about 470 km (Sutherland et al., 2007) and shortening normal to the fault is 90 ± 20 km (Little et al., 2005; Fig. 3.1). The central segment of the Alpine Fault, located between Toaroha River and Martyr River (Fig. 3.1a), accommodates strike-slip displacement at a rate of 27 ± 5 mm yr^{-1} (Norris and Cooper, 2000), corresponding to about 70 % of the total relative velocity between the Australian and the Pacific Plate (DeMets et al., 2010). In this central fault segment, hanging wall greenschist and amphibolite facies rocks are exhumed along a NE – SW striking and 30 ° – 50 ° SE dipping fault plane from 35 km depth at a long-term uplift rate of about 6 – 9 mm yr^{-1} (Little et al., 2005). This rapid exhumation transports heat from deep to shallow crustal levels resulting in elevated geothermal gradients of locally up to 125 °C km^{-1} (Sutherland et al., 2017).

Considered to be capable to rupture along its entire onshore segment, the fault generates large magnitude earthquakes (i.e., $M_W > 8$) with up to 8 – 9 m of lateral slip and up to 1 m of fault normal displacement (Sutherland et al., 2007). The average recurrence interval along the fault section south of Haast (Fig. 3.1a) during the last 8000 years is 291 ± 23 years (Cochran et al., 2017) and roughly 250 years for the central fault segment (Nicol, 2016) with the last event dating to 1717 AD (Sutherland et al., 2007). Consequently, the fault is late in its seismic cycle (Cochran et al., 2017). Currently, it is locked down to a depth of 12 – 18 km with most of the elastic strain being accumulated within a 30 km wide zone (Beavan et al., 2007; Beavan et al., 2010; Wallace et al., 2007).

In the hanging wall, (ultra)mylonites of the quartzofeldspathic Alpine Schist, progressively deformed by ductile creep, crop out within one kilometer of the fault plane. The high-

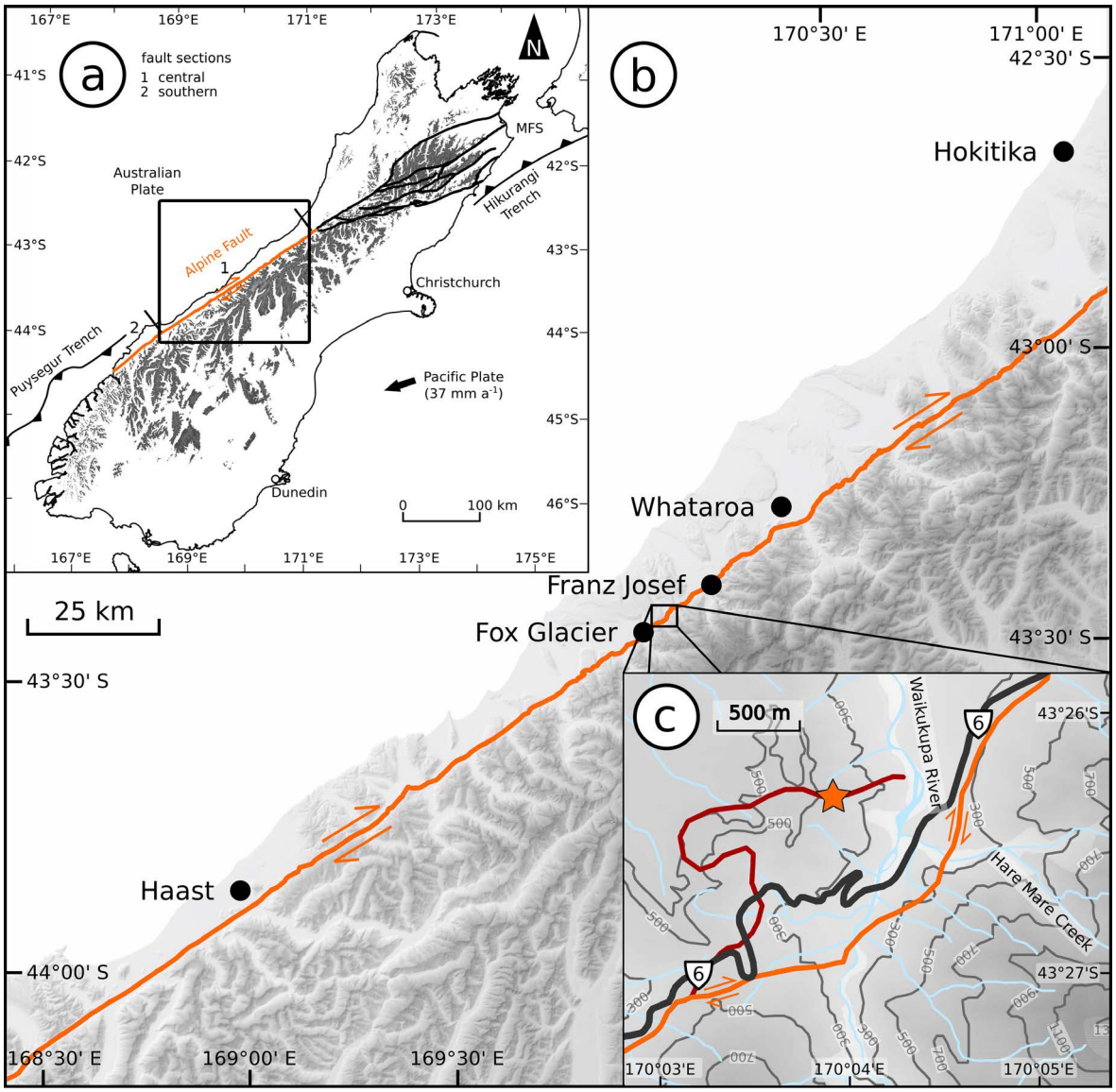

Figure 3.1: (a) Map of New Zealand's South Island showing the major plate boundary forming faults with the Alpine Fault's onshore segment in orange. Elevation higher than 1000 m is shown in grey. Onshore faults provided by GNS (Active Fault Database: `http://data.gns.cri.nz/af/`). Rectangle indicates location of (b). **(b)** Digital elevation model (DEM) image of the fault's central segment using a 15 m DEM (Columbus et al., 2011). **(c)** Waikukupa Thrust (dark red line) is an abandoned segment of the Alpine Fault. Star marks sampling location.

temperature fabric of the schist is overprinted by fractures that form a cataclastic damage zone exposed within 30 m of the fault core. The pale-green cataclasites were cemented mainly by phyllosilicates and carbonates (Sutherland et al., 2012; Toy et al., 2015; Williams et al., 2016). Cataclasites and an incohesive, fine-grained and impermeable fault gouge, identified as principal slip zone (PSZ), form the 2 – 30 cm thick fault core (Boulton et al., 2012; Sutherland et al., 2012). The footwall comprises Quaternary fluvioglacial sediments, overlying metasediments intruded by Paleozoic to Cretaceous granitoids (Toy et al., 2015).

The Waikukupa Thrust (Fig. 3.1c) sampling location, is an abandoned thrust segment of the Alpine Fault with a 4 km long curvilinear surface trace, where a layered PSZ sharply separates mylonites and cataclasites from fluvioglacial Quaternary gravel (Norris and Cooper, 1997).

3.4 Methods

3.4.1 Sampling and sample preparation

We sampled the fault core across the exposed PSZ, juxtaposing the hanging wall material and the Quaternary gravel forming the footwall using a hand-held chainsaw equipped with a silicon-carbide chain. After recovery, specimen were wrapped immediately in aluminum and plastic foil to slow down drying. Later, samples were embedded in resin and subsamples parallel and perpendicular to the fault trace were obtained from dry cuts with a low-speed saw. These subsamples were used for optical, scanning and transmission electron microscopy (SEM / TEM) to image the micro- and nanostructures, X-ray diffraction analysis (XRD) to investigate the mineralogical composition, and inductively coupled plasma – optical emission spectroscopy (ICP-OES) to quantitatively study geochemical variations. Results presented in this study relate to an oriented, approximately $10 \times 10 \times 8$ cm large sample spanning the entire fault core (Fig. 3.2). This allowed to investigate the individual units of the fault core at high-resolution and to study variations with respect to rheology, mineralogy and geochemistry associated with the transition from one unit to another one. Application of the described methodology, especially the microstructural analysis, to other samples from the same location gave similar results.

3.4.2 Microstructures

After a first optical inspection of the dry-polished thin sections with a Leica DM RX microscope, detailed scanning electron microscopy allowed observations down to the microscale on carbon-coated thin sections to be made using a FEI Quanta 3D SEM equipped with a field emission gun and a focused ion beam (FIB; dual-beam machine), operating at 20 kV in backscatter electron (BSE) mode. The attached EDAX energy dispersive X-ray analyser (EDX) enabled semi-quantitative geochemical analysis. Cathodoluminescence (CL) analyses on calcite veins and calcite cementation were carried out with an Olympus polarising microscope. The Lumic HC1-LM hot-cathode CL microscope operated at 14 kV and 0.0001 mbar with about 0.6 mA electron beam and 2.5 A filament current, respectively.

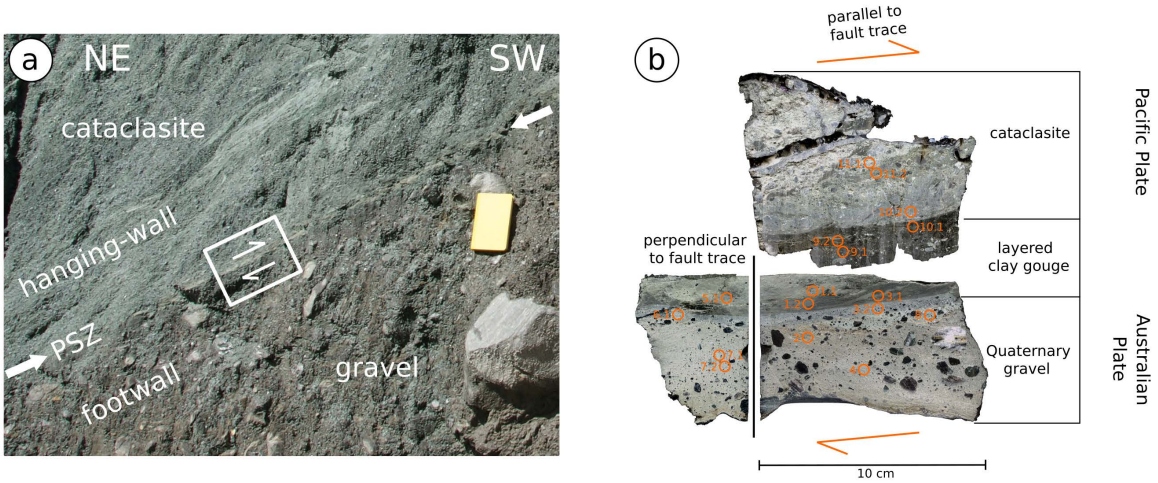

Figure 3.2: (a) Outcrop image of the Waikukupa Thrust fault segment. The ~3.5 cm thick ochre to medium-brown PSZ (indicated by white arrows) sharply separates hanging wall cataclasites from fluvioglacial footwall gravel. Height of yellow fieldbook is 15 cm. White box shows location of investigated sample displayed in (b); white arrows indicate dextral sense of shear. **(b)** Scanned image of sample investigated in this study. Footwall was scanned parallel and perpendicular to fault trace. Orange spots and labels are locations of powder samples for XRD and ICP-OES analyses, respectively. Sample broke along the PSZ during shipment resulting in material loss of roughly 5 mm.

Preparation of thin foils ($10 \times 8 \times 0.15\,\mu m$) for TEM analysis followed the procedure outlined in Wirth (2004) and Wirth (2009) to minimise surface damage. Sampling sites for TEM foils were identified with the FEI Quanta 3D SEM in BSE mode before its FIB was used to deposit a platinum strip for further preparation with a FEI FIB 200 (Wirth, 2004). Nanostructures were investigated with a FEI Tecnai G2 F20 X-Twin TEM equipped with a Gatan Tridiem energy filter, a Fischione high-angle annular dark field detector (HAADF) and an EDX operating at 200 kV.

3.4.3 Mineralogy and geochemistry

XRD analysis and ICP-OES were used to characterise mineralogical and geochemical variations across the fault (Fig. 3.2b). Samples were taken using a gimlet, equipped with a diamond-bit at high resolution (distance between individual spots: ~0.5 cm to < 2 cm; spot size: ∅ 3 mm, ~5 mm penetration).

Mineral compositions of the samples were determined by XRD analysis on oriented mounts. The sample material (45 mg) was crushed to a fine powder, dispersed in 1.5 ml of de-ionised water and disaggregated in an ultrasonic bath. The suspension was placed on round (∅ 3.1 cm) glass slides and air-dried. XRD analysis was performed using a PANalytical Empyrean X-ray diffractometer operating with Bragg-Brentano geometry at 40 mA and 40 kV with CuKα radiation and a step size of 0.013 °2Θ from 2.4 to 50 °2Θ. Repeated measurements were conducted after ethylene glycolation at 45 °C for at least 12 h to identify smectite (2.4 - 27.9 °2Θ) and heating to 550 °C for one hour to differentiate between chlorite and kaolinite (2.4 - 35.5 °2Θ; Moore and Reynolds, 1997). Diffractograms are provided in the electronic supplement.

Based on the assumption that the identical amount of sample material and preparation procedure for all investigated samples allows to semi-quantitatively assess the variations of individual

mineral phases across the PSZ, the peak-area of identified phases was used as proxy for this estimate. It was calculated with the open-access software "MacDiff" (`http://www.geol-pal.uni-frankfurt.de/Staff/Homepages/Petschick/classicsoftware.html`; peak-areas can be found in the supplementary material Table S3.1).

For ICP-OES analysis, powdered samples were dried at 110 °C for two days before 125 mg of sample material was subjected to several acid treatments (see supplementary material Table S3.2). Element geochemistry of Al_2O, CaO, Fe_2O_3, K_2O, MgO, MnO, Na_2O and TiO_2 was determined using a Varian VistaMPX ICP-OES operating with axial Ar-plasma. The procedure for sample preparation does not allow analysis of SiO_2. Results are given as weight percent (wt %). Calibration was carried out with internal GFZ standards and the external standards JB-3 and SCO-1. Errors are estimated to be about 5 % for Al_2O, CaO, Fe_2O_2, MgO, MnO, TiO_2 and up to 10 % for Na_2O and K_2O.

The geochemical composition was evaluated using the isocon method (Grant, 1986; Grant, 2005) to assess element mobilisation and enrichment due to fluid-related alteration. Element concentrations of altered units are plotted against those of the unaltered host rock. The isocon – a straight line through the origin – separates elements enriched (plotting above) from elements depleted (plotting below) by fluid alteration. Isocons are derived assuming stable Al and Ti, respectively, as both elements are frequently considered to be immobile species (e.g., Dolejš and Manning, 2010; Grant, 2005 and references therein). The formation of authigenic minerals (see Section 3.5.1) indicates it is not valid to assume constant mass or volume as suggested by Grant (1986) and Grant (2005). Enrichment or depletion of individual elements based on immobile Ti and Al, respectively, is calculated as follows:

$$\frac{\Delta \mathrm{C_i}}{\mathrm{C_i}} = \frac{\mathrm{C_{im}^O}}{\mathrm{C_{im}^A}} \times \frac{\mathrm{C_i^A}}{\mathrm{C_i^O}} - 1 \tag{3.1}$$

with i denoting the element of interest, im the immobile phase (Al and Ti, respectively), A the altered and O the unaltered rock. Volume gains or losses associated with metasomatic alterations such as mineral dissolution or vein formation are calculated based on immobile elements according to Gresens (1967):

$$\mathrm{f_V} = \frac{\mathrm{C_O}}{\mathrm{C_A}} \times \frac{\rho_\mathrm{O}}{\rho_\mathrm{A}} \tag{3.2}$$

with $\mathrm{f_V}$ being the volume factor and C and ρ being concentration (Ti and Al, respectively) and density of altered (A) and unaltered host rock (O). Volume factors greater than 1 indicate volume gain, volume factors smaller than 1 are associated with volume loss.

3.5 Results

3.5.1 Fault rock lithology and microstructures

At the Waikukupa location, the Alpine Fault is exposed parallel and normal to fault slip. The PSZ is oriented ~50° / 44° E and is ~3.5 cm thick with an ochre to medium-brown colour (Fig. 3.2a). It shows two layers with distinctly different colours and clearly separates

pale-green hanging wall cataclasites from brown riverbed gravels forming the footwall (Fig. 3.2). The gravels increase in size with increasing distance from the PSZ and contain clasts up to 20×40 cm in size and dm-sized blocks of reworked mylonite and cataclasites. Microstructural results are presented in detail below, and Table 3.1 provides a summary of our key-observations.

Table 3.1: Summary of observed microstructures.

	hanging wall
matrix	- detrital: mica, clastic fragments (Qtz, Fsp, ± Hbl); $< 10\,\mu$m in size - authigenic: phyllosilicates (mainly Chl); size: up to $2\,\mu$m, mainly $\ll 500$ nm - clay-clast-aggregates
clasts	- reworked Myl and QFsp clasts; irregularly dispersed; size: 11×8 mm (subangular) down to $\varnothing\, 30\,\mu$m (subrounded) - Bt / Ms, fractured and kinked; length: up to $50\,\mu$m - dissolution of grain edges
breccias	- angular fragments of reworked matrix and detrital clasts with size from ~3 to $< 100\,\mu$m; cemented by Cc
	fault-gouge / principal slip zone
- mainly fine-grained QFsp clasts (size: < 200 nm to $< 100\,\mu$m), alteration-related phyllosilicates (mainly Chl; $\ll 100$ nm in size) and moderately rounded to subangular clasts of reworked matrix (size: $3\,\mu$m to > 6 mm) - clay-clast-aggregates	
HW-proximal	- fine-grained (size: $< 2\,\mu$m) and reworked matrix with dispersed remnants of clastic particles (Qtz, Myl), rare displacement-normal veins and abundant micro-pores
FW-proximal	- anastomosing network of Cc veins (crystal size $< 5\,\mu$m, offset up to $100\,\mu$m) - dense, low-porosity matrix with gouge clasts (up to $300 \times 500\,\mu$m) and (sub)rounded clastic particles (size typically $< 5\,\mu$m; up to 2×4 mm)
	footwall
- mineralogically comparable to hanging wall	
matrix	- abundant (sub)angular, subgrain-bearing QFsp and subrounded Myl clasts - uppermost 2.5 – 3 mm contain Cc dispersed as cement, as tiny veins (size: $< 10\,\mu$m) and as rims at clasts (normal to displacement; $< 5\,\mu$m thick)
clasts	- ellipsoidal Myl clasts, Qtz, Fsp and mica

Qtz: quartz; Fsp: feldspar; Hbl: hornblende; Chl: chlorite; Myl: mylonite; QFsp: quartzofeldspathic; Bt: biotite; Ms: muscovite; Cc: calcite; HW: hanging wall; FW: footwall.

3.5.1.1 Hanging wall – cataclasites

The cataclasites in the hanging wall of the fault display a fine-grained matrix consisting of detrital mica (biotite, muscovite, illite), authigenic phyllosilicates, mainly chlorite, as well as clastic fragments of quartz, feldspar and, to a minor extent, hornblende (Fig. 3.3). In general, the detrital components of the matrix are smaller than $10\,\mu$m. With $\ll 500$ nm in size, authigenic phyllosilicates are primarily even smaller and do not exceed the clay-size fraction. Larger fragments and clasts of reworked mylonites of greenschist- and amphibolite-facies are irregularly dispersed in the matrix (Fig. 3.3a). The size of these detrital particles decreases significantly from unfractured mylonite forming the fault zone wall rock with decreasing distance towards the PSZ fault gouge. Roundness increases with decreasing particle size. Within 3 cm off the contact with the PSZ, quartzofeldspathic-micaceous clasts with mylonitic fabric are (sub)angular and up to 11×8 mm in size. At the contact to the PSZ, clasts are (sub)rounded and have diameters down to $30\,\mu$m. Kinked and fractured biotite and muscovite grains of up to $50\,\mu$m length indicate a dextral sense of shear (Fig. 3.3b). Their size and

abundance decrease towards the PSZ. Particle edges, particularly of smaller grains, show evidence of mineral dissolution (Fig. 3.3b). However, there are no indicators of pressure solution, such as indented and embayed clasts or seams of relatively insoluble material. On all scales, phyllosilicates wrap around larger clasts, locally forming clay-clast-aggregates (CCA; Boutareaud et al., 2008) and constitute most of the crack fillings. Breccias, reworked and dispersed in the cataclastic matrix, become less frequent towards the PSZ. These breccias consist of angular fragments of detrital grains such as quartz and fine-grained reworked matrix clasts with sizes ranging from a few micrometer to $< 100\,\mu m$ (Fig. 3.3c). They are cemented by calcite showing few dislocations. Calcite cement and feldspar grains are heavily corroded. The resulting intergranular pore space is filled by authigenic phyllosilicates (Fig. 3.3d). Locally euhedral flake- to needle-shaped authigenic chlorite grains grow at mineral edges and within intra- and intergranular pores (Fig. 3.3e), resulting in matrix cementation, which increases towards the PSZ.

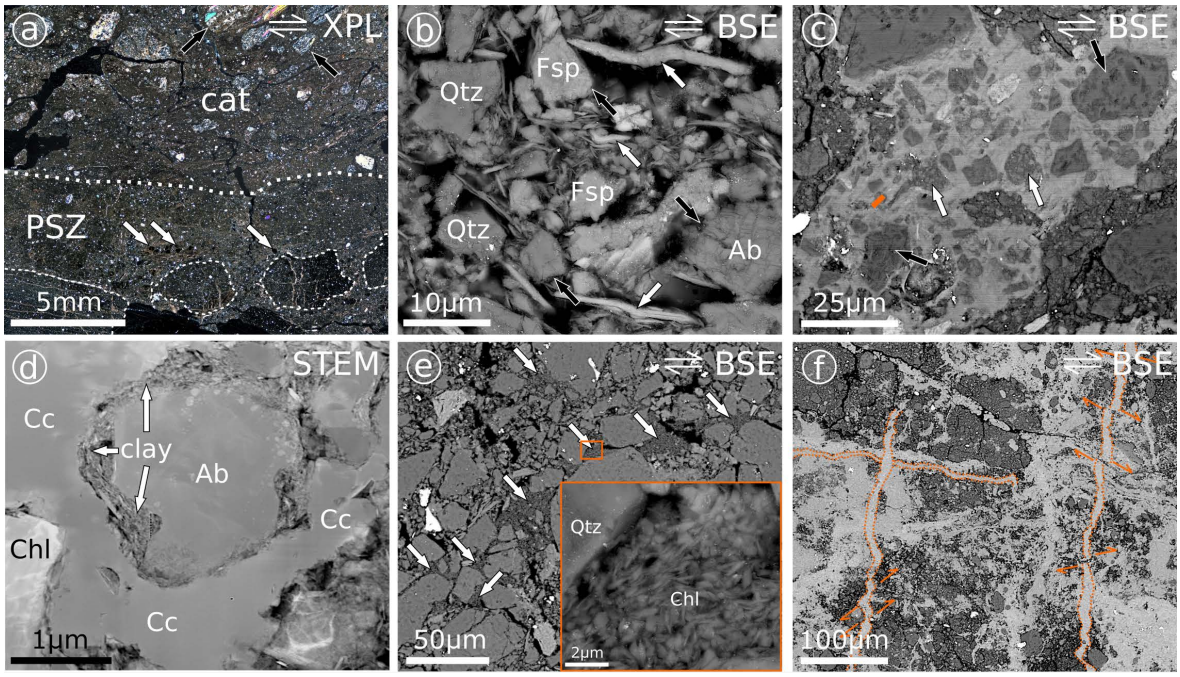

Figure 3.3: Cataclasite microstructures (a) Transitional contact (dotted line) between cataclasite and PSZ. Cataclasite contains large (up to 2×1 mm) mylonite clasts (black arrows). Stippled outlines indicate larger gouge clasts, white arrows indicate smaller ones. Here, larger gouge clasts are cross-cut by calcite veins. **(b)** Muscovites and biotites (white arrows) in the cataclasite are kinked and fractured. Pores are empty or loosely filled with fractured and authigenic grains. Edges of feldspar grains show evidence of mineral dissolution (black arrows). **(c)** Brecciated fault rock cemented by calcite containing angular clasts of single grains (black arrows) and reworked gouge (white arrows). Orange bar gives location of TEM-foil for (d). **(d)** Calcite precipitated around clasts cements breccias. Subsequent feldspar alteration causes formation of authigenic clays. **(e)** Locally, pores are filled with grains giving uniform grey-values in BSE mode (white arrows). Orange box gives position of inset. Inset: These pores are filled with densely packed euhedral flake- to needle-shaped authigenic chlorite. **(f)** Around the contact between cataclasite and gouge, calcite is predominantly present as cement. There are only a few calcite veins (dotted lines), cross-cutting each other and showing minor dextral offset (orange arrows). XPL: cross-polarised light; BSE: backscatter electron microscopy; STEM: scanning transmission electron microscopy; cat: cataclasite; PSZ: principal slip zone; Qtz: quartz; Fsp: feldspar; Ab: albite; Cc: calcite. White arrows (top right) indicate fault movement as derived from the oriented sample taken at the outcrop.

The cataclasite microstructures show significant porosity. Due to unroofing, weathering and sample preparation it is difficult to estimate the amount of primary porosity of the cataclasites. Particularly larger pores may result from weathering or drying. However, BSE and TEM images reveal abundant micron- and submicron-sized primary pores (Figs. 3.3b, d & e). The

observed porosity of the cataclasite matrix indicates a general trend to decreasing pores sizes with decreasing distance to the PSZ (see also Kirilova, 2017).

Fracture healing and matrix cementation by calcite is insignificant. However, calcite veins (sub)parallel and perpendicular to fault displacement as well as calcite cementation become more abundant towards the PSZ. Calcite cementation is more pronounced where grain size is smaller. Calcite is locally affected by leaching. However, there are no systematic dissolution patterns. Multiple vein-formation is revealed by cross-cutting relations and small dextral offsets in the range of 10 – 20 µm along microfaults (Fig. 3.3f).

3.5.1.2 PSZ – fault gouge

At both outcrop and hand specimen scale the contact between hanging wall cataclasites and PSZ is marked by a sharp colour change, from pale-green to medium-brown and dark-grey (Fig. 3.2). It is only in thin section that the contact is revealed to be transitional. It is characterised by a gradual variation over about 4 mm from a matrix-supported, mylonite-clast-bearing unit with locally high porosity, to a very dense matrix (Fig. 3.3a). Two microstructurally distinct units make up the PSZ fault gouge at both meso- and microscale (Fig. 3.2b). The gouge immediately underlying the hanging wall (and potentially derived from it) comprises remnants of clastic particles in a fine-grained matrix (Figs. 3.3 & 3.4a – d). This part of the gouge is termed hanging wall-proximal gouge. It is different from the portion of the PSZ overlying the footwall, the footwall-proximal gouge, which can be distinguished by its abundant, multi-generation calcite veinlets forming a dense, anastomosing network (Figs. 3.5a – c).

The PSZ matrix has a similar composition as the cataclasites in the hanging wall. It mostly contains fine-grained clastic minerals (dominantly quartz, feldspar, biotite and muscovite), authigenic chlorite and moderately rounded to (sub)angular gouge clasts (Figs. 3.4a – c). These are aggregates having similar mineralogy and grain size distribution as the surrounding matrix, ranging in size from >6 mm to 3 µm. The aggregates are cross-cut by calcite veins (Figs. 3.3a & 3.4a), that are offset locally by 10 – 20 µm. Sharp contacts of clasts and veins with the surrounding matrix suggest clast rotation so the veins now show no systematic orientation. While the size of gouge clasts increases towards the footwall, the size of clastic feldspar and quartz grains generally decreases. Gouge clasts have a lower porosity than the surrounding gouge matrix, which is less consolidated (Fig. 3.4a). The clasts contain finely dispersed calcite cement, as indicated by elevated Ca concentrations in EDX overview maps. Heterogeneous composition of the gouge clasts is apparent as greyscale variations in BSE-SEM images (Fig. 3.4c & d). Darker grey patches contain fractured, angular quartz and dissolved feldspar grains (up to a few 100 nm in size) with intergranular pores (Fig. 3.4e), and lighter grey material forms a dense matrix, with very few pores. The matrix mostly comprises authigenic phyllosilicates and rare larger angular clasts (size <1 µm). An alteration front, 1 - 2 µm wide (Fig. 3.4e), which contains angular and dissolved clasts and authigenic phyllosilicates in the interparticle space and pores, separates highly porous, phyllosilicate-poor areas from less porous, phyllosilicate-rich areas. Authigenic chlorites are wrapped around clastic particles and form clay-clast-aggregates (Fig. 3.4f). Close to the contact to the hanging wall, breccias contain angular clasts of rigid particles and reworked matrix cemented by calcite.

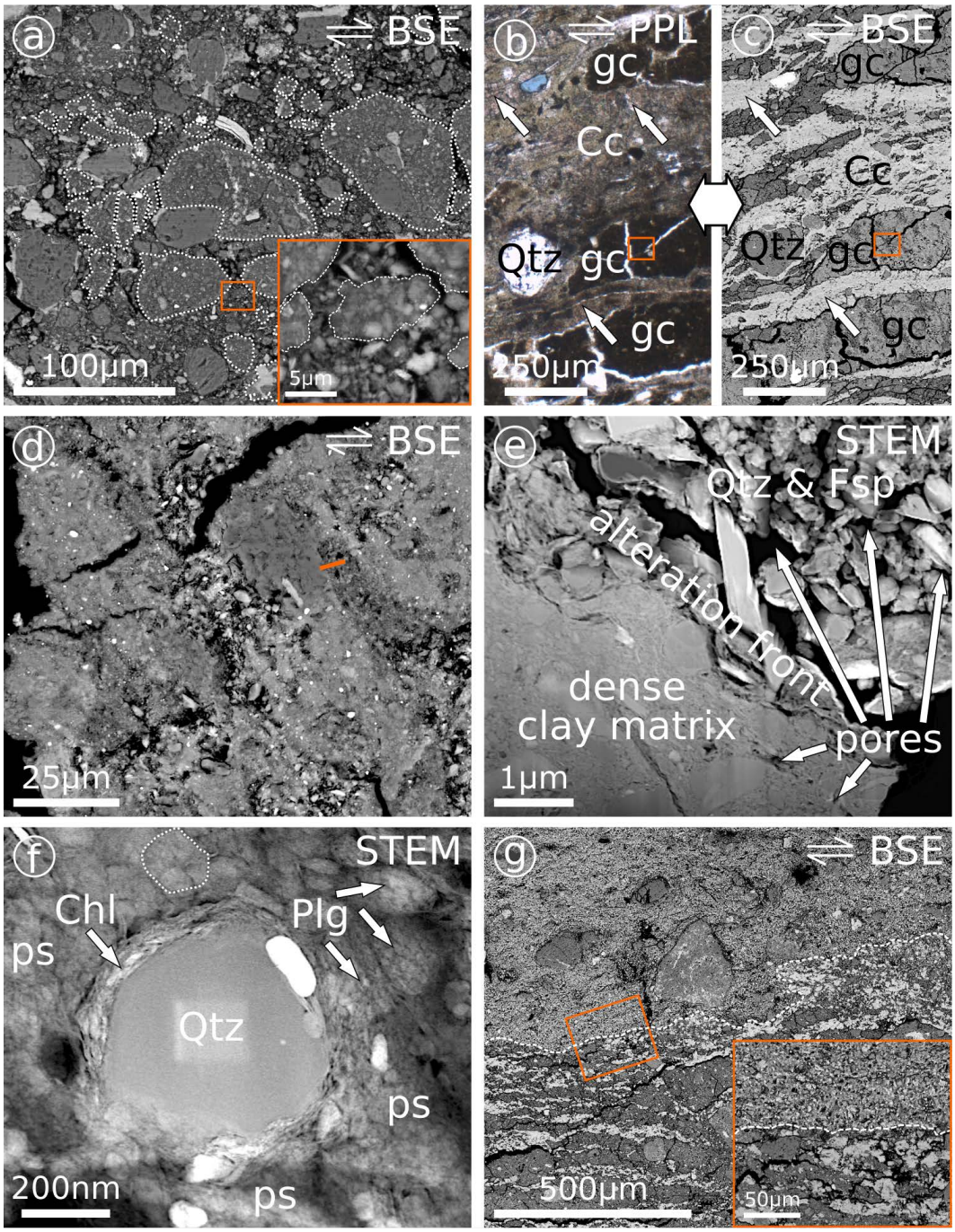

Figure 3.4: PSZ microstructures (a) Gouge clasts (dotted outlines) are (sub)angular and constitute most of the gouge. Orange box gives location of inset. Inset: Gouge clasts (dotted outlines) are composed of comminuted particles (mostly quartz and feldspar), cemented by phyllosilicates and finely dispersed calcite. Surrounding matrix is formed by larger quartz and feldspar clasts, micas and smaller amounts of authigenic phyllosilicates. **(b & c)** Corresponding (b) optical and (c) SEM micrographs. Gouge clasts in a fine-grained matrix are cross-cut by calcite veins with median lines (white arrows). Box gives position of (d). **(d)** Detail of (b & c). The composition of gouge clasts is not uniform and varies between porous and dense. Cracks are probably preparation-induced. Orange bar gives location of TEM foil in (e). **(e)** Fine-grained phyllosilicates with a few larger quartz and feldspar grains form the dense matrix of gouge clasts (lower left). The porosity between fractured quartz and feldspar grains (upper right), the latter are dissolved at the edges, is relatively high with only a few authigenic phyllosilicates being present. An alteration front with pronounced phyllosilicate formation separates matrix and clasts. **(f)** Clay-clast-aggregate (CCA; Boutareaud et al., 2008) formed by a rounded quartz grain wrapped by authigenic chlorites. CCA is embedded in a fine-grained matrix mostly composed of authigenic phyllosilicates with plagioclase grains being altered to clay. Dotted outline highlights well-rounded intensively fractured clast. **(g)** Contact between hanging wall-proximal (top) and footwall-proximal (bottom) portion of the gouge. Box gives location of inset. BSE: backscatter electron microscopy; PPL: plane polarised light; STEM: scanning transmission electron microscopy; Cc: calcite; Qtz: quartz; gc: gouge clast; Fsp: feldspar; ps: phyllosilicates; Chl: chlorite; Plg: plagioclase. White arrows (top right) indicate fault movement as derived from the oriented sample taken at the outcrop.

There are also a few fault displacement-normal veins in this hanging wall-proximal portion of the PSZ. Clastic grains typically vary between $< 200\,\text{nm}$ and $< 100\,\mu\text{m}$, but rare reworked and sub-rounded mylonite fragments are $< 2 \times 4\,\text{mm}$ in size. Authigenic phyllosilicates are $\ll 100\,\text{nm}$. Identification of nanoscale clastic particles is made difficult by the presence of abundant alteration-related authigenic phyllosilicates (Fig. 3.4f). In the footwall-proximal gouge, the composition of the matrix is homogenous, with many micro-pores and dispersed rounded clasts (mostly quartz and mylonites; Fig. 3.4g). Matrix grain sizes do not exceed the clay-size fraction. The contact between the gouge units is sharp but undulating.

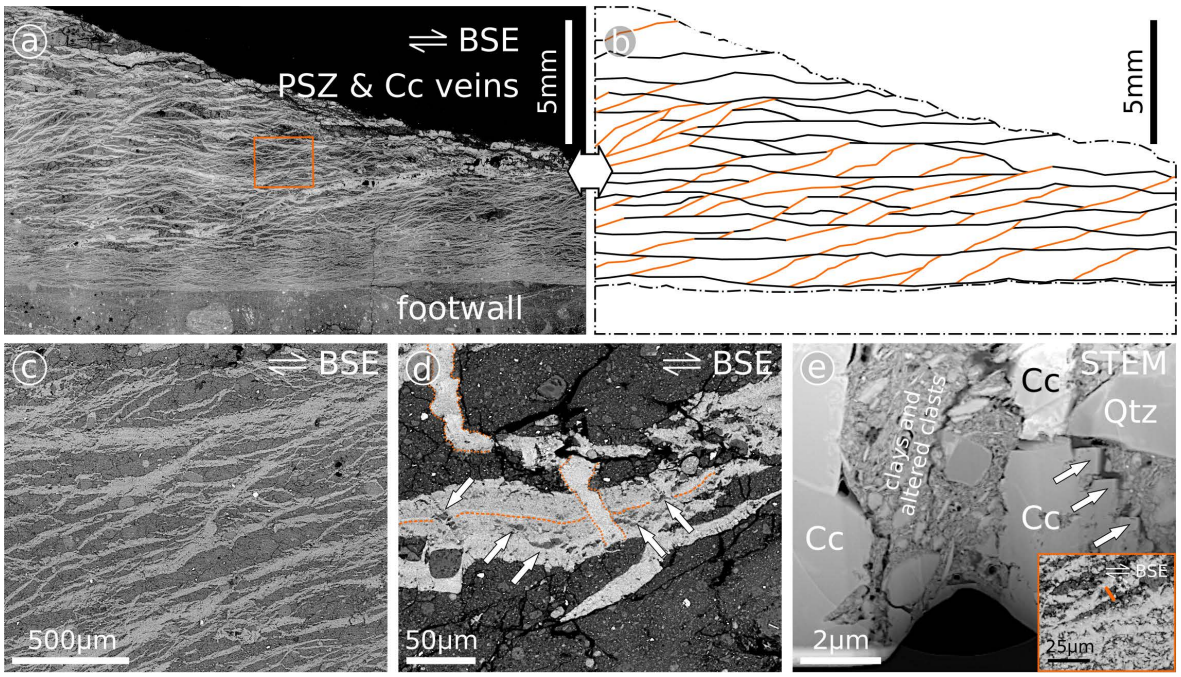

Figure 3.5: PSZ, calcite veins. **(a)** The footwall-proximal portion of the PSZ is characterised by a dense, anastomosing network of calcite veins. The contact to the footwall is well defined and forms a sharp line. Orange box indicates position of (c). **(b)** The network of calcite veins shown in (a) forms a characteristic pattern. Veins subparallel to fault displacement (black) dip at an angle of ~44°. Orange lines indicate subvertically oriented veins. **(c)** Detail of calcite vein network depicting the characteristic pattern of veins. **(d)** Calcite veins in the gouge cross-cut each other (dotted outline). Distal to the contact with the footwall these veins often contain median lines (stippled lines) and wall-rock inclusions (white arrows). **(e)** Calcite veins cross-cut a dense, fine-grained matrix of phyllosilicates and altered angular clasts. There is a large mosaic calcite crystal (Bloss, 1994) with blocky crystal edges (white arrows) on the right. Inset: Orange bar indicates position of TEM foil. Calcite veins close to the contact between gouge and gravel are thinner and more densely spaced. Locally, the space between the veins is cemented by calcite. BSE: backscatter electron microscopy; STEM: scanning transmission electron microscopy; PSZ: principal slip zone; Cc: calcite; Qtz: quartz. White arrows (top right) indicate fault movement as derived from the oriented sample taken at the outcrop.

The matrix of the footwall-proximal gouge is dense, shows low porosity and contains small gouge clasts ($< 300 \times 500\,\mu\text{m}$), as well as clastic grains, mostly quartz, which are (sub)rounded with few intragranular cracks. Larger clasts show undulose extinction and sometimes twinning and bulging. Clastic particle sizes in this footwall-proximal gouge typically do not exceed $\sim 5\,\mu\text{m}$ although a few rounded clasts are significantly larger, with sizes $< 2 \times 4\,\text{mm}$. Authigenic phyllosilicates are usually $< 100\,\text{nm}$.

In the footwall-proximal portion of the PSZ, calcite is mostly present as thin veins. In particular, the contact of the PSZ to the footwall is characterised by abundant calcite veinlets forming a dense anastomosing network with a thickness of $\sim 2\,\text{cm}$. Veinlets display mutual cross-cutting relationships indicating that they belong to different generations (Fig. 3.5a - c).

This is a notable difference to the hanging wall-proximal portion of the PSZ previously described, where calcite occurs as cement and is present in only a few veins.

Calcite veins show three prevailing orientations: (sub)parallel to the fault plane (i.e., dip ~44°) as well as slightly oblique to it (i.e., dip subvertical; Fig. 3.5b) and, less frequently, normal to fault-movement (Figs. 3.6a - c). The angle between the first two of these sets of veins averages ~67°. Veins range in thickness between 200 µm and 1.5 µm. Towards the footwall the average vein thickness decreases from ~60 µm down to ~5 µm. The spacing between individual veins also decreases towards the footwall from typical values of ~200 µm to ~10 µm. Veins thicker than ~15µm usually contain wall-rock inclusions, often well-defined median lines, and have a chaotic internal structure (Fig. 3.5d). Within 300 – 400 µm just above the contact between gravel and gouge, individual veinlets become poorly-defined (see inset Fig. 3.5e). Fault displacement-normal veins are abundant adjacent to the contact with the footwall, where they commonly terminate (Figs. 3.6a – c).

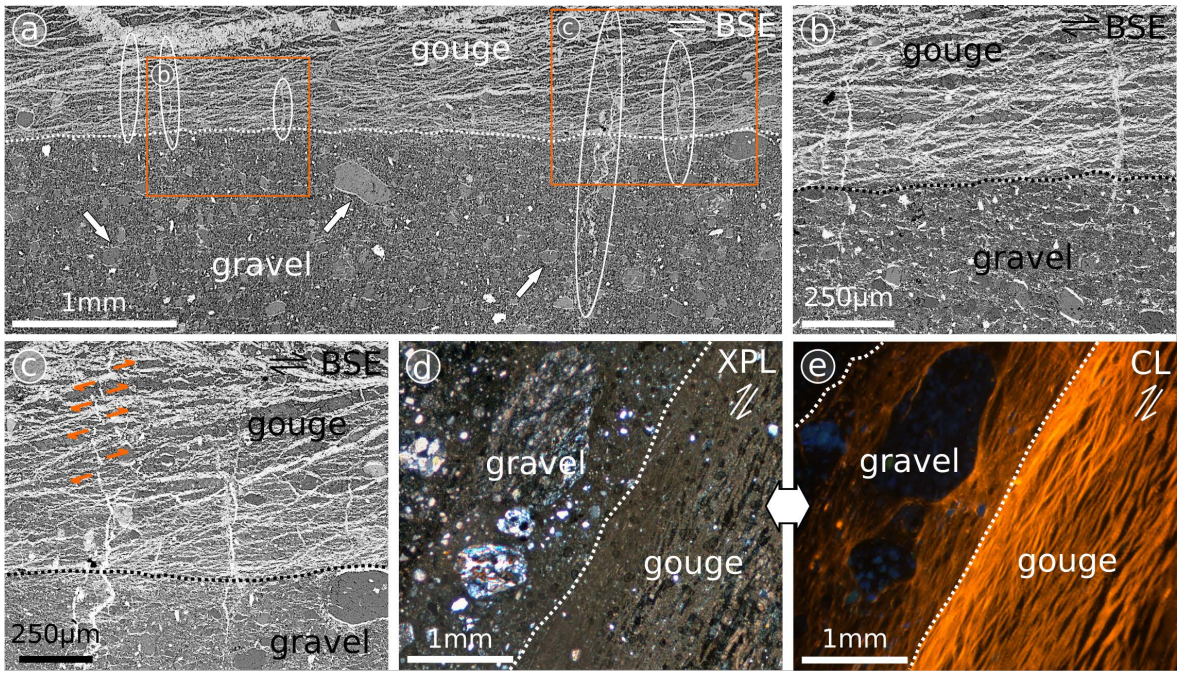

Figure 3.6: Microstructures interface PSZ - gravel (a) Overview image of contact between gouge and footwall gravel. Ellipses highlight displacement-normal veins. This type of veins either terminates at the contact (left side) or cross-cuts both units (right side). Clasts in the uppermost part of the gravel have calcite rims parallel to displacement (white arrows). **(b)** Detail of (a). Displacement-normal veins terminating at the contact between gouge and gravel. **(c)** Detail of (a). Veins cross-cutting gouge and gravel show subsequent dextral displacement (orange arrows). **(d & e)** Corresponding (d) optical and (e) CL micrographs showing the contact between gouge and footwall gravel. The density of calcite veins in the gouge increases towards the contact. The contact is defined by the appearance of (sub)angular – (sub)rounded clasts often having a mylonitic fabric. CL microscopy indicates that the uppermost 2.5 – 3 mm of the footwall have calcite veins, which are less frequent compared to the gouge. BSE: backscatter electron microscopy; XPL: cross-polarised light; CL: cathodoluminescence. Arrows (top right) indicate fault movement as derived from the oriented sample taken at the outcrop.

Calcite crystals in the veinlets are small (~5 µm), and locally blocky and euhedral (Fig. 3.5e). A few larger crystals have elongated shapes and twins. Transmission electron microscopy reveals the presence of mosaic crystals (Bloss, 1994) up to 2 µm in size (Fig. 3.5e). Calcite veinlets exhibit uniform yellow-orange CL colours (Figs. 3.6d & e) and show mutual cross-cutting relations with dextral offsets. In contrast to the cataclasites and the hanging wall-proximal gouge unit, where offset of calcite veins is minor, fault displacement-normal veins

in the lowermost part of the gouge are offset by up to 100 µm. In some cases, displacement (sub)parallel veins are stretched forming boudins with spacings of up to 120 µm. In addition to deformation, calcite in both veins and cement is locally dissolved, although without any systematic orientation.

3.5.1.3 Footwall – gravel

The contact between gouge and footwall is sharp and characterised by the transition from the almost clast-free and calcite-vein-rich gouge-matrix to a footwall-matrix rich in (sub)angular, subgrain-bearing quartz, feldspar and subangular, ellipsoidal mylonite clasts (> 50 µm; Fig. 3.6). These clasts are embedded in a fractured, fine-grained matrix of similar composition as cataclasites and gouge, respectively. Their size increases continuously with increasing distance from the gouge. In addition, the footwall contains lenses with abundant kinked and bent biotite and muscovite grains with sizes up to 50×200 µm. Within 2.5 - 3 mm from the PSZ the footwall contains abundant calcite as finely dispersed cement and thin veinlets (< 10 µm; Fig. 3.6e). Clasts in this calcite-rich layer have thin calcite rims (thickness: < 5 µm) oriented parallel to fault displacement (Fig. 3.6a). Except for this narrow band at the contact to the PSZ, which has a sharp contact to the underlying part, the footwall is almost calcite-free. The porosity of the footwall-matrix increases with increasing distance from the contact with the overlying fault gouge.

3.5.2 Mineralogy

The mineralogical composition and its variation across the PSZ as revealed by XRD analysis are displayed in Figure **??**a. Mineral phases of the hanging wall cataclasites, the fault gouge and the footwall gravel are very similar. Across the entire section main mineral constituents are quartz, plagioclase, calcite, chlorite, kaolinite, mica (biotite, muscovite, illite), traces of pyrite and hornblende. However, the relative amounts of the individual phases vary significantly across the investigated transect: amounts of quartz and plagioclase decrease towards the bottom of the PSZ, but are again more prominent in the footwall. The calcite content increases from the hanging wall towards the contact of the PSZ with the footwall due to the presence of abundant calcite veinlets there. Calcite is nearly absent in the footwall.

XRD analysis also indicates a decrease in phyllosilicates from the hanging wall to the PSZ gouge, and increased amounts in the footwall (Fig. **??**a). This contrasts with petrographic observations (see Section 3.5.1), which clearly demonstrate that both units contain large amounts of phyllosilicates. Their grain size decreases towards the bottom of the PSZ, where grains are $\ll 2$ µm in size. As the clay-size fraction was not explicitly analysed because of the lack of sample material, this study may underestimate its amount. Based on the results presented by Warr and Cox (2001) the clay-size fraction in the Alpine Fault gouge is considered to represent ~ 50 % of the exposed cataclasites and gouge with phyllosilicates accounting for most of the phases. Heating indicates that the amount of kaolinite compared to chlorite decreases with distance from the hanging wall to the base of the PSZ (Fig. **??**a). The

comparison of air-dried with glycolated oriented slides reveals that smectite is either absent or only present in quantities below the detection limit in any of the investigated samples.

3.5.3 Geochemistry

The measured element quantities comprise between one third and almost half of the total element concentrations (Tab. 3.2). Whereas Al and Ca are the most abundant elements, Mn and Ti are present in minor amounts (Fig. **??**b). The element concentrations show distinct patterns across the investigated transect from the hanging wall into the footwall. Fe, Al, Mg and Ti concentrations are relatively constant from the hanging wall to the footwall-proximal gouge with slight enrichments in the hanging wall-proximal PSZ, and occur in higher concentrations in the footwall. Ca and Mn quantities increase towards the footwall-proximal gouge, where their concentrations are highest before reaching minimum values in the footwall. Na shows an opposite pattern: constantly decreasing, the minimum amount is encountered in the footwall-proximal PSZ with footwall concentrations being relatively high. K concentration slightly increases along the transect and is nearly stable within the PSZ.

3.6 Discussion

3.6.1 Fluid-related alteration and element mobility

The abundance of calcite veins in the footwall-proximal portion of the PSZ and the presence of authigenic phyllosilicates throughout all lithologies is supported by Sutherland et al. (2012), who discuss the presence of fluid-related alteration assemblages in the fault's damage zone and their dominant occurrence within 20 m of the PSZ. In general, calcite veins are abundant within the fault's alteration zone (e.g., Sutherland et al., 2012; Townend et al., 2013; Toy et al., 2015; Boulton et al., 2017a). However, veins in the fault gouge are up to three orders of magnitude thinner than in the cataclasites (Williams et al., 2017). Isotopic analyses indicate that the PSZ may act as a hydraulic barrier and forces up-fault fluid-flow of dominantly meteoric origin (Menzies et al., 2016). It is saturated with Ca from the Alpine Schist, resulting in abundant hot-springs in the hanging wall (Menzies et al., 2016; Sutherland et al., 2017, Williams et al., 2017 and references therein). The uniform cathodoluminescence colours (Fig. 3.6e) do not indicate that the geochemical composition of these fluids changed significantly over time.

The Alpine Schist is the non-deformed portion of the hanging wall along the central segment of the fault and thus represents the host rock for comparison to the studied fault rocks. However, as the Alpine Schist itself is derived from several protoliths, its chemical composition slightly varies (Roser and Cooper, 1990), which might limit its use to quantify the degree of alteration. Nonetheless, we use the data presented by Roser and Cooper (1990) to assess fluid-related alteration, because these authors sampled the Alpine Schist close to the fault trace, i.e., a level structurally comparable to the rocks immediately taken at the fault plane. Additionally, rocks at their sample location and the ones of this study are both derived from the same protolith unit, which allows assuming comparable mineralogical compositions (Cooper and Norris, 2011). The same applies to the Alpine Fault mylonite data reported

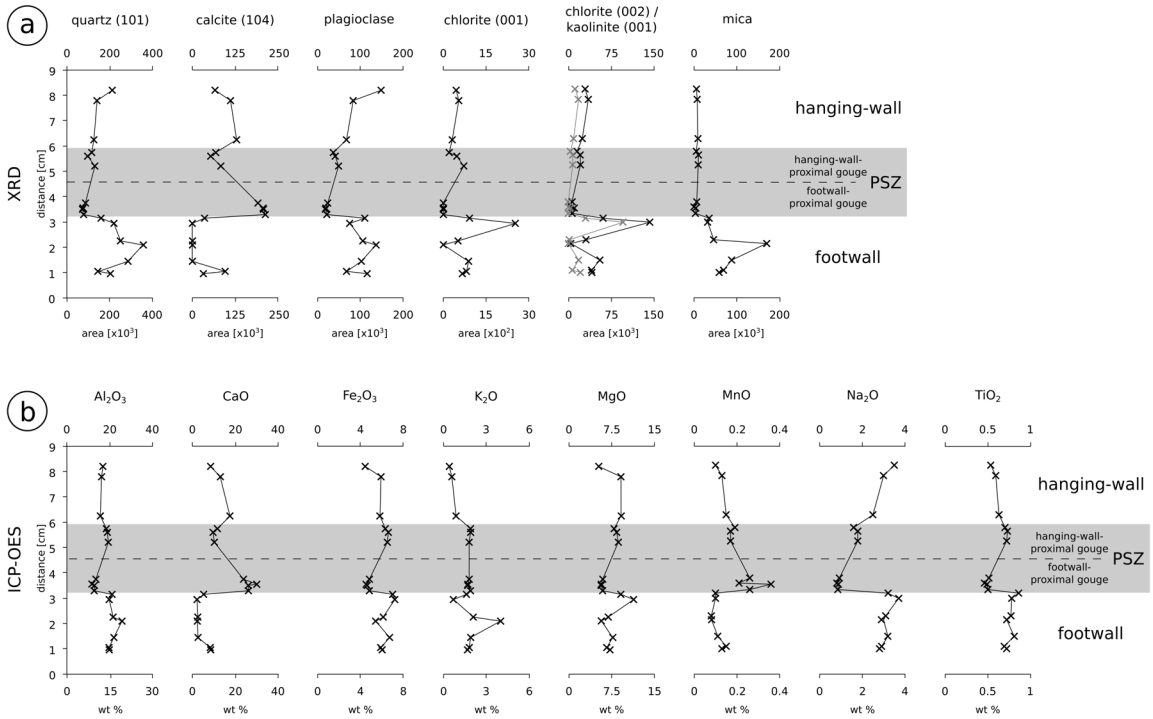

Figure 3.7: (a) Results of XRD analysis on oriented mounts based on the assumption that identical procedure for sample preparation and analysis allows comparing the variations of the same phase in different samples by plotting the peak-area as function of distance across the fault. Number in brackets identifies analysed peak. "Plagioclase" refers to either the 002-peak of albite or the 004-peak of anorthite. "Mica" comprises the 10 Å peak of muscovite, biotite and illite, which cannot be distinguished in oriented mounts. Grey points in the chlorite / kaolinite plot show data after heating for one hour at 550 °C. **(b)** Results of ICP-OES analysis. Concentrations are plotted as function of distance across the fault. For sample spots of (a) and (b) see Figure 3.2b.

by McClintock and Cooper (2003). Individual data points reported in the literature and from this study are grouped to provide averages of elemental concentrations of the unit of interest (Tab. 3.3).

Isocon analysis reveals relatively little alteration of the mylonite by fluid-rock interaction compared to the other units investigated (Fig. 3.8). Towards the footwall, fluid alteration becomes more pronounced. Isocon diagrams (Fig. 3.8) and derived enrichment factors (Tab. 3.4) show that alteration is highest in the footwall-proximal portion of the PSZ. Proximal to the PSZ, the footwall is still affected by alteration but to a smaller degree compared to the overlying units. All units show depletion in K, which can be explained by the dissolution of schist-derived muscovite, biotite and K-feldspar. Enrichment in Na in the mylonite compared to the Alpine Schist reflects the greater burial depth and associated degree of metamorphic grade prior to thrusting (Grapes and Watanabe, 1994). Na-depletion in cataclasites, gouge and gravel reflects albite dissolution, potentially due to subaerial alteration. Absolute and relative depletion of Mg and Fe in the schists and the mylonites, respectively, originating from mafic phases might have facilitated subsequent formation of authigenic chlorite in cataclasites and gouge (Warr and Cox, 2001; Duan et al., 2016). Ca has the highest element mobility as evidenced by an enrichment in the footwall-proximal gouge of ~13 (immobile Ti) to ~16.5 (immobile Al) times compared to the host rock (Tab. 3.4). This enrichment is manifested by the formation of abundant calcite veins and cements.

Table 3.2: Concentration of elements analysed with ICP-OES. Values are given in weight-%. For sample location see Figure 3.2 b.

	sample	Al_2O_3	CaO	Fe_2O_3	K_2O	MgO	MnO	Na_2O	TiO_2
	11.1	12.7	8.5	4.5	0.41	2.1	0.1	3.5	0.54
HW	11.2	12.2	13.1	6.0	0.58	3.7	0.13	3.0	0.60
	10.2	11.8	17.6	5.9	0.88	3.7	0.15	2.5	0.64
	10.1	13.9	11.8	6.4	1.9	3.2	0.19	1.6	0.71
	9.2	14.2	9.7	6.7	1.9	3.4	0.17	1.8	0.74
	9.1	14.6	10.3	6.6	1.8	3.5	0.17	1.8	0.73
Gouge	1.1	10.2	24.0	4.9	1.8	2.4	0.26	0.93	0.52
	3.1	8.9	30.2	4.6	1.7	2.3	0.21	0.80	0.47
	5.1	9.6	26.3	4.7	1.7	2.3	0.36	0.89	0.50
	1.2	9.6	26.3	4.9	1.9	2.4	0.26	0.85	0.51
	3.2	15.9	5.3	7.1	1.6	3.7	0.1	3.2	0.87
	8	14.9	2.2	7.3	0.7	4.6	0.1	3.7	0.79
	6.2	16.3	2.6	6.2	2.1	2.8	0.08	3.1	0.78
FW	2	19.4	2.3	5.5	4.0	2.3	0.08	3.0	0.73
	7.1	16.5	2.7	6.8	1.9	3.1	0.11	3.2	0.82
	7.2	14.8	8.3	6.0	1.8	2.7	0.15	2.9	0.70
	4	14.8	8.5	6.1	1.7	2.9	0.13	2.8	0.73

HW: hanging wall; FW: footwall.

Varying enrichment factors as well as isocons having different slopes demonstrate that the assumption of immobile Ti and Al is applicable only with restrictions. Whereas Ti is enriched assuming immobile Al, Al is removed from the system based on immobile Ti (Tab. 3.4). The formation of soluble complexes might explain a certain degree of mobility for Ti and Al (Dolejš and Manning, 2010).

A volumetric analysis indicates that all hanging wall fault rock units gained volume (Tab. 3.3). The absolute values of the volume factor differ significantly depending on the immobile element chosen. However, in both cases they show the same trend. The hanging wall-proximal portion of the PSZ gained less volume (4 – 31%) compared to the overlying cataclasites (17 – 40%) and the footwall-proximal gouge (48 – 90%). The large volume gains in the gouge might be overestimated, as this unit is a hydraulic barrier and consequently has a low permeability, which complicates density measurements based on Archimedes' principle. Whereas large volume gains in the footwall-proximal gouge are probably associated with the formation of calcite veins, the volume loss of the gravel is probably associated with consolidation as consequence of thrusting along the PSZ rather than dissolution processes.

3.6.2 Influence of fluids on the geomechanical behaviour of the fault

Microstructural evidence (Figs. 3.3 – 3.6) demonstrates that fluids contribute to the failure of the Alpine Fault and the evolution of its geomechanical properties. Due to cementation by calcite and authigenic phyllosilicates, the PSZ forms an impermeable barrier (e.g., Boulton et al., 2012; Sutherland et al., 2012), that supports suprahydrostatic fluid pressures in the hanging wall. Current measurements within the frame of the Deep Fault Drilling Project phase 2 (DFDP-2) indicate fluid pressures at the Alpine Fault are up to 10 % above hydrostatic conditions (Sutherland et al., 2017). Topographic variations affecting flow of meteoric fluids potentially cause these elevated fluid pressures (Menzies et al., 2016; Sutherland et al., 2017). The Alpine Fault is unfavourably oriented for frictional reactivation in the current stress

Table 3.3: Elemental concentrations (in wt%) used for isocon analysis, bulk rock densities and volume change with regard to the initial volume of the Alpine Schist based on immobile Ti and Al, respectively.

	TiO_2	Al_2O_3	$Fe_2O_{3,\ tot*}$	MnO	MgO	CaO	Na_2O	K_2O	ρ [g cm^{-3}]	ΔV [%] (Ti_{im})	ΔV [%] (Al_{im})
Schist	0.63[1]	15.49[1]	4.64[1]	0.07[1]	1.75[1]	2.46[1]	3.23[1]	3.23[1]	2.7027[4]	0.0	0.0
Mylonite	0.60[2]	15.01[2]	4.44[2]	0.07[2]	1.66[2]	2.33[2]	3.69[2]	2.20[2]	2.7360[4]	3.7	1.9
Cataclasite	0.59[3]	12.23[3]	5.47[3]	0.13[3]	3.17[3]	13.07[3]	3.00[3]	0.62[3]	2.4576[5]	17.4	39.3
Gouge (HW-prox.)	0.73[3]	14.23[3]	6.57[3]	0.18[3]	3.37[3]	10.60[3]	1.73[3]	1.87[3]	2.2459[5]	3.9	31.0
Gouge (FW-prox.)	0.50[3]	9.58[3]	4.78[3]	0.27[3]	2.35[3]	26.70[3]	0.87[3]	1.78[3]	2.2961[5]	48.3	90.3
Gravel	0.78[3]	16.03[3]	6.51[3]	0.11[3]	3.23[3]	4.74[3]	3.14[3]	1.91[3]	2.6874[5]	- 18.7	- 2.8

HW-prox.: hanging wall-proximal; FW-prox.: footwall-proximal.
[1] Data are average values calculated from Roser and Cooper (1990), Table 2. Concentrations determined with XRF.
[2] Data are average values calculated from McClintock and Cooper (2003), Table 3, samples 69764, 69778, 69784, 69811, 69818, 69819, 69820, 69846 and 69847. Concentrations measured with XRF.
[3] This study. Data from Table 2 were averaged (Gouge, HW-prox.: samples 9.1, 9.2, 10.1; Gouge, FW-prox.: samples 1.1, 1.2, 3.1, 5.1).
[4] Data are average values calculated from Kluge et al. (2017).
[5] Density measurements were conducted following Archimedes' principle.
* Total Fe expressed as Fe^{3+}.

Table 3.4: Element enrichment (in %) with regard to the initial element concentration in the Alpine Schist based on immobile Ti and Al, respectively.

	TiO_2		Al_2O_3		$Fe_2O_{3,\ tot*}$		MnO		MgO		CaO		Na_2O		K_2O	
	Ti_{im}	Al_{im}	Ti_{im}	Al_{im}	Ti_{im}	Al_{im}	Ti_{im}	Al_{im}	Ti_{im}	Al_{im}	Ti_{im}	Al_{im}	Ti_{im}	Al_{im}	Ti_{im}	Al_{im}
Schist	0.0	0.0	0.0	0.0	0.0	0.0	0.0	0.0	0.0	0.0	0.0	0.0	0.0	0.0	0.0	0.0
Mylonite	0.0	- 1.9	1.9	0.0	0.7	- 1.2	- 4.5	- 6.3	- 0.7	2.6	- 0.3	- 2.2	20.2	17.9	- 28.4	- 29.7
Cataclasite	0.0	18.6	- 15.7	0.0	25.8	49.2	87.2	122.1	92.8	128.7	467.0	572.6	- 0.9	17.6	- 79.4	- 75.6
Gouge (HW-pr.)	0.0	25.5	- 20.30	0.0	22.9	54.2	116.2	171.3	66.8	109.2	273.8	369.1	- 53.6	41.7	- 49.8	- 37.0
Gouge (FW-pr.)	0.0	27.7	- 21.7	0.0	30.4	66.5	377.9	510.4	69.8	116.9	1274.8	1656.0	- 66.0	56.6	- 30.4	- 11.1
Gravel	0.0	19.0	- 16.0	0.0	14.0	35.6	23.7	47.2	49.6	78.0	56.5	86.2	- 21.1	6.1	- 52.0	- 42.8

HW-pr.: hanging wall-proximal; FW-pr.: footwall-proximal.
* Total Fe expressed as Fe^{3+}.

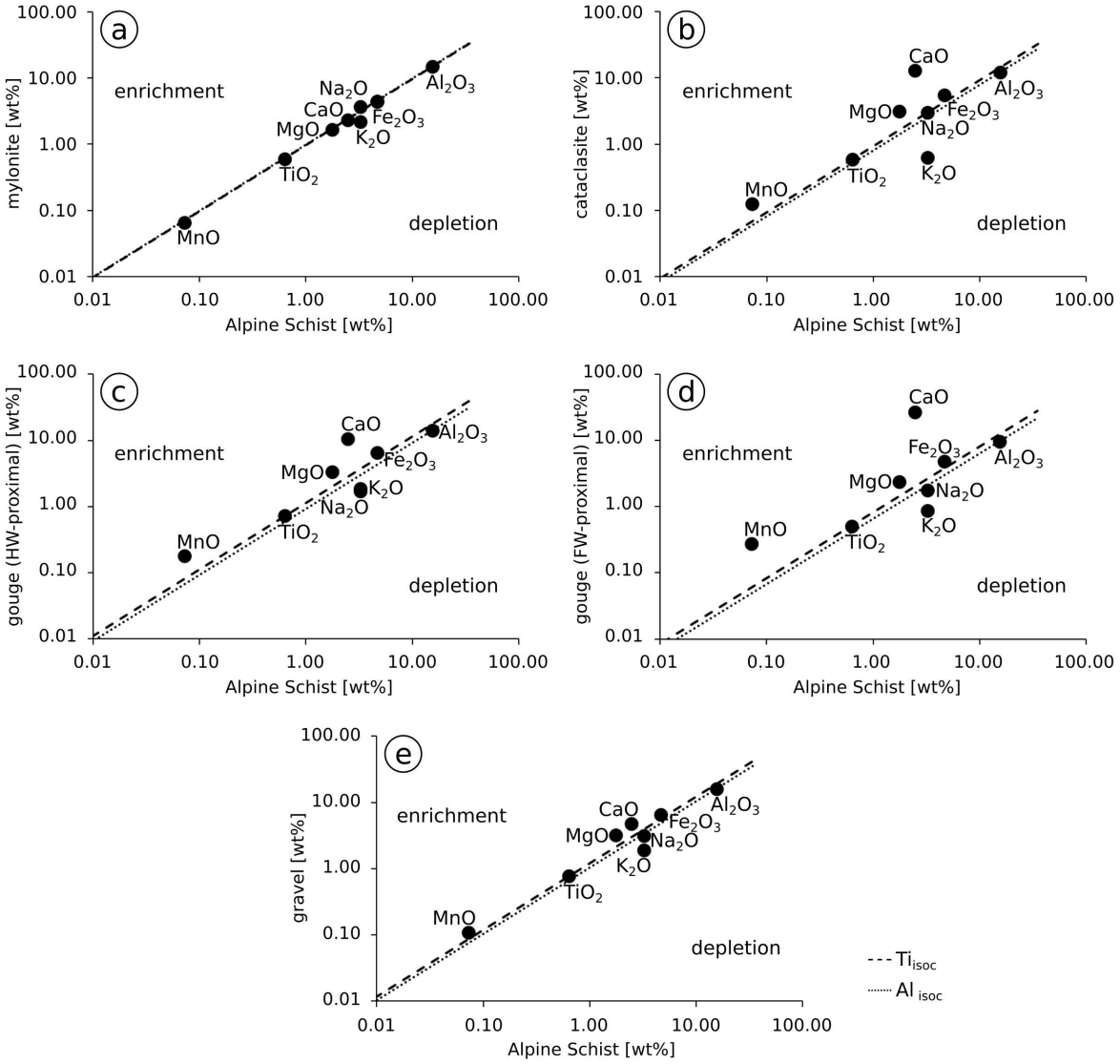

Figure 3.8: Isocon diagrams according to Grant (1986) and Grant (2005) assuming immobile Ti and Al, respectively. Using the Alpine Schist as host rock, the degree of fluid-rock interaction increases with increasing distance towards the PSZ. Geochemical data for the schist are derived from Roser and Cooper (1990), for the mylonite from McClintock and Cooper (2003); see Table 3.3. HW: hanging wall; FW: footwall.

field (Sibson, 1992a; Boese et al., 2012; Warren-Smith et al., 2017). It is assumed that the least compressive stress (σ_3) must be tensile for repeated failure, which requires overpressured fluids (Sibson, 1992a). In other fault systems, such as the Mother Lode in California, failure driven by such high fluid pressures resulted in the formation of hydraulic breccias (Knopf, 1929) and the provision of pore space and permeability for fluid flow. The breccias and the calcite vein network we describe, represent a similar significant volume increase and confirm the importance of fluid-driven PSZ dilatancy in the shallow portion of the Alpine Fault. The circulation of Ca-saturated fluids and subsequent precipitation leading to the formation of calcite veins and cement in hydraulic breccias requires that the fault gouge was highly permeable at some point during the seismic cycle. As these Ca-saturated fluids provide material for calcite precipitation, the typical sizes of calcite crystals of well-below 5 µm are interpreted to point to short periods of crystal growth. Considering that the impermeable

nature of the gouge allows fluid-pressures to build up in the interseismic period, co-seismic dilatancy and associated increases in permeability may result in sudden pressure-drops and related decreases of calcite solubility associated with calcite precipitation (Li and Duan, 2011). This precipitation caused near instantaneous sealing which restored the impermeable nature of the gouge.

The mutually cross-cutting relationships (Figs. 3.5a - d & 3.6a) and wall-rock fragments (Fig. 3.5d) suggest that there was no single weak plane to accommodate the episodic failure leading to the formation of the observed complex pattern of calcite veinlets in the footwall-proximal gouge. Median lines in footwall-distal veins (Figs. 3.4b, c & 3.5d) and mosaic crystals (Fig. 3.5e) indicate that these veins were subject to various crack-seal cycles. However, crystal growth after failure did not always continue at the same growth surface, which resulted in the lack of classical crack-seal microstructures (cf. Bons et al., 2012 and references therein).

The degree of fluid-assisted alteration differs between individual structural units and varies with time. Abundant microstructural evidence of corrosion of calcite cementing breccias and continued alteration of feldspars to phyllosilicates (Fig. 3.3d) indicates significant interseismic fluid-related alteration of minerals in the hanging wall cataclasites. By contrast, calcite microstructures in the fault gouge do not show evidence of abundant dissolution (Fig. 3.5e), which we attribute to the interseismic impermeable nature of this unit. In addition to sealing by calcite, formation of authigenic phyllosilicates counteracts increases in porosity and permeability created by co-seismic dilatancy (e.g., Figs. 3.3e & 3.4e). This might lead to a fast restoration of the gouge's impermeable state quickly resulting in a closed and equilibrated system slowing down or ceasing dissolution or authigenic growth of minerals.

3.6.3 Implications for faulting behaviour: temperature and depth constraints for authigenic mineral formation

Field and seismological studies indicate only minor variations in lithology and fault zone architecture in the Alpine Fault's central segment (e.g., Roser and Cooper, 1990; Little et al., 2005; Boulton et al., 2017a). Consequently, deformation mechanisms and geochemical behaviour deduced from microstructures and mineralogy described here in detail may be considered typical for the entire central segment. This will be further elaborated in a separate paper and further constrained by additional data.

Figure 3.9 provides a summary of microstructural key-observations throughout the fault core. Combined with the mineralogical and geochemical results of this study they confirm increasing degrees of fracture healing and matrix cementation by authigenic phyllosilicates and carbonates towards the footwall-proximal fault gouge resulting in an impermeable PSZ (e.g., Sutherland et al., 2012; Toy et al., 2015; Williams et al., 2017). Hydraulic brecciation (Fig. 3.3c), abundant alteration of feldspars to phyllosilicates (Figs. 3.3d & 3.4f), as well as precipitation of calcite as cement (Fig. 3.3f) and veinlets (Fig. 3.5) are evidence for episodic fluid-related alteration processes in the fault rocks.

However, in contrast to previous investigations (e.g., Boulton et al., 2012, Boulton et al., 2017a; Schleicher et al., 2015; Toy et al., 2015), dissolution seams or indented and embayed clasts, indicative of dissolution processes and localised mass removal (Blenkinsop, 2000; Gratier

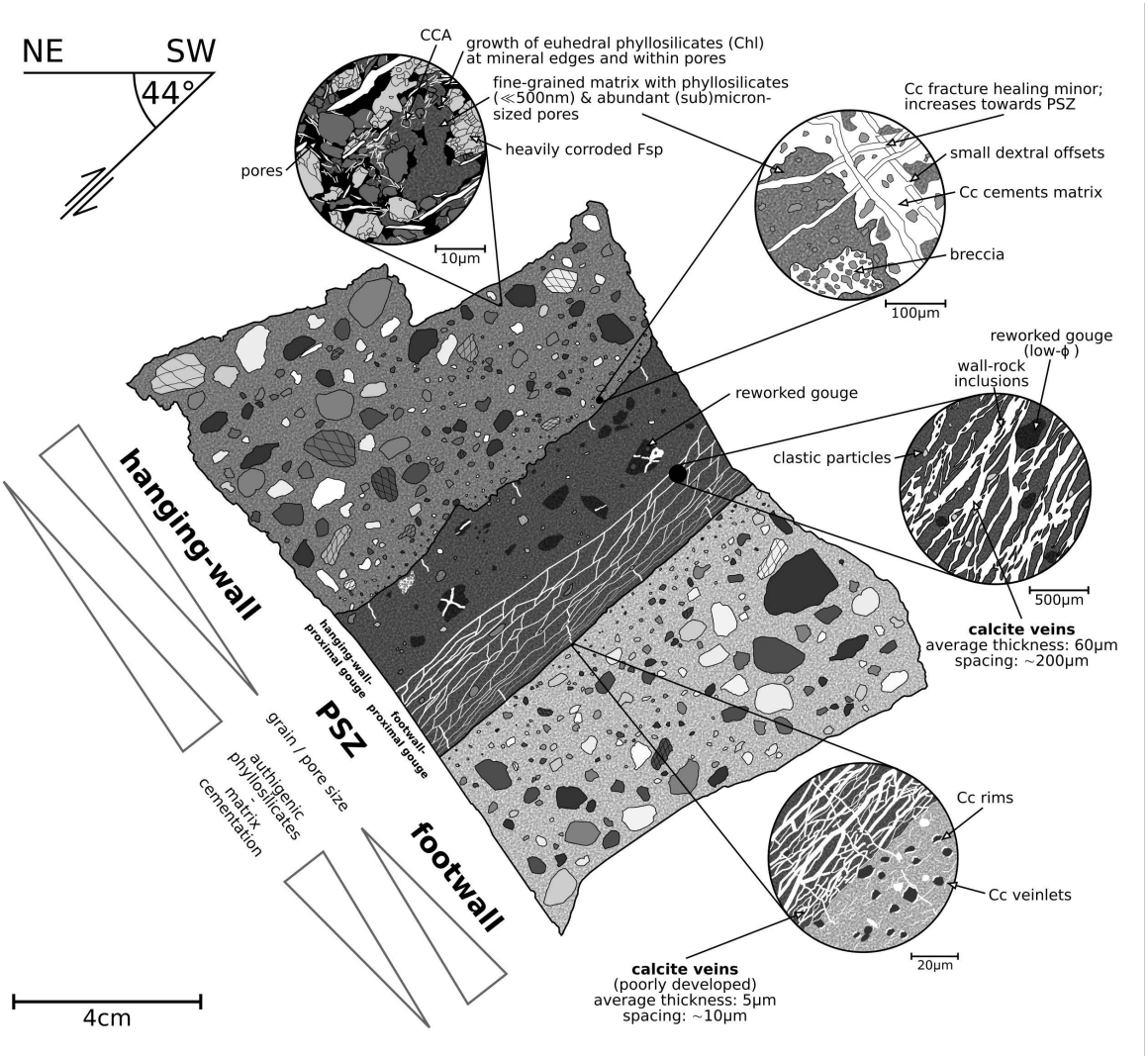

Figure 3.9: Idealised summary of microstructural observations along the investigated transect across the Alpine Fault's core. CCA: clay-clast-aggregate; Chl: chlorite; Fsp: feldspar; Cc: calcite.

et al., 2013), were not found. Additionally, smectite is absent in the fault rocks investigated. This frictionally weak mineral phase is thought to significantly affect the geomechanical behaviour of the Alpine Fault in its central and southern segment (e.g., Warr and Cox, 2001; Boulton et al., 2012, Boulton et al., 2017b) and other large-scale faults such as the San Andreas Fault (Lockner et al., 2011) by lowering the faults' friction coefficient. Our observation of smectite-absence in the central segment is confirmed by other studies (Barth et al., 2013; A. Boles, 2016, personal communication).

Stable at low temperatures, smectite dehydration starts at ~50 °C, and might be completed at temperatures between 88 °C and 142 °C (Colten-Bradley, 1987; Freed and Peacor, 1989). Recent findings demonstrate that near-surface geothermal gradients in the Alpine Fault Zone can be extremely high - for example a gradient of 125 °C km^{-1} persists to at least ~900 m depth at the site of the DFDP-2 boreholes (Sutherland et al., 2017). However, other borehole measurements as well as numerical simulations indicate that the geothermal gradient is highly variable along strike such that absolute values vary significantly within a few kilometers distance (Shi et al., 1996; Sutherland et al., 2012; Sutherland et al., 2017). The reported

extremely high gradients seem to be restricted to valleys, where topographically driven fluids focus heat (Sutherland et al., 2017). Therefore, smectite is not expected to be stable in these areas at depths greater than 700 – 1140 m. As Pacific Plate material is uplifted from seismogenic depths, smectite formation follows a retrograde path. Consequently, it is unlikely that smectite dehydration and associated rising fluid pressure in the impermeable PSZ resulted in an increase of degradation temperature (Koster van Groos and Guggenheim, 1984). Additionally, the PSZ is impermeable and thus inhibits influx and circulation of fluids. This prevents the formation of smectite, irrespective of temperature conditions (Mancktelow et al., 2016 and references therein). Therefore, although temperature is the major control of smectite stability (e.g., Pollastro, 1993), this mineral phase is not expected to be present in larger quantities at depth, even in the areas where a lower geothermal gradient favours the presence of smectite.

At the San Andreas Fault Observatory at Depth (SAFOD), calcite veins, which are potentially related to local fluid overpressures, occur mostly in the damage zone and are absent in the actively creeping segment (Mittempergher et al., 2011; Rybacki et al., 2011). At SAFOD, smectite clay minerals, which likely originate from fluid-assisted alteration, dominate (e.g., Schleicher et al., 2010; Holdsworth et al., 2011; Lockner et al., 2011). This mineralogical composition relates to the material's observed velocity-strengthening behaviour (Carpenter et al., 2015), which is expected to prevent localised deformation and rupture propagation (Scholz, 2002). Deformation experiments on Alpine Fault gouge from outcrop and drill core samples indicate velocity-strengthening behaviour at temperatures below 140 °C (Boulton et al., 2012, Boulton et al., 2014), which should promote fault creep comparable to the San Andreas Fault at shallow depths. However, this conflicts with the fact that large earthquakes occur quasi-periodically (Cochran et al., 2017) and geodetic observations suggest that the Alpine Fault is currently locked and not creeping along its entire length, potentially down to a depth of 12 - 18 km (Sutherland et al., 2007; Wallace et al., 2007; Beavan et al., 2010). These observations together with episodic rupture within a narrow, chlorite-dominated PSZ and subsequent calcite vein precipitation point to velocity-weakening and thus frictionally strong material promoting localised failure potentially propagating to the surface (Warr and Cox, 2001; Scholz, 2002). This interpretation is further supported by experiments on Alpine Fault gouge samples indicating that this unit is, especially when chlorite-bearing, frictionally strong ($0.61 < \mu < 0.76$; Boulton et al., 2014; Ikari et al., 2015). Smectite locally observed in outcrop and shallow borehole samples (Boulton et al., 2012; Schleicher et al., 2015; Toy et al., 2015; Boulton et al., 2017a) might result from the alteration of abundant plagioclase, and may play a role only at very shallow depths (Taboada and Garcia, 1997).

Our microstructural and mineralogical analysis shows that cataclastic processes dominate deformation along the Alpine Fault, especially, when the absence of weak mineral phases, such as smectite, smectite mixed-layered clays or talc, is considered. The dominating role of cataclasis agrees with previous studies (e.g., Toy et al., 2015; Boulton et al., 2017a). The significant and systematic decrease of particle size towards the footwall (Fig. 3.9) results in a gouge matrix with large amounts of nanoscale (< 100 nm) particles, originating from comminution of clastic phases and neoformation of phyllosilicates. (Sub)angular to (sub)rounded

quartzofeldspathic clasts with mylonitic fabric (Fig. 3.3a) as well as gouge clasts (Fig. 3.4a), potentially reworked from the PSZ's matrix, and clay-clast-aggregates (Fig. 3.4f) imply particle fragmentation, translation and rotation contributing significantly to deformation within the fault core. We suggest that powder lubrication and grain rolling, particularly supported by abundant nanoparticles, mainly control the fault core's velocity-weakening behaviour rather than frictional sliding (Han et al., 2011). This agrees with the absence of a foliation within the gouge, e.g., originating from a preferred alignment of phyllosilicates (Collettini et al., 2009b). These processes are co-seismic and contribute to the localised, cyclic faulting within the PSZ and the generation of the observed microstructures. Additionally, as faulting might be triggered by supralithostatic fluid pressures leading to subsequent fluid-flow and co-seismic mineral precipitation, calcite vein formation may occur almost simultaneously with cataclastic processes. This is in accordance with previous studies in different settings where transient cataclastic flow was enabled by dilatancy-hardening associated with hydrofracturing (Doblas et al., 1997) and the formation of slip-parallel calcite veins of co-seismic origin (Nuriel et al., 2012; Collettini et al., 2014).

Our observations show that calcite veinlets and cements contain few dislocations (Fig. 3.3d) and that fault displacement-normal calcite veins deform the footwall-gravels (Figs. 3.6a – c & 3.9), which are only present close to the surface, as well as the PSZ. This indicates that authigenic mineral formation continued close to subaerial conditions. Shallow authigenic mineral formation is further supported by the presence of euhedral chlorite crystallites, which do not show any evidence for cataclastic deformation (i.e., fragmentation; Fig. 3.3e). Chlorite formation is strongly influenced by the geological setting and associated temperatures. Whereas in diagenetic environments the minimum formation temperature of chlorite can be as low as 40 °C, it is around 200 °C in hydrothermal systems (Beaufort et al., 2015). However, the minimum temperature for chlorite stability in low-grade metamorphic settings has been estimated to be as low as 50 °C (de Caritat et al., 1993 and references therein). Consequently, authigenic chlorite formation at shallow-crustal levels at the Alpine Fault is reasonable, especially considering the elevated temperature conditions. In addition, crystal growth at greater depths and subsequent thrusting and exhumation would have resulted in higher calcite dislocation densities (Rybacki et al., 2011) than those observed here. Isotope analyses give a formation temperature for cataclasite cement at Waikukupa Thrust of 125 °C (Menzies et al., 2016). This, in combination with calcite microstructures indicating shallow and fast co-seismic precipitation, demonstrates that pulses of high-temperature fluids facilitated the near-surface authigenic mineral formation.

3.7 Conclusions

Microstructures such as particles comminuted from unfractured mylonites to nanoscale-fragments, intensely reworked gouge matrix, hydraulic breccias and mutually cross-cutting calcite veins with wall rock inclusions, indicate the Alpine Fault failed episodically due to stimulation by high fluid pressures. During these events, cataclasis was the dominant deformation mechanism and preferentially localised in the fault core. The cyclic evolution of

the fault's strength is controlled by an extremely high geothermal gradient, the associated presence of high-temperature fluids and the formation of authigenic minerals, such as chlorite and calcite, sealing the PSZ for fluid flow. This results in conditions adverse for smectite growth and limits its stability to shallow depths, minimising the influence of this weak phase on the fault's geomechanical properties and possibly promoting its velocity-weakening behaviour. Consequently, quasi-periodical ruptures can easily propagate from seismogenic depths to the surface. Transient co-seismic increases of permeability facilitate flow of high-temperature fluids and enable subsequent authigenic formation of calcite veins and cements as well as phyllosilicates close to subaerial depths. Fluid-related precipitation of calcite veins results in significant volume gains in the PSZ. Fracture healing by authigenic mineral formation quickly restores the strength and the impermeable nature of the PSZ, which fosters inter-seismic stress accumulation.

3.8 Acknowledgements

Stefan Gehrman and Anja Schreiber are acknowledged for thin section and TEM foil preparation, respectively. Richard Wirth acquired TEM images. Heike Rothe and Sabine Tonn are thanked for ICP-OES sample preparation and analyses, respectively. Uwe Wollenberg (EMR Group, Geological Institute, RWTH Aachen University) enabled access to and provided help with CL analyses. Discussions with Erik Rybacki are gratefully acknowledged. We thank A. Billi and K. K. Bradburry for their constructive reviews, which helped to improve the manuscript. This project was funded by DFG grant JA 573/8-2.

4 Fault and landslide slip zone comparisons yield new insight about the processes that operate within them, and their hazard potential

4.1 Abstract

Earthquakes and landslides are one of the most important natural hazards responsible for numerous casualties and economic losses. Furthermore, as the world's population continues to increase, more areas susceptible to landslides are becoming populated, so the impact of landslide hazards is increasing. Slip zone characterisation studies employ a broad range of state-of-the-art approaches to understand the relation between material properties and deformation down to the nanoscale. Despite some differences, mostly related to the fact that deformation in fault zones occurs across a broader range of different depths, and hence ambient pressures and temperatures, slip zones of landslides share many characteristic features with those of faults such as mineralogy and rheology, manifested by the predominance of cataclastic processes and demonstrated by identical microstructures. We compare typical mineralogy, characteristic microstructures and rheological processes of fault and landslide slip zones. This comparison allows identification of key similarities, and highlights differences that indicate what sort of future investigation may contribute to a better understanding of the hazard originating from landslides.

4.2 Introduction

The world population is expected to reach more than 11 billion people by the end of this century (United Nations, 2017). This increase of almost 50 % compared to the current population will most likely be accompanied by a global increase of socioeconomic vulnerabilities to natural hazards (Pesaresi et al., 2017). Earthquakes and landslides are among the most devastating geohazards causing thousands of fatalities and severe economic losses (Dilley et al., 2005). For example in 1999, the $M > 7$ earthquakes of Izmit and Düzce caused more than 20,000 casualties and had an economic impact of up to 25 billion USD (Sahin and Tari, 2000). In 2008, the M_S 8.0 Wenchuan Earthquake (China) and the more than 56,000 co-seismic landslides killed 60,000 people and injured 370,000 (Dai et al., 2011; Huang and Li, 2011). The earthquake accounted for about 170 billion USD of direct and indirect economic losses (Wu et al., 2012).

Earthquakes are the results of fault rupture and slip that results in the catastrophic release of stress in combination with the radiation of seismic energy because of fast rupture velocities ($> 10^3\,\mathrm{m\,s^{-1}}$) and slip rates ($> 10^{-4}\,\mathrm{m\,s^{-1}}$; Rowe and Griffith, 2015). Fault planes are mechanical discontinuities in the Earth's crust where strain localises, manifested by shear displacement along the plane (Fossen, 2016). Their rheological behaviour is governed by a variety of factors including their effective frictional strength (Byerlee, 1978) which is related to mineralogical composition (e.g., Brantut et al., 2008; Tembe et al., 2006; Solum et al., 2010; Lockner et al., 2011) as well as the fluid pressures (Hickman et al., 1995; Mittempergher et al., 2011) and orientations and magnitudes of stresses within the rock volume they dissect (Sibson, 1985; Rice, 1992).

The term *landslide* describes the gravity-driven downslope movement of rock and soil on a rupture surface, commonly as a (semi)coherent body, with limited amounts of internal deformation, as well as the resulting landform (Lin et al., 2001; Kawamura et al., 2007; Highland and Bobrowsky, 2008; Ferri et al., 2011). Landslides may result from one or a combination of multiple failure mechanisms such as fall, topple, slide, spread and flow (Cruden and Varnes, 1996). They occur on- and offshore, and in a wide variety of global settings (e.g., mountains, cultivated land, forests, permafrost). The understanding of these phenomena requires an interdisciplinary approach involving pedology, geomorphology, hydrology, geology, mineralogy, seismology, climatology and engineering (e.g., Bhandary et al., 2005; Kawamura et al., 2007; Wen et al., 2007; Highland and Bobrowsky, 2008; Preuth et al., 2010; Ferri et al., 2011; Ward and Day, 2011; Schäbitz et al., 2018).

Natural events, anthropogenic action, or a combination of both can act as landslide-triggers, influenced by factors such as topography, water saturation and mineral composition (e.g., Morgenstern and Tchalenko, 1967; Skempton, 1985; Wen and Aydin, 2004; Bhandary et al., 2005; Yalcin, 2007; Froude and Petley, 2018; Schäbitz et al., 2018). Natural triggers are changes in fluid pressure (e.g., by rain, snowmelt, groundwater), seismic activity and volcanic events (e.g., Gomberg et al., 1995; Lin et al., 2001; Bhandary et al., 2005; Wen and Aydin, 2005; Huang and Li, 2011; Regmi et al., 2013a; Handwerger et al., 2016), and many landslides result from other natural disasters such as floods or earthquakes. However, they can act also as triggers for new hazards - for example, underwater landslides commonly cause tsunamis (Miller, 1960; Ward and Day, 2011; Harbitz et al., 2014; Kremer et al., 2015).

Although the basal slip surfaces of landslides are also planes across which shear displacement occurs, there are pronounced differences between landslide slip surfaces and seismogenic faults. Poorly consolidated soils and sediments, typical for many landslides, exhibit a rheological behaviour that is quite different to that of the lithified rocks that host most faults, except in their very near surface portions (e.g., Drucker et al., 1957; Roscoe et al., 1958; Byerlee, 1978; Sibson, 1986; Rybacki et al., 2011). Rupture velocities across faults are rapid ($> 10^3\,\mathrm{m\,s^{-1}}$; Rowe and Griffith, 2015) compared to landslides, which show a broad variety ranging from extremely rapid (e.g., $\sim 10^2\,\mathrm{m\,s^{-1}}$ for fast debris avalanches) to extremely slow (i.e., $< 16\,\mathrm{mm\,yr^{-1}}$ for creeping soils; Cruden and Varnes, 1996; Highland and Bobrowsky, 2008). Ambient conditions at the depths at which earthquakes typically nucleate (3 - 15 km in standard continental crust; Scholz, 2002) such as temperature, confining and fluid pressure, and the resulting deformation

conditions, can only be inferred indirectly by extrapolating experimental results (Bürgmann and Dresen, 2008; Rybacki et al., 2008; Rybacki et al., 2013) or interpreting remote geophysical data (Raub et al., 2017; Boese et al., 2018).

Additionally, microstructures, mineralogical composition and geochemistry present at seismogenic depths may be overprinted during exhumation (Warr and Cox, 2001; Toy et al., 2015). The only hope of sampling fault zone materials from within their seismogenic zones is through scientific drilling (Zoback et al., 2007). However, due to technical limitations, the scientific drillholes thus far put down have mostly penetrated faults at shallower than seismogenic depths (e.g., Boullier, 2011; Toy et al., 2015; Zoback et al., 2011, and references therein). There are only a few exceptions, such as the DEEPAK (Deep Drilling at Koyna) Project, which aim to probe seismogenic depths (Gupta et al., 2015). Additionally, some fault ruptures do propagate to the surface; for example Integrated Ocean Discovery Program (IODP) Expedition 343 Japan Trench Fast Drilling Project (JFAST) sampled the Japan Trench plate boundary thrust responsible for the M_W 9.0 Tohoku-Oki Earthquake (Chester et al., 2013). However, these are not the materials or conditions at which ruptures initiated in these materials, and the mechanics of fault slip differ (e.g., rupture propagation rate, radiated energy frequency spectrum). In contrast, the subaerial setting of landslides allows in-situ monitoring of faulting conditions, and the materials within which slip occurred can easily be sampled (Gomberg et al., 1995).

Despite these differences, seismogenic faults and landslides share a couple of characteristic features. (I) movement is typically confined to discrete planes (of variable thickness) accumulating most of the displacement (Fig. 4.1). In case of faults, this plane is commonly known as a *principal slip zone* (PSZ; e.g., Sibson, 2003; Janssen et al., 2014; Toy et al., 2015). The *surface of rupture*, separating the slipped body from the bedrock is the landslide-equivalent to a PSZ (e.g., Cruden and Varnes, 1996; Wen and Aydin, 2003; Chen et al., 2014). (II) Intrinsic properties (e.g., frictional strength) may evolve over time. This might be caused by changing boundary conditions such as temperature-reduction during uplift (faults; Warr and Cox, 2001) or water chemistry (landslides; Preuth et al., 2010; Zhang and McSaveney, 2018). However, under constant boundary conditions material properties might also evolve, for example because formation of authigenic minerals reduces the coefficient of friction (e.g., Schleicher et al., 2010; Solum et al., 2010; Holdsworth et al., 2011; Schäbitz et al., 2018). (III) Dimensions of both types of structures extend over several orders of magnitude with landslides ranging from decimeter-sized pieces of rock falling off cliffs to square-kilometer-wide earthflows (Highland and Bobrowsky, 2008) and faults showing positive displacement-thickness correlations over more than four orders of magnitude (Hull, 1988; Faulkner et al., 2010). (IV) Most importantly, landslide and fault slip surfaces commonly display similar internal microstructures such as Riedel shears, polished fault planes and alignment of particles. Consequently, the same deformation mechanisms (particularly cataclasis and particulate flow) are considered to be responsible for the observed structures in both cases (e.g., Morgenstern and Tchalenko, 1967; Skempton and Petley, 1967; Skempton, 1985; Gomberg et al., 1995; Wen and Aydin, 2003; Wen and Aydin, 2004; Kawamura et al., 2007; Smith et al., 2011; Chen et al., 2014; Bradbury et al., 2015; Schäbitz et al., 2018; Schuck et al., 2018).

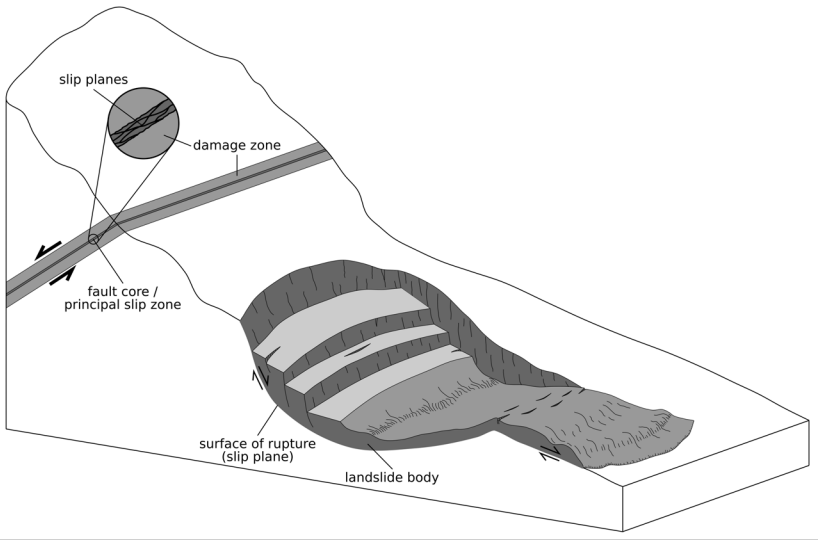

Figure 4.1: Sketch showing main features of faults and landslides. Despite quite complex internal processes, most strain is accumulated by major slip zones. Internal geometries of these slip planes might be complex as exemplified for faults. Figure based on sketches by Caine et al. (1996), Cruden and Varnes (1996) and Faulkner et al. (2003).

These observations suggest that some aspects of the governing physics of deformation are common to both sorts of structures. Because the relationship between rock microstructures and deformation mechanisms are fairly well known (e.g., Passchier and Trouw, 2005), by examining microstructures in faults and landslide samples we may clarify which processes control faulting and landsliding. This possibility has inspired us to consider comparisons between our previous microstructural analyses of outcrop and drillcore samples from several faults and landslides (Janssen et al., 2012; Janssen et al., 2014; Schäbitz et al., 2018; Schuck et al., 2018).

We herein present an overview of existing characterisation methods and compile a survey of available data, with new results. Significant progress in understanding failure processes of faults and landslides has been made possible by integrating field observations with analytical methods. Consequently, our comparison profits from a broad range of methodological approaches such as field work, optical microscopy, scanning and transmission electron microscopy (SEM and TEM), texture, mineralogical and geochemical analyses. Our results demonstrate key similarities and differences between the near-surface deformation mechanisms that operate in slip zones formed by seismic processes and landslides. Our data also yield more advanced understanding of the complex interplay between preconditioning and triggering factors influencing landslides. We anticipate that our comparative study will provide new insights into how landslide hazard assessment can be performed.

4.3 Mineralogy

4.3.1 Mineral composition of failure zones and its influence on fault and landslide strength

The geomechanical behaviour of earth materials is strongly influenced by mineralogy and the associated large variations in strength. Failure of landslides and faults is controlled by

frictional processes and there are strong similarities between them in the material properties necessary for failure, as well as in the range of failure modes (e.g., Handwerger et al., 2016). Frictionally weak phases such as serpentine, talc and clay minerals are important constituents of many fault zones and landslide rupture surfaces (e.g., Skempton, 1985; Moore et al., 1997; Saffer et al., 2001; Warr and Cox, 2001; Wen and Aydin, 2003; Bhandary et al., 2005; Moore and Rymer, 2007; Moore and Lockner, 2008; Collettini et al., 2009a; Collettini et al., 2009b; Schleicher et al., 2010; Tembe et al., 2010; Bradbury et al., 2011; Holdsworth et al., 2011; Lockner et al., 2011; Moore and Rymer, 2012; Janssen et al., 2014).

Clay minerals also influence effective frictional strength and effective stresses by drastically reducing permeabilities (e.g., Morrow et al., 1992; Moore and Lockner, 2007; Janssen et al., 2011; Sutherland et al., 2012; Neuzil, 2019) and even small amounts of these phases are sufficient to cause fault weakness (Tembe et al., 2006; Solum et al., 2010); especially when they form interconnected networks (Collettini et al., 2009a; Collettini et al., 2009b; Schleicher et al., 2010). In addition to promoting catastrophic failure of faults and landslides by their frictional weakness, clay minerals may promote aseismic (e.g., slow-slip, creep) behaviour (e.g., Bhandary et al., 2005; Kawamura et al., 2007; Schleicher et al., 2010; Lockner et al., 2011; Schleicher et al., 2012).

Furthermore, changing boundary conditions may affect phyllosilicate stability, which can thus change the geomechanical behaviour. For example, creep of the Vaiont Landslide (Italy) was localised in centimeter-thick, clay-rich layers, and triggered by reservoir-filling and rainfall reducing effective stresses. Processes responsible for the catastrophic failure of the landslide in 1963 succeeding more than three years of creep are still not fully understood but most likely involve chemical pressurisation of pore fluids resulting from the conversion of smectite to illite (Ferri et al., 2011).

The stability of clay minerals is mostly controlled by temperature (Pollastro, 1993). Smectites, the weakest clay phases, are stable only at temperatures below $\sim 140\,^{\circ}\mathrm{C}$ (Colten-Bradley, 1987; Freed and Peacor, 1989), thus are significant at the shallow depths typically associated with landslides and the shallowest parts of faults where ruptures propagated to the surface. Water saturation and salinity also impact clay stability (Moore and Lockner, 2007; Morrow et al., 2017) allowing smectites to be stable at temperatures $> 140\,^{\circ}\mathrm{C}$ (Koster van Groos and Guggenheim, 1984).

Clay minerals demonstrably significantly control geomechanical behaviour in the San Andreas Fault, California (USA), the Chelungpu Fault (Taiwan) and the detachment of the Japan Trench. Representative X-ray diffraction (XRD) patterns of SAFOD (San Andreas Fault Observatory at Depth) fault gouge material reveal they are particularly rich in clay minerals such as serpentine-saponite mixed layers, saponite, chlorite and illite. The creeping behaviour of the San Andreas Fault's Parkfield segment is attributed to the presence of these weak phyllosilicates (Schleicher et al., 2010; Bradbury et al., 2011; Holdsworth et al., 2011; Lockner et al., 2011; Moore and Rymer, 2012; Schleicher et al., 2012). Serpentine, another major constituent of some San Andreas Fault gouge samples, is also thought to contribute to the fault's weakness (Moore and Lockner, 2007; Bradbury et al., 2011; Moore and Rymer, 2012).

Hosted in silt- and shale-rich lithologies, the fault gouge forming the core of the Chelungpu Fault mostly comprises the phyllosilicates illite, chlorite and kaolinite (Kuo et al., 2009; Boullier, 2011). Seismological observations during the 1999 Chi-Chi Earthquake indicate this fault experiences co-seismic slip-weakening behaviour, which is attributed to the clay-dominated gouge (Boullier et al., 2009; Boullier, 2011). The low frictional strength of the plate-boundary detachment zone of the Japan Trench (Fulton et al., 2013; Ujiie et al., 2013) is also attributed to its mineralogical composition (~60 %, ~14 %; Chester et al., 2013; Janssen et al., 2015).

Gouges that develop on landslide rupture surfaces are typically clay-rich, which is expectable given the shallow-depths, hence temperatures, of most landslide slip surfaces (e.g., Skempton, 1985; Shuzui, 2001; Wen and Aydin, 2003; Schäbitz et al., 2018). Studies of Japanese landslide rupture surfaces have revealed a negative correlation between clay content and shear strength: as smectite content increases, the angle of internal friction decreases, facilitating continuous sliding (Shuzui, 2001; Bhandary et al., 2005).

Owing their typically very low permeabilities (e.g., Neuzil, 2019), abundant presence of clays might promote high fluid pressures and consequently weakening (Janssen et al., 2011; Handwerger et al., 2013; Schulz et al., 2018); especially, when related to deformation-induced porosity reduction (Iverson et al., 2000). Clay-rich, low-permeability basal shear zones are susceptible to seasonal pore-water-driven changes of effective normal stresses causing variations of landslide slip velocities (e.g., Handwerger et al., 2013; Schulz et al., 2018). However, while increasing pore pressures result in lower effective stresses, hence lower shear resistances, swelling of clays associated with these elevated pore pressures counteracts pressure-related decreases of shear resistance (Moore and Lockner, 2007; Schulz et al., 2018).

Graphite may also be important in controlling the frictional strength of many faults and landslides. Because it is a very weak phase ($\mu = 0.1$) and its presence in amounts as small as ~10 % along slip planes is sufficient to cause drastic weakening, it is commonly called a 'solid lubricant' (Oohashi et al., 2011; Oohashi et al., 2013). It is distinct from weak clay phases because it is stable at high temperatures, so the presence of graphite may be related to the weakness of many faults to greater depth than clays (e.g., Oohashi et al., 2012; Kuo et al., 2013; Oohashi et al., 2013; Nakamura et al., 2015). Graphite and the phyllosilicate pyrophyllite are important constituents of the sliding surfaces of several creeping landslides in Northwest China (Fig. 4.2a; Schäbitz et al., 2018). The extremely low coefficients of friction of both phases provide strong evidence that landslide creep is controlled by the presence of these weak minerals.

Graphite in fault zones and landslide rupture surfaces originates from a variety of processes such as rearrangement of disseminated graphite by shear motion (Nakamura et al., 2015; Kirilova et al., 2017), enrichment by diffusive mass transfer (see also Section 4.4.2; Oohashi et al., 2012), fluid-related alteration (see also Section4.3.2; Oohashi et al., 2012; Kirilova et al., 2017) or the co-seismic transformation of carbonaceous material into graphite (Oohashi et al., 2011; Kuo et al., 2013; Nakamura et al., 2015). Friction experiments suggest that this co-seismic transformation of carbon into graphite can take place at pT-conditions characteristic for subaerial landslides (Oohashi et al., 2011). Consequently, current creep of landslides in

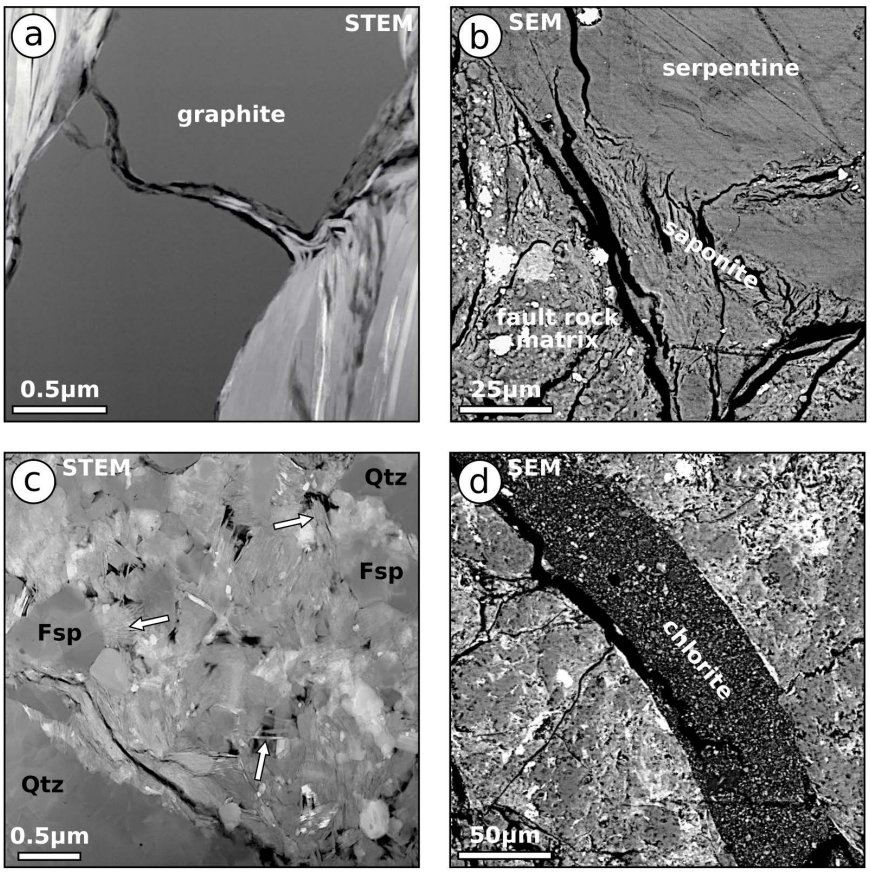

Figure 4.2: (a) Graphite encountered within the slip zone of the Suertou Landslide. Figure from Schäbitz et al. (2018). **(b)** Saponite within the creeping segment of the San Andreas Fault at Parkfield formed by metasomatic alteration of serpentine and quartzofeldspathic phases. For details refer to Janssen et al. (2014) and Moore and Rymer (2012). **(c)** Phyllosilicates, mostly chlorite, seal open space within the principal slip zone of the Alpine Fault. White arrows highlight individual chlorite crystallites. **(d)** Chlorite formed in a crack within the cataclastic hanging wall of the Alpine Fault. For details of c & d see Schuck et al. (2018). STEM: scanning transmission electron microscopy; SEM: scanning electron microscopy. Qtz: quartz; Fsp: feldspar.

Northwest China is considered to result from phase transitions triggered by earthquakes or co-seismic landslides (Schäbitz et al., 2018).

In summary, the presence of phyllosilicates and graphite in gouges constituting fault cores as well as landslide slip zones has an important impact on the mechanical strength of faults and landslides.

4.3.2 Fluid-related alteration and its effects on mineral composition and mechanical strength

Numerous fault zone studies have identified the process of fluid-related alteration substantially influences fault mechanics (e.g., Warr and Cox, 2001; Boullier et al., 2009; Schleicher et al., 2009; Boullier, 2011; Oohashi et al., 2012; Sutherland et al., 2012).

The most important fluid-related alteration processes currently recognised are the authigenic formation and dissolution of minerals, which affect both frictional strength and permeability, hence the geomechanical behaviour of rocks and soils. Because of their low frictional strength and their relatively simple formation conditions, abundantly encountered phyllosilicates are

the most important group of authigenic mineral phases in fault rocks (Boullier et al., 2009; Schleicher et al., 2010; Boullier, 2011; Bradbury et al., 2011; Lockner et al., 2011).

Most of the creep-promoting phyllosilicates encountered in the San Andreas Fault are of authigenic origin and result from fluid-related alteration (e.g., Bradbury et al., 2011; Lockner et al., 2011; Moore and Rymer, 2012; Janssen et al., 2014). Saponite is the product of metasomatic reactions between serpentinite entrained in the fault zone and adjacent quartzofeldspathic host rocks (Fig. 4.2b; Moore and Rymer, 2007; Holdsworth et al., 2011). Pervasive fluid-related alteration is also reported from fault rocks of the Alpine Fault, New Zealand (Sutherland et al., 2012; Schleicher et al., 2015). Alteration assemblages control rheology and hydrology of the Alpine Fault Zone by sealing the PSZ for cross-fault fluid-flow and enabling supra-lithostatic fluid-pressures to build up in its hanging wall (Fig. 4.2c; Sutherland et al., 2012; Menzies et al., 2016; Schuck et al., 2018). Reaction weakening by clay formation started at $< 320\,^{\circ}\mathrm{C}$ by growth of Mg-chlorites (Fig. 4.2d) and subsequent formation of further phyllosilicate phases (Warr and Cox, 2001; Schleicher et al., 2015). Graphite may also be the product of fluid-related alteration and element mobilisation (Oohashi et al., 2012; Kirilova et al., 2017; MacKenzie et al., 2017).

In addition to authigenic clays, abundant veins in many of the Earth's large-scale fault zones provide evidence for passage of fluids through and their interaction with these systems (Bradbury et al., 2011; Janssen et al., 2016; Schuck et al., 2018). Apart from the possibility that fluid pressure variations could trigger faulting (Sibson, 1992b), veins have the potential to act as heterogeneities that enable subsequent localisation of further strain (Virgo et al., 2013).

Fluid-related alteration that effects the mineral composition of landslide slip zones is well-documented (e.g., Yalcin, 2007; Regmi et al., 2013a; Regmi et al., 2013b; Schäbitz et al., 2018). Fluids reduce material strength by allowing replacement of more competent components such as feldspars with weak (hydrous) phyllosilicates such as smectite, kaolinite and illite. In addition to promoting authigenic formation of weak mineral phases, the mechanical strength of landslides can be negatively affected by mineral dissolution resulting from fast, subaerial weathering: carbonate dissolution by acid rain was implicated for the Jiweishan Landslide in southwest China (Zhang and McSaveney, 2018).

The major contrast between landslides and faults in this case is that, to our knowledge, veins formed as immediate consequence of transient fluid-flow during landslide failure have not been documented so far. However, this aspect is worthy of further investigations, since it is known that within fault zones calcite veins can form within weakly consolidated sediments close to the Earth's surface (Schuck et al., 2018). A caveat here is that most veins form as a result of hydrofracturing, which requires quite elevated fluid pressures (e.g., Sibson, 1992a). It is possible that such conditions are not easily realised in landslide slip surfaces because of their typical shallow burial depth.

In summary, reaction-weakening promoted by fluid-related alteration is an important mechanism to change the strength of faults and landslides. Furthermore, landslides are especially prone to fluid-related alteration due to the typically shallow burial depth of their slip zones.

4.4 Deformation mechanisms and associated microstructures

4.4.1 Cataclasis

Both seismogenic faults, and landslides, fail in the brittle regime, with cataclasis being the most important deformation mechanism. This involves fracturing, displacement and / or rotation of rigid particles without permanent lattice distortion (Fig. 4.3). Fundamental deformation processes are cracking and frictional sliding. Particle size reduction occurs during both processes, by fragmentation and attrition, respectively (Blenkinsop, 2000).

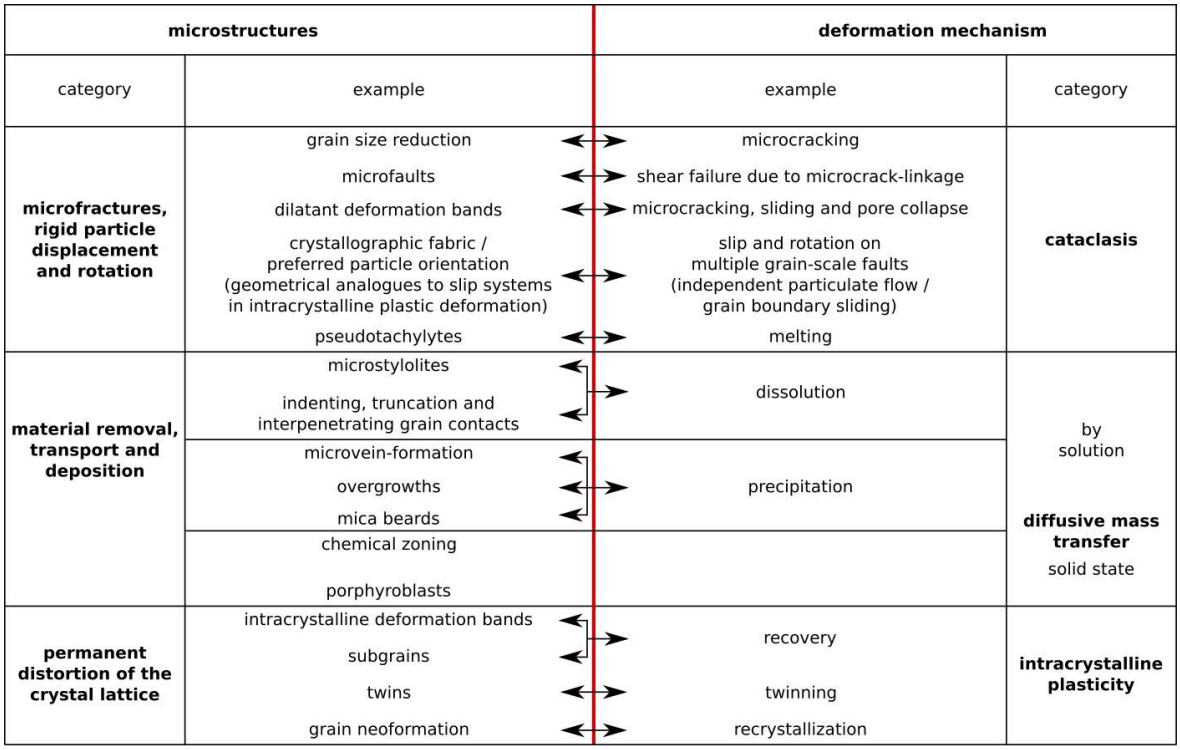

Figure 4.3: Microstructures can be related to one of three categories; each of which is associated with a specific kind of deformation mechanism or a combination of them. Figure modified after Blenkinsop (2000).

4.4.1.1 Particle comminution

The slip zones of most seismogenic faults and landslides comprise gouge, which is incohesive, ultrafine-grained, pulverised material (Figs. 4.4 & 4.5a). These comminuted particles drastically reduce the mechanical strength of slip zones by the mechanism of powder lubrication, so their presence promotes slip (Wen and Aydin, 2003; Wen and Aydin, 2004; Han et al., 2010; Han et al., 2011). This weakening mechanism is considered to be comparably as efficient as the more commonly-discussed mechanisms of melt lubrication and thermal pressurisation (see also Section 4.4.1.3; Han et al., 2011). Particle sizes are reduced through fluid-related alteration reactions, such as replacement of feldspars by phyllosilicates (see also Section 4.3.2; Blenkinsop, 1991) and pressure solution (see also Section 4.4.2; Gratier and Gamond, 1990; Collettini et al., 2009a; Collettini et al., 2009b; Gratier et al., 2011; Schäbitz et al., 2018), as well as by fracturing and shear failure of asperities with subsequent particle comminution

(Sammis et al., 1987; Blenkinsop, 1991; Blenkinsop, 2000; Wilson et al., 2005; Brantut et al., 2008). These processes are active over a wide range of slip rates (Stünitz et al., 2010).

<table>
<tr><td colspan="4"></td><td>non-foliated</td><td>foliated</td></tr>
<tr><td rowspan="2">> 30% clasts (> 2mm)</td><td rowspan="2">incohesive</td><td colspan="2"></td><td colspan="2">fault breccia</td></tr>
<tr><td rowspan="5">< 30% clasts (> 2mm)</td><td colspan="2"></td><td colspan="2">fault gouge</td></tr>
<tr><td rowspan="4">cohesive</td><td colspan="2">(devitrified) glass</td><td>pseudotachylyte</td><td></td></tr>
<tr><td rowspan="3"># of matrix [%]</td><td>0 - 50</td><td>protocataclasite</td><td>protomylonite</td></tr>
<tr><td>50 - 90</td><td>cataclasite</td><td>mylonite</td></tr>
<tr><td>90 - 100</td><td>ultracataclasite</td><td>ultramylonite</td></tr>
<tr><td colspan="2">pronounced grain growth</td><td></td><td>blastomylonite</td></tr>
</table>

Figure 4.4: Fault rock classification based on Sibson (1977) and Woodcock and Mort (2008).

Within faults, particle pulverisation, which involves fragmentation of particles but no relative shear displacement between them, is thought to occur during propagation of a single earthquake rupture (Wilson et al., 2005; Brantut et al., 2008), and pulverised fault rocks might indicate high rupture velocities (Sammis and Ben-Zion, 2008; Mitchell et al., 2011). Like in fault slip zones, the fine grain sizes of landslide slip zone gouges result from a combination of particle fragmentation (Wen and Aydin, 2003; Wen and Aydin, 2004; Zuo et al., 2019) and alteration (e.g., Regmi et al., 2013a; Regmi et al., 2013b, see also Section 4.3.2). It is reasonable to think that the latter will dominate within landslide slip zones both because of low confining pressures and also because fluids are easily able to access these exposed or shallow-depth gouges (Wen and Aydin, 2004). At greater depths, hence higher confining pressures, it is much more difficult for a shearing gouge to dilate in order to relieve the high contact stresses that develop between particles - the same stresses that cause those particles to yield when they deform in constrained comminution (Sammis et al., 1987; Biegel and Sammis, 2004). Furthermore, owing to its typically clayey (i.e., phyllosilicate-rich) composition, landslide material will probably support overall lower stresses, so rigid clasts may be less likely to pulverise (Wen and Aydin, 2003; Wen and Aydin, 2004). Consequently, mechanical abrasion of weaker phases like phyllosilicates by more rigid phases such as quartz grains, which act as indentors (Fig. 4.5b), might be a significant comminution process in these cases (Baudett et al., 1999; Schäbitz et al., 2018; Zuo et al., 2019).

Pulverisation and associated slip zone weakening is an important process in fault zones and landslides. However, owing the smaller normal stresses and because of typical mineralogical compositions lack rigid phases, this process might not be as important in landslides as it is in fault zones.

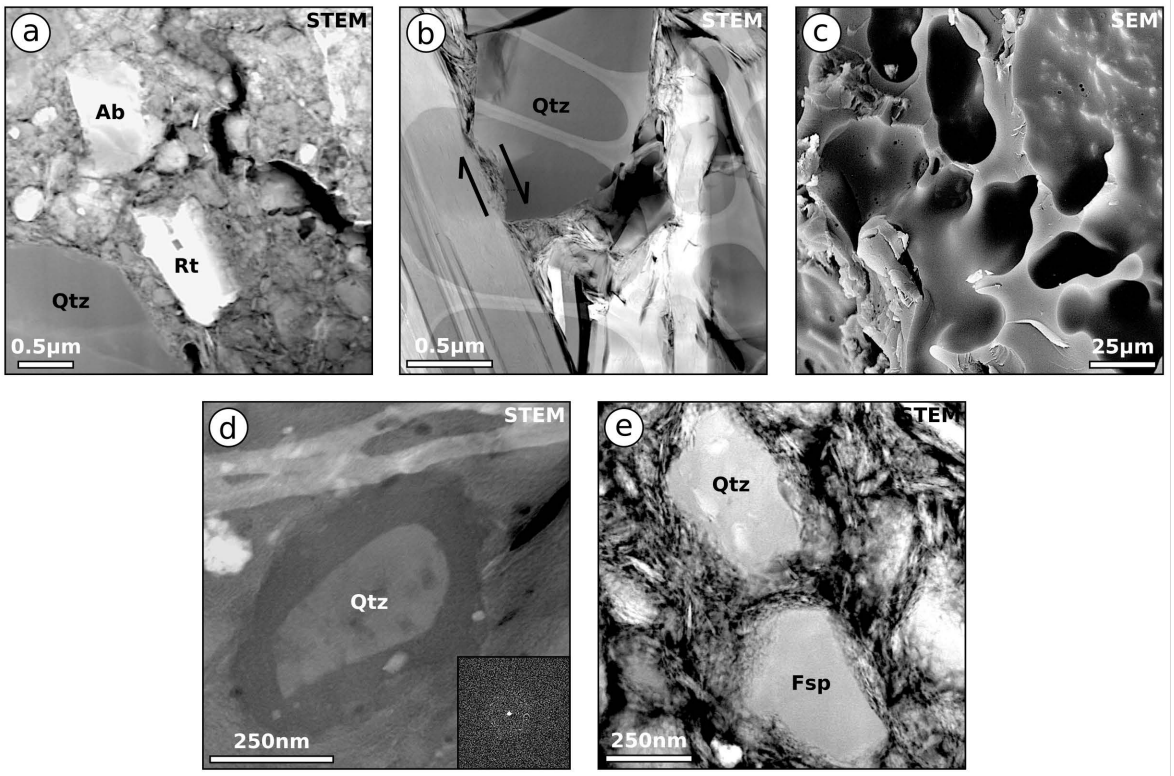

Figure 4.5: Microstructures formed by cataclasis. **(a)** Pulverised fault rock from the principal slip zone of the Alpine Fault. For details see Schuck et al. (2018). **(b)** Rigid quartz grain abrades weaker phyllosilicates (illite) within the slip zone of the Duang-He-Ba Landslide. Figure from Schäbitz et al. (2018). **(c)** Vesicles resulting from frictional melting within the principal slip zone of the Chelungpu Fault. Figure from Janssen et al. (2014). **(d)** Amorphous material surrounds a quartz grain within the ultracataclasites of the San Andreas Fault. Inset shows diffraction pattern confirming the amorphous nature of the rim. Figure from Janssen et al. (2010). **(e)** Clay-clast-aggregates (cf. Boutareaud et al., 2008) from the principal slip zone of the Alpine Fault. For details see Schuck et al. (2018). STEM: scanning transmission electron microscopy; SEM: scanning electron microscopy. Qtz: quartz; Ab: albite; Rt: rutile; Fsp: feldspar.

4.4.1.2 Indicators of seismic slip rates

Frictional melting and graphitisation of amorphous carbon

Both graphitisation (i.e., increase in crystallinity) of amorphous carbon (Oohashi et al., 2011) and generation of glass by the destruction of a material's crystal lattice are processes thought to require seismic slip rates ($> 1\,\mathrm{m\,s^{-1}}$; Sibson, 1975; Sibson, 2003; Kuo et al., 2013). Consequently, these microstructures are generally considered to be indicative of these high slip rates.

Glass, an amorphous material, where found in deformed rocks is termed pseudotachylyte (Fig. 4.4; Shand, 1916). However, the amorphous material transforms relative quickly to smectite, which hampers its identification (Sibson, 2003; Kuo et al., 2009; Kirkpatrick and Rowe, 2013). Pseudotachylyte formation is attributed to melting due to impact or frictional

heating (e.g., Sibson, 1975). The rate of frictional heat generation per unit area ($\dot{Q}$) is a function of frictional shear resistance (τ_f) and slip rate (v; Sibson, 1975):

$$\dot{\mathrm{Q}} = \tau_{\mathrm{f}} \times \mathrm{v} \tag{4.1}$$

$$\dot{\mathrm{Q}} = \mu_{\mathrm{k}} \times \sigma_{\mathrm{N}} \times \mathrm{v} \tag{4.2}$$

with μ_k being the coefficient of kinetic friction, a material constant, and σ_N being the normal stress on the slip plane. Assuming identical slip rates, this definition implies that for lower normal stresses, i.e., shallower depths, larger displacements have to be realised to result in frictional melting (Sibson, 1975). However, formation of amorphous material by comminution is also discussed (e.g., Wenk, 1978; Brantut et al., 2008) and in these cases there is no definitive argument that slip occurred at seismic rates. There are a few features that definitely demonstrate that frictional melting (and thus seismic slip rate) were realised, such as devitrification textures, dendritic crystallites, vesicles, spherulites and amygdales, quenched vein margins, newly crystallised minerals such as sulfide droplets, and flow structures (e.g., Magloughlin and Spray, 1992; Lin, 1994; Wenk et al., 2000; Ujiie et al., 2007). In contrast, pseudotachylytes formed by comminution do not show any of these characteristic structures (Otsuki et al., 2009, and references therein).

Amorphous material formed by frictional melting has been described in both faults and landslides. For example, fault rock samples from the San Andreas Fault, Chelungpu Fault and the Wenchuan Fault show evidence for frictional melting (Kuo et al., 2009; Janssen et al., 2010; Kuo et al., 2013; Wang et al., 2015). Borehole samples from the Taiwan Chelungpu Fault Drilling Project (TCDP) exhibit pseudotachylytes displaying typical melt structures such as vesicles and spherulites (Fig. 4.5c; Hirono et al., 2006; Kuo et al., 2009; Otsuki et al., 2009; Janssen et al., 2014). TEM analysis of ultracataclasite and gouge samples from the creeping zones of the SAFOD phase III core demonstrates the presence of amorphous material without any melt textures suggesting a crush origin (Fig. 4.5d; Janssen et al., 2010). Frictional melting in landslides is described from Langtang (Nepal) and Köfels (Austria). These landslide slip zone materials have glassy matrices (Masch et al., 1985). In some of them, the melt structures are similar to those observed in San Andreas Fault material. In both cases, clasts, mostly quartz and very rarely feldspar, are surrounded by rims of amorphous material. TEM images reveal that partial melting typically corroded these clast-surrounding rims. Finally, combining the two settings, frictional fusion due to coseismic landsliding during the 1999 Chi-Chi (Taiwan) $\mathrm{M_L}$ 7.3 earthquake resulted in the formation of pseudotachylytes on the glide plane (Lin et al., 2001).

Pseudotachylytes that demonstrably originated as glasses indicate high temperatures ($> 1000\,^{\circ}\mathrm{C}$) and were stimulated by slip at seismic rates ($> 1\,\mathrm{m\,s^{-1}}$). While boundary conditions at seismogenic depths are commonly suitable to facilitate frictional melting within faults, low ambient stresses typical for most landslide

slip zones require large displacements to cause sufficient temperature rises in order to produce frictional melts.

Clay-clast-aggregates

Clay-clast-aggregates (CCAs) are typical microstructures associated with cataclasis. These comprise (sub)rounded clasts wrapped in a cortex of concentric, aggregated, fine-grained carbonates or phyllosilicates (Fig. 4.5e; Boutareaud et al., 2008; Rempe et al., 2014). They have been observed in many fault zones around the world, such as the San Andreas Fault (Janssen et al., 2014), the Alpine Fault ("clast surrounded by 'snowballed' rim"; Warr and Cox, 2001; Schuck et al., 2018), the Chelungpu Fault (Boullier et al., 2009; Janssen et al., 2014) and the Tre Monti Fault, Italy (Smith et al., 2011). Additionally, CCAs are very common in landslide slip zones (Beutner and Craven, 1996; Anders et al., 2000; Wen and Aydin, 2004; Beutner and Gerbi, 2005; Anders et al., 2010; Schäbitz et al., 2018; Zuo et al., 2019). It has been suggested that CCA-formation is related to thermal pressurisation resulting from frictional heating during slip at seismic rates at shallow depths (Boutareaud et al., 2008; Boullier et al., 2009; Ferri et al., 2010; Ferri et al., 2011; Smith et al., 2011). CCA formation appears to not necessarily require fluids, although some of the previous work describing CCAs identified deformation processes involving fluids (Han and Hirose, 2012; Rempe et al., 2014, and references therein). Furthermore, it has been demonstrated experimentally that CCAs form over large ranges of slip rates (down to $50\,\mu m\,s^{-1}$) at low normal stresses ($\leq 5\,MPa$; Han and Hirose, 2012; Rempe et al., 2014), which relates to formation at shallow depths. Consequently, it seems reasonable to consider CCAs being a phenomenon more common in landslides than in faults.

The presence of CCAs probably reflects formation under low normal stresses (i.e., shallow depths), but does not provide any constraints on the influence of fluids during faulting and slip velocities.

4.4.1.3 Indicators of high-velocity sliding – Frictional heating recorded by trace elements

Frictional heating because of slip generates temperature peaks. While these temperature anomalies might well-exceed local background levels, they might not be sufficiently large to melt the material within and adjacent to the slip plane (e.g., Rowe and Griffith, 2015, and references therein). When fluids are present within materials of low permeability, this frictional heating may reduce the effective normal stresses, thus cause rheological weakening. This process is commonly referred to as thermal pressurisation (Sibson, 1973; Rice, 2006).

During this process, fluids are recognised to have mobilised trace elements, and thus their variation serves as proxy indicative of slip-induced temperature rises. Only certain elements are strongly affected. For example, diffusion processes leading to enrichment of Sr and depletion of Cs and Rb are strongly temperature-dependent and most effective at high temperatures, which prevents overprinting during cooling (Rowe and Griffith, 2015). Mobilisation of Li appears to result in its depletion (Ishikawa et al., 2008; Hamada et al., 2011; Honda et al., 2011), although this is not unequivocally confirmed (Yamaguchi et al., 2014).

Depth profiles across the PSZ gouge of the Chelungpu Fault display systematic variations of trace element concentrations (Figure 1 in Ishikawa et al., 2008) that suggest that pore-fluids were co-seismically heated to temperatures exceeding 350 °C, which stimulated thermal pressurisation and associated fault weakening (Ishikawa et al., 2008). Subsequently, this proxy has been successfully applied to estimate frictional heating in fault zones (Hirono et al., 2009; Hamada et al., 2011; Honda et al., 2011; Yamaguchi et al., 2014).

Geochemical data presented in Figure 4.6 suggest that this proxy could also be successfully applied to study landslides (please refer to the supplementary material for the methodological procedure and geochemical data). Investigated samples, which correspond to samples X1 - X5, X7 and X8 of Schäbitz et al. (2018), originate from the creeping Xieliupo Landslide in Northwest China (Schäbitz et al., 2018, and references therein) and represent a continuous transect across its slip surface. Results show statistically very significant ($p < 0.01$) anomalies in element concentration within and structurally immediately above the slip zone compared to the surrounding material. This suggests frictional heating was stimulated by landslide slip. In accordance with results from previous fault zone investigations Sr (Ishikawa et al., 2008; Hamada et al., 2011; Honda et al., 2011; Yamaguchi et al., 2014) and Li (Yamaguchi et al., 2014) are both enriched within the PSZ. However, in the landslides, the slip zone is also enriched in Cs and Rb.

Analyses of fault zone materials have demonstrated that characteristic variations of trace element concentrations indicate frictional heating. This approach has the potential for future applications in landslide investigations.

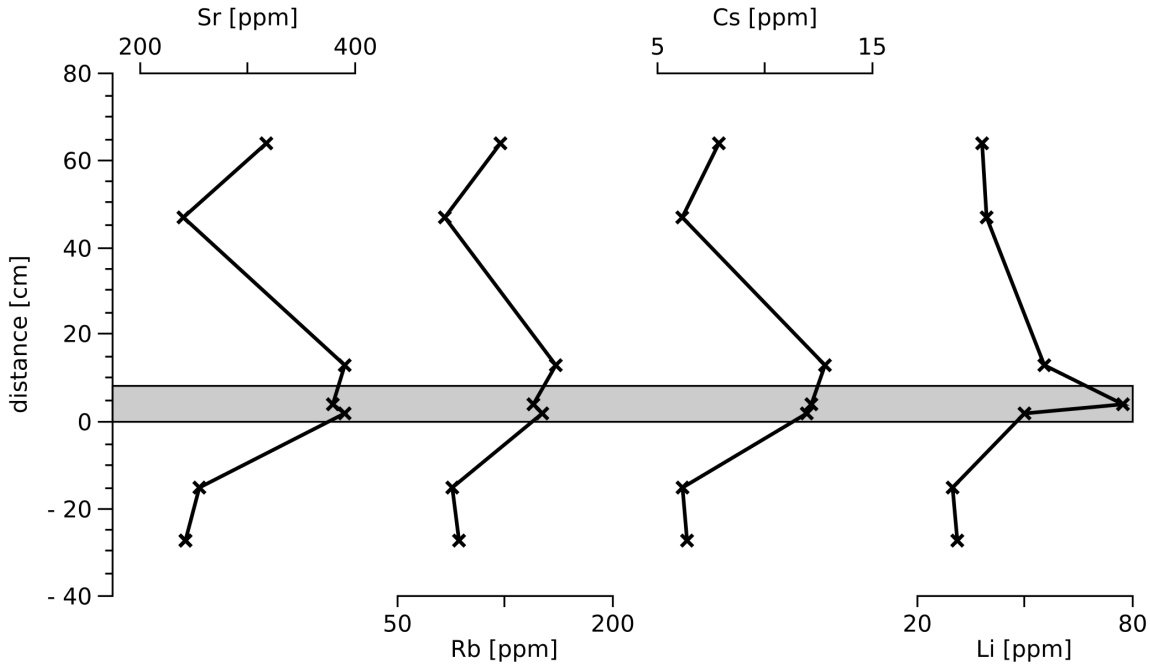

Figure 4.6: Concentration changes of selected trace elements across the slip zone of the Xieliupo Landslide (for details see supplementary material). Patterns shown statistically very significant ($p < 0.01$) anomalies related to the slip zone.

4.4.1.4 Particulate flow – recorded by clay fabrics?

Individual particles sliding along grain boundaries without fragmentation results in particulate flow (Borradaile, 1981; Porter et al., 2000). As a direct consequence of this process, elongate grains like phyllosilicates can develop strong fabrics, i.e., non-random orientations of particles (Fig. 4.7a; e.g., Lupini et al., 1981; Haines et al., 2009). Two commonly used techniques to investigate preferred orientation of phyllosilicates are X-ray texture goniometry (e.g., van der Pluijm et al., 1994; Haines et al., 2009; Schleicher et al., 2015) and synchrotron X-ray diffraction (e.g., Wenk et al., 2008; Buatier et al., 2012; Janssen et al., 2016). Since clays are important constituents of slip zones (see Section 4.3.1), we should gain new insight into the mechanical behaviour of faults and landslides by investigating the relationship between clay fabric and rheology. However, there is controversy surrounding the influence of clay fabric on overall mechanical strength (cf. Haines et al., 2009, and references therein). Some investigations have concluded that strong fabrics are associated with high strengths of slip zones (e.g., Chiou et al., 1991), others have associated strong fabrics with low strengths (e.g., Mitchell and Soga, 2005). It would be valuable to clarify these associations more rigorously.

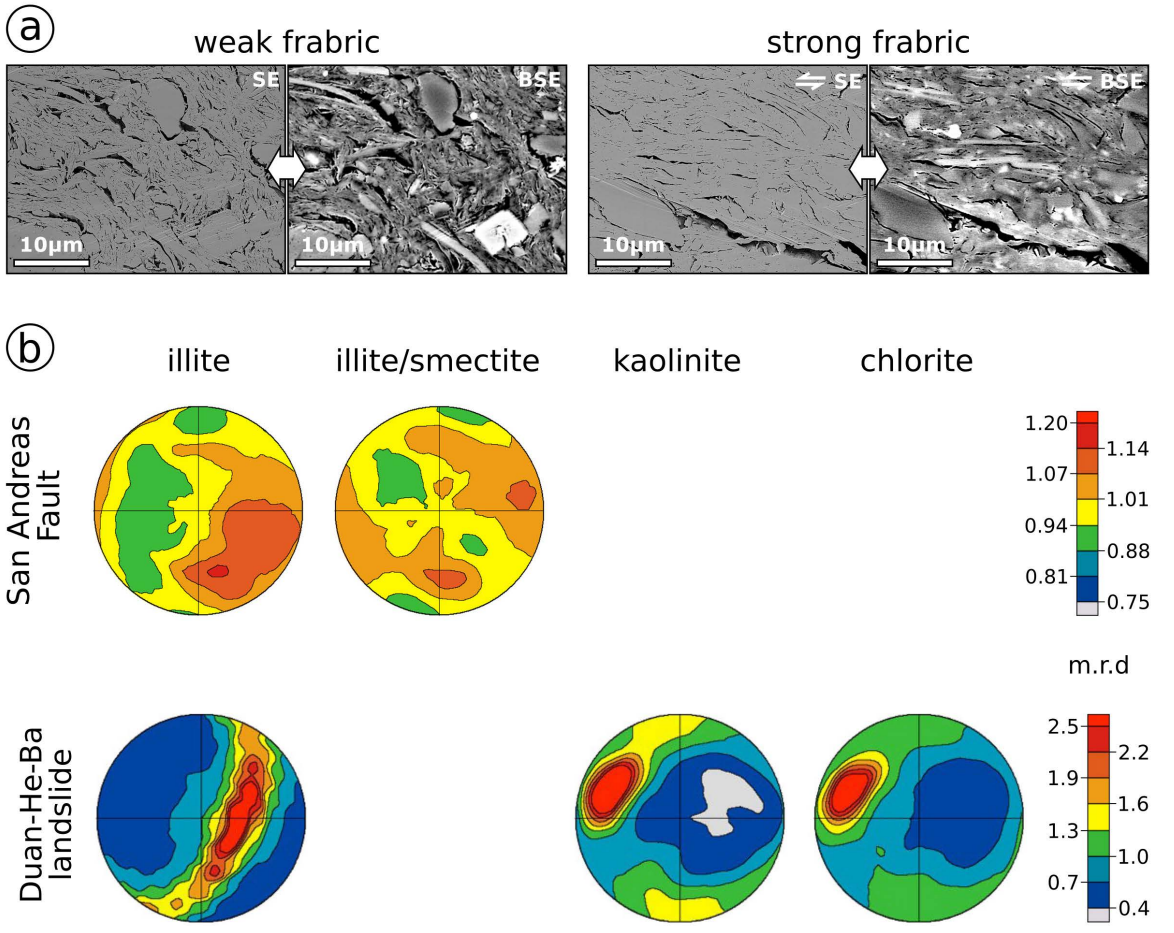

Figure 4.7: (a) Pores, highlighted by secondary electron (SE) and corresponding backscatter electron (BSE) images, as proxy of orientation of phyllosilicates within Boom Clay. Whereas, undeformed samples (left) have weak fabrics, phyllosilicate fabrics within the shear zone of deformed samples are strong (right). For details see Schuck et al. (2015). **(b)** (001) pole figures for fabric analyses of clay phases using high-resolution synchrotron X-ray diffraction. Fault gouge samples from the San Andreas Fault Observatory at Depth have weak fabrics (for details see Janssen et al., 2012). This contrasts fabrics of the slip zone of the Duang-He-Ba Landslide (for details see Schäbitz et al., 2018), which are strong. Equal area projection; contours in multiples of random distribution (m.r.d.).

Analyses of various faults including major plate-bounding fault zones such as Alpine Fault (Schleicher et al., 2015), Chelungpu Fault (Janssen et al., 2014), Carboneras Fault (Spain; Solum and van der Pluijm, 2009), Gulf of Corinth (Janssen et al., 2016), and San Andreas Fault (Schleicher et al., 2009; Janssen et al., 2014) indicate that phyllosilicate-rich fault slip zones typically have poorly developed fabrics irrespective of tectonic regime (Fig. 4.7b; Solum et al., 2005; Haines et al., 2009; Wenk et al., 2010; Buatier et al., 2012). Nevertheless, these fault rocks are texturally distinct from other phyllosilicate-rich rocks like shales and schists (Haines et al., 2009; Wenk et al., 2010). Additionally, there is no correlation between mineral composition and fabric intensity (Haines et al., 2009). Instead, the weak clay fabrics typical of fault slip zones mostly form by authigenic growth of phyllosilicates into open pore space during the interseismic period, which seems to cause weak clay fabrics of fault slip zones (Haines et al., 2009; Schleicher et al., 2009; Schleicher et al., 2015). Consequently, mechanically weak faults might not be related to anisotropic mineral fabrics but rather to the presence of small amounts of fine-grained phyllosilicates forming interconnected weak layers promoting slip (Collettini et al., 2009a; Collettini et al., 2009b; Schleicher et al., 2010; Haines et al., 2013).

Most investigations of fabrics in landslide slip zones have relied on microscopic analyses to qualify phyllosilicate orientations (e.g., Chen et al., 2014) and only a few studies report (semi)quantitative results (e.g., Wen and Aydin, 2003; Wen and Aydin, 2004; Kawamura et al., 2007; Schäbitz et al., 2018). Landslide slip zone fabrics are strong and characterised by aligned (Fig. 4.7b; Wen and Aydin, 2003; Wen and Aydin, 2004; Wen and Aydin, 2005; Chen et al., 2014; Schäbitz et al., 2018) or imbricated particles (Kawamura et al., 2007). Mechanisms that have been proposed to result in development of observed strong fabrics range from sedimentary processes (Schäbitz et al., 2018) to particle rearrangement by particulate flow (Wen and Aydin, 2003; Wen and Aydin, 2004; Wen and Aydin, 2005; Chen et al., 2014) to syndeformational alignment during creep (Kawamura et al., 2007). It is notable that most fault zones do not have such strong fabrics. For example, the San Andreas Fault at Parkfield demonstrably experiences aseismic creep but fault zone samples have very weak clay fabrics (Schleicher et al., 2009; Janssen et al., 2014), whereas creep is thought to have caused strong fabrics in Japanese landslides (Kawamura et al., 2007). Additionally, mineralogical composition is considered to be more important for fabric development in landslides than the amount of clay-sized particles (Wen and Aydin, 2003). This is the opposite to typical relationships observed in natural and artificial fault gouges (Haines et al., 2009). Finally, Schäbitz et al. (2018) relate strong fabrics to reduced landslide shear strength. To our knowledge and unlike to faults, weak clays forming interconnected layers and causing slip zone weakness have so far not been reported in landslides.

Unlike fault gouges, landslide slip zones show strong clay fabrics. These strong fabrics may be responsible for significant reduction of shear strengths of landslides. However, more quantitative analyses of clay fabric of these landslide slip zones are needed to confirm this relationship. Also, clay fabrics do not solely reflect grain alignment during particulate flow, as strong fabrics might be subsequently overprinted by authigenic processes.

4.4.2 Diffusive mass transfer – pressure solution

Diffusive mass transfer results in the removal, transportation and deposition of material. In the brittle regime at sub-metamorphic conditions, this process occurs predominantly via fluid-assisted diffusion along grain boundaries, in a process commonly known as pressure solution (Fig. 4.3). This mechanism does not require fragmentation, lattice distortion or melting of mineral phases (Blenkinsop, 2000; Fossen, 2016). Typical microstructures of pressure solution are indented and embayed clasts, and seams of relatively insoluble opaque minerals (Fig. 4.8a; Blenkinsop, 2000; Gratier et al., 2013). Furthermore and in addition to the presence of frictionally weak mineral phases (see Section 4.3.1), pressure-solution is one important mechanism promoting creep (e.g., Gratier et al., 2011).

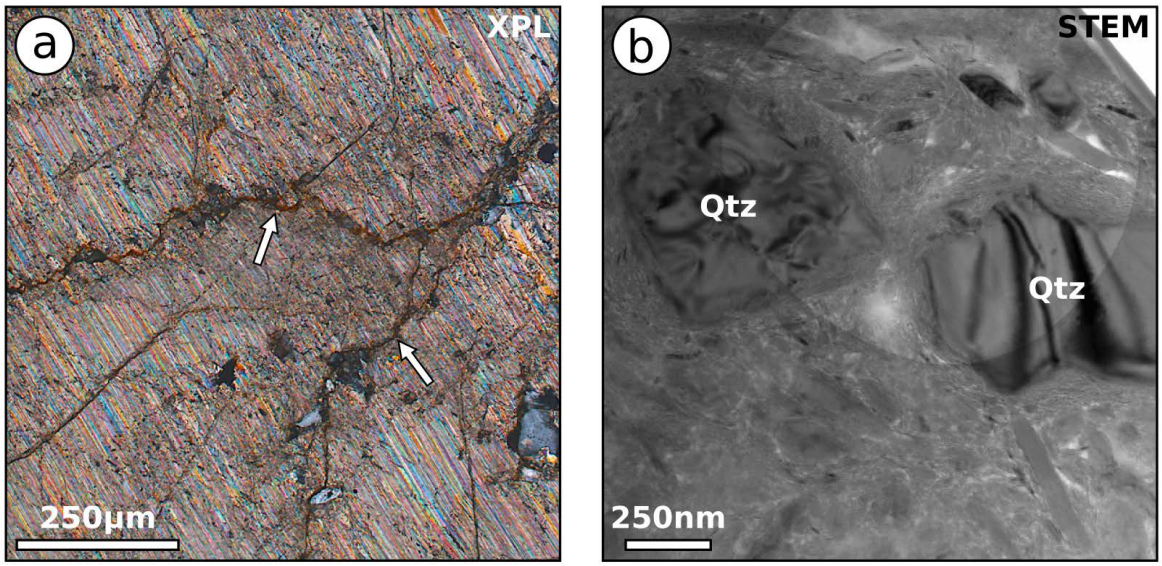

Figure 4.8: (a) Deformation twins in calcite from the San Andreas Fault Observatory at Depth. White arrows highlight dissolution seams. Figure from Janssen et al. (2014). **(b)** Two quartz grains (Qtz) with higher (left) and lower (right) dislocation densities. Grains are embedded in the pulverised matrix of the principal slip zone of the Alpine Fault. For details see Schuck et al. (2018). XPL: crossed-polarised light; TEM - BF: transmission electron microscopy - bright field.

Pressure solution is especially recognised in carbonate-hosted faults such as the Maggio Fault (Italy) and the Aigion Fault (Greece; Collettini et al., 2014; Janssen et al., 2016), but has also been reported from faults hosted in non-carbonatic protoliths such as the San Andreas Fault, the Chelungpu Fault and the Japan Trench (Fig. 4.8a; Gratier et al., 2011; Janssen et al., 2014; Janssen et al., 2015). However, in some systems, such as New Zealand's Alpine Fault - even though there is abundant evidence of a very active hydrological system - pressure solution was not an important process. Instead, the abundant fluids caused alteration of fault rocks and shallow-depth weathering leading to mineral alteration and dissolution (Barth et al., 2013; Schuck et al., 2018). However, in this system there is recognition that the absence or presence of microstructures resulting from pressure solution depends on sample location (Boulton et al., 2012; Barth et al., 2013; Toy et al., 2015; Boulton et al., 2017a; Schuck et al., 2018).

To our knowledge, there is only one example where pressure solution has been identified as an active deformation mechanism related to deformation rather than weathering by meteoric

fluids within a landslide body (Schäbitz et al., 2018). The microstructural record of pressure solution in this case was predominantly dissolution seams but some calcite and clastic grains also displayed microstructures characteristic of pressure solution assisted grain size reduction such as dissolved grain boundaries (cf. Blenkinsop, 2000). Microscopic investigations found the entire landslide body was affected by pressure solution, but that this mechanism was most important within the slip zone. Noteworthy, this mass transfer within the slip zone lead to the passive enrichment of clay minerals substantially affecting the rheology of the landslide (see also Section 4.3.2 and Gratier et al., 2013). This observation is of special importance, because this passive enrichment is also considered to be one of the main mechanisms leading to the accumulation of graphite within slip zones (Oohashi et al., 2012).

Pressure solution is distinct from fluid-related alteration processes described in Section 4.3.2, because it operates along grain boundaries and does not involve the percolation of a free fluid. However, both processes may substantially alter the mechanical properties of geomaterials.

Microstructural records of pressure solution are widely described in fault zones. Further research is necessary to assess the importance of this mechanism in landslides, as it might promote creep.

4.4.3 Crystal plastic deformation

Intracrystalline plasticity - due to dislocation creep and recovery - leads to permanent lattice distortion without brittle fracturing (Fig. 4.3). These mechanisms involve motion of dislocations leading to characteristic microstructures such as undulose extinction, twins, subgrains, deformation lamellae, kink bands and lattice preferred orientations (Fig. 4.8; Blenkinsop, 2000; Passchier and Trouw, 2005).

Microstructures indicative of intracrystalline plasticity such as undulose extinction due to the presence of dislocations, and deformation twins, record permanent lattice distortions that relieved elastic strain (and thus stresses) during deformation (e.g., de Bresser, 1996; Rybacki et al., 2011, and references therein). Dauphiné twins in quartz grains encountered in numerous fault rocks are thought to indicate high differential stresses associated with seismic and aseismic deformation (e.g., Wenk et al., 2011; Janssen et al., 2014; Janssen et al., 2015). Stresses at the San Andreas Fault's creeping Parkfield segment have been quantified by using deformation twin and dislocation densities, respectively, of calcite (Rybacki et al., 2011), a phase also encountered in landslides (e.g., Anders et al., 2010). To our knowledge, microstructures resulting from intracrystalline plasticity have so far not been used to estimate stresses achieved in landslides.

Paleo-piezometers using microstructures related to intracrystalline plasticity appear promising to access the state of stress of landslides providing insights into boundary conditions of failure.

4.5 Conclusions

Boundary conditions, such as ambient pressures and temperatures, for slip along fault planes and landslide rupture surfaces are only comparable for the shallowest portions of faults, where

ruptures originating at seismogenic depths propagate to the surface. Nonetheless, we have shown that comparable deformation mechanisms operate in both faults and landslides and result in identical, characteristic microstructures. Similar mineral compositions, potentially affected by fluid-related alteration processes, are one of the major controls on this rheological behaviour dominated by cataclastic processes. However, poorly consolidated soils and sediments in combination with low normal stresses typical for landslides promote dilation in favour of fracturing and associated particle comminution and vein formation, which both require higher stresses.

Fault investigations profit from a broad range of methodological concepts enabling the microstructural, mineralogical and geochemical characterisation of these structures. Landslide studies could profit from this integrated approach, especially where it provides strategies to indirectly access past deformation processes, such as frictional heating by trace element analysis. Furthermore, methods commonly employed for fault investigations, such as the analysis of clay fabrics within slip zones, could be used to quantitatively examine landslide characteristics. This is of special interest as comparisons of fabric analyses of creeping faults and landslides so far have provided contradictory results, demonstrating the necessity for further investigations. Conversely, landslide analysis could provide insights to understand complex fault deformation processes such as creep. Combining common approaches from fault and landslide analyses could improve our understanding of these important geohazards.

4.6 Acknowledgements

We are grateful to Andrea Gottsche and Heike Rothe for trace element analyses by XRF and ICP-MS, respectively. Discussions with Virginia Toy and Georg Dresen helped to substantially improve the manuscript.

5 Discussion and Conclusions - Rheology of exposed slip zones: lessons from Alpine Fault gouge analyses

5.1 Architecture and dominating deformation mechanisms along the Alpine Fault Zone

Reed (1964) provided the first comprehensive description of Alpine Fault rocks. By conducting extensive field work along strike of the fault zone, Sibson et al. (1979) were able to compile a schematic composite section through the Alpine Fault Zone (Fig. 5.1). The section shows Alpine Schists in the SE succeeded by mylonites and cataclasites juxtaposed to granitic footwalls in the NW. There is general agreement that this composite depicts the fault rock sequence at depth (e.g., Townend et al., 2009; Toy et al., 2015; Toy et al., 2017). Furthermore, this sequence is considered to record progressive ductile deformation from undeformed schist to proto- and ultramylonites overprinted by brittle mechanisms producing cataclasites (e.g., Sibson et al., 1979; Warr and Cox, 2001; Boulton et al., 2012; Toy et al., 2015). However, in their schematic section Sibson et al. (1979) do not describe progressive brittle deformation manifested by a transition from cataclasites to fault gouge towards the footwall. Instead, gouge zones are considered to cross-cut fault rocks formed under ductile conditions. In this, the composite of Sibson et al. (1979) differs substantially from the fault rock sequence of Norris and Cooper (2007, Fig. 2.2c), which is based on subsequent work (Norris and Cooper, 2007, and references therein). Generally accepted (e.g., Townend et al., 2009; Toy et al., 2015; Williams et al., 2016), this fault rock sequence considers a fault gouge unit to constitute the fault's PSZ juxtaposing hanging and footwall-rocks.

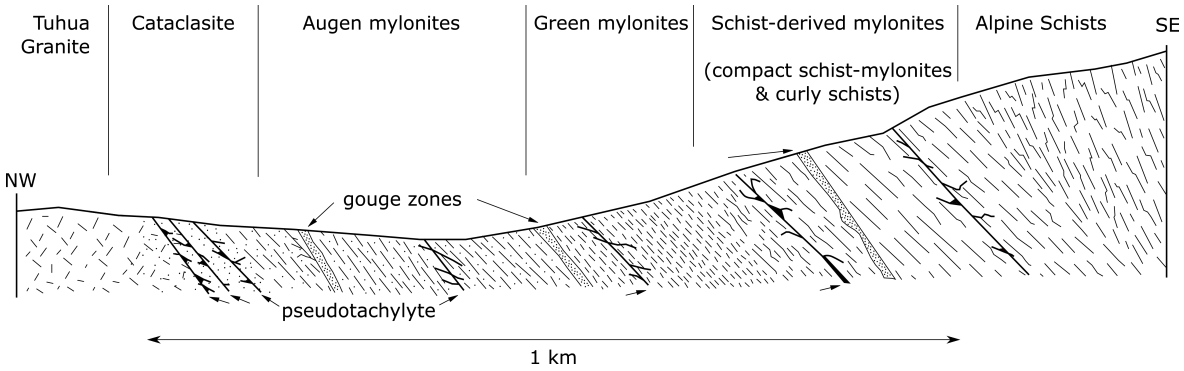

Figure 5.1: Composite section through the Alpine Fault Zone by Sibson et al. (1979).

Warr and Cox (2001) constrained the onset of brittle deformation producing cataclasites to a depth between 6 and 12 km. Meteoric fluids percolating down to 6 km depth (Menzies et al., 2016) enabled subsequent hydrous chloritisation at temperatures below 320 °C and associated reaction weakening (Warr and Cox, 2001). Smectites found in exposed fault gouges lead to suggestions that reaction weakening became even more pronounced once uplift resulted in ambient temperatures low enough to allow formation of smectite particles (i.e., < 120 °C; Warr and Cox, 2001; Boulton et al., 2012; Schleicher et al., 2015). However, it is debatable if pT-conditions were suitable to enable smectite formation in sufficient amounts to affect fault rock rheology (Schuck et al., 2018, Section 3.6.3). In addition to reaction weakening, progressive comminution of cataclasites produced frictionally weaker fault gouges (Boulton et al., 2012).

The results of the studies presented in Chapters 2 and 3 indicate we need to re-examine the existing paradigm that the Alpine Fault is a geometrically relatively simple structure as suggested by the schematic cross sections of Sibson et al. (1979) and Norris and Cooper (2007). Chapter 2 particularly reveals this paradigm does not describe the complexity of this fault zone in its full extent. It has been demonstrated that within the Alpine Fault Zone variations in deformation mechanisms, differing mineralogy or heterogeneities in the stress field – aspects commonly considered responsible for fault zone complexities elsewhere – cannot adequately explain observed along-strike variations in fault gouge thickness and associated fault zone geometry (see Section 2.6.3.2 and references therein).

The natural environment complicates exploration of the geometric relationships of proposed multiple slip planes hosted within the Alpine Fault's relatively narrow core (Fig. 2.2). Outcrops are at the north-western boundary of the Southern Alps, where topography rises from sea level to elevations of more than 3,700 m within ~30 km, fostering abundant orogenic rainfall and associated dense vegetation as well as rapid erosion yielding thick footwall Quaternary sedimentary sequences (Cooper and Norris, 1994; Norris and Cooper, 1997, and references therein).

It appears reasonable to assume that the more complex geometry of the Alpine Fault Zone as proposed in Section 2.6.3.2 following the conceptual model of Faulkner et al. (2003, Fig. 2.1b) is associated with brittle deformation, hence the shallower portions of the fault. Seismic imaging demonstrated deformation at depth is accommodated by a 100 km wide shear zone rooted in the mantle (Stern et al., 2001; Little et al., 2005; Norris and Toy, 2014).

The results presented in Chapter 2 not only have direct implications for understanding of the Alpine Fault's geometry, but may also allow better characterisation of the seismic hazard the fault poses. Paleoseismic investigations based on offset of Quaternary features indicate that some Alpine Fault earthquakes rupture to the surface along strike distances of up to ~600 km, generating lateral displacements of up to 9 m (Sutherland et al., 2007; Nicol et al., 2016). These surface ruptures and associated co-seismic landslides present a substantial hazard to infrastructure (roads, buildings; Robinson, 2018). Displacements of Alpine Fault earthquakes accommodated simultaneously by multiple slip zones may be smaller compared to displacements accommodated along a single slip zone. Consequently, while local adverse site-effects could be smaller, the area affected by surface ruptures could be larger having

substantial implications for hazard mitigation, as this would require larger fault avoidance zones, buffer zones that most likely accommodate significant deformation (Langridge et al., 2011).

Chapter 3 comprises a detailed investigation of microstructures across the Alpine Fault gouge at a single location and interpretation of the deformation mechanisms by which they were generated. Comparison of microstructural, geochemical and mineralogical results presented in this chapter (Fig. **??**; Tabs. 3.1 & 3.2) with data provided in Chapter 2 (Fig. 2.8; Tabs. 2.1 - 2.5) demonstrates that along-strike variations are insignificant. This consequently implies that it is valid to assume cataclastic, i.e., brittle, mechanisms dominate not only at Waikukupa Thrust but most likely along-strike of the entire Alpine Fault Zone. Chapter 3, also demonstrates that factors substantially controlling the rheology of the Alpine Fault operate on different time-scales. For example, principal slip zone strength is regained in the interseismic period both gradually, by quasi-static authigenic formation of phyllosilicates (mostly chlorite) and rapidly by transient, co-seismic fragmentation and rapid healing by calcite. Evidence is also presented for significant fluid-related alteration along the entire fault zone, which varies in intensity between individual locations (Figs. 2.9 & 3.8; Tabs. 2.6 & 3.4). In this system, the almost complete absence of evidence of pressure-solution processes (Fig. 3.7; Sections 3.5.1, 3.6.1 & 3.6.3) is somewhat surprising. Admittedly, pressure-solution should not easily occur in the fault gouge because, at least in the interseismic period, it is impermeable (Sections 3.6.2 & 3.6.3). However, there are no observations that explain why this process should not be active in the more permeable hanging wall (Boulton et al., 2012; Carpenter et al., 2014).

5.2 How does the Alpine Fault compare to other plate-bounding transform faults?

In some respects the Alpine Fault and other plate-bounding transverse faults such as the San Andreas Fault (SAF) or the North Anatolian Fault Zone are similar. For example they all have accommodated large displacements, fail regularly in $M_W > 7$ earthquakes and all post significant societal and / or economic hazard to the local population (Eguchi et al., 1998; Sahin and Tari, 2000; Toppozada et al., 2002; Sutherland et al., 2007; Bohnhoff et al., 2016). However, there are some fundamental differences in intrinsic properties such as fault strike, mineralogical composition, and magnitude and orientation of stresses in the surrounding rock mass. In the Alpine Fault Zone these aspects are relatively uniform along-strike, which helps earthquakes to rupture the entire fault (Sutherland et al., 2007; Boese et al., 2012; Barth et al., 2013; Warren-Smith et al., 2017, see also Chapter 2).

The major differences between the Alpine Fault and the SAF are variability of fault orientation and mineralogy, as well as differing deformation mechanisms along-strike of the SAF. This fault is composed of several closely associated, active and inactive structures that extend for 1,200 km along the West Coast of California and form the splintered boundary between the Pacific Plate and the North American Plate (Crowell, 1979; Ben-Zion and Sammis, 2003). Individual segments of this system display large variations in fault geometry,

mineralogy and deformation mechanisms (e.g., Chester and Logan, 1986; Chester et al., 1993; Faulkner et al., 2003; Zoback et al., 2011). The constituent Punchbowl Fault and the North Branch of the San Gabriel Fault are relatively narrow structures (15 to 100 m wide) displaying strong internal strain gradients (Chester and Logan, 1986; Chester et al., 1993), the creeping segment of the SAF at Parkfield is wider (~200) and has several 1 - 2 m wide discrete zones of low seismic velocities and resistivities (Holdsworth et al., 2011; Zoback et al., 2011). Mineralogy is the main difference between these segments. The Punchbowl Fault and North Branch of the San Gabriel Fault have both phyllosilicate-rich fault gouges, and dominantly quartzofeldspathic compositions like their protoliths (Chester and Logan, 1986; Chester et al., 1993), creeping fault strands and surrounding host rocks at Parkfield are phyllosilicate-rich (e.g., Solum et al., 2006; Schleicher et al., 2010; Holdsworth et al., 2011). The SAF fault zone width is fundamentally influenced by different mineralogies, particularly different amounts of frictionally weak phyllosilicates that control the overall geomechanical behaviour, i.e., seismic vs. aseismic stress release, of individual segments of the SAF system (Schleicher et al., 2010; Lockner et al., 2011).

The 1,200 km long, E-W-trending North Anatolian Fault Zone is relatively narrow (a few hundreds of meters wide) in the East (Bozkurt, 2001) but splays to the West into three major branches with complex geometry (e.g., Janssen et al., 2009) resulting in a total width of ~130 km (Barka and Kadinsky-Cade, 1988). This broadening is related to the transition along strike to an extensional tectonics regional stress field related to the rollback of the Hellenic trench (Parke et al., 2002; Flerit et al., 2004; Bohnhoff et al., 2016). Conversely, in the Alpine Fault, it is unlikely that the relatively uniform stress field along the fault causes variations in fault zone architecture (e.g., Boese et al., 2012; Warren-Smith et al., 2017).

5.3 Investigating exposed slip zones

It is difficult to deconvolve shallow deformation processes from those operating at seismogenic depth, because microstructures, mineralogy and related geomechanical properties evolve along the exhumation path changing any record of initial rock properties that might have been responsible for early strain localisation (Segall and Pollard, 1983; Ben-Zion and Sammis, 2003; Biegel and Sammis, 2004; Faulkner et al., 2008; Fossen and Cavalcante, 2017).

This is exemplified by the results presented in this study (see Chapters 2 & 3), which deals with outcrops of material actively exhumed from seismogenic depths within the last 10 Myr (Stern et al., 2001; Little et al., 2005), hence over broad stress and possibly temperature ranges. This implies a variety of different deformation mechanisms operated, each generating unique microstructures that overprinted preceding ones (Passchier and Trouw, 2005). This does not only imply that deduced deformation mechanisms might reflect boundary conditions only representative for shallow depths (see below and Section 2.6.3.2), but also that it could be impossible to identify structures and the underlying processes associated with seismogenic depths.

Furthermore, the serial partitioning into oblique thrust segments linked by subvertical right-lateral faults down to a maximum depth of about ~1 - 2 km (Norris and Cooper, 1995;

Barth et al., 2012) imparts a complex 3D structure to the fault zone. In addition, structural features within the weak sediments and the large variations in topography cause local stress perturbations at shallow depths (Norris and Cooper, 1995; Faulkner et al., 2006; Barth et al., 2012) adding further complexity to the fault zone structure close to and at the surface. However, the stress field at earthquake nucleation depths might not be affected by these variations in topography (Boese et al., 2012).

Seismic investigations and ground penetrating radar (GPR) would be powerful tools to unravel the 3D subsurface geometry of the Alpine Fault with high resolution. However, because of the required flat topography and sparse vegetation, these studies are usually conducted in areas where the hanging wall is, like most of the footwall, covered by several tens or even a few hundred meters of poorly-consolidated Quaternary sediments (Kaiser et al., 2009; Carpentier et al., 2012; Lay et al., 2016; Lukács et al., 2018). Consequently, these studies usually image only shallow fault zone structures such as multiple fault strands within mechanically weak Holocene sediments and do not provide any information on the basement structures (Sibson, 2003; Kaiser et al., 2009; Carpentier et al., 2012). The Alpine Fault Zone is subject to high amounts of annual rainfall (Norris and Cooper, 1997, and references therein) leading to substantial alteration of both microstructures and mineral composition of exposed fault rocks paving the way to misidentification of governing material properties and associated rheological characteristics. Furthermore, the dense vegetation along the north-western side of the Southern Alps further limits access to outcrops and thus complicates investigations of the Alpine Fault's geometry.

The results of this study (see Chapters 2 & 3) highlight further obstacles to fault zone investigations based on exposed slip planes. There is some evidence of dissolution of grains (e.g., Figs. 2.6 & 3.3) implying fluid-assisted mass removal. However, there is little other evidence of pressure-solution processes (Sections 3.5.1, 3.6.1 and 3.6.3) suggesting that grain dissolution results from weathering of exposed rocks rather than from wet diffusion along grain boundaries (cf. Blenkinsop, 2000). Other evidences that shallow processes may bias the ability to infer geomechanical processes that operated at depth in the Alpine Fault are frictionally weak smectite phases encountered in fault gouges at shallow depth or in outcrops (e.g., Warr and Cox, 2001; Boulton et al., 2012; Boulton et al., 2017b) and layered fault gouges (Figs. 2.4 & 2.10; Boulton et al., 2012).

Smectite has low peak and steady-state friction coefficient, so its presence at shallow depth would result in overall mechanical weakening, potentially promoting aseismic stress-release, as is well known from the Parkfield segment of the San Andreas Fault (Schleicher et al., 2010; Lockner et al., 2011). However, other datasets indicate that the Alpine Fault is seismically locked and regularly fails in large earthquakes (Beavan et al., 2007; Sutherland et al., 2007; Wallace et al., 2007; Beavan et al., 2010), thus reaction weakening due to smectite growth is insignificant. In addition to these macroscopic observations, Section 3.6.3 demonstrates by microstructural evidence that the extremely high geothermal gradients of up to $125\,^{\circ}\,km^{-1}$ (Sutherland et al., 2017) and exhumation from seimogenic depths imply temperature conditions adverse for smectite formation. Furthermore, the impermeable nature of the fault gouge and the consequently geochemically closed system it constitutes would - even if temperature

conditions were favourable - hamper smectite growth. Taking all these considerations into account, it is evident the observed smectites form at shallow depth.

It is more difficult to attribute meso- and microstructural complexity exhibited by layered fault gouges to shallow-depth conditions not representative of the vast majority of the rock record. The interpretation of Cowan et al. (2003) adapted for the kinematic regime of the Alpine Fault (Section 2.6.3.2), which relates complex gouge geometries to shallow-depth interaction of weak sediments with stronger fault gouges, is plausible.

It is debatable if fluid pressure variations during (along strike heterogeneous) formation of calcite networks (Section 3.6.2) imply that fluid pressure variations triggered earthquakes at these locations, which subsequently ruptured the entire fault (Sibson, 1985; Sibson, 1992a). However, the calcite veins present a rheological discontinuity that could stimulate further slip (Ben-Zion and Sammis, 2003; Ben-Zion, 2008; Wibberley et al., 2008; Virgo et al., 2013). A few experiments indicate that calcite-bearing gouges from the central Alpine Fault may indeed be weaker than gouges without calcite, but further studies are certainly required (Boulton et al., 2012; Boulton et al., 2017a).

While these examples from a specific case study clearly show how investigations of fault zone rheology might be biased by shallow-depth processes, Chapter 4 widens and generalises the scope of this thesis by reviewing factors controlling geomechanical properties and deformation behaviour of both fault and landslide slip zones, the latter of which are substantially affected by near surface processes. Weathering and associated fluid-related changes to mineralogical composition, hence geomechanical properties, are well-known alteration processes in landslides (see Section 4.3.2). Furthermore, landslides are more susceptible to changes of effective stresses driven by fluid pressure variations, because of their typically low normal stresses, promoting either slow (creep) or catastrophic failure (see Section 4.3.1 and references therein). Consequently, comparing slip zones of landslides and fault zones allows to better understand how subaerial alteration processes and deformation under low confining pressures modify fault rock records of processes active at greater depths. Conversely, studies investigating landslides can profit from commonly deployed approaches to analyse fault zones. If boundary conditions and deformation processes within landslides could be characterised entirely, it is worth to consider using these structures as natural analogues to study deformation processes known to exist at deeper crustal level, but not yet understood such as slow-slip events.

Chapters 2 and 3 in combination with the discussion above support the main conclusion of Chapter 4, namely that the plethora of studies aiming to characterise fault zones and the broad range of methodological concepts commonly deployed should be applied in landslides as well because they provide valuable strategies to investigate landslide deformation processes and the hazard they pose.

6 Outlook

Chapters 2 and 3 provide a geomechanical and petrological characterisation of the Alpine Fault's slip plane based on a holistic approach combining microstructural, mineralogical and geochemical analyses of exposed fault rocks. However, this characterisation is biased by shallow-depth processes. Furthermore, active exhumation, hence progressive overprint of structures formed at seismogenic depths, limits the insights to be gained by investigations of exposed Alpine Fault rocks. Obviously, this can be overcome by sampling the Alpine Fault at depths where the influence of superficial processes is minimised or negligible so that properties imposed at seismogenic depths will be conserved. Phase 2 of the Deep Fault Drilling Project (DFDP-2) was one attempt to obtain samples of the Alpine Fault Zone that are less affected by weathering than outcrop samples (Townend et al., 2009), but failed to penetrate the fault plane (Toy et al., 2017). While aiming for another approach to drill the fault zone at depth will heavily depend on funding to be raised for expensive drilling operations, the influence of structures originating from mechanical layering on fault gouge investigations can be minimised by aiming to sample the slip plane at locations, where it juxtaposes hard-rock hanging to hard-rock footwall (Fig. 2.2). However, there is lack of outcrops exposing contacts of hard-rocks (Townend et al., 2009).

In light of these restrictions resulting from active exhumation, and associated destruction of microstructures and artefacts originating from non-representative shallow-depth processes presented here, further proxies, insensitive to cataclastic processes, could aid to better constrain the fault zone architecture of the Alpine Fault: pseudotachlytes are a well-known feature of the Alpine Fault Zone, commonly attributed to frictional melting as a result of seismic slip (e.g., Sibson et al., 1979; Toy et al., 2011). Encountered in all hanging and footwall units and most extensively present in the cataclasites, pseudotachylytes are absent in the fault gouge (Sibson et al., 1979; Toy et al., 2011). This absence in the fault gouge is expected, given that Alpine Fault pseudotachlytytes commonly display various stages of devitrification and alteration (Sibson et al., 1979; Toy et al., 2011) and that associated fluid-assisted alteration processes are most strongly pronounced in this unit (Sections 2.5.4 & 2.6.1). Nonetheless, by assuming that Alpine Fault gouges accommodated most strain, variations of trace element concentrations (see Section 4.4.1.3) should indirectly provide evidence of high temperatures due to frictional sliding. However, preliminary results based on geochemical analyses presented in Table S6.1 do not provide clear indications of pronounced geochemical anomalies within the fault gouge attributed to high temperatures (Fig. S6.1). Consequently, a re-evaluation of samples investigated in Chapters 2 and 3 with respect to concentrations of Cs, Li, Rb and Sr could provide further insights into the fault zone architecture of the Alpine Fault: if preliminary results will be confirmed, it could imply that fault gouges accommodate less

strain or that strain is less localised than previously expected. Furthermore, it could question the interpretation of Alpine Fault gouges as principal slip zones.

As already indicated in Section 2.7, dating fault gouges at individual locations along-strike (Ring et al., 2017) could help to clarify, if gouge formation at individual sites occurred simultaneously, and whether large earthquakes rupture the entire Alpine Fault or at least individual sections entirely (Sutherland et al., 2007; Howarth et al., 2018, and references therein).

Supplementary material to Chapter 2

Table S2.1: Data used for isocon analysis (see Figure 2.9) of structural units of the outcrops investigated in this study as well as derived isocon slopes (m) and mass gains. Data for structural units (hanging wall; PSZ; footwall) are averages calculated from data presented in Table 2.5.

location	unit	MnO	P_2O_5	TiO_2	Na_2O	K_2O	CaO	MgO	Fe_2O_3[a]	Al_2O_3	SiO_2	LOI	m	mass gain [%]
Alpine Schist[b]	host rock	0.09	0.16	0.66	3.27	2.75	2.02	1.63	4.48	15.35	67.20	2.01		
Brook Street Terrane[c]	host rock	0.18	0.13	0.84	2.39	0.59	11.16	7.67	10.37	15.14	47.80	3.74		
Havelock Creek	PSZ	0.13	0.20	0.81	1.77	1.39	7.85	4.20	6.49	13.60	51.70	11.49	0.78	27.40
Gaunt Creek	PSZ	0.13	0.19	0.76	1.94	3.27	6.78	3.64	6.66	13.43	51.40	11.38	0.78	28.07
	footwall	0.11	0.21	0.79	2.10	2.94	5.22	3.67	6.05	13.92	55.35	9.28	0.84	19.70
DFDP-1A	hanging wall	0.09	0.16	0.63	1.18	3.50	4.49	3.07	4.75	13.31	55.51	13.02	0.84	19.72
	PSZ	0.06	0.18	0.56	1.29	3.80	2.03	2.12	4.00	13.25	62.62	9.71	0.93	7.37
Waikukupa Thrust	hanging wall	0.12	0.10	0.67	3.52	0.42	4.16	3.84	6.29	13.30	57.65	9.53	0.87	15.58
	PSZ	0.21	0.14	0.65	1.12	1.95	17.53	2.70	5.67	11.41	44.47	13.74	0.68	47.02
	footwall	0.11	0.15	0.81	3.03	1.82	2.47	2.74	6.12	14.75	64.98	2.74	0.97	3.22
Martyr River	hanging wall	0.11	0.18	0.69	2.27	1.80	8.74	4.50	6.11	13.45	52.67	8.96	1.05	- 4.44
	PSZ	0.10	0.14	0.56	2.09	1.55	3.50	10.59	5.99	11.07	56.61	7.34	1.09	- 8.54

[a] Fe_2O_3 is total Fe content.

[b] Alpine Schist data is average from (i) samples from DFDP-2B drill cuttings ICDP5052EXGY601, ICDP5052EXOY601 and ICDP5052EXLY601 (presented in Table 4 of Toy et al., 2017; (ii) samples from the Whitcombe River area (presented in Table 1 of Roser and Cooper, 1990; (iii) samples from the Big Bluff drillcore (presented in Table 2 of Roser and Cooper, 1990; except for sample 45591, which has an unusual composition); (iv) samples from the Franz Josef – Fox Glacier area (presented in Grapes et al., 1982.

[c] Values presented are averages derived from Table 1 in Spandler et al. (2005) and exclude data from Bluff Complex and Takitimu Mountains.

Table S2.2: Enrichment (positive values) or depletion (negative values) (%) of individual elements with regard to fault rock units at locations studied. Data are averages calculated from data presented in Table 2.6.

location	unit	MnO	P_2O_5	TiO_2	Na_2O	K_2O	CaO	MgO	Fe_2O_3[a]	Al_2O_3	SiO_2	LOI
Havelock Creek	PSZ	94.85	65.08	55.91	-31.00	-35.68	395.11	228.83	84.44	12.86	-1.98	629.70
Gaunt Creek	PSZ	98.89	52.93	47.97	-23.97	52.11	329.87	186.48	90.26	12.03	-2.03	626.44
	footwall	52.05	57.04	43.80	-23.26	27.66	209.11	170.12	61.67	8.56	-1.41	454.19
DFDP-1A	hanging wall	30.72	27.58	16.60	-57.33	52.86	194.04	135.07	29.61	4.05	-1.20	726.69
	PSZ	-26.74	22.07	-8.06	-57.62	48.18	7.90	39.87	-4.20	-7.34	0.05	419.42
Waikukupa Thrust	hanging wall	64.97	-26.90	17.53	24.26	-82.46	138.77	171.91	61.83	0.11	-0.83	455.16
	PSZ	281.26	34.50	44.46	-50.56	4.37	1263.34	144.54	86.67	9.35	-2.81	912.78
	footwall	37.22	0.31	26.31	-4.30	-31.77	26.22	73.80	40.91	-0.83	-0.18	41.14
Martyr River	hanging wall	-43.42	26.05	-21.40	-9.39	189.57	-25.18	-43.95	-43.67	-15.12	5.29	128.73
	PSZ	-49.46	-1.42	-39.56	-20.16	138.65	-71.32	26.24	-47.15	-33.13	8.31	79.31

[a] Fe_2O_3 is total Fe content.

Supplementary material to Chapter 3

Table S3.1: Peak area of identified major mineral phases calculated with the open-access software "MacDiff". Number in brackets give analysed peak. "Plagioclase" refers to either the 002-peak of albite or the 004-peak of anorthite. "Mica" comprises the 10 Å peak of muscovite, biotite and illite, which cannot be distinguished in oriented mounts. See Figure 3.2 for sample location.

	sample	**quartz (101)**	**calcite (104)**	**plagioclase**	**chlorite (001)**	**chl (002) / kln (001)**	**chl (002) / kln (001) (heated)**	**mica**
	11.1	212.725	66.130	150.936	4.467	28.610	11.737	6.218
HW	11.2	140.829	111.313	84.574	5.431	34.119	17.182	8.040
	10.2	126.067	128.855	68.263	3.075	24.110	8.678	9.333
	10.1	116.104	68.105	36.996	2.007	14.912	3.284	5.458
	9.2	96.698	53.989	41.955	4.588	20.284	7.657	10.620
	9.1	130.976	82.982	49.511	7.155	20.544	7.248	9.618
Gouge	1.1	86.482	191.061	24.277	0	5.656	0	7.041
	3.1	75.517	205.921	19.449	0	5.079	0	0
	5.1	72.690	207.263	18.622	0	9.307	4.026	5.193
	1.2	78.005	212.553	21.711	0	5.888	0	3.620
	3.2	159.515	36.078	112.418	9.229	59.390	29.472	34.883
	8	219.533	0	76.514	25.305	142.646	94.445	38.788
	6.2	250.874	0	107.273	5.099	30.118	1.686	32.164
FW	2	355.777	0	137.874	0	4.022	0	46.161
	7.1	285.339	0	103.276	8.790	54.736	17.740	1699.630
	7.2	149.199	95.855	69.373	8.128	40.091	7.046	88.710
	4	205.117	31.845	117.390	6.543	41.002	21.249	69.495

HW: hanging wall; FW: footwall.

Table S3.2: Acid treatment procedure for ICP-OES analyses.

#	treatment	temperature	duration	agents
1	heating	160 °C	at least 12 hrs	de-ionised water, 2 ml HF (50 %), 2 ml aqua regia (HNO_3: 70 %; HCl: 37 %)
2	adding			1 ml $HClO_4$ (70 %)
3	evaporation	185 °C		
4	adding			2 ml de-ionised water, 1 ml HNO_3 (70 %)
5	evaporation	185 °C		
6	heating	100 °C	at least 12 hrs	5 ml de-ionised water, 1 ml HNO_3 (70 %)
7	evaporation	185 °C		
8	repetition #1 – #5			
9	adding			50 ml de-ionised water, 1 ml HNO_3 (70 %)

Supplementary material to Chapter 4

Methodological procedure to analyse variations in trace element composition in landslide samples from Schäbitz et al., 2018

Samples X1 – X5, X7 and X8 from Schäbitz et al. (2018) originate from the Xieliupo landslide (China).

Variations in element composition have been investigated by X-ray fluorescence (XRF; Rb, Sr) and high-resolution sector field mass spectrometry using inductively coupled plasma as ion source (HR-ICP-MS; Cs, Ls).

For XRF analyses 1 g dry (105 °C for > 12 h) bulk rock powder was fusion digested with 6 g $LiBO_2$ and ~0.6 g oxidising agent (NH_4NO_3) using increasing temperatures from 400 °C to 1150 °C. Analyses were performed with a PANalytical AXIOS Advanced spectrometer (Tab. S4.1).

For HR-ICP-MS analyses 125 mg dry bulk rock powder was subjected to several acid treatments before element composition was conducted using an ELEMENT 2XR HR-ICP-MS calibrated with the SCO-1 standard (Tab. S4.1; Govindaraju, 1994).

Table S4.1: Results of geochemical analyses.

sample no	distance to base of slip zone [cm]	Cs [ppm]	Li [ppm]	Rb [ppm]	Sr [ppm]
X1	64	7.9	38	121	317
X2	47	6.2	39	83	241
X3	13	13	55	160	390
X5	4	12	77	143	380
X4	2	12	50	150	391
X7	- 15	6.2	30	88	256
X8	- 27	6.4	31	92	243

P-values (Tab. S4.2) to check if element peaks of (near)slip zone samples are statistically significant were determined using t-tests with the free web-application T-Test Calculator (`https://www.graphpad.com/quickcalcs/ttest1/` – accessed 2019/04/17). Values used for t-tests are listed in Table S4.2.

Table S4.2: Values (mean ± stdev) used for t-test analyses and derived p-values.

	sample no [ppm]	Cs [ppm]	Li [ppm]	Rb [ppm]	Sr [ppm]
anomaly	X3 – X5	12 ± 0.340	61 ± 11.897	387 ± 4.967	151 ± 6.976
background	X1, X2, X7, X8	7 ± 0.693	34 ± 4.231	264 ± 30.995	96 ± 14.782
p-value		0.0001	0.0077	0.0012	0.002

Supplementary material to Chapter 6

Table S6.1: Composition of selected trace elements of fault rocks from DFDP-1A and Waikukupa Thrust. Methodological procedure is outlined in Section 2.4.3.2.

sample	location	lithology	distance to PSZ [cm]	Sr [ppm]	Rb [ppm]	Ba [ppm]
120	DFDP-1A	cataclasite	292	169	220	454
119		cataclasite	270	344	93	710
118		cataclasite	135	178	215	506
117		cataclasite	87	185	155	404
116		cataclasite	25	293	146	585
115		gouge	0	180	203	405
132	Waikukupa Thrust	cataclasite	70	112	18	116
124		cataclasite	25	161	13	77
125_1		cataclasite	8	152	16	90
131_2		gouge	2	269	96	349
131_1		gouge	0	366	77	296
133		gravel	- 10	278	88	403

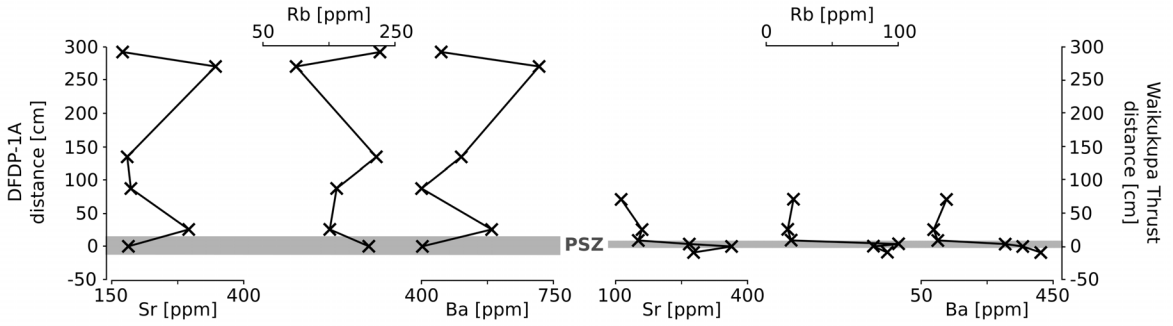

Figure S6.1: Variations in selected trace element concentrations. While there is no anomaly in DFDP-1A samples (left), concentration changes of Waikukupa Thrust (right), are less clear. This demonstrates the necessity for further investigations.

Bibliography

Aksu, A.E., Calon, T.J. and Hiscott, R.N. (2000): Anatomy of the North Anatolian Fault Zone in the Marmara Sea, Western Turkey: Extensional basins above a continental transform. GSA Today 6, pp. 3–7.

Anders, M.H., Aharonov, E. and Walsh, J.J. (2000): Stratified granular media beneath large slide blocks: Implications for mode of emplacement. Geology 28, pp. 971–974.

Anders, M.H., Fouke, B.W., Zerkle, A.L., Tavarnelli, E., Alvarez, W. and Harlow, G.E. (2010): The role of calcining and basal fluidization in the long runout of carbonate slides: An example from the Heart Mountain slide block, Wyoming and Montana, U.S.A. The Journal of Geology 118, pp. 577–599. DOI: 10.1086/656383.

Anders, M.H. and Wiltschko, D.V. (1994): Microfracturing, paleostress and the growth of faults. Journal of Structural Geology 16, pp. 795–815.

Antonellini, M. and Aydin, A. (1994): Effect of faulting on fluid flow in porous sandstones: Petrophysical properties. AAPG Bulletin 78, pp. 355–377.

Barka, A.A. and Kadinsky-Cade, K. (1988): Strike-slip fault geometry in Turkey and its influence on earthquake activity. Tectonics 7, pp. 663–684.

Barth, N.C., Toy, V.G., Langridge, R.M. and Norris, R.J. (2012): Scale dependence of oblique plate-boundary partitioning: New insights from LiDAR, central Alpine Fault, New Zealand. Lithosphere 4, pp. 435–448. DOI: 10.1130/L201.1.

Barth, N.C., Boulton, C., Carpenter, B.M., Batt, G.E. and Toy, V.G. (2013): Slip localization on the southern Alpine Fault, New Zealand. Tectonics 32, pp. 620–640. DOI: 10.1002/tect.20041.

Baudett, G., Perrotel, V., Seron, A. and Stellatelli, M. (1999): Two dimensions communition of kaolinite clay particles. Powder Technology 105, pp. 125–134.

Beaufort, D., Rigault, C., Billon, S., Billault, V., Inoue, A., Inoue, S. and Patrier, P. (2015): Chlorite and chloritization processes through mixed-layer mineral series in low-temperature geological systems – a review. Clay Minerals 50, pp. 497–523. DOI: 10.1180/claymin.2015.050.4.06.

Beavan, J., Ellis, S., Wallace, L. and Denys, P. (2007): Kinematic constraints from GPS on oblique convergence of the Pacific and Australian plates, central South Island, New Zealand. In: Okaya, D., Stern, T.A. and Davey, F. (eds.): A continental plate boundary: Tectonics at South Island, New Zealand. AGU Geophysical Monograph 175, pp. 75–94.

Beavan, J., Denys, P., Denham, M., Hager, B., Herring, T. and Molnar, P. (2010): Distribution of present-day vertical deformation across the Southern Alps, New Zealand, from 10 years of GPS data. Geophysical Research Letters 37. DOI: 10.1029/2010GL044165.

Ben-Zion, Y. and Sammis, C.G. (2003): Characterization of fault zones. Pure and Applied Geophysics 160, pp. 677–715.

Ben-Zion, Y. (2008): Collective behavior of earthquakes and faults: Continuum-discrete transitions, progressive evolutionary changes, and different dynamic regimes. Reviews of Geophysics 46. DOI: 10.1029/2008RG000260.

Bercovici, D. (2003): The generation of plate tectonics from mantle convection. Earth and Planetary Science Letters 205, pp. 107–121.

Berryman, K., Cochran, U., Clark, K., Biasi, G., Langridge, R. and Villamor, P. (2012): Major Earthquakes Occur Regularly on an Isolated Plate Boundary Fault. Science 336, pp. 1690–1693.

Beutner, E.C. and Craven, A.E. (1996): Volcanic fluidization and the Heart Mountain detachement, Wyoming. Geology 24, pp. 595–598.

Beutner, E.C. and Gerbi, G.P. (2005): Catastrophic emplacement of the Heart Mountain block slide, Wyoming and Montana, USA. BSA Bulletin 117, pp. 724–735. DOI: 10.1130/B25451.1.

Bhandary, N.P., Yatabe, R. and Takata, S. (2005): Clay minerals contributing to creeping displacement of fracture zone landslides in Japan. In: Sassa, K., Fukuoka, H., Wang, F. and Wang, G. (eds.): Landslides. Springer, pp. 219–223.

Biegel, R.L. and Sammis, C.R. (2004): Relating fault mechanics to fault zone structures. Advances in Geophysics 47, pp. 65–111.

Blenkinsop, T. (1989): Thickness-displacement relationships for deformation zones: Discussion. Journal of Structural Geology 11, pp. 1051–1054.

Blenkinsop, T. (1991): Catalcasis and processes of particle size reduction. Pure and Applied Geophysics 136, pp. 59–86.

Blenkinsop, T. (2000): Deformation microstructures and mechanisms in minerals and rocks. Kluwer Academic Publishers, Dordrecht.

Bloss, F.D. (1994): Crystallography and crystal chemistry. Mineralogical Society of America.

Boese, C.M., Stern, T.A., Michailos, K., Townend, J. and Chamberlain, C.J. (2018): Implications of upper-mantle seismicity for deformation in the continental collision zone beneath the Alpine Fault, South Island, New Zealand. New Zealand Journal of Geology and Geophysics 61, pp. 283–308. DOI: 10.1080/00288306.2018.1509357.

Boese, C.M., Townend, J., Smith, E. and Stern, T. (2012): Microseismicity and stress in the vicinity of the Alpine Fault, central southern Alps, New Zealand. Journal of Geophysical Research 117. DOI: 10.1029/2011JB008460.

Bohnhoff, M., Martínez-Garzón, P., Bulut, F., Stierle, E. and Ben-Zion, Y. (2016): Maximum earthquake magnitudes along different sections of the North Anatolian Fault Zone. Tectonophysics 674, pp. 147–165. DOI: 10.1016/j.tecto.2016.02.028.

Bohnhoff, M., Wollin, C., Domigall, D., Küpperkoch, L., Martínez-Garzón, P., Kwiatek, G. and Malin, P.E. (2017): Repeating Marmara Sea earthquakes: indication for fault creep. Geophysical Journal International 210, pp. 332–339. DOI: 10.1002/2015GL066478.

Bons, P.D., Elburg, M.A. and Gomez-Rivas, E. (2012): A review of the formation of tectonic veins and their microstructures. Journal of Structural Geology 43, pp. 33–62. DOI: 10.1016/j.jsg.2012.07.005.

Borradaile, G.J. (1981): Particulate flow of rock and the formation of cleavage. Tectonophysics 72, pp. 305–321.

Boullier, A.-M., Yeh, E.-C., Boutareaud, S., Song, S.-R. and Tsai, C.-H. (2009): Microscale anatomy of the 1999 Chi-Chi earthquake fault zone. Geochemistry, Geophysics, Geosystems 10, pp. 17–37. DOI: 10.1029/2008GC002252.

Boullier, A.-M. (2011): Fault-zone geology: lessons from drilling through the Nojima and Chelungpu Faults. In: Fagereng, Å., Toy, V.G. and Rowland, J.V. (eds.): Geology of the earthquake source: A volume in honour of Rick Sibson. Geological Society London, Special Publications 359, pp. 17–37. DOI: 10.1144/SP359.2.

Boulton, C., Carpenter, B.M., Toy, V. and Marone, C. (2012): Physical properties of surface outcrop cataclastic fault rocks, Alpine Fault, New Zealand. Geochemistry, Geophysics, Geosystems 13, pp. 238–265. DOI: 10.1029/2011GC003872.

Boulton, C., Moore, D.E., Lockner, D.A., Toy, V.G., Townend, J. and Sutherland, R. (2014): Frictional properties of exhumed fault gouges in DFDP-1 cores, Alpine Fault. Geophysical Research Letters 41, pp. 356–362. DOI: 10.1002/2013GL058236.

Boulton, C., Menzies, C.D., Toy, V.G., Townend, J. and Sutherland, R. (2017a): Geochemical and microstructural evidence for interseismic changes in fault zone permeability and strength, Alpine Fault, New Zealand. Geochemistry, Geophysics, Geosystems 18, pp. 238–265. DOI: 10.1002/2016GC006588.

Boulton, C., Yao, L., Faulkner, D.R., Townend, J., Toy, V.G., Sutherland, R., Ma, S. and Shimamoto, T. (2017b): High-velocity frictional properties of Alpine Fault rocks: mechanical data, microstructural analysis and implications for rupture propagation. Journal of Structural Geology 97, pp. 71–92. DOI: 10.1016/j.jsg.2017.02.003.

Boutareaud, S., Calugaru, D.-G., Han, R., Fabbri, O., Mizoguchi, K., Tsutsumi, A. and Shimamoto, T. (2008): Clay-clast aggregates: a new textural evidence for seismic fault sliding? Geophysical Research Letters 35. DOI: 10.1029/2007GL032554.

Bozkurt, E. (2001): Neotectonics of Turkey - a synthesis. Geodinamica Acta 14, pp. 3–30. DOI: 1029/2008JB006254.

Bradbury, K.K., Evans, J.P., Chester, J.S., Chester, F.M. and Kirschner, D.L. (2011): Lithology and internal structure of the San Andreas Fault at depth based on characterization of Phase 3 whole-rock core in the San Andreas Fault Observatory at Depth (SAFOD) borehole. Earth and Planetary Science Letters 310, pp. 131–144. DOI: 10.1016/j.epsl.2011.07.020.

Bradbury, K.K., Colter, R.D., Shervais, J.W., Janecke, S.U. and Evans, J.P. (2015): Composition, alteration, and texture of fault-related rocks from SAFOD core and surface outcrop analogs: evidence for deformation processes and fluid-rock interaction. Pure and Applied Geophysics 172, pp. 1053–1078. DOI: 10.1007/s00024-014-0896-6.

Brantut, N., Schubnel, A., Rouzaud, J.-N., Brunet, F. and Shimamoto, T. (2008): High-velocity frictional properties of a clay-bearing fault gouge and implications for earthquake mechanics. Journal of Geophysical Research 113. DOI: 10.1029/2007JB005551.

Brodsky, E., Gilchrist, J., Sagy, A. and Collettini, C. (2011): Faults smooth gradually as a function of fault slip. Earth and Planetary Science Letters 302, pp. 185–193.

Bruhn, R.L., Parry, W.T., Yonkee, W.A. and Thompson, T. (1994): Fracturing and hydrothermal alteration in normal fault zones. Pure and Applied Geophysics 142, pp. 609–644.

Buatier, M.D., Chauvet, A., Kanitpanyacharoen, W., Wenk, R., Ritz, J.F. and Jolivet, M. (2012): Origin and behavior of clay minerals in the Bogd fault gouge, Mongolia. Journal of Structural Geology 34, pp. 77–90. DOI: 10.1016/j.jsg.2011.10.006.

Bürgmann, R. and Dresen, G. (2008): Rheology of the lower crust and upper mantle: Evidence from rock mechanics, geodesy and field observations. Annual Reviews of Earth and Planetary Sciences 36, pp. 531–567. DOI: 10.1146/annurev.earth.36.031207.124326.

Byerlee, J. (1978): Friction of rocks. Pure and Applied Geophysics 116, pp. 615–626.

Caine, J.S., Evans, J.P. and Forster, C.B. (1996): Fault zone architecture and permeability structure. Geology 24, pp. 1025–1028.

Carpenter, B.M., Kitajima, H., Sutherland, R., Townend, J., Toy, V.G. and Saffer, D.M. (2014): Hydraulic and acoustic properties of the active Alpine Fault, New Zealand: Laboratory measurements on DFDP-1 drill core. Earth and Planetary Science Letters 390, pp. 45–51. DOI: 10.1016/j.epsl.2013.12.023.

Carpenter, B.M., Saffer, D.M. and Marone, C. (2015): Composition, alteration, and texture of fault-related rocks from SAFOD core and surface outcrop analogs: evidence for deformation processes and fluid-rock interaction. Pure and Applied Geophysics 172, pp. 5273–5289. DOI: 10.1002/2015JB011963.

Carpentier, S.F.A., Green, A.G., Langridge, R., Boschetti, S., Doetsch, J., Abächerli, A.N., Horstmeyer, H. and Finnemore, M. (2012): Flower structures and Riedel shears at a step over zone along the Alpine Fault (New Zealand) inferred from 2-D and 3-D GPR images. Journal of Geophysical Research 117. DOI: 10.1029/2011JB008749.

Chen, J., Dai, F., Xu, L., Chen, S., Wang, P., Long, W. and Shen, N. (2014): Properties and microstructure of a natural slip zone in loose deposits of red beds, southwestern China. Engineering Geology 183, pp. 53–64. DOI: 10.1016/j.enggeo.2014.10.004.

Chester, F.M. and Logan, J.M. (1986): Implications for mechanical properties of brittle faults from observations of the Punchbowl Fault Zone, California. Pure and Applied Geophysics 124, pp. 79–106.

Chester, F.M., Evans, J.P. and Biegel, R.L. (1993): Internal structure and weakening mechanisms of the San Andreas Fault. Journal of Geophysical Research 98, pp. 771–786.

Chester, F.M., Rowe, C., Ujiie, K., Kirkpatrick, J., Regalla, C., Remitti, F., Moore, J.C., Toy, V., Wolfson-Schwehr, M., Bose, S., Kameda, J., Mori, J.J., Brodsky, E.E., Eguchi, N., Toczko, S., Expedition 343 and 343T Scientists (2013): Structure and composition of the plate-boundary slip zone for the 2011 Tohoku-Oki Earthquake. Science 342, pp. 1208–1211. DOI: 10.1126/science.1243719.

Chester, J.S., Chester, F.M. and Kronenberg, A.K. (2005): Fracture surface energy of the Punchbowl Fault, San Andreas System. Nature Letters 437, pp. 133–136. DOI: 10.1038/nature03942.

Chiou, W.A., Bryant, W.R. and Bennett, R.H. (1991): Clay fabric of gassy submarine sediments. In: Bennett, R.H., Bryant, W.R., Hulbert, M.H., Chiou, W.A., Faas, R.W., Kasprowicz, J.,

Li, H., Lomenick, T., O'Brien, N.R., Pamukcu, S., Smart, P., Weaver, C.E. and Yamamoto, T. (eds.): Microstructure of fine-grained sediments. Frontiers in Sedimentary Geology, pp. 333–352.

Cochran, U.A., Clark, K.J., Howarth, J.D., Biasi, G.P., Langridge, R.M., Villamor, P., Berryman, K.R. and Vandergoes, M.J. (2017): A plate boundary earthquake record from a wetland adjacent to the Alpine Fault in New Zealand refines hazard estimates. Earth and Planetary Science Letters 464, pp. 175–188. DOI: 10.1016/j.epsl.2017.02.026.

Collettini, C., Carpenter, B.M., Viti, C., Cruciani, F., Mollo, S., Tesei, T., Trippetta, F., Valoroso, L. and Chiaraluce, L. (2014): Fault structure and slip localization in carbonate-bearing normal faults: an example from the Northern Apennines of Italy. Journal of Structural Geology 67, pp. 154–166. DOI: 10.1016/j.jsg.2014.07.017.

Collettini, C., Niemeijer, A., Viti, C. and Marone, C. (2009a): Fault zone fabric and fault weakness. Nature 426, pp. 907–910. DOI: 10.1038/nature08585.

Collettini, C., Viti, C., Smith, S.A.F. and Holdsworth, R.E. (2009b): Development of interconnected talc networks and weakening of continental low-angle normal faults. Geology 37, pp. 567–570. DOI: 10.1130/G25645A.1.

Colten-Bradley, V.A. (1987): Role of pressure in smectite dehydration – effects on geopressure and smectite-to-illite transformation. AAPG Bulletin 71, pp. 1414–1427.

Columbus, J., Sirguey, P. and Tenzer, R. (2011): A free fully assessed 15 meter digital elevation model for New Zealand. Survey Quarterly 66, pp. 16–19.

Cooper, A.F. and Norris, R.J. (1990): Estimates for the timing of the last co-seismic displacement on the Alpine Fault, northern Fiordland, New Zealand. New Zealand Journal of Geology and Geophysics 33, pp. 303–307.

Cooper, A.F. and Norris, R.J. (1994): Anatomy, structural evolution, and slip rate of a plate-boundary thrust: The Alpine fault at Gaunt Creek, Westland, New Zealand. GSA Bulletin 106, pp. 627–633.

Cooper, A.F. and Norris, R.J. (2011): Inverted metamorphic sequences in Alpine Fault mylonites produced by oblique shear within a plate boundary fault zone, New Zealand. Geology 39, pp. 1023–1026.

Cowan, D.S., Cladouhos, T.T. and Morgan, J.K. (2003): Structural geology and kinematic history of rocks formed along low-angle normal faults, Death Valley, California. GSA Bulletin 115, pp. 1230–1248.

Cox, S.F., Etheridge, M.A. and Wall, V.J. (1986): The role of fluids in syntectonic mass transport and the localization of metamorphic vein-type ore deposits. Ore Geology Reviews 2, pp. 65–86.

Cox, S.F. (1995): Faulting processes at high fluid pressures: an example of fault valve behavior from the Wattle Gully Fault, Victoria, Australia. Journal of Geophysical Research 100, pp. 12841–12859.

Crowell, J.C. (1979): The San Andreas fault system through time. Journal of the Geological Society 136, pp. 293–302.

Cruden, D.M. and Varnes, D.J. (1996): Landslide types and processes. In: Turner, A.K. and Shuster, R.L. (eds.): Landslides: Investigation and Mitigation. Transportation Research Board, Special Report 247, pp. 36–75.

Czaplinska, D., Piazolo, S. and Zibra, I. (2015): The influence of phase and grain size distribution on the dynamics of strain localization in polymineralic rocks. Journal of Structural Geology 72, pp. 15–32. DOI: 10.1016/j.jsg.2015.01.001.

Dai, F.C., Xu, C., Yao, X., Xu, L., Tu, X.B. and Gong, Q.M. (2011): Spatial distribution of landslides triggered by the 2008 M_S 8.0 Wenchuan Earthquake, China. Journal of Asian Earth Sciences 40, pp. 883–895. DOI: 10.1016/j.jseaes.2010.04.010.

de Bresser, J.H.P. (1996): Steady state dislocation densities in experimentally deformed calcite materials: Single crystals versus polycrystals. Journal of Geophysical Research 101, pp. 22189–22201.

de Caritat, P., Hutcheon, I. and Walshe, J.L. (1993): Chlorite geothermometry: a review. Clays and Clay Minerals 41, pp. 219–239.

DeMets, C., Gordon, R.C. and Argus, D.F. (2010): Geologically current plate motion. Geophysical Journal International 181, pp. 1–80. DOI: 10.1111/j.1365-246X.2009.04491.x.

Dilley, M., Chen, R.S., Deichmann, U., Lerner-Lam, A.L. and Arnold, M. (2005): Natural disaster hotspots – a global risk analysis. The World Bank Hazard Management Unit, Washington.

Döbelin, N. and Kleeberg, R.. (2015): Profex: A graphical user interface for the Rietveld refinement program BGMN. Journal of Applied Crystallography 48, pp. 1573–1580. DOI: 10.1107/S16000576715014685.

Doblas, M., Faulkner, D., Mahecha, V., Aparicio, A., López-Ruiz, J. and Hoyos, M. (1997): Geologically current plate motion. Journal of Structural Geology 19, pp. 1045–1054.

Dolejš, D. and Manning, C.E. (2010): Thermodynamic model for mineral solubility in aqueous fluids: theory, calibration and application to model fluid-flow systems. Geofluids 10, pp. 20–40. DOI: 10.1111/j.1468-8123.2010.00282.x.

Drucker, D.C., Gibson, R.E. and Henkel, D.J. (1957): Soil mechanics and work-hardening theories of plasticity. Transactions of the American Society of Civil Engineers 122, pp. 338–346.

Duan, Q., Yang, X., Ma, S., Chen, J. and Chen, J. (2016): Fluid-rock interactions in seismic faults: implications from the structures and mineralogical and geochemical compositions of drilling cores from the rupture of the 2008 Wenchuan earthquake, China. Tectonophysics 666, pp. 260–280. DOI: 10.1016/j.tecto.2015.11.008.

Edbrooke, S.W., Hern, D.W., Forsyth, P.J. and Jongens, R. (compilers) (2015): Geological Map of New Zealand 1:1,000,000. GNS Science Geological Map 2. Lower Hut, New Zealand. GNS Science.

Eguchi, R.T., Goltz, J.D., Taylor, C.E., Chang, S.E., Flores, P.J., Johnson, L.A., Seligson, H.A. and Blais, N.C. (1998): Direct economic losses in the Northridge Earthquake: A three-year post-event perspective. Earthquake Spectra 14, pp. 245–264.

Ergintav, S., Doğan, U., Gerstenecker, C., Çakmak, R., Belgen, A., Demirel, H., Aydin, C. and Reilinger, R. (2007): A snapshot (2003 – 2005) of the 3D postseismic deformation for

the 1999, $M_W = 7.4$ Izmit earthquake in the Marmara Region, Turkey, by first results of joint gravity and GPS monitoring. Journal of Geodynamics 44, pp. 1–18. DOI: 10.1016/j.jog.2006.12.005.

Evans, J.P. (1990): Thickness-displacement relationships for fault zones. Journal of Structural Geology 12, pp. 1061–1065.

Fagereng, Å., Remitti, F. and Sibson, R.H. (2010): Shear veins observed within anisotropic fabric at high angles to the maximum compressive stress. Nature Geoscience 3, pp. 482–485. DOI: 10.1038/NGE898.

Faulkner, D.R. and Rutter, E.H. (2001): Can the maintenance of overpressured fluids in large strike-slip fault zones explain their apparent weakness? Geology 29, pp. 503–506.

Faulkner, D.R., Lewis, A.C. and Rutter, E.H. (2003): On the internal structure and mechanics of large strike-slip fault zones: field observations of the Carboneras Fault in southeastern Spain. Tectonophysics 367, pp. 235–251. DOI: 10.1016/S0040-1951(03)00134-3.

Faulkner, D.R., Mitchell, T.M., Healy, D. and Heap, M.J. (2006): Slip on 'weak' faults by the rotation of regional stress in the fracture damage zone. Nature Letters 444, pp. 922–925. DOI: 10.1038/nature05353.

Faulkner, D.R., Mitchel, T.M., Rutter, E.H. and Cembrano, J. (2008): On the structure and mechanical properties of large strike-slip faults. In: Wibberley, C.A.J., Kurz, W., Imber, J., Holdsworth, R.E. and Collettini, C. (eds.): The Internal Structure of Fault Zones: Implications for Mechanical and Fluid-Flow Properties. Geological Society, London, Special Publications 299, pp. 139–150.

Faulkner, D.R., Jackson, C.A.L., Lunn, R.J., Schlische, R.W., Shipton, Z.K., Wibberley, C.A.J. and Withjack, M.O. (2010): A review of recent developments concerning the structure, mechanics and fluid flow properties of fault zones. Journal of Structural Geology 32, pp. 1557–1575. DOI: 10.1016/j.jsg.2010.06.009.

Ferri, F., Di Toro, G., Hirose, T. and Shimamoto, T. (2010): Evidence of thermal pressurization in high-velocity friction experiments on smectite-rich gouges. Terra Nova 22, pp. 347–353. DOI: 10.1111/.1365-3121.2010.00955.x.

Ferri, F., Di Toro, G., Hirose, T., Han, R., Noda, H., Shimamoto, T., Quaresimin, M. and de Rossi, N. (2011): Low- to high-velocity frictional properties of the clay-rich gouges from the slipping zone of the 1963 Vaiont slide, northern Italy. Journal of Geophysical Research 116, pp. 347–353. DOI: 10.1029/2011JB008338.

Fialko, Y. (2006): Interseismic strain accumulation and the earthquake potential on the southern San Andreas Fault system. Nature 441, pp. 468–571. DOI: 10.1038/nature04797.

Flerit, F., Armijo, R., Kong, G. and Mayer, B. (2004): The mechanical interaction between the propagating North Anatolian Fault and the back-arc extension in the Aegean. Earth and Planetary Science Letters 224, pp. 347–362. DOI: 10.1016/j.epsl.2004.05.028.

Fossen, H. (2016): Structural Geology. 2nd edition. Cambridge University Press.

Fossen, H. and Cavalcante, G.C.G. (2017): Shear zones - A review. Earth-Science Reviews 171, pp. 434–455. DOI: 10.1016/j.earscirev.2017.05.002.

Freed, A.M., Bürgmann, R., Calais, E., Freymueller, J. and Hreinsdóttir, S. (2006): Implications of deformation following the 2002 Denali, Alaska, earthquake for postseismic relaxation

processesand lithospheric rheology. Journal of Geophysical Research 111. DOI: 10.1029/2005JB003894.

Freed, R.L. and Peacor, D.R. (1989): Variability and temperature of the smectite/illite reaction on gulf coast sediments. Clay Minerals 24, pp. 171–180.

Froude, M.J. and Petley, D.N. (2018): Global fatal landslide occurrence from 2004 to 2016. Natural Hazards of Earth System Sciences 18, pp. 2161–2181. DOI: 10.5194/nhess-18-2161-2018.

Fuis, G.S., Scheirer, D.S., Langenheim, V.E. and Kohler, M.D. (2012): A new perspective on the geometry of the San Andreas Fault in Southern California and its relationship to lithospheric structure. Bulletin of the Seismological Societiy of America 102, pp. 236–251. DOI: 10.1785/0120110041.

Fulton, P.M., Brodsky, E.E., Kano, Y., Mori, J., Chester, F., Ishikawa, T., Harris, R.N., Lin, W., Eguchi, N., Toczko, S. and Expedition 343, 343T and KR13-08 Scientists (2013): Low Coseismic Friction on the Tohoku-Oki Fault Determined from Temperature Measurements. Science 342, pp. 1214–1217. DOI: 10.1126/science.1243641.

Gardner, R., Piazolo, S., Evans, L. and Daczko, N. (2017): Patterns of strain localization in heterogeneous, polycrystalline rocks – a numerical perspective. Earth and Planetary Science Letters 463, pp. 253–265. DOI: 10.1016/j.epsl.2017.01.039.

Gomberg, J., Bodin, P., Savage, W. and Jackson, M.E. (1995): Landslide faults and tectonic faults, analogs?: The Slumgullion earthflow, Colorado. Geology 23, pp. 41–44.

Govindaraju, K. (1994): 1994 Compilation of Working Values and Sample Description for 383 Geostandards. Geostandards Newsletter 18, pp. 1–158.

Grant, J.A. (1986): The Isocon Diagram – a simple solution to Gresens' equation for metasomatic alteration. Economic Geology 81, pp. 1976–1982.

Grant, J.A. (2005): Isocon analysis: a brief review of the method and applications. Physics and Chemistry of the Earth 30, pp. 997–1004. DOI: 10.1016/j.pce.2004.11.003.

Grapes, R.H. and Watanabe, T. (1992): Metamorphism and uplift of Alpine Schist in the Franz Josef - Fox Glacier area of the Southern Alp, New Zealand. Journal of Metamorphic Geology 10, pp. 171–180.

Grapes, R.H. and Watanabe, T. (1994): Mineral composition variation in Alpine schist, southern Alps, New Zealand: implications for recrystallization and exhumation. The Island Arc 3, pp. 163–181.

Grapes, R.H., Watanabe, T. and Palmer, K. (1982): XRF analyses of quartzofeldspathic schists and metacherts, Franz Josef — Fox Glacier area, Southern Alps of New Zealand. Victoria University of Wellington Geology Department publication 25, p. 11.

Gratier, J.P. and Gamond, J.F. (1990): Transition between seismic and aseismic deformation in the upper crust. In: Knipe, R.J. and Rutter, E.H. (eds.): Deformation mechanisms, rheology and tectonics. Geological Society Special Publication 54, pp. 461–473.

Gratier, J.-P., Richard, J., Renard, F., Mittempergher, S., Doan, M.-L., Di Toro, G., Hadizadeh, J. and Boullier, A.-M. (2011): Aseismic sliding of active faults by pressure solution creep: Evidence from the San Andreas Fault Observatory at Depth. Geology 12, pp. 1131–1134. DOI: 10.1130/G32073.1.

Gratier, J.-P., Dysthe, D. and Renard, F. (2013): The role of pressure solution creep in the ductility of the Earth's upper crust. Advances in Geophysics 54. DOI: 10.1016/B978-0-12-380940-7.00002-0.

Gresens, R.L. (1967): Composition-volume relationships of metasomatism. Chemical Geology 2, pp. 47–65.

Gupta, H., Rao, N.P., Roy, S., Arora, K., Tiwari, V.M., Patro, P.K., Satyanarayana, H.V.S., Shashidhar, D., Mallika, K., Akkiraju, V.V., Goswami, D., Vyas, D., Ravi, G., Srinivas, K.N.S.S.S., Srihari, M., Mishra, S., Dubey, C.P., Raju, D.Ch.V, Borah, U., Reddy, K.C., Babu, N., Rohilla, S., Dhar, U., Sen, M., Rao, Y.J.B., Bansal, B.K. and Nayak, S. (2015): Investigations related to scientific deep drilling to study reservoir-triggered earthquakes at Koyna, India. International Journal of Earth Sciences 104, pp. 1511–1522. DOI: 10.1007/s00531-014-1128-0.

Haines, S.H. and van der Pluijm, B.A. (2008): Clay quantification and Ar–Ar dating of synthetic and natural gouge: Application to the Miocene Sierra Mazatán Detachment Fault, Sonora, Mexico. Journal of Structural Geology 30, pp. 525–538. DOI: 10.1016/j.jsg.2007.11.012.

Haines, S.H., van der Pluijm, B.A., Ikari, M.J., Saffer, D.M. and Marone, C. (2009): Clay fabric intensity in natural and artificial fault gouges: Implications for brittle fault zone processes and sedimentary basin clay fabric evolution. Journal of Geophysical Research 114. DOI: 10.1029/2008JB005866.

Haines, S.H., Kaproth, B., Marone, C., Saffer, D. and van der Pluijm, B. (2013): Shear zones in clay-rich fault gouge: A laboratory study of fabric development and evolution. Journal of Structural Geology 51, pp. 206–225. DOI: 10.1016/j.jsg.2013.01.002.

Hamada, Y., Hirono, T. and Ishikawa, T. (2011): Coseismic frictional heating and fluid-rock interaction in a slip zone within a shallow accretionary prism and implications for earthquake slip behavior. Journal of Geophysical Research 116. DOI: 10.1029/2010JB007730.

Han, R., Hirose, T. and Shimamoto, T. (2010): Strong velocity weakening and powder lubrication of simulated carbonate faults at seismic slip rates. Journal of Geophysical Research 115. DOI: 10.1029/2008JB006136.

Han, R., Hirose, T., Shimamoto, T., Lee, Y. and Ando, J.-I. (2011): Granular nanoparticles lubricate faults during seismic slip. Geology 39, pp. 599–602. DOI: 10.1130/G31842.1.

Han, R. and Hirose, T. (2012): Clay-clast aggregates in fault gouge: An unequivocal indicator of seismic faulting at shallow depth? Journal of Structural Geology 43, pp. 92–99. DOI: 10.1016/j.jsg.2012.07.008.

Handwerger, A.L., Rempel, A.W., Skarbek, R.M., Roering, J.J. and Hilley, G. E. (2016): Rate-weakening friction characterizes both slow sliding and catastrophic failure of landslides. Proceedings of the National Academy of Sciences of the United States of America 113, pp. 10281–10286. DOI: 10.1073/pnas.1607009113.

Handwerger, A.L., Roering, J.J. and Schmidt, D.A. (2013): Controls on the seasonal deformation of slow-moving landslides. Earth and Planetary Science Letters 377–378, pp. 239–247. DOI: 10.1016/j.epsl.2013.06.047.

Harbitz, C.B., Glimsdal, S., Løvholt, F., Kveldsvik, V., Pedersen, G.K. and Jensen, A. (2014): Rockslide tsunamis in complex fjords: From an unstable rock slope at Åkerneset to tsunami

risk in western Norway. Coastal Engineering 88, pp. 101–122. DOI: 10.1016/j.coastaleng.2014.02.003.

Hickman, S., Sibson, R.H. and Bruhn, R. (1995): Introduction to special section: mechanical involvement of fluids in faulting. Journal of Geophysical Research 100, pp. 12831–12840.

Highland, L.M. and Bobrowsky, P. (2008): The landslide handbook – A guide to understanding landslides. Reston, Virginia, U.S. Geological Survey Circular 1,325.

Hirono, T., Ikehara, M., Otsuki, K., Mishima, T., Sakaguchi, M., Soh, W., Omori, M., Lin, W., Yeh, E.-C., Tanikawa, W. and Wang, C.-Y. (2006): Evidence of frictional melting from disk-shaped black material, discovered within the Taiwan Chelungpu fault system. Geophysical Research Letters 33. DOI: 10.1029/2006GL027329.

Hirono, T., Ujiie, K., Ishikawa, T., Mishima, T., Hamada, Y., Tanimizu, M., Soh, W. and Kinoshita, M. (2009): Estimation of temperature rise in a shallow slip zone of the megasplay fault in the Nankai Trough. Tectonophysics 478, pp. 215–220. DOI: 10.1016/j.tecto.2009.08.001.

Hobbs, B.E., Mühlhaus, H.-B. and Ord, A. (1990): Instability, softening and localization of deformation. In: Knipe, R.J. and Rutter, E.H. (eds.): Deformation Mechanisms, Rheology and Tectonics, Geological Society Special Publication 54, pp. 143–165.

Holdsworth, R.E., van Diggelen, E.W.E., Spiers, C.J., de Bresser, J.H.P., Walker, R.J. and Bowen, L. (2011): Fault rocks from the SAFOD core samples: implications for weakening at shallow depths along the San Andreas Fault, California. Journal of Structural Geology 33, pp. 132–144. DOI: 10.1016/j.jsg.2010.11.010.

Hollingsworth, J., Ye, L. and Avouac, J.-P. (2017): Dynamically triggered slip on a splay fault in the M_W 7.8, 2016 Kaikoura (New Zealand) earthquake. Geophysical Research Letters 44, pp. 3517–3525. DOI: 10.1002/2016GL072228.

Honda, G., Ishikawa, T., Hirono, T and Mukoyoshi, H. (2011): Geochemical signals for determining the slip-weakening mechanism of an ancient magasplay fault in Shimanto accretionary complex. Geophysical Research Letters 38. DOI: 10.1029/2011GL046722.

Howarth, J.D., Cochran, U.A., Langridge, R.M., Clark, K., Fitzsimons, S.J., Berryman, K., Villamor, P. and Strong, D.T. (2018): Past large earthquakes on the Alpine Fault: paleoseismological progress and future directions. New Zealand Journal of Geology and Geophysics 61, pp. 309–328. DOI: 10.1080/00288306.2018.1464658.

Huang, R. and Li, W. (2011): Formation, distribution and risk control of landslides in China. Journal of Rock Mechanics and Geotechnical Engineering 3, pp. 97–116. DOI: 10.3724/SP.J.1235.2011.00097.

Hull, J. (1988): Thickness-displacement relationships for deformation zones. Journal of Structural Geology 10, pp. 431–435.

Ikari, M.J., Saffer, D.M. and Marone, C. (2009): Frictional and hydrologic properties of clay-rich fault gouge. Journal of Geophysical Research 114. DOI: 10.1029/2008JB006089.

Ikari, M.J., Trütner, S., Carpenter, B.M. and Kopf, A.J. (2015): Shear behavior of DFDP-1 borehole samples from the Alpine Fault, New Zealand, under a wide range of experimental conditions. International Journal of Earth Sciences 104, pp. 1523–1535. DOI: 10.1007/s00531-014-1115-5.

Ishikawa, T., Tanimizu, M., Nagaishi, K., Matsuoka, J., Tadai, O., Sakaguchi, M., Hirono, T., Mishima, T., Tanikawa, W., Lin, W., Kikuta, H., Soh, W. and Song, S.-R. (2008): Coseismic fluid-rock interactions at high temperatures in the Chelungpu Fault. Nature Geoscience 1, pp. 679–683. DOI: 10.1038/ngeo308.

Iverson, R.M., Reid, M.E., Iverson, N.R., LaHusen, R.G., Logan, M., Mann, J.E. and Brien, D.L. (2000): Acute Sensitivity of Landslide Rates to Initial Soil Porosity. Science 290, pp. 513–516. DOI: 10.1126/science.290.5491.513.

Janku-Capova, L., Sutherland, R., Townend, J., Doan, M.-L., Massiot, C., Coussens, J. and Célérier, B. (2018): Fluid flux in fractured rock of the Alpine Fault hanging-wall determined from temperature logs in the DFDP-2B borehole, New Zealand. Geochemistry, Geophysics, Geosystems 9, pp. 2631–2646. DOI: 10.1029/2017GV007317.

Janssen, C., Laube, N., Bau, M. and Gray, D.R. (1998): Fluid regime in faulting deformation of the Waratah Fault Zone, Australia, as inferred from major and minor element analyses and stable isotopic signatures. Tectonophysics 204, pp. 109–130.

Janssen, C., Bohnhoff, M., Vapnik, Y., Görgün, E., Bulut, F., Plessen, B., Pohl, D., Aktar, M., Okay, A.I. and Dresen, G. (2009): Tectonic evolution of the Ganos segment of the North Anatolian Fault (NW Turkey). Journal of Structural Geology 31, pp. 11–28. DOI: 10.1016/j.jsg.2008.09.010.

Janssen, C., Wirth, R., Reinicke, A., Rybacki, E., Naumann, R., Wenk, H.-R. and Dresen, G. (2010): Amorphous material in SAFOD core samples (San Andreas Fault): Evidence for crush-origin pseudotachylytes? Geophysical Research Letters 37. DOI: 10.1029/2009GL040993.

Janssen, C., Wirth, R., Reinicke, A., Rybacki, E., Naumann, R., Wenk, H.-R. and Dresen, G. (2011): Nanoscale porosity in SAFOD core samples (San Andreas Fault). Earth and Planetary Science Letters 301, pp. 179–189. DOI: 10.1016/j.epsl.2010.10.040.

Janssen, C., Kanitpanyacharoen, W., Wenk, H.-R., Wirth, R., Morales, L., Rybacki, E., Kienast, M. and Dresen, G. (2012): Clay fabrics in SAFOD core samples. Journal of Structural Geology 43, pp. 118–127. DOI: 10.1016/j.jsg.2012.07.004.

Janssen, C., Wirth, R., Wenk, H.-R., Morales, L., Naumann, R., Kienast, M., Song, S.-R. and Dresen, G. (2014): Faulting processes in active faults - evidences from TCDP and SAFOD drill core samples. Journal of Structural Geology 65, pp. 100–116. DOI: 10.1016/j.jsg.2014.04.004.

Janssen, C., Naumann, R., Morales, L., Wirth, R., Rhede, D. and Dresen, G. (2015): Co-seismic and/or a-seismic microstructures of JFAST 343 core samples from the Japan Trench. Marine Geology 362, pp. 33–42. DOI: 10.1016/j.margeo.2015.01.013.

Janssen, C., Wenk, H.-R., Wirth, R., Morales, L., Kemnitz, H., Sulem, J. and Dresen, G. (2016): Microstructures and their implications for faulting processes – insights from DGLab core samples from the Gulf of Corinth. Journal of Structural Geology 86, pp. 62–74. DOI: 10.1016/j.jsg.2016.03.008.

Jessell, M.W., Bons, P.D., Griera, A., Evans, L.A. and Wilson, C.J.L. (2009): A tale of two viscosities. Journal of Structural Geology 31, pp. 719–736. DOI: 10.1016/j.jsg.2009.04.010.

Kaduri, M., Gratier, J.-P., Renard, F., Çakir, Z. and Lasserre, C. (2017): The implications of fault zone transformation on aseismic creep: example of the North Anatolian Fault, Turkey. Journal of Geophysical Research: Solid Earth 122, pp. 4208–4236. DOI: 10.1002/2016JB013803.

Kaiser, A.E., Green, A.G., Campbell, F.M., Horstmeyer, H., Manukyan, E., Langridge, R.M., McClymont, A.F., Mancktelow, N., Finnemore, M. and Nobes, D.C. (2009): Ultrahigh-resolution seismic reflection imaging of the Alpine Fault, New Zealand. Journal of Geophysical Research 114. DOI: 10.1029/2009JB006338.

Kawamura, K., Ogawa, Y., Oyagi, N., Kitahara, T. and Anma, R. (2007): Structural and fabric analyses of basal slip zone of the Jin'nosuke-dani landslide, northern central Japan: its application to the slip mechanism of decollement. Landslides 4, pp. 371–380. DOI: 10.1007/s10346-007-0094-z.

Kirilova, M., Toy, V.G., Timms, N., Halfpenny, A., Menzies, C., Craw, D., Beyssac, O., Sutherland, R., Townend, J., Boulton, C., Carpenter, B.M., Cooper, A., Grieve, J., Little, T., Morales, L., Morgan, C., Mori, H., Sauer, K.M., Schleicher, A.M., Williams, J. and Craw, L. (2017): Textural changes of graphitic carbon by tectonic and hydrothermal processes in an active plate boundary fault zone, Alpine Fault, New Zealand. In: Gessner, K., Blenkinsop, T.G. and Sorjonen-Ward, P. (eds.): Characterization of ore-forming systems from geological, geochemical and geophysical studies. . Geological Society, London, Special Publications 453. DOI: 10.1144/SP453.13.

Kirilova, M. (2017): The Effects of Graphite and Porosity on the Mechanics of the Alpine Fault. PhD thesis. University of Otago, New Zealand.

Kirkpatrick, J., Shervais, K. and Ronayne, M. (2018): Spatial Variation in the Slip Zone Thickness of a Seismogenic Fault. Geophysical Research Letters 45, pp. 7542–7550.

Kirkpatrick, J.D. and Rowe, C.D. (2013): Disappearing ink: How pseudotachylytes are lost from the rock record. Journal of Structural Geology 52, pp. 183–198. DOI: 10.1016/j.jsg.2013.03.003.

Kluge, K.E., Toy, V.G., Lockner, D. and Ohneiser, C. (2017): Electrical Properties of Schist and Mylonite from the South Island, New Zealand: Exploring the Source of the Southern Alps Anomalous Conductor. Geophysical Research Abstracts 19, EGU General Assembly 2017, EGU2017–10139.

Knopf, A. (1929): The Mother Lode System of California. USGS, Professional Paper 157.

Kohlstedt, D.L., Evans, B. and Mackwell, S.J. (1995): Strength of the lithosphere: Constraints imposed by laboratory experiments. Journal of Geophysical Research 100, pp. 17587–17602.

Koster van Groos, A.F. and Guggenheim, S. (1984): The effect of pressure on the dehydration reaction of interlayer water in Na-montmorillonite (SWy-1). American Mineralogist 69, pp. 872–879.

Kremer, K., Hilbe, M., Simpson, G., Decrouy, L., Wildi, W and Girardclos, S. (2015): Reconstructing 4000 years of mass movement and tsunami history in a deep peri-Alpine lake (Lake Geneva, France-Switzerland). Sedimentology 62, pp. 1305–1327. DOI: 10.1111/sed.12190.

Kuo, L.-W., Song, S.-R., Yeh, E.-C and Chen, H.-F. (2009): Clay mineral anomalies in the fault zone of the Chelungpu Fault, Taiwan, and their implications. Geophysical Research Letters 36. DOI: 10.1029/2009GL039269.

Kuo, L.-W., Li, H., Smith, S.A.F., Di Toro, G., Suppe, J., Song, S.-R., Nielsen, S., Sheu, H.-S. and Si, J. (2013): Gouge graphitization and dynamic fault weakening during the 2008 M_W,7.9 Wenchuan Earthquake. Geology 42, pp. 47–50. DOI: 10.1130/G34862.1.

Langridge, R.M., Trayes, M. and Ries, W. (2011): Designing and implementing a Fault avoidance zone strategy for the Alpine Fault in the West Coast region. Proceedings of the Ninth Pacific Conference on Earthquake Engineering Building an Earthquake-Resilient Society 14-16 April, 2011, Auckland, New Zealand.

Laurich, B., Urai, J.L. and Nussbaum, C. (2017): Microstructures and deformation mechanisms in Opalinus Clay: insights from scaly clay from the Main Fault in the Mont Terri Rock Laboratory (CH). Solid Earth 8, pp. 27–44. DOI: 19.5194/se-8-27-2017.

Laurich, B., Urai, J.L., Vollmer, C. and Nussbaum, C. (2018): Deformation mechanisms and evolution of the microstructure of gouge in the Main Fault in Opalinus Clay in the Mont Terri Rock Laboratory (CH). Solid Earth 9, pp. 1–24. DOI: 10.5194/se-9-1-2018.

Lay, V., Buske, S., Lukács, A., Gorman, A.R., Bannister, S. and Schmitt, D.R. (2016): Advanced seismic imaging techniques characterize the Alpine Fault at Whataroa (New Zealand). Journal of Geophysical Research: Solid Earth 121, pp. 8792–8812. DOI: 10.1002/2016JB013534.

Li, H., Wang, H., Xu, Z., Si, J., Pei, J., Li, T., Huang, Y., Song, S.-R., Kuo, L.-W., Sun, Z., Chevalier, M.-L. and Liu, D. (2013): Characteristics of the fault-related rocks, fault zones and the principal slip zone in the Wenchuan Earthquake Fault Scientific Drilling Project Hole-1 (WFSD-1). Tectonophysics 584, pp. 23–42. DOI: 10.1016/j.tecto.2012.08.021.

Li, J. and Duan, Z. (2011): A thermodynamic model for the prediction of phase equilibria and speciation in the H_2O-CO_2-NaCl-$CaCO_3$-$CaSO_4$ system from 0 to 250 °C, 1 to 1000 bar with NaCl concentrations up to halite saturation. Geochimica Cosmochimica Acta 75, pp. 4351–4376. DOI: 10.1016/j.gca.2011.05.019.

Lin, A. (1994): Glassy pseudotachylyte veins from the Fuyun fault zone, northwest China. Journal of Structural Geology 16, pp. 71–83.

Lin, A., Chen, A., Liau, C.-F., Lee, C.-T., Lin, C.-C., Lin, P.-S., Wen, S.-C. and Ouchi, T. (2001): Frictional fusion due to coseismic landsliding during the 1999 Chi-Chi (Taiwan) M_L 7.3 earthquake. Geophysical Research Letters 28, pp. 4011–4014.

Lindsey, E.O., Fialko, Y., Bock, Y., Sandwell, D.T. and Bilham, R. (2014): Localized and distributed creep along the southern San Andreas Fault. Journal of Geophysical Research: Solid Earth 119, pp. 7909–7922. DOI: 10.1002/2014JB011275.

Little, T.A., Cox, S., Vry, J.K. and Batt, G. (2005): Variations in exhumation level and uplift rate along the oblique-slip Alpine Fault, central Southern Alps, New Zealand. GSA Bulletin 117, pp. 707–723. DOI: 10.1130/B25500.1.

Lockner, D.A., Morrow, C., Moore, D. and Hickman, S. (2011): Low strength of deep San Andreas Fault gouge from SAFOD core. Nature 472, pp. 82–86. DOI: 10.1038/nature09927.

Lukács, A., Gorman, A.R. and Norris, R.J. (2018): Quaternary structural and paleo-environmental evolution of the Alpine Fault near Haast, New Zealand, from 2D seismic reflection and gravity data. New Zealand Journal of Geology and Geophyics 31, pp. 181–213. DOI: 10.1080/00288306.2018.1544153.

Lupini, J.F., Skinner, A.E. and Vaughan, P.R. (1981): The drained residual strength of cohesive soils. Géotechnique 31, pp. 181–213.

Ma, K.–F., Tanaka, H., Song, S.-R., Wang, C.-Y., Hung, J.-H., Tsai, Y.-B., Mori, J., Song, Y.–F., Yeh, E.–C., Soh, W., Sone, H., Kuo, L.-W. and Wu, H.-Y. (2006): Slip zone and energetics of a large earthquake from the Taiwan Chelungpu-fault Drilling Project. Nature 444, pp. 473–475. DOI: 10.1038/nature05253.

MacKenzie, D., Farmer, L., Moore, J. and Craw, D. (2017): Contrasting coeval paragenesis of gold and scheelite in an orogenic hydrothermal system, Macraes mine, New Zealand. Ore Geology Reviews 80, pp. 645–657. DOI: 10.1016/j.oregeorev.2016.08.011.

Magloughlin, J.F. and Spray, J.G. (1992): Frictional melting processes and products in geological materials: introduction and discussion. Tectonophysics 204, pp. 197–206.

Mancktelow, N., Zwingmann, H. and Mulch, A. (2016): Timing and conditions of clay fault gouge formation on the Naxos detachment (Cyclades, Greece). Tectonics 35, pp. 2334–2344. DOI: 10.1002/2016TC004251.

Martínez-Garzón, P., Bohnhoff, M., Ben-Zion, Y. and Dresen, G. (2015): Scaling of maximum observed magnitudes with geometrical and stress properties of strike-slip faults. Geophysical Research Letters 42, pp. 10230–10238. DOI: 10.1093/gji/ggx169.

Masch, L., Wenk., H.R. and Preuss, E. (1985): Electron microscopy study of hyalomylonites - evidence for frictional melting in landslides. Tectonophysics 115, pp. 131–160.

Massiot, C., Célérier, B., Doan, M.-L., Little, T.A., Townend, J., McNamara, D.D., Williams, J., Schmitt, D.R., Toy, V.G., Sutherland, R., Janku-Capova, L., Upton, P. and Pezard, P.A. (2018): The Alpine Fault hanging-wall viewed from within: Structural analysis of ultrasonic image logs in the DFDP-2B borehole, New Zealand. Geochemistry, Geophysics, Geosystems 19, pp. 2492–2515. DOI: 10.1029/2017GC007368.

McClintock, M. and Cooper, A.F. (2003): Geochemistry, mineralogy, and metamorphic history of kyanite-orthoamphibole-bearing Alpine Fault mylonite, South Westland, New Zealand. New Zealand Journal of Geology and Geophysics 46, pp. 47–62.

Menzies, C.D., Teagle, D., Niedermann, S., Cox, S.C., Craw, D., Zimmer, M., Cooper, M.J. and Erzinger, J. (2016): Frictional strength of wet and dry montmorillonite. Earth and Planetary Science Letters 455, pp. 125–135. DOI: 10.1016/j.epsl.2016.03.046.

Miller, D.J. (1960): Giant waves in Lituya Bay, Alaska. U.S. Geological Survey Professional Paper 354-C, pp. 51–84.

Mitchell, J.K. and Soga, K. (2005): Fundamentals of Soil Behavior, 3rd edition. Wiley, New York.

Mitchel, T.M. and Faulkner, D.R. (2009): The nature and origin of off-fault damage surrounding strike-slip fault zones with a wide range of displacements: A field study from the Atacama fault system, northern Chile. Journal of Structural Geology 31, pp. 802–816.

Mitchell, T.M., Ben-Zion, Y. and Shimamoto, T. (2011): Pulverized fault rocks and damage asymmetry along the Arima-Takatsuki Tectonic Line, Japan. Earth and Planetary Science Letters 308, pp. 284–297. DOI: 10.1016/j..epsl.2011.04.023.

Mittempergher, S., Di Toro, G., Gratier, J.-P., Hadizadeh, J., Smith, S.A.F. and Spiess, R. (2011): Evidence of transient increases of fluid pressure in SAFOD phase III cores. Geophysical Research Letters 38. DOI: 10.1029/2010GL046129.

Moore, D.E., Lockner, D.A., Shengli, M., Summers, R. and Byerlee, J.D. (1997): Strength of serpentinite gouges at elevated temperatures. Journal of Geophysical Research 102, pp. 14787–14801. DOI: 10.1029/2010GL046129.

Moore, D.M. and Reynolds Jr., R.C. (1997): X-Ray Diffraction and the Identification of clay Minerals. Oxford University Press, Oxford.

Moore, D.E. and Lockner, D.A. (2007): Friction of smectite clay montmorillonite. In: Dixon, T. and Moore, C. (eds.): The Seismogenic Zone of Subduction Thrust Faults. Columbia University Press, pp. 317–345.

Moore, D.E. and Rymer, M.J. (2007): Talc-bearing serpentinite and the creeping section of the San Andreas Fault. Nature 448, pp. 795–797. DOI: 10.1038/nature06064.

Moore, D.E. and Lockner, D.A. (2008): The talc friction in the temperature range 25 ° – 400 °C: Relevance for Fault-Zone Weakening. Tectonophysics 449, pp. 120–132. DOI: 10.1016/j.tecto.2007.11.039.

Moore, D.E. and Rymer, M.J. (2012): Correlation of clayey gouge in a surface exposure of serpentinite in the San Andreas Fault with gouge from the San Andreas Fault Observatory at Depth (SAFOD). Journal of Structural Geology 38, pp. 51–60. DOI: 10.1016/j.jsg.2011.11.014.

Morgenstern, N.R. and Tchalenko, J.S. (1967): Microstructural observations on shear zones from slips in natural clays. Proceedings of the Geotechnical Conference Oslo, pp. 147–152.

Morrow, C, Radney, B. and Byerlee, J. (1992): Frictional Strength and the Effective Pressure Law of Montmorillonite and Illite Clays. In: Evans, B. and Wong, T.-F. (eds.): Fault mechanics and transport properties of rocks – A festschrift in honor of W. F. Brace. International Geophysics 51, pp. 69–88.

Morrow, C.A., Moore, D.E. and Lockner, D.A. (2017): Frictional strength of wet and dry montmorillonite. Journal of Geophysical Research: Solid Earth 122, pp. 3392–3409. DOI: 10.1002/2016JB013658.

Nakamura, Y., Oohashi, K., Toyoshima, T., Satish-Kumar, M. and Akai, J. (2015): Strain-induced amorphization of graphite in fault zones of the Hidaka metamorphic belt, Hokkaido, Japan. Journal of Structural Geology 72, pp. 142–161. DOI: 10.1016/jsg.2014.10.012.

Nardini, L., Rybacki, E., Döhmann, M.J.E.A., Morales, L.F.G., Brune, S. and Dresen, G. (2018): High-temperature shear zone formation in Carrara marble: The effect of loading conditions. Tectonophysics 749, pp. 120–139. DOI: 10.1016/j.tecto.2018.10.022.

Neuzil, C.E. (2019): Permeability of Clays and Shales. Annual Reviews of Earth and Planetary Sciences 47, pp. 247–273. DOI: 10.1146/annurev-earth-053018-060437.

Nicol, A. (2016): Alpine Fault paleoseismic record and seismic hazard analysis. In: Proceedings of the Annual Conference of the Geoscience Society of New Zealand, Nov 28 - Dec 1, 2016.

Nicol, A., Robinson, R., Van Dissen, R.J. and Harvison, A. (2016): Variability of recurrence interval and single-event slip for surface-rupturing earthquakes in New Zealand. New Zealand Journal of Geology and Geophysics 59, pp. 97–116. DOI: 10.1080/00288306.2015.1127822.

Norris, R.J. and Cooper, A.F. (1995): Origin of small-scale segmentation and transpressional thrusting along the Alpine Fault, New Zealand. GSA Bulletin 107, pp. 231–240.

Norris, R.J. and Cooper, A.F. (1997): Erosional control on the structural evolution of a transpressional thrust complex on the Alpine Fault, New Zealand. Journal of Structural Geology 19, pp. 1323–1342.

Norris, R.J. and Cooper, A.F. (2000): Late Quaternary slip rates and slip partitioning on the Alpine Fault, New Zealand. Journal of Structural Geology 23, pp. 507–520. DOI: 10.1002/2016JB013658.

Norris, R.J. and Cooper, A.F. (2003): Very high strains recorded in mylonites along the Alpine Fault, New Zealand: Implications for the deep structure of plate boundary faults. Journal of Structural Geology 25, pp. 2141–2157.

Norris, R.J. and Cooper, A.F. (2007): The Alpine Fault, New Zealand: Surface geology and field relationships. In: Okaya, D., Stern, T.A. and Davey, F. (eds.): A continental plate boundary: Tectonics at South Island, New Zealand. AGU Geophysical Monograph 175, pp. 157–175.

Norris, R.J. and Toy, V.G. (2014): Continental transforms: A view from the Alpine Fault. Journal of Structural Geology 64, pp. 3–31. DOI: 10.1016/j.jsg.2014.03.003.

Nuriel, P., Rosenbaum, G., Zhao, J.-X., Feng, Y., Golding, S.D., Villemant, B. and Weinberger, R. (2012): U-Th dating of striated fault planes. Geology 40, pp. 647–650. DOI: 10.1016/j.jsg.2011.12.010.

Oohashi, K., Hirose, T. and Shimamoto, T. (2011): Shear-induced graphitization of carbonaceous materials during seismic fault motion: Experiments and possible implications for fault mechanics. Journal of Structural Geology 33, pp. 1122–1134. DOI: 10.1016/j.jsg.2011.01.007.

Oohashi, K., Hirose, T., Kabayashi, K. and Shimamoto, T. (2012): The occurrence of graphite-bearing fault rocks in the Atotsugawa fault system, Japan: Origins and implications for fault creep. Journal of Structural Geology 38, pp. 39–50. DOI: 10.1016/j.jsg.2011.10.011.

Oohashi, K., Hirose, T. and Shimamoto, T. (2013): Graphite as lubricating agent in fault zones: An insight from low- to high-velocity friction experiments on a mixed graphite-quartz gouge. Journal of Geophysical Research 188, pp. 2067–2084. DOI: 10.1002/jgrb.50175.

Otsuki, K., Hirono, T., Omori, M., Sakaguchi, M., Tanigawa, W., Lin, W., Soh, W. and Rong, S.-S. (2009): Analyses of pseudotachylyte from Hole-B of Taiwan Chelungpu Fault Drilling Project (TCDP); their implications for seismic slip behaviors during the 1999 Chi-Chi earthquake. Tectonophysics 469, pp. 13–24. DOI: 10.1016/j.tecto.2009.01.008.

Parke, J.R., White, R.S., McKenzie, D., Minshull, T.A., Bull, J.M., Kuşçu, I., Görür, N. and Sengör, C. (2002): Interaction between faulting and sedimentation in the Sea of Marmara, western Turkey. Journal of Geophysical Research 107. DOI: 10.1029/2001JB000450.

Passchier, C.W. and Trouw, R.A.J. (2005): Microtectonics. 2nd edition. Springer.

Peacock, D.C.P., Nixon, C.W., Rotevatn, A., Sanderson, D.J. and Zuluaga, L.F. (2016): Glossary of fault and other fracture networks. Journal of Structural Geology 92, pp. 12–29. DOI: 10.1016/j.jsg.2016.09.008.

Pennacchioni, G. and Mancktelow, N.S. (2007): Nucleation and initial growth of a shear zone network within compositionally and structurally heterogeneous granitoids under amphibolite facies conditions. Journal of Structural Geology 29, pp. 1757–1780. DOI: 10.1016/j.jsg.2007.06.002.

Pesaresi, M., Ehrlich, D., Kemper, T., Siragusa, A., Florczyk, A.J., Freire, S. and C., Corbane (2017): Atlas of the human planet 2017: Global exposure to natural hazards. DOI: 10.2760/19837.

Pollastro, R.M. (1993): Considerations and applications of the illite/smectite geothermometer in hydrocarbon-bearing rocks of Miocene to Mississippian age. Clays and Clay Minerals 41, pp. 119–133. DOI: 10.1346/CCMN.1993.0410202.

Porter, J.R., Knipe, R.J., Fisher, Q.J., Farmer, A.B., Allin, N.S., Jones, L.S., Palfrey, A.J., Garrett, S.W. and Lewis, G. (2000): Deformation processes in the Britannia Field, UKCS. Petroleum Geoscience 6, pp. 241–254.

Preuth, T., Glade, T. and Demoulin, A. (2010): Stability analysis of a human-influenced landslide in eastern Belgium. Geomorphology 120, pp. 38–47. DOI: 10.1016/geomorph.2009.09.013.

Raub, C., Martínez-Garzón, P., Kwiatek, G., Bohnhoff, M. and Dresen, G. (2017): Variations of seismic b-value at different stages of the seismic cycle along the North Anatolian Fault Zone in northwestern Turkey. Tectonophysics 712–713, pp. 232–248. DOI: 10.1016/j.tecto.2017.05.028.

Reed, J.J. (1964): Myonites, cataclasites, and associated rocks along the Alpine Fault, South Island, New Zealand. New Zealand Journal of Geology and Geophysics 7, pp. 645–684. DOI: 10.1080/00288306.1964.10428124.

Regmi, A.D., Yoshida, K., Dhital, M.R. and Devkota, K. (2013a): Effect of rock weathering, clay mineralogy, and geological structures in the formation of large landslide, a case study from Dumre Besei landslide, Lesser Himalaya Nepal. Landslides 10, pp. 1–13. DOI: 10.1007/s10346-011-0311-7.

Regmi, A.D., Nagata, K.Y.H., Pradhan, A.M.S., Pradhan, B. and Pourghasemi, H.R. (2013b): The relationship between geology and rock weathering on the rock instability along Mugling–Narayanghat road corridor, Central Nepal Himalaya. Natural Hazards 66, pp. 501–532. DOI: 10.1007/s11069-012-0497-6.

Rempe, M., Smith, S.A.F., Ferri, F., Mitchell, T.M. and Di Toro, G. (2014): Clast-cortex aggregates in experimental and natural calcite-bearing fault zones. Journal of Structural Geology 68, pp. 142–157. DOI: 10.1016/j.jsg.2014.09.007..

Rice, J.R. (1992): Fault stress states, pore pressure distributions, and the weakness of the San Andreas Fault. In: Evans, B. and Wong, T.-F. (eds.): Fault mechanics and transport properties of rocks – A festschrift in honor of W. F. Brace. International Geophysics 51, pp. 475–503.

Rice, J.R. (2006): Heating and weakening of faults during earthquake slip. Journal of Geophysical Research 111. DOI: 10.1029/2005JB004006.

Ring, U., Uysal, I.T., Glodny, J., Cox, S.C., Little, T., Thomson, S.N., Stübner, K. and Bozkaya, Ö. (2017): Fault-gouge dating in the Southern Alps, New Zealand. Tectonophysics 717, pp. 321–338. DOI: 10.1016/j.tecto.2017.08.007.

Robinson, T.R. (2018): Road impacts from the 2016 Kaikõura earthquake: an analogue for a future Alpine Fault earthquake? New Zealand Journal of Geology and Geophysics. DOI: 10.1080/00288306.2018.1470539.

Roscoe, K.H., Schofield, A.N. and Wroth, C.P. (1958): On the yielding of soils. Géotechnique 8, pp. 22–53.

Roser, B.P. and Cooper, A.F. (1990): Geochemistry and terrane affiliation of Haast schist from the western southern Alps, New Zealand. New Zealand Journal of Geology and Geophysics 33, pp. 1–10. DOI: 10.1080/00288306.1990.10427567.

Rowe, C.D. and Griffith, W.A. (2015): Do faults preserve a record of seismic slip: A second opinion. Journal of Structural Geology 78, pp. 1–26. DOI: 10.1016/j.jsg.2015.06.06.

Rybacki, E., Wirth, R. and Dresen, G. (2008): High-strain creep of feldspar rocks: Implications for cavitation and ductile failure in the lower crust. Geophysical Research Letters 35. DOI: 10.1029/2007GL032478.

Rybacki, E., Janssen, C., Wirth, R., Chen, K., Wenk, H.-R., Stromeyer, D. and Dresen, G. (2011): Low-temperature deformation in calcite veins of SAFOD core samples (San Andreas Fault) – microstructural analysis and implications for fault rheology. Tectonophysics 509, pp. 107–119. DOI: 10.1016/j.tecto.2011.05.014.

Rybacki, E., Evans, B., Janssen, C., Wirth, R. and Dresen, G. (2013): Influence of stress, temperature, and strain on calcite twins constrained by deformation experiments. Tectonophysics 601, pp. 20–36. DOI: 10.1016/j.tecto.2013.04.021.

Rybacki, E., Morales, L.F.G., Naumann, M. and Dresen, G. (2014): Strain localization during high temperature creep of marble: The effect of inclusions. Tectonophysics 634, pp. 182–197. DOI: 10.1016/j.tecto.2014.07.032.

Saffer, D.M., Frye, K.M., Marone, C. and Mair, K. (2001): Laboratory results indicating complex and potentially unstable frictional behavior of smectite clay. Geophysical Research Letters 28, pp. 2297–2300.

Sagy, A. and Brodsky, E. (2009): Geometric and rheological asperities in an exposed fault zone. Journal of Geophysical Research 114. DOI: 10.1029/2008JB005701.

Sahin, M. and Tari, E. (2000): The August 17 Kocaeli and the November 12 Düzce earthquakes in Turkey. Earth Planets Space 52, pp. 753–757. DOI: 10.1016/j.tecto.2011.05.014.

Sammis, C., King, G. and Biegel, R. (1987): The Kinematics of Gouge Deformation. Pure and Applied Geophysics 125, pp. 777–812.

Sammis, C.G. and Ben-Zion, Y. (2008): Mechanics of grain-size reduction in fault zones. Journal of Geophysical Research 113. DOI: 10.1029/2006JB004892.

Schäbitz, M., Janssen, C., Wenk, H.-R., Wirth, R., Schuck, B., Wetzel, H.-U., Meng, X. and Dresen, G. (2018): Microstructures in landslides in northwest China – Implications for

creeping displacements? Journal of Structural Geology 106, pp. 70–85. DOI: 10.1016/j.jsg.2017.11.009.

Schindelin, J., Arganda-Carreras, I., Frise, E., Kaynig, V., Longair, M., Pietzsch, T., Preibisch, S., Rueden, C., Saalfeld, S., Schmid, B., Tinevez, J.-Y., White, D.J., Hartenstein, V., Eliceiri, K., Tomancak, P. and Cardona, A. (2012): Fiji: an open-source platform for biological-image analysis. Nature methods 9, pp. 676–682.

Schleicher, A.M., Tourscher, S.N., van der Pluijm, B.A. and Warr, L.N. (2009): Constraints on mineralization, fluid-rock interaction, and mass transfer during faulting at 2 – 3 km depth from the SAFOD drill hole. Journal of Geophysical Research 114. DOI: 10.1029/2008JB006092.

Schleicher, A.M., van der Pluijm, B.A. and Warr, L.N. (2010): Nanocoatings of clay and creep of the San Andreas Fault at Parkfield. Geology 38, pp. 667–670. DOI: 10.1130/G31091.1.

Schleicher, A.M., van der Pluijm, B.A. and Warr, L.N. (2012): Chlorite-smectite clay minerals and fault behavior: new evidence from the San Andreas Fault observatory at depth (SAFOD) core. Lithosphere 4, pp. 209–220. DOI: 10.1130/L158.1.

Schleicher, A.M., Sutherland, R., Townend, J., Toy, V.G. and van der Pluijm, B.A. (2015): Clay mineral formation and fabric development in the DFDP-1B borehole, central Alpine Fault, New Zealand. New Zealand Journal of Geology and Geophysics 58, pp. 13–21. DOI: 10.1080/00288306.2014.979841.

Schneider, C.A., Rasband, W.S. and Eliceiri, K.W. (2012): NIH Image to ImageJ: 25 years of image analysis. Nature methods 9, pp. 671–675.

Scholz, C.H. (1987): Wear and gouge formation in brittle faulting. Geology 15, pp. 493–495.

Scholz, C.H. (2002): The Mechanics of Earthquakes and Faulting. 2nd edition. Cambridge University Press, Cambridge.

Schrank, C.E., Handy, M.R. and Fusseis, F. (2008): Multiscaling of shear zones and the evolution of the brittle-to-viscous transition in continental crust. Journal of Geophysical Research 113. DOI: 10.1029/2006JB004833.

Schuck, B., Desbois, G. and Urai, J.L. (2015): On the workflow of the microstructural analysis of experimentally deformed clay-rocks. In: von Hagke, C., Urai, J., Reicherter, K., Wellmann, F., Hilgers, C. (eds.): 20th International Conference on Deformation Mechanisms, Rheology & Tectonics, Geotectonic Research 97 - Special Issue, pp. 158–159.

Schuck, B., Janssen, C., Schleicher, A.M., Toy, V.G. and Dresen, G. (2018): Microstructures imply cataclasis and authigenic mineral formation control geomechanical properties of New Zealand's Alpine Fault. Journal of Structural Geology 110, pp. 172–186. DOI: 10.1016/jsg.2018.03.001.

Schulz, W.H., Smith, J.B., Wang G.and Jiang, J. and Roering, J.J. (2018): Clayey landslide initiation and acceleration strongly modulated by soil swelling. Geophysical Research Letters 45, pp. 1888–1896. DOI: 10.1002/2017GL076807.

Scott, J.M., Auer, A., Muhling, J.R., Czertowicz, T.A., Cooper, A.F., Billia, M.A. and Kennedy, A.K. (2015): New P-T and U-Pb constraints on Alpine Schist metamorphism in south Westland, New Zealand. New Zealand Journal of Geology and Geophysics 58, pp. 385–397. DOI: 10.1080/00288306.2015.1093005.

Segall, P. and Pollard, D.D. (1983): Nucleation and growth of strike slip faults in granite. Journal of Geophysical Research 88, pp. 555–568. DOI: 10.1080/00288306.2015.1093005.

Shand, S.J. (1916): The pseudotachylytes of Parijs (Orange Free State), and its relation to 'trap-shotten gneiss' and 'flinty crush-rock'. Quarterly Journal of the Geological Society 72, pp. 198–222.

Shervais, K. and Kirkpatrick, J. (2016): Smoothing and re-roughening processes: The geometric evolution of a single fault zone. Journal of Structural Geology 98, pp. 130–143.

Shi, Y., Allis, R. and Davey, F. (1996): Thermal modeling of the southern Alps, New Zealand. Pure and Applied Geophysics 146, pp. 469–501.

Shuzui, H. (2001): Process of slip-surface development and formation of slip-surface clay in landslides in Tertiary volcanic rocks, Japan. Engineering Geology 61, pp. 199–219.

Sibson, R.H. (1973): Interactions between temperature and pore-fluid pressure during earthquake faulting and a mechanism for partial or total stress relief. Nature Physical Science 243, pp. 66–68.

Sibson, R.H. (1975): Generation of pseudotachylyte by ancient seismic faulting. Geophysical Journal of the Royal Astronomical Society 43, pp. 775–794.

Sibson, R.H. (1977): Fault rocks and fault mechanisms. Journal of the Geological Society London 113, pp. 191–213.

Sibson, R.H., White, S.H. and Atkinson, B.K. (1979): Fault rock distribution and structure within the Alpine Fault Zone: A preliminary account. In: Walcott, R.I. and Cresswell, M.M. (eds.): The origin of the Southern Alps. Bulletin of the Royal Society of New Zealand 18, pp. 55–65.

Sibson, R.H. (1985): A note on fault reactivation. Journal of Structural Geology 7, pp. 751–754.

Sibson, R.H. (1986): Earthquakes and rock deformation in crustal fault zones. Annual Reviews of Earth and Planetary Sciences 14, pp. 149–175.

Sibson, R.H., Robert, F.R. and Poulson, K.H. (1988): High-angle reverse faults, fluid-pressure cycling, and mesothermal gold-quartz deposits. Geology 16, pp. 551–555. DOI: 10.1002/ggge.20236.

Sibson, R.H. (1992a): Fault-valve behavior and the hydrostatic-lithostatic fluid pressure interface. Earth Science Reviews 32, pp. 141–144.

Sibson, R.H. (1992b): Implications of fault-valve behavior for rupture nucleation and recurrence. Tectonophysics 211, pp. 283–293.

Sibson, R.H. (2003): Thickness of the Seismic Slip Zone. Bulletin of the Seismological Society of America 93, pp. 1169–1178.

Skempton, A.W. and Petley, D.J. (1967): The strength along structural discontinuities in stiff clays. Proceedings of the Geotechnical Conference Oslo, pp. 29–46.

Skempton, A.W. (1985): Residual strength of clays in landslides, folded strata and the laboratory. Géotechnique 35, pp. 3–18.

Smeraglia, L., Bettucci, A., Billi, A., Carminati, E., Cavallo, A., Di Toro, G., Natali, M., Passeri, D., Rossi, M. and Spagnuolo, E. (2017): Microstructural evidence for seismic and aseismic slip along clay-bearing, carbonate faults. Journal of Geophysical Research: Solid Earth 122, pp. 3895–3915. DOI: 10.1002/2017JB014042.

Smith, S.A.F., Billi, A., Di Toro, G. and Spiess, R. (2011): Principal slip zones in limestones: Microstructural characterization and implications for the seismic cycle (Tre Monti Fault, central Apennines, Italy). Pure and Applied Geophysics 168, pp. 2365–2393. DOI: 10.1007/s00024-011-0267-5.

Solum, J.G., van der Pluijm, B.A. and Peacor, D.R. (2005): Neocrystallization, fabrics and age of clay minerals from an exposure of the Moab Fault, Utah. Journal of Structural Geology 27, pp. 1563–1576. DOI: 10.1016/2010.07.009.

Solum, J.G., Hickman, S.H., Lockner, D.A., Moore, D.E., van der Pluijm, B.A., Schleicher, A.M. and Evans, J.P. (2006): Mineralogical characterization of protolith and fault rocks from the SAFOD Main Hole. Geophysical Research Letters 33. DOI: 10.1029/2006GL027285.

Solum, J.G. and van der Pluijm, B.A. (2009): Quantification of fabrics in clay gouge from the Carboneras fault, Spain and implications for fault behavior. Tectonophysics 475, pp. 554–562. DOI: 10.1016/j.tecto.2009.07.006.

Solum, J.G., Davatzes, N.C. and Lockner, D.A. (2010): Fault-related clay authigenesis along the Moab Fault: Implications for calculations of fault rock composition and mechanical and hydrologic fault zone properties. Journal of Structural Geology 32, pp. 1899–1911. DOI: 10.1016/2010.07.009.

Spandler, C., Worden, K., Arculus, R. and Eggins, S. (2005): Igneous rocks of the Brook Street Terrane, New Zealand: implications for Permian tectonics of eastern Gondwana and magma genesis in modern intra-oceanic volcanic arcs. New Zealand Journal of Geology and Geophysics 48, pp. 167–183.

Stern, T.A., Kleffmann, S., Okaya, D., Scherwath, M. and Bannister, S. (2001): Low seismic-wave speeds and enhanced fluid pressure beneath the Southern Alps of New Zealand. Geology 29, pp. 679–682.

Stünitz, H., Keulen, N., Hirose, T. and Heilbronner, R. (2010): Grain size distribution and microstructures of experimentally sheared granitoid gouge at coseismic slip rates – Criteria to distinguish seismic and aseismic faults? Journal of Structural Geology 32, pp. 59–69. DOI: 10.1016/j.jsg.2009.08.002.

Sutherland, R., Berryman, K. and Norris, R. (2006): Quaternary slip rate and geomorphology of the Alpine Fault: Implications for kinematics and seismic hazard in southwest New Zealand. GSA Bulletin 118, pp. 464–474. DOI: 10.1130/B25627.1.

Sutherland, R., Eberhart-Phillips, D., Harris, R.A., Stern, T., Beavan, J., Ellis, S., Henrys, S., Cox, S., Norris, R.J., Berryman, K.R., Townend, J., Bannister, S., Pettinga, J., Leitner, B., Wallace, L., Little, T.A., Cooper, A.F., Yetton, M. and Stirling, M. (2007): Do great earthquakes occur on the Alpine Fault in central South Island, New Zealand? In: Okaya, D., Stern, T.A. and Davey, F. (eds.): A continental plate boundary: Tectonics at South Island, New Zealand. AGU Geophysical Monograph 175, pp. 235–251.

Sutherland, R., Toy, V.G., Townend, J., Cox, S.C., Eccles, J.D., Faulkner, D.R., Prior, D.J., Norris, R.J., Mariani, E., Boulton, C., Carpenter, B.M., Menzies, C.D., Little, T.A., Hasting, M., De Pascale, G.P., Langridge, R.M., Scott, H.R., Lindroos, Z.R., Fleming, B. and Kopf, A.J. (2012): Drilling reveals fluid control on architecture and rupture of the Alpine Fault, New Zealand. Geology 40, pp. 1143–1146. DOI: 10.1130/G33614.1.

Sutherland, R., Townend, J., Toy, V., Allen, M., Baratin, L., Barth, N., Becroft, L., Benson, l., Boese, C., Boles, A., Boulton, C., Capova, L., Carpenter, B., Célérier, B., Chamberlain, C., Conze, R., Cooper, A., Coussens, J., Coutts, A., Cox, S., Craw, L., Doan, M., Eccles, J., Faulkner, D., Grieve, J., Grochowski, J., Gulley, A., Henry, G., Howarth, J., Jacobs, K., Jeppson, T., Kato, N., Keys, S., Kirilova, M., Kometani, Y., Kovacs, A., Langridge, R., Lin, W., Little, T., Mallyon, D., Mariani, B., Marx, R., Massiot, C., Mathewson, L., Melosh, B., Menzies, C., Moore, J., Morales, L., Morgan, C., Mori, H., Niemeijer, A., Nishikawa, O., Nitsch, O., Paris Cavailhès, J., Pooley, B., Prior, D., Pyne, A., Sauer, K., Savage, M., Schleicher, A., Schmitt, D., Shigematsu, N., Taylor-Offord, S., Tobin, H., Upton, P., Valdez, R., Weaver, K., Wiersberg, T., Williams, J., Yeo, S. and Zimmer, M. (2015): Deep Fault Drilling Project (DFDP), Alpine Fault Boreholes DFDP-2A and DFDP-2B Technical Completion Report. GNS Science Report 2015/50.

Sutherland, R., Townend, J., Toy, V., Upton, P., Coussens, J., Allen, M., Baratin, L.-M., Barth, N., Becroft, L., Boese, C., Boles, A., Boulton, C., Broderick, N.G.R., Janku-Capova, L., Carpenter, B.M., Célérier, B., Chamberlain, C., Cooper, A., Coutts, A., Cox, S., Craw, L., Doan, M.-L., Eccles, J., Faulkner, D., Grieve, J., Grochowski, J., Gulley, A., Hartog, A., Howarth, J., Jacobs, K., Jeppson, T., Kato, N., Keys, S., Kirilova, M., Kometani, Y., Langridge, R., Lin, W., Little, T., Lukacs, A., Mallyon, D., Mariani, E., Massiot, C., Mathewson, L., Melosh, B., Menzies, C., Moore, J., Morales, L., Morgan, C., Mori, H., Niemeijer, A., Nishikawa, O., Prior, D., Sauer, K., Savage, M., Schleicher, A., Schmitt, D.R., Shigematsu, N., Taylor-Offord, S., Teagle, D., Tobin, H., Valdez, R., Weaver, K., Wiersberg, T., Williams, J., Woodman, N. and Zimmer, M. (2017): Extreme hydrothermal conditions at an active plate-bounding fault. Nature 545, pp. 137–140. DOI: doi:10.1038/nature22355.

Taboada, T. and Garcia, C. (1997): Smectite formation produced by weathering in a coarse granite saprolite in Galicia (NW Spain). Catena 35.

Tembe, S., Lockner, D.A., Solum, J.G., Morrow, C.A., Wong, T.-F. and Moore, D.E. (2006): Frictional strength of cuttings and core from SAFOD drillhole phases 1 and 2. Geophysical Research Letters 33. DOI: 10.1029/2006GL02726.

Tembe, S., Lockner, D.A. and Wong, T.-F. (2010): Effects of clay content and mineralogy on frictional sliding behavior of simulated gouges: Binary and ternary mixtures of quartz, illite, and montmorillonite. Journal of Geophysical Research 115. DOI: 10.29/2009JB006383.

Toby, B.H. (2006): R factors in Rietveld analysis: How good is good enough? Powder Diffraction 21, pp. 67–70.

Toppozada, T.R., Branum, D.M., Reichle, M.S. and Hallstrom, C.L. (2002): San Andreas Fault Zone, California: M $\geq$ 5.5 earthquake history. Bulletin of the Seismological Society of America 92, pp. 2555–2601.

Townend, J. and Zoback, M.D. (2000): How faulting keeps the crust strong. Geology 28, pp. 399–402.

Townend, J., Sutherland, R. and Toy, V. (2009): Deep Fault Drilling Project - Alpine Fault, New Zealand. Scientific Drilling 8, pp. 75–82.

Townend, J., Sutherland, R., Toy, V.G., Eccles, J.D., Boulton, C., Cox, S.C. and McNamara, D. (2013): Late-interseismic state of a continental plate-bounding fault: Petrophysical results

from DFDP-1 wireline logging and core analysis, Alpine Fault, New Zealand. Geochemistry, Geophysics, Geosystems 14, pp. 3801–3820. DOI: 10.1002/ggge.20236.

Townend, J., Sutherland, R., Toy, V.G., Doan, M.-L., Célérier, B., Massiot, C., Coussens, J., Jeppson, T., Janku-Capova, L., Remaud, L., Upton, P., Schmitt, D.R., Williams, J., Allen, M.J., Baratin, L.-M., Barth, N., Becroft, L., Boese, C.M., Boulton, C., Broderick, N., Carpenter, B., Chamberlain, C.J., Cooper, A., Coutts, A., Cox, S.C., Craw, L., Eccles, J.D., Faulkner, D., Grieve, J., Grochowski, J., Gulley, A., Hartog, A., Henry, G., Howarth, J., Jacobs, K., Kato, N., Keys, S., Kirilova, M., Kometani, Y., Langridge, R., Lin, W., Little, T., Lukacs, A., Mallyon, D., Mariani, E., Mathewson, L., Melosh, B., Menzies, C., Moore, J., Morales, L., Mori, H., Niemeijer, A., Nishikawa, O., Nitsch, O., Paris, J., Prior, D.J., Sauer, K., Savage, M.K., Schleicher, A., Shigematsu, N., Taylor-Offord, S., Teagle, D., Tobin, H., Valdez, R., Weaver, K., Wiersberg, T. and Zimmer, M. (2017): Petrophysical, geochemical, and hydrological evidence for extensive fracture-mediated fluid and heat transport in the Alpine Fault's hanging-wall damage zone. Geochemistry, Geophysics, Geosystems 18, pp. 4709–4732. DOI: 10.1002/2017GC007202.

Toy, V.G., Craw, D., Cooper, A.F. and Norris, R.J. (2010): Thermal regime in the central Alpine Fault zone, New Zealand: constraints from microstructures, biotite chemistry and fluid inclusion data. Tectonophysics 485, pp. 178–192. DOI: 10.1016/j.tecto.2009.12.013.

Toy, V.G., Ritchie, S. and Sibson, R.H. (2011): Diverse habitats of pseudotachylytes in the Alpine Fault Zone and relationships to current seismicity. In: Fagereng, Å., Toy, V.G. and Rowland, J.V. (eds.): Geology of the earthquake source: A volume in honour of Rick Sibson. Geological Society London, Special Publications 359, pp. 115–133.

Toy, V.G., Norris, R.J., Prior, D.J., Walrond, M. and Cooper, A.F. (2013): How do lineations reflect the strain history of transpressive shear zones? The example of the active Alpine Fault Zone, New Zealand. Journal of Structural Geology 50, pp. 187–198. DOI: 10.1016/j.jsg.2012.06.006.

Toy, V.G., Boulton, C.J., Sutherland, R., Townend, J., Norris, R.J., Little, T.A., Prior, D.J., Mariani, E., Faulkner, D., Menzies, C.D., Scott, H. and Carpenter, B.M. (2015): Fault rock lithologies and architecture of the central Alpine Fault, New Zealand, revealed by DFDP-1 drilling. Lithosphere 7, pp. 155–173. DOI: 10.1130/L395.1.

Toy, V.G., Sutherland, R., Townend, J., Allen, M.J., Becroft, L., Boles, A., Boulton, C., Carpenter, B., Cooper, A., Cox, S.C., Daube, C., Faulkner, D.R., Halfpenny, A., Kato, N., Keys, S., Kirilova, M., Kometani, Y., Little, T., Mariani, E., Melosh, B., Menzies, C.D., Morales, L., Morgan, C., Mori, H., Niemeijer, A., Norris, R., Prior, D., Sauer, K., Schleicher, A.M., Shigematsu, N., Teagle, D.A.H., Tobin, H., Valdez, R., Williams, J., Yea, S., Baratin, L.-M., Barth, N., Benson, A., Boese, C., Célérier, B., Chamberlain, C.J., Conze, R., Coussens, J., Craw, L., Doan, M.-L., Eccles, J., Grieve, J., Grochowski, J., Gulley, A., Howarth, J., Jacobs, K., Janku-Capova, L., Jeppson, T., Langridge, R., Mallyon, D., Marx, R., Massiot, C., Mathewson, L., Moore, J., Nishikawa, O., Pooley, B., Pyne, A., Savage, M.K., Schmitt, D., Taylor-Offord, S., Upton, P., Weaver, K.C., Wiersberg, T., Zimmer, M. and DFDP-2 Science Team (2017): Bedrock geology of DFDP-2B, central Alpine Fault,

New Zealand. New Zealand Journal of Geology and Geophysics 60, pp. 497–518. DOI: 10.1080/00288306.2017.1375533.

Twiss, R.J. and Moores, E.M. (2007): Structural Geology. 2nd edition. W.H. Freeman and Company.

Ujiie, K., Yamaguchi, H., Sakaguchi, A. and Toh, S. (2007): Pseudotachylytes in an ancient accretionary complex and implications for melt lubrication during subduction zone earthquakes. Journal of Structural Geology 29, pp. 599–613. DOI: 10.1016/j.jsg.2006.10.012.

Ujiie, K., Tanaka, H., Saito, T., Tsutsumi, A., Mori, J.J., Kameda, J., Brodsky, E.E., Chester, F.M., Eguchi, N., Toczko, S. and Expedition 343 and 343T Scientists (2013): Low Coseismic Shear Stress on the Tohoku-Oki Megathrust Determined from Laboratory Experiments. Science 342, pp. 1211–1214. DOI: 10.1126/science.1243485.

United Nations, Department of Economic & Social Affairs - Population Division (2017): World population prospects. The 2017 revision, key findings and advance tables. Working Paper ESA/P/WP/248.

Upton, P., Song, B. and Koons, P. (2017): Topographic control on shallow fault structure and strain partitioning near Whataroa, New Zealand demonstrates weak Alpine Fault. New Zealand Journal of Geology and Geophysics 61, pp. 1–8. DOI: 10.1080/00288306.2017.1397706.

van der Pluijm, B.A., Ho, N.-C. and Peacor, D.R. (1994): High-resolution X-ray texture goniometry. Journal of Structural Geology 16, pp. 1029–1032.

Van Eijs, R.M.H.E., Mulders, F.M.M., Nepveu, M., Kenter, C.J. and Scheffers, B.C. (2006): Correlation between hydrocarbon reservoir properties and induced seismicity in the Netherlands. Engineering Geology 84, pp. 99–111. DOI: 19.1016/j.enggeo.2006.01.002.

Vannucchi, P., Maltman, A., Bettelli, G. and Clennell, B. (2003): On the nature of scaly fabric and scaly clay. Journal of Structural Geology 25, pp. 673–688.

Virgo, S., Abe, S. and Urai, J.L. (2013): Extension fracture propagation in rocks with veins: Insight into the crack-seal process using Discrete Element Method modeling. Journal of Geophysical Research: Solid Earth 118, pp. 5236–5251. DOI: 10.1002/2013JB010540.

Wallace, L.M., Beavan, J., McCaffrey, R., Berryman, K. and Denys, P. (2007): Balancing the plate motion budget in the South Island, New Zealand using GPS, geological and seismological data. Geophysical Journal International 168, pp. 332–352. DOI: 10.1111/j.1365-246X.2006.03183.x.

Wang, H., Haibing, L., Janssen, C., Sun, Z. and Jailing, S. (2015): Multiple generations of pseudotachylyte in the Wenchuan fault zone and their implications for coseismic weakening. Journal of Structural Geology 74, pp. 159–171. DOI: 10.1016/j.jsg.2015.03.007.

Ward, S.N. and Day, S. (2011): The 1963 Landslide and Flood at Vaiont Reservoir Italy. A tsunami ball simulation. Italien Journal of Geosciences 130, pp. 16–26. DOI: 10.3301/ijg.2010.21.

Warr, L.N. and Cox, S. (2001): Clay mineral transformations and weakening mechanisms along the Alpine Fault, New Zealand. In: Holdsworth, R.E., Strachan, R.A., Magloughlin, J.F. and Knipe, R.J. (eds.): The nature and tectonic significance of fault zone weakening. Geological Society, London, Special Publications 186, pp. 85–101.

Warren-Smith, E., Lamb, S. and Stern, T.A. (2017): Stress field and kinematics for diffuse microseismicity in a zone of continental transpression, South Island, New Zealand. Journal of Geophysical Research: Solid Earth 122, pp. 2798–2811. DOI: 10.1002/2017JB013942.

Wells, D.L. and Coppersmith, K.J. (1994): New empirical relationships among magnitude, rupture length, rupture width, rupture area, and surface displacement. Bulletin of the Seismological Society of America 84, pp. 974–1002.

Wen, B.-P. and Aydin, A. (2003): Microstructural study of a natural slip zone: quantification and deformation history. Engineering Geology 68, pp. 289–317.

Wen, B.-P. and Aydin, A. (2004): Deformation history of a landslide slip zone in light of soil microstructure. Environmental & Engineering Geoscience 10, pp. 123–149.

Wen, B.-P. and Aydin, A. (2005): Mechanism of a rainfall-induced slide-debris flow: Constraints from microstructure of its slip zone. Engineering Geology 78, pp. 69–88. DOI: 10.1016/j.enggeo.2004.10.007.

Wen, B.-P., Aydin, A., Duzgoren-Aydin, N.S., Li, Y.R., Chen, H.Y. and Xiao, S.D. (2007): Residual strength of slip zones of large landslides in the Three Gorges area, China. Engineering Geology 93, pp. 82–98. DOI: 1016/j.enggeo.2007.05.006.

Wenk, H.-R. (1978): Are pseudotachylites products of fracture of fusion? Geology 6, pp. 507–511.

Wenk, H.-R., Johnson, L.R. and Ratschbacher, L. (2000): Pseudotachylites in the Eastern Peninsular Ranges of California. Tectonophysics 321, pp. 253–277.

Wenk, H.-R., Voltolini, M., Mazurek, M., van Loon, L.R. and Vinsot, A. (2008): Preferred Orientations and Anisotropy in Shales: Callovo-Oxfordian Shale (France) and Opalinus Clay (Switzerland). Clays and Clay Minerals 56, pp. 285–306.

Wenk, H.-R., Kanitpanyacharoen, W. and Voltolini, M. (2010): Preferred orientation of phyllosilicates: Comparison of fault gouge, shale and schist. Journal of Structural Geology 32, pp. 478–489. DOI: 10.1016/j.jsg.2010.02.003.

Wenk, H.-R., Janssen, C., Kenkmann, T. and Dresen, G. (2011): Mechanical twinning in quartz: Shock experiments, impact, pseudotachylites and fault breccias. Tectonophysics 510, pp. 69–79. DOI: 10.1016/j.tecto.2011.06.016.

Wibberley, C.A.J., Yielding, G. and Di Toro, G. (2008): Recent advances in the understanding of fault zone internal structure: a review. In: Wibberley, C.A.J., Kurz W., Imber, J., Holdsworth, R.E. and Collettini, C. (eds.): The Internal Structure of Fault Zones: Implications for Mechanical and Fluid-Flow Properties. Geological Society, London, Special Publications 299, pp. 5–33. DOI: 10.1144/SP299.2.

Williams, J.N., Toy, V.G., Massiot, C., McNamara, D.D. and Wang, T. (2016): Damaged beyond repair? Characterizing the damage zone of a fault late in its interseismic cycle, the Alpine Fault, New Zealand. Journal of Structural Geology 90, pp. 76–94. DOI: 10.1016/j.jsg.2016.07.006.

Williams, J.N., Toy, V.G., Smith, S.A.F. and Boulton, C. (2017): Fracturing, fluid-rock interaction and mineralization during the seismic cycle along the Alpine Fault. Journal of Structural Geology 103, pp. 151–166. DOI: 10.1016/j.jsg.2017.09.011.

Williams, J.N., Toy, V.G., Massiot, C., McNamara, D.D., Smith, S.A.F. and Mills, S. (2018): Controls on fault zone structure and brittle fracturing in the foliated hanging wall of the Alpine Fault. Solid Earth 9, pp. 469–489. DOI: 10.5194/se-9-469-2018.

Wilson, B., Dewers, T., Reches, Z. and Brune, J. (2005): Particle size and energetics of gouge from earthquake rupture zones. Nature 434, pp. 749–752.

Wirth, R. (2004): A novel technology for advanced application of micro- and nanoanalysis in geosciences and applied mineralogy. European Journal of Mineralogy 16, pp. 863–876. DOI: 10.1127/0935-1221/2004/0016-0863.

Wirth, R. (2009): Focused Ion Beam (FIB) combined with SEM and TEM: advanced analytical tools for studies of chemical composition, microstructure and crystal structure in geomaterials on a nanometre scale. Chemical Geology 261, pp. 217–229. DOI: 10.1016/j.chemgeo.2008.05.019.

Woodcock, N.H. and Mort, K. (2008): Classification of fault breccias and related fault rocks. Geological Magazine 145, pp. 435–440. DOI: 10.1017/S0016756808004883.

Wu, J., Li., N., Hallegatte, S., Shi, P., Hu, A. and Liu, X. (2012): Regional indirect economic impact evaluation of the 2008 Wenchuan Earthquake. Environmental Earth Sciences 65, pp. 161–172. DOI: 10.1007/s12665-011-1078-9.

Yalcin, A. (2007): The effects of clay on landslides: A case study. Applied Clay Science 38, pp. 77–85. DOI: 10.1016/j.clay.2007.01.007.

Yamaguchi, A, Ishikawa, T., Kato, Y., Nozaki, T., Meneghini, F., Rowe, C.D., Moore, J.C., Tsutsumi, A. and Kimura, G. (2014): Fluid-rock interaction recorded in black fault rocks in the Kodiak accretionary complex, Alaska. Earth, Planets and Space 66. DOI: 10.1186/1880-5981-66-58.

Zhang, M. and McSaveney, M.J. (2018): Is air pollution causing landslides in China? Earth and Planetary Science Letters 81, pp. 284–289. DOI: 10.1016/j.epsl.2017.10.045.

Zoback, M., Hickman, S., Ellsworth, W. and the SAFOD Science Team (2011): Scientific Drilling Into the San Andreas Fault Zone - An Overview of SAFOD's First Five Years. Scientific Drilling 11, pp. 14–28. DOI: 10.2204/iodp.sd.11.02.2011.

Zoback, M.D., Hickman, S. and Ellsworth, W. (2007): The role of fault zone drilling. In: Kanamori, H. and Schubert, G. (eds.): Earthquake seismology – Treatise on geophysics. Elsevier, pp. 649–674.

Zuo, L., Lourenco, S.D.N. and Baudet, B.A. (2019): Experimental insight into the particle morphology changes associated with landslide movement. Landslides 16, pp. 787–798. DOI: 10.1007/s10346-018-1113-y.

List of Figures

List of Tables